Project report

TGB4930 Engineering Geology and Rock Mechanics Master's Thesis

Leena Jaakola

Properties of Deep Weathered Swelling Clay and its Stability Implications in Tunneling

Trondheim, 10 June, 2019

NTNU
Norwegian University of Science and Technology
Faculty of Engineering
Department of Geoscience and Petroleum

NTNU

Abstract

Remains of subtropical deep weathered clay found in fracture and weakness zones in the bedrock in the Trøndelag area yields poor conditions for tunnel construction and have resulted in expensive difficulties for such projects. Smectite has a high swelling potential when hydrated, which can induce swelling pressure and damage the structures it surrounds. This study was designed as an extension of a previous study performed at NTNU that showed ambiguity between free swell and swelling pressure measurements. 55 samples exhibiting swelling behavior were obtained from old SINTEF projects. Swelling minerals were identified using X-Ray diffraction and the fine particle fraction grain size distribution was measured using laser diffraction spectroscopy. Swelling potential was quantified using constant volume oedometer testing and free swell tests. The potential of variance (r^2) between mineral content and maximum swelling pressure was 0.8. Free swell was less correlated with smectite content, yielding an r^2 value of 0.4 and several outliers. Free swell was affected by other physical parameters in addition to smectite content. Additional tests, which could not be performed due to limited sample material, are desired to better understand the physical properties behind each measure of swelling potential.

Contents

1 | Introduction

1.1 Purpose and Objectives of this Study

The interest of this study is to better understand the mechanisms behind swelling clay minerals, which can cause stability problems in subsurface constructions such as tunnels, slopes, and foundations. This study is exploratory in nature and will cover a large variety of physical parameters related to swelling clay material in attempt to find relationships. These relationships could ultimately improve the predictability of the affects of swelling clay material on the stability of subsurface structures. The main objectives of this study are thus defined as follows:

- To identify knowledge gaps in the most important mechanisms behind the swelling potential of clay minerals
- To explore variables affecting the swelling behavior of clay material, including variation in clay minerals, grain size distribution (especially the fraction less than 20 micrometers), compaction, water content and drying procedures, and uncertainties in X-Ray Diffraction at low diffraction angles
- To perform a variety of laboratory experiments which measure the physical properties of clay and swelling potential, and assess the reliability of the methods used
- To investigate relationships between mineralogical content and grain size distribution of a material and its swelling potential

1.2 Background

Tunnelling stability problems experienced in Norway such as water leakage and rock instability are partially attributed to the presence of deep weathered swelling clay minerals, including smectite, formed by chemical weathering under subtropical conditions in the Jurassic and Cretaceous Periods. Repeated glacial events have stripped large volumes of surface rock, leaving behind subtropical saprolite remnants that have been preserved deep in bedrock. Gouge material found in weakness zones, consists of both clay minerals and rock fragments, and is a major threat to the stability of subsurface structures. The clay material often exhibits swelling characteristics and the rock mass becomes disturbed, resulting in low quality construction material.

Swelling minerals that are constricted by a subsurface structure such as a tunnel will exert external pressure and result in structural damage. Weakness zones containing deep weathered swelling clay are one of the main causes of stability problems associated with hard rock tunnelling in Norway [28]. Water leakage and cave-ins resulting from swelling clay areas requiring additional reinforcement are common and costly. In extreme cases, a tunnel must be diverted or abandoned. The swelling potential of clay minerals should be quantified and interpreted such that an accurate prediction of the in-situ behavior of the material can

be made, and ultimately to design sufficient support resistant to the pressure that will be exerted on the subsurface structure.

1.3 Swelling Potential

The definition of swelling potential given by ISRM (1983) forms the basis of this study:

> *Swelling is a physio-chemical reaction involving water and stress relief. When volume expansion is restricted, the material expresses itself instead with an increased pressure acting on its surroundings* [12].

Swelling clay results from a combination of physical and chemical processes. The primary stage of swelling involves hydration, where water molecules are adsorbed on the clay mineral surface. A second stage of swelling, called osmotic swelling, occurs due to a higher concentration of ions in the water between two backbone layers than in the surrounding pore water. Water flows towards equilibrium, or towards the highest ion concentration. In most cases, the swelling potential of a material is described in terms of swelling pressure and free swell. Swelling pressure develops if a structure is located on or among expanding material, prohibiting volume expansion. Free swelling describes an increase in volume of the material without any application of external forces. These parameters can be found using standardized oedometer and free swell tests, respectively.

1.4 Outline of Sections

The outline of the study is organized as follows:

- **Section 2: Theories and State of the Art of Clay Swelling Potential**
  Background information regarding the formation of swelling clays, swelling clay mineralogy, macroscopic classification schemes, and internal and external factors affecting swelling potential
- **Section 3: Methods**
  Laboratory techniques used to measure clay properties and swelling potential
- **Section 4: Results**
  Findings of the laboratory experiments
- **Section 5: Discussion**
  Critical discussion of the laboratory results and the reliability of the methods used

2 | Theories and State of the Art of Clay Swelling Potential

Formation of deep weathered swelling clay in Norway is presented in this Section, followed by case studies of historical failures in tunnelling projects due to the presence of swelling clay, macroscopic measurements of swelling, and the variables effecting swelling potential.

2.1 Formation of Swelling Clay Minerals

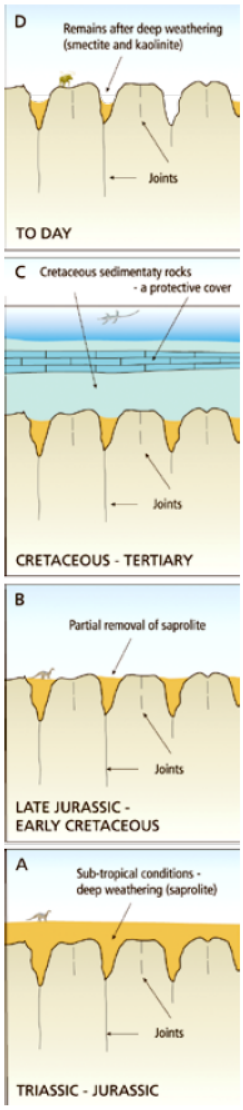

Figure 2.1: Geological timeline of smectite [1]

Clay minerals are fine-grained sheet silicate minerals which form as a result of weathering in the presence of water [16]. Soil particles that contribute most to soil swelling phenomena are the clay-sized particles (less than 2 micrometers in diameter), and more specifically the clay minerals [27]. Clay minerals are often found in gouges and weakness zones, formed from altered rock masses. Clay minerals are unique from other minerals found in Earth's rock masses because they are formed as the products of chemical alteration processes where the conditions favor the formation of hydrous fine-grained minerals. Given their small particle size and high surface-to-volume ratio, clay minerals are highly chemically active compared to other soil and sediment constituents.

The chemically weathered bedrock found within Norway, termed saprolite, is thought to have formed from acidic groundwater percolating bedrock in humid subtropical conditions during the Jurassic and early Cretaceous Periods [24]. A schematic illustration of the geological processes describing the formation of saprolites is provided in Figure 2.1. During the Jurassic Period, the climate of today's Norway was warm. Faulting, volcanic activity, and hydrothermal activity formed weak zones where acidic water was able to penetrate deep into the bedrock, attacking silicate minerals and breaking them down into clay. The saprolite products of this weathering include smectite and kaolinite (Figure 2.1A). Mechanical weathering processes partially removed the surface saprolites until the beginning of the Cretaceous Period (Figure 2.1B) [33].

The Cretaceous Period was characterized by sea level rise of 300-400 meters, which flooded mainland Norway and deposited soft rocks such as claystone and chalk (Figure 2.1C). The movement of ice and meltwater during the ice ages of the Quaternary Period removed these soft rocks and weathered material from the surface, but the weathered material present in deep fracture zones to depths of 200-300 meters were preserved and is now being exposed through tunnelling operations (Figure 2.1D) [33].

2.2 Failures Due to Deep Weathered Clay

Primary causes of deep weathered clay related failures in tunnelling excavations are introduced in this Section, as well as case studies of major damages and failures in Norwegian construction projects. Figure 2.2 shows the areas of Norway and Sweden with extensive clay bearing bedrock remaining and yielding poor tunnelling conditions.

Figure 2.2: Areas with remains of subtropical deep weathering in fracture zones [33]

Jointing of a Rock Mass
Joints and discontinuities present within a rock mass largely govern its in-situ properties [21]. From a distance, weakness zones in the bedrock appear as trenches or gorges on the surface which extend down into the bedrock. Most faults and crushed zones result from shear movement. They may develop as pictured in Figure 2.3 from left to right, with increasing shear stress.

Rock high in clay minerals, talc, graphite, or mica content have a generally lower shear strength; reduction of the binding material between mineral grains due to alterations can also affect rock strength. Water can carry various minerals through weakness zones, which may also alter the chemical state of minerals. Feldspar, for example, can be hydrolyzed into clay minerals, causing a strength reduction in the material. In addition, some clay minerals found in gouge material have the tendency to swell when exposed to water.

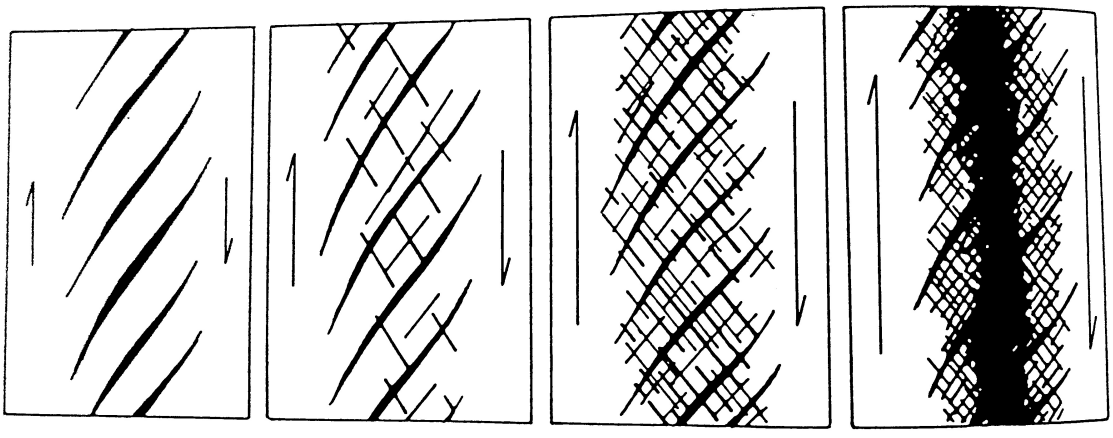

Figure 2.3: Development of shear faults in a brittle rock mass [21]

Tunnels at all depths have reported encounters with weakness zones. Weakness zones containing deep weathered swelling clay are one of the main causes of stability problems asso-

ciated with hard rock tunnelling in Norway. Lineaments on the surface can be extrapolated down to the depth of the tunnel alignment using the measured orientation to prevent interception.

Problems with Water Inflow

The construction of hydropower tunnels are especially sensitive to the presence of swelling clay. Ventilation air is blown through the tunnel during its construction, causing reduced water content in the clay and greater strength [21]. Stability problems may be either greatly underestimated or neglected completely. Later, when the tunnel is filled with water, the material expands and may lead to dangerous rockfalls and slides. Based on the formation of clay zones in bedrock alone, tunnel stability problems should decrease with depth. However, water leakage problems tend to increase with depth, complicating the situation. The combined stability and water leakage problems are shown in Figure 2.4 [33].

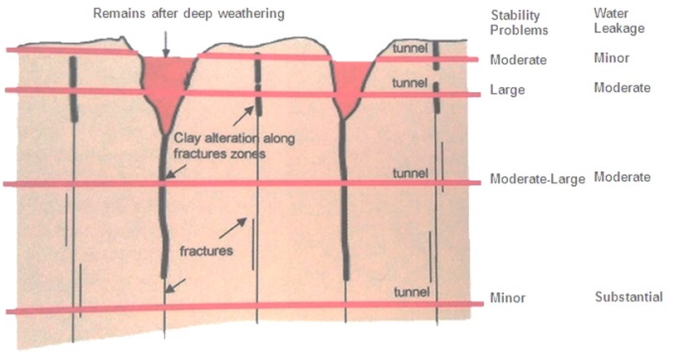

Figure 2.4: Variation of tunnel problems with depth [33]

The weathering and strength reducing effects of water can reduce the stability of the tunnel. The stability of the weakness zones are also compromised due to washout and dissolution of minerals. An example is the dissolution of calcite due to acidic water can cause large water inflows through karst channels. Sulfide oxidation producing sulfuric acid is another potentially damaging chemical reaction that can result in rapid corrosion of structural supports [21].

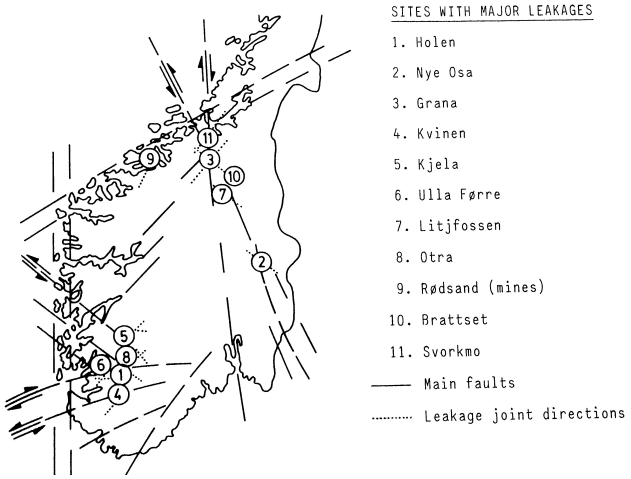

Figure 2.5: Cases of large water inflow problems [21]

Figure 2.5 maps cases of various large water inflows into hydropower tunnels in the crystalline rocks of southern Norway. Experience in Norway has shown that large water inflows are difficult to predict. The cites represent a large variation of leakage volume and water head. However, there are a number of common features reported in the incidents that might help prevent future large inflows of water. In each case, the rock was strong and had a high Elastic Modulus. The leakage joints were parallel tensile feather joints (like the ones shown in Figure 2.3). The main leakages were often caused by channels created by the dissolution of calcite.

Case Studies of Damages and Failures due to Deep Weathered Clay
Although the typical hard rock found in Norway provides very stable tunnelling conditions, the history of tunnel construction in Norway is peppered with several examples of expensive difficulties and failures due to the unexpected presence of deep weathered clay. The Tunnsjødal hydropower tunnel was a $40m^2$ tailtrace tunnel, located in an area primarily characterized by Palaeooic granitic gneiss, a supposedly "high quality" material expected to require little to no additional support. A set of feather joints was found during excavation, and water started leaking from a brecciated zone between the joints. A slide occurred two weeks after excavation along a 30 meter section, requiring immediate and complex rock support, primarily consisting of the installation of a cast-in-place concrete lining. The slide is pictured in Figure 2.6.

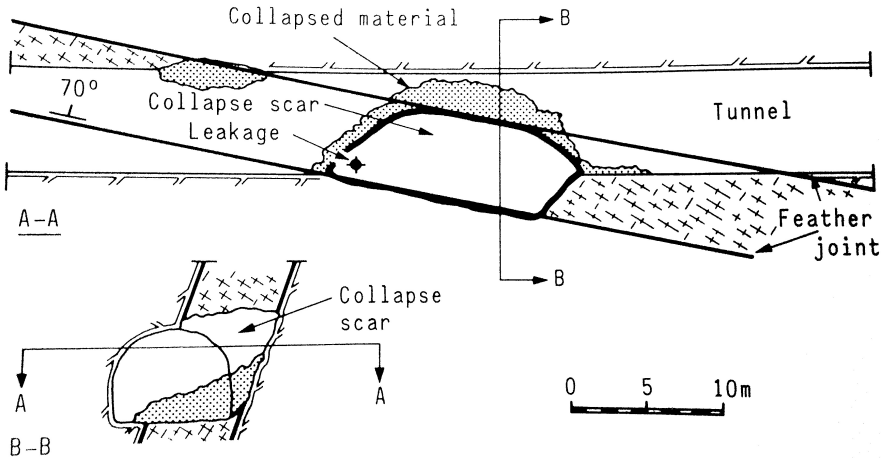

Figure 2.6: Slide at Tunnsjødal hydropower tunnel caused by smectite [21]

After the excavation was stabilized, it was observed that the granitic rock had disintegrated into a clayey mud containing smectite. A slow adsorption rate due to low permeability of the altered granite allowed the rock to maintain standing for a long period before the slide, but if smectite had been present as a gouge filling the stand up time in similar conditions would have been much shorter [21].

Construction of the Holmenkollbanen subway tunnel met ongoing groundwater drainage issues and rock-falls in clay bearing zones that drove the development company into bankruptcy [33]. Blasting of the railway tunnel through Lieråsen was halted when swelling clay alteration along linear weakness zones caused water leakage and cave-ins and ultimately forced the tunnel to be diverted [23]. More recently, construction of the Romeriksporten and Oslo Fjord tunnels faced costly water leakage and rock falls [23].

The history of damages caused by the presence of swelling clay and the large number of ongoing tunnelling projects in Norway justify the need for investment in mapping and better understanding the material present in weakness zones.

2.3 Macroscopic Measures of Swelling

Swelling pressure development and volume change are the two main measurements used to describe the combined effect of all swelling processes occurring within the clay system.

Swelling Pressure
If a subsurface structure is built in an area of expansive soil, an increase in volume of soil is prohibited by its presence, causing a swelling pressure which can have serious structural consequences. Norsk Bergmekanikkgruppe classifies the swelling potential of clay according to the maximum swelling pressure obtained from oedometer testing according to Table 2.1:

Table 2.1: Swelling potential classified by oedometer swelling pressure [22]

Swell Potential	Not Active	Slightly Active	Active	Very Active
Swelling Pressure [MPa]	< 0.10	0.10 - 0.30	0.30 - 0.75	> 0.75

Volume Change
Norsk Bergmekanikkgruppe classifies the swelling potential of clay according to the free swelling percentage according to Table 2.2.

Table 2.2: Swelling potential classified by free swelling [22]

Free Swell Potential	Inactive	Slightly Active	Active	Very Active
Free Swelling [%]	< 100	100 - 140	140 - 200	> 200

Swellability Index

Swellability index (SI) is a measure of how water content varies with the stress condition of the material, equal to the difference in water content between 0.025 and 2 MN/m^2 (Equation (2.1)).

$$SI = w_2 - w_{0.025} \tag{2.1}$$

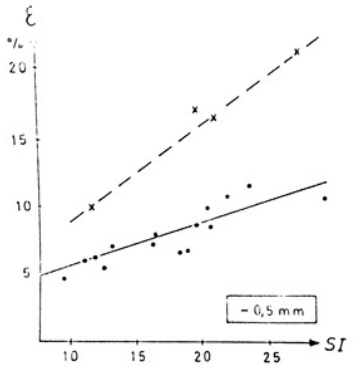

Figure 2.7: Swellability index and percent swelling by unloading from 2 to 0.025 MN/m^2[32].

SI is an appropriate description of materials whose consolidating properties are correlated with swelling properties. SI is a good assumption in particular for clay with a very low mica content, as shown by the experimental results in Figure 2.7, since mica is an elastic mineral and undergoes mechanical deformation [32]. Samples with high mica content are characterized by the dashed trendline in Figure 2.7 while samples with little to no mica are characterized by the solid trendline.

2.4 Preliminary Study

This study was designed as an extension of a project performed at Norges teknisk-naturvitenskapelige universitet (NTNU) in Autumn, 2019. XRD and free swelling tests were performed on six samples obtained from two locations in the Trøndelag area. The compiled results, provided in Table 2.3, include the measured fine fraction of particle size less than 20µm, the smectite-chlorite mixed-layer content, smectite content, and free swelling results.

Table 2.3: Results from preliminary study [13]

Sample	Fines <20µm (%)	Smectite-Chlorite (%)	Smectite (%)	Free Swell
697	2.4	0.0	0.0	140
698	11.8	0.0	0.0	109
699	17.1	0.0	0.0	128
700	3.7	5.0	6.0	100
701	5.9	7.0	0.0	168

The results of the free swelling tests did not clearly demonstrate the effect of smectite content in the material. Three samples (697, 698, 699) displayed one-dimensional swelling behavior even though the XRD did not indicate the presence of swelling minerals. Material containing a large fine fraction, such as 698 and 699, draws in more water through capillary action, resulting in a certain degree of expansion even with zero smectite content. In addition, sample 700 had a swelling mineral of 11 percent and did not display any free swelling activity in the free swelling test, while sample 701 contained 7 percent swelling minerals and showed relatively active free swelling at 168 percent. The difference in free swelling results was though to be attributed to 700 having less smectite in the <20µm fraction compared to 701.

2.5 Microstructural Behavior

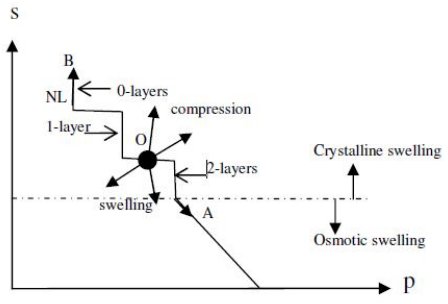

Figure 2.8: The neutral line (NL) during crystalline and osmotic swelling [36]

The expansion mechanisms prevalent soil include hydration, capillarity, and osmosis. The neutral line (NL) plotted in a pressure-suction regime indicates the boundary of swelling or compression. Suction expresses the ability of the material to hold water by the pressure required to squeeze out water [28].

Surface and cation hydration are predominant in the 20-550MPa range of suction for water contents less than 30%; reductions in suction cause step-wise microstructural expansion related to the hydration layer states. Osmotic swelling governs at suction values less than 20MPa [18], creating a NL in the swelling pressure-suction regime (Figure 2.8).

2.5.1 Hydration

During particle surface hydration, water molecules are adsorbed to the negatively charged surface of the clay molecule, to an exposed oxygen or hydroxyl on the tetrahedral layer surfaces, to balance the charge deficiency on the surface. This phase is predominantly intracrystalline swelling due to sorption of the first two or three water layers between unit layers. Strongly hydrating cations Na^+, Ca^{2+}, and Mg^{2+} draw water molecules between the individual 2:1 layers, forcing the crystalline layers apart. The charge deficit induced by isomorphous substitution is balanced by exchangeable cations. Cations Na^+, K^+, Ca^{2+}, and Mg^{2+} have relatively high enthalpies of hydration, so are capable of drawing water molecules into the interlayer and forcing the crystal layers of the molecule apart [4].

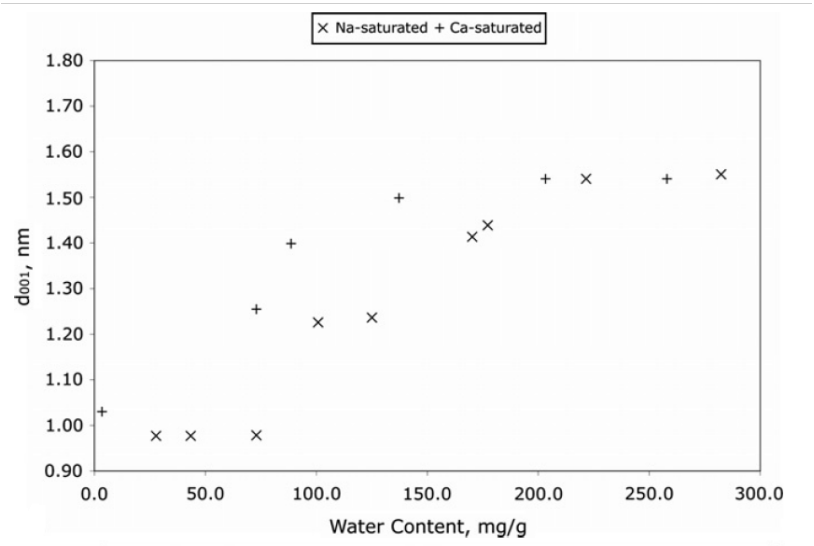

Figure 2.9: Water content [mg/g] versus layer spacing d [nm] for Na^+- and Ca^{2+}-rich smectite [4]

The degree of interlayer hydration is determined by the hydration potential of the interlayer cation, the surface density of exchangeable cations between silicate sheets, and the number of hydration layers that form [9]. Layer spacing increases step-wise with the discrete number of water molecules present in the interlayer (0, 1, 2, 3, or 4 layers of water molecules distinguished by the corresponding basal spacings of 10.0, 12.5, 15.0, 17.5, and 20.0 Å). Figure 2.9 shows the relationship between water content and the ideal layer spacing for Na^+- and Ca^{2+}-rich smectite. As seen in Figure 2.9, crystalline clay swelling due to the addition of one layer of water molecules is equal to the diameter of the water molecule, approximately 2.5Å or 0.25nm. Smectite rich in Ca^{2+} hydrates more readily at a lower water content, as it jumps to a three-layer hydrate at a lower water content than Na^+ smectite in Figure 2.9.

The U.S. Geological Survey suggests the degree of swelling from hydration is related to the extent of cation dissociation in water [7]. When a clay mineral is dispersed in water, the cations in between the structural sheets dissociate, leaving behind negatively charged particles which repel each other. The charge deficit can be great enough to create a measurable expansion. The cation exchange capacity (CEC) and location of cation substitution for common swelling clay minerals are provided in Table 2.4:

Table 2.4: CEC and location of substitution in swelling minerals [4]

Clay Mineral	Substitution Location	Cation Substitution	Substitutions per $O_{10}(OH)_2$	CEC $[cmol/kg]$
Montmorillonite	Octahedral	$Mg^{2+} -> Al^{3+}$	0.25-0.6	60-140
Beidellite	Tetrahedral	$Al^{3+} -> Si^{4+}$	0.25-0.6	60-140
Nontronite	Tetrahedral	$Al^{3+} -> Si^{4+}$	0.25-0.6	60-140
Vermiculite	Tetrahedral	$Al^{3+} -> Si^{4+}$	0.6-0.7	140-165

As seen in Table 2.4, montmorillonite and beidellite have similar CEC but substitution occurs in different layers. Vermiculite has the highest CEC. CEC is generally equivalent to the surface charge if all charged cations are available for exchange. This is not the case, however, with minerals such as mica, who have fixed K^+ minerals in the interlayer. The molecule uptakes water more readily when the negative charge is in the octahedral, such as in montmorillonite, rather than in the tetrahedral location, as in the rest of the minerals listed in Table 2.4 as well as in mica.

2.5.2 Osmosis

Osmotic swelling, which results from a greater concentration of ions in the interlayer than in the pore water outside [10]. The process, considered intercrystalline swelling, aims to equalize the ion concentration difference. Water flows in the direction of the highest ion concentration, towards the interlayers of the clay minerals. The degree of osmotic swelling depends on the interlayer spacing, the availability of pore water, the chemistry of the pore water, and the concentration and valence of the exchangeable ion (Na^+ and Ca^{2+}) [28]. Among smectites, sodium (Na^+) and calcium (Ca^{2+}) smectite are commonly studied because they occur most frequently in nature. Sodium ions promote continuous osmotic swelling of smectite, but potassium ions do not have the hydration energy to swell the interlayer. This is why potassium saturated smectites resist swelling. Isomorphous substitution for silicon or aluminum results in an electrical charge deficiency which can be satisfied with adsorbing exchangeable cations Na^+ or Ca^{2+}. Na^+'s ability to totally dissociate in water creates a larger increase in active surface area (electric double layer), corresponding to a larger increase in free swelling [15].

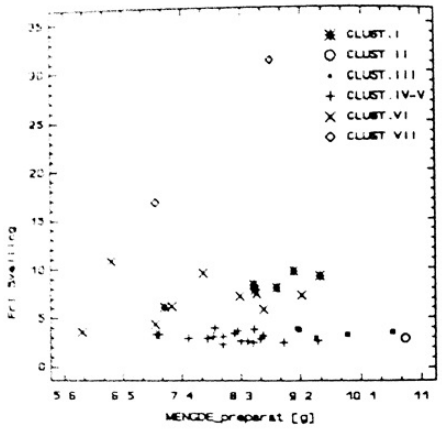

Figure 2.10: Increasing the weight of Na^+ smectite (curve I) increases the free swell potential, but Ca^{2+} smectite (remaining curves) does not [15]

Osmotic swelling is a slow process and decreases as clay minerals absorb more water [10], but increases continuously as the salt concentration of the solution increases. Figure 2.11 illustrates that osmotic swelling as influenced by ionic strength increases in a continuous

swelling regime, as opposed to the step-wise nature of interlayer hydration seen in Figure 2.9.

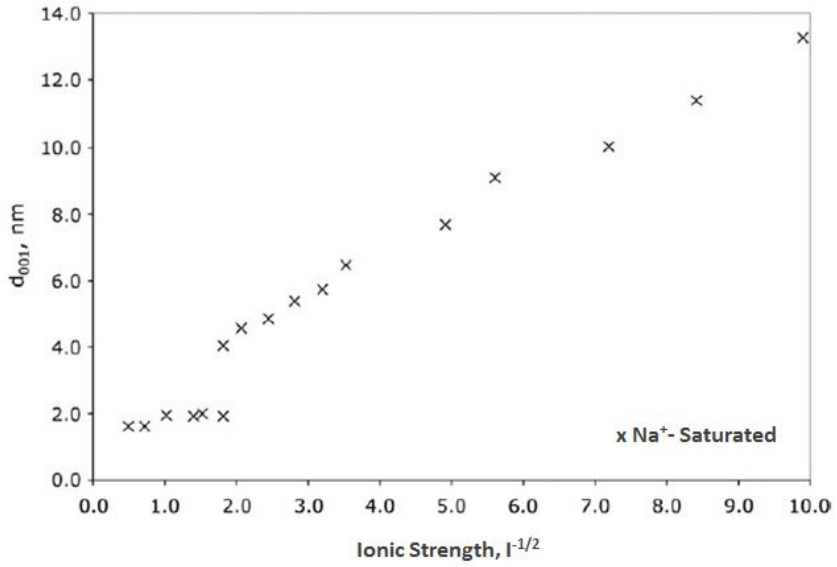

Figure 2.11: Osmotic swelling of smectite illustrated by the increasing relationship between salt concentration and sodium ions [4]

Double layer repulsion forces occur when the diffuse double layers between two particles with similar electrical charge overlap (Figure 2.12 Curve a). Two particles that have come so near to each other that they begin to take up the same space experience Born repulsion forces (Figure 2.12 Curve c). Van der Walls forces are an attractive force resulting from electrical asymmetry of atoms and molecules of clay particles, inversely proportional to the square of the distance between the particles (Figure 2.12 Curve b). The energy of the particles is ultimately the sum of the repulsive and attractive potential energies (Figure 2.12 Curve d).

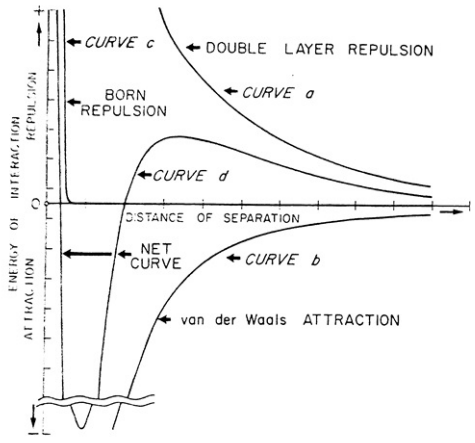

Figure 2.12: Attractive and repulsive forces governing particle bonding [15]

2.5.3 Capillarity

Material without swelling mineral content may also experience swelling, as the material will still hydrate exchangeable cations on the outer surface and saturate its pores. The presence of phyllosilicates such as mica, smectite, and chlorite should cause the particles to absorb more water and have stronger capillary pressures than material rich in quartz or feldspar. The cation concentration difference between the particle surface and pore water causes water

to make its way into the diffuse layer, creating an increased distance between some clay particles, and an overall increase in material volume.

There is a relationship between the suction and the effective radius of the pores emptied at a given suction. Clay soils can remain saturated up to high levels of suction relative to sandy soils. Water loss is accompanied by a subsequent decrease in volume by increasing the suction, and the magnitude of suction at a given water content is approximately equal to the swelling pressure [35]. Capillarity forces depend on the surface tension of the pore fluid, degree of saturation, and capillary radius. Greater saturation enlarges pore-water menisci, reducing the suction.

2.6 Soil Properties Which Influence Clay Swelling Potential

Swelling as a response to water exposure can occur as a function of various physical and chemical characteristics, including soil structure, mineralogy, pore structure, the concentration and valence of the ions, water absorption capacity, compaction, stress history, temperature, the availability and chemistry of pore water [25], and other local conditions. The influence of various internal variables on the swelling potential of clay is explored in this Section.

2.6.1 Mineralogy

Clay mineralogy is a fundamental factor controlling expansive behavior, particularly the smectite content. Clay minerals are fine-grained sheet silicate minerals which form as a result of weathering in the presence of water [4], or as a byproduct of hydrolysis, a process where water reacts with the crystalline structure of the rock and causes a chemical breakdown, from hydrothermal deposition, or as a result of mechanical weathering. Silicates are especially susceptible to hydrolysis, but the severity of weathering and the products are dependent on the chemical composition of the rock and water which are interacting, and the permeability of the rock mass [27]. Clay particles are usually ultra fine-grained, less than 2 micrometers in diameter.

Figure 2.13: Ball-and-stick models and polyhedral models for tetrahedra (a) and octahedra (b) molecular structures [4]

Clay minerals are fundamentally classified as 1:1 or 2:1, built respectively by one tetrahedral sheet and one octahedral sheet (T-O) or one octahedral sheet between two tetrahedral sheets

(T-O-T). The tetrahedral sheet is a plane built of tetrahedra with oxygen ions in the tips and a silicon ion in the center (Figure 2.13a). The octahedral sheet is a plane of built of octahedra containing oxygen or hydroxyl ions at the six tips and an aluminum ion at the center (Figure 2.13b) [17]. 1:1 clay includes kaolinite; 2:1 clay includes smectite, illite, vermiculite and chlorite.

Clay minerals can also be classified according to their tendency to expand. Kaolinite and illite are classified as non-expansive. Vermiculite is a moderately expansive mineral, and montmorillonite is highly expansive. Most swelling soils contain minerals in the smectite or vermiculite family, because these minerals have an expandable interlayer and a large enough specific surface area to produce water adsorption forces in their naturally occurring state [18].

Smectite

Smectite is a group of swelling clay mineral that can greatly increase in volume. The structural formula of smectite is: $Ca_{0.17}(Al, Mg, Fe)_2(Si, Al)_4O_{10}(OH)_2nH_2O$ [2]. Smectite is formed from the alteration of in-situ rock forming minerals or solution deposits commonly in relatively flat, alkaline areas such as marine environments in the presence of silicon and magnesium. Smectite minerals are associated with weakness zones or gouges such as faults, feather joins, crushed rock, or other discontinuities [21]. Smectite encompasses a large number of 2:1 clay minerals with cations and water molecules between the layers, with a general schematic illustrated by Figure 2.14a and simplified in Figure 2.14b.

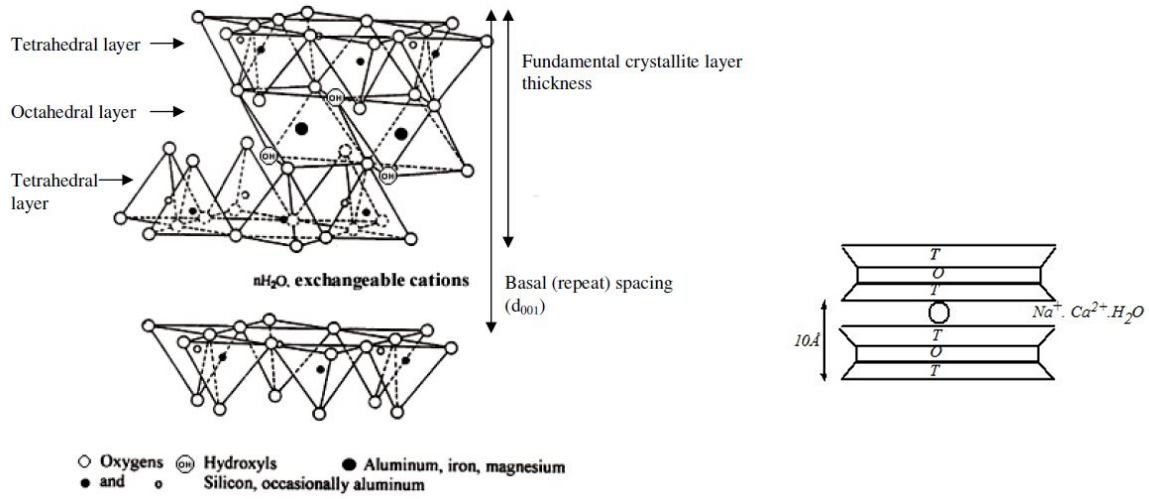

Figure 2.14: Schematic diagram for smectite [18] (a) and simplified (b) [15]

Studies have previously shown that smectite content can dramatically affect swelling pressure development, but a material containing less than 75% smectite does not dramatically affect free swelling [15].

Montmorillonite

Smectite in the form of dioctahedral aluminum micas fall in the range of montmorillonite-

beidellite (Figure 2.15a), where the montmorillonite pole of the series has a variable Mg content, and the beidellite pole contains no Mg. It has the following chemical formula: $(Na, Ca)0.3(Al, Mg)2Si_4O_{10}(OH)_2 * n(H_2O)_{10}$ [2]. Montmorillonites are found in weakness zones, created by surface weathering of rocks in the presence of Na, Ca, Mg, and ferrous iron. These minerals are characterized by the partial replacement of aluminum by magnesium, resulting in a charge deficit balanced by exchangeable cations, usually Na^+ or Ca^{2+}. Montmorillonite has a dramatic shrink-swell capacity and is prone to large volume changes with water content. Water penetration makes the basal distance between layers variable, but it is typically between 14 to 15Å [17]. Large spacing implies weak bonds between layers. Montmorillonite is considered highly active in swelling due to its ability to reversible shrinking and swelling during drying and re-wetting. On the contrary, clays containing kaolinite or illite show an initial large volume decrease on drying with only limited swelling upon re-wetting.

Vermiculite

Vermiculites are another type of swelling clay with layers of water molecules between each T-O-T layer, usually formed by the oxidation of Fe^{2+} to Fe^{3+} in iron rich biotite (Figure 2.15b). It has the following chemical formula: $Mg_{1.8}Fe^{2+}_{0.9}Al_{4.3}SiO_{10}(OH)_24(H_2O)$[2]. The spacing between the unit layers let the water molecules and cations enter freely and the unit layers are drawn apart as a result of high repulsive forces. Vermiculites have a basal spacing of 14Å but are distinguishable from chlorites because their basal spacing collapses to 10Å after heating, and from montmorillonites because they do not expand beyond 14Å with glycerol treatment [17]. The spacing between the layers allow free flowing cations and water molecules to enter, creating repulsive forces which draw the layers further apart.

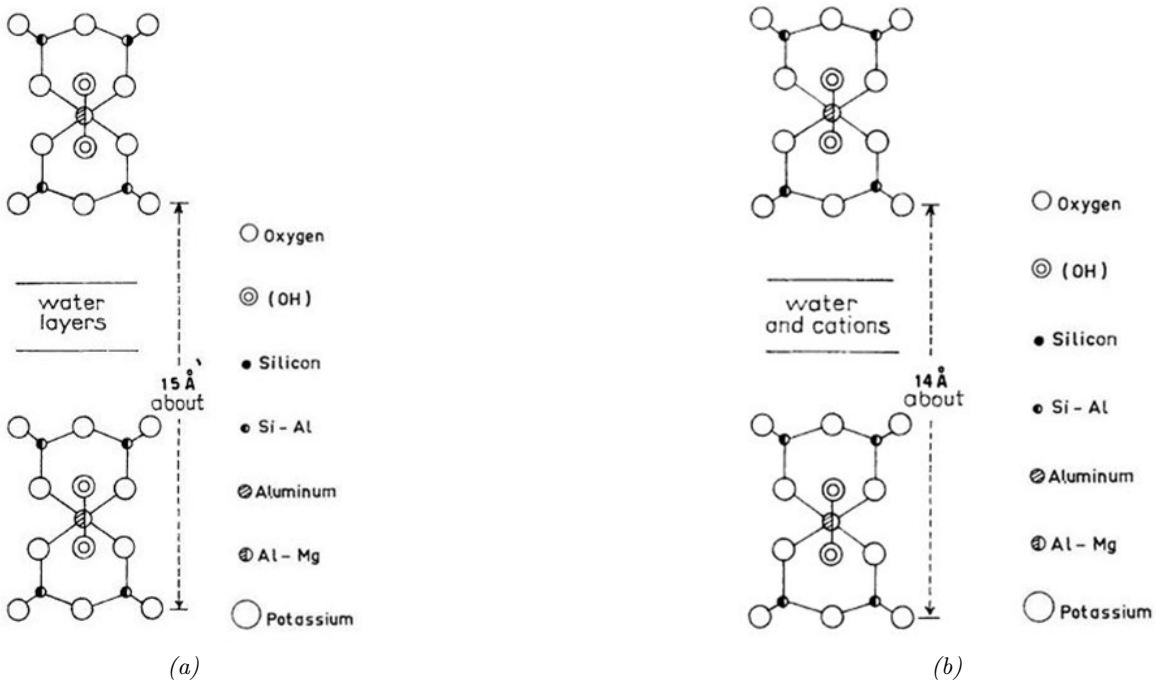

Figure 2.15: Schematic structures of montmorillonite (a) and vermiculite (b) [17]

Mixed Layer Clay Minerals
Montmorillonite mixed with other minerals also cause expansion. The majority of layer-making minerals include illite, montmorillonite, vermiculite, and chlorite [17]. Mixed-layer clay mineral structures are subdivided into regular (R1) or irregular (R0) ordering. Mixed-layer minerals with perfect R1 sequences are often assigned a new name, such as corrensite. Corrensite is a mixed-layer chlorite, subdivided into two categories. Group 1 corrensites encompass regular interstratification of chlorite and swelling chlorite, and are distinguishable from other chlorites by shifting to 17.7Å after glycerol treatment. Group 2 are well defined smectite-chlorites with a basal distance of 12Å [11].

2.6.2 Particle Size

Soil has the tendency to expand upon hydration when the particle size making up the material is very fine, even when it is composed of normally non-expansive minerals. A sample that contains a large fine fraction draws in more water than a sample with less fines due to capillary action, resulting in volumetric expansion to some degree even with zero smectite content [32]. Swelling increases with surface area of the soil particles, area upon which electrical double layers can occur. Table 2.5 lists the average particle thickness of different clay minerals and the degree to which they tend to expand.

Table 2.5: Particle size and swelling potential of some clay minerals [27]

Mineral	**Particle Thickness** $[nm]$	**Average Specific Surface Area** $[m^2/g]$	**Volume Change** -
Montmorillonite	2.0	700-800	High
Illite	20	80-120	Moderate
Kaolinite	100	10-15	Low

The table provides minerals with average particle sizes at three different orders of magnitude. Montmorillonite minerals are one order of magnitude smaller than illite and two orders of magnitude smaller than kaolinite particles, and exhibit the highest volume change due to a greater average surface area enabling water molecule and cation bonding.

2.6.3 Particle Arrangement

Swelling pressure development is dependent on particle arrangement. For high swelling clays, swelling pressure and volume change is greater for material that tends to a parallel orientation. Leafy minerals such as mica loosely packed in the dry state, can be paralleled by sedimentation and have a low free swelling compared to others. For low to slightly active swelling material, higher swelling is observed in random particle arrangement [35].

2.6.4 Plasticity

The plasticity of a material is indicative of the degree of volumetric deformation it will undergo. Holz and Gibbs demonstrated that the Atterberg Limits of the material largely determine the degree of expansivity [11]. Their classification of swelling potential defined by the liquid limit and plasticity index is listed in Table 2.6.

Table 2.6: Swelling potential estimated from Atterberg Limits [14]

Liquid Limit (%)	**Plasticity Index (%)**	**Swelling Potential (%)**
<50	<25	Low
50-60	25-35	Marginal
>60	>35	High

A study by Patil et al. elaborated on the classification proposed by Holz and Gibbs, suggesting that the Atterberg Limits of the material affect the different indicators of swelling potential differently by demonstrating that lower plasticity soils exhibited a shallower trend line on the free swell vs. swelling pressure plot [25]. That is, a higher plasticity material would result in a higher volume change for the swelling same pressure.

According to Rokoengen, swelling pressure increases rapidly at first and collapses after some time due to unstable packing of the pulverized sample. The collapse is detected by both a drop in sample height and pressure [29]. The collapse should be compensated with some amount of expansion, but is instead compensated for at higher pressures with a degree of apparatus deformation (Figure 2.16).

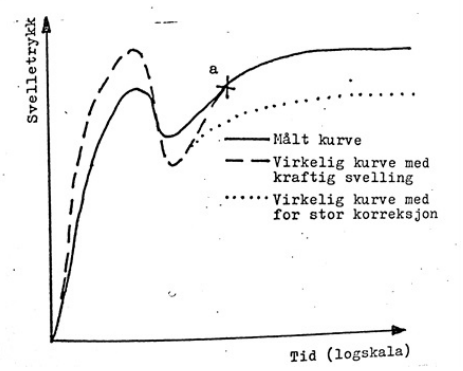

Figure 2.16: Swelling pressure over log time during constant volume oedometer testing with measured curve (solid) actual (dashed) and the corrected (dotted) [29]

The plasticity of the material is a major component of the collapsing behavior; as water is sucked into clay, particles rearrange by compacting further to form positive-to-negative charged points, to overcome the electrostatic repulsive forces from negatively charged surfaces. After the repulsive forces are overcome, less force is needed to compact the sample further.

Percent swell and pressure increase are related to the plasticity index (PI) according to the experimentally generated Figures 2.17a and 2.17b. For remoulded samples, the increase in swelling potential with SI is due to a combination of water sorption to mineral surfaces and mechanical deformation of elastic minerals such as mica. Samples showing greater swelling than expected based on the PI contained considerable amounts of mica. The high scatter in Figure 2.17a was attributed to differences in porosity.

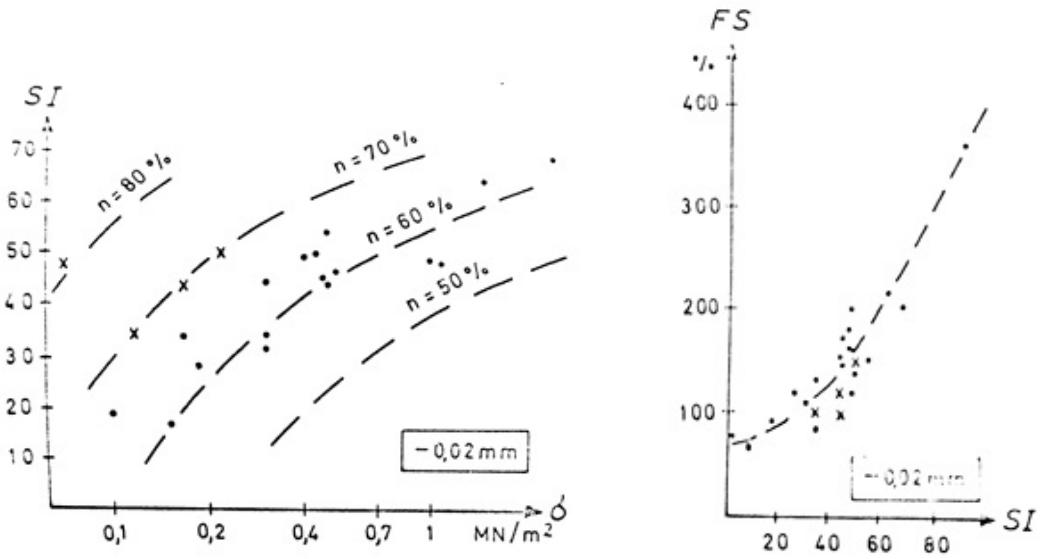

(a) *(b)*

Figure 2.17: SI vs. swelling pressure (a) and SI vs. free swell (b) where x marks samples with high mica content [32]

2.6.5 Consolidation

A highly consolidated clay with normally low swelling potential will yield a higher swelling pressure than clay with low consolidation and high swelling potential [32]. The degree of consolidation can be estimated by comparing in-situ water content with Atterberg Limits. The relationship between plastic index (PI) and swellability index, or the difference in water content between 0.025 and 2 MN/m^2, is pictured in Figure 2.18a. The SI shows an increase with PI.

2.6.6 Compaction and Density

The initial void ratio and therefore the stress history of a soil is shown to have an influence on the measured swelling pressure and volume change associated with water adsorption. The axial strain as a function of the initial void ratio at 93% relative humidity for Na^+ and Ca^{2+} rich smectite is shown in Figure 2.18b.

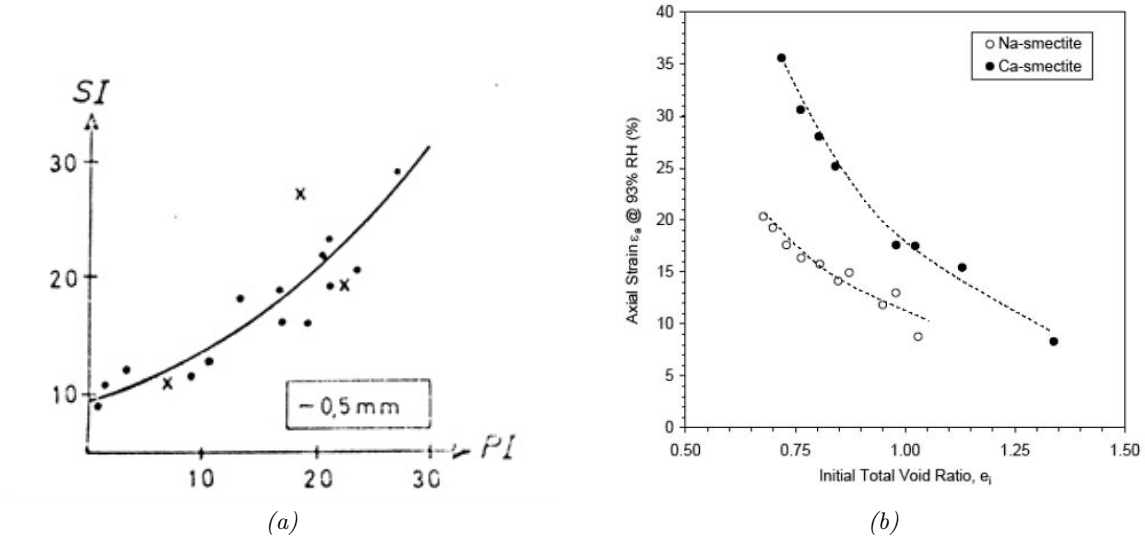

(a) *(b)*

Figure 2.18: SI vs. PI where x marks samples with very high mica content [32](a) and Axial strain as a function of initial void ratio at 93% relative humidity for Na^+ and Ca^{2+} rich smectite [36] (b)

Constant volume oedometer and free swell tests were conducted by [19] on expansive soils of different dry densities. The study showed, with reproducible results, that for an identical relative humidity, the amount of swell increases with increasing dry density of the material (Figure 2.19).

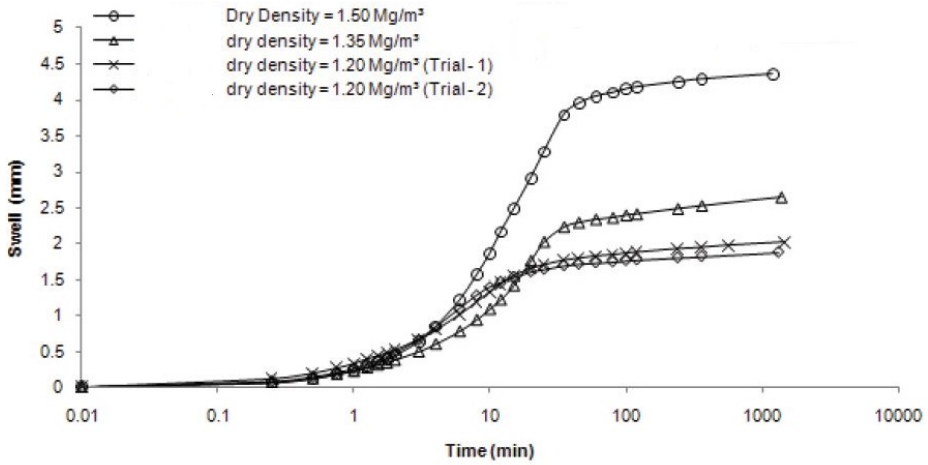

Figure 2.19: Free swelling as a function of time for varying densities [19]

Swelling deformations is highly dependent on the stress paths followed by the sample, and repercussionally, on the stress history of the sample. The interaction between two yield curves in different structural states (densely packed and loosely packed clay) are shown in Figure 2.20. Pressure develops in response to a decrease in suction to maintain a constant volume. Figure 2.20a shows a maximum normal stress at 1332 kPa and 7860kPa for loose and dense specimens, respectively.

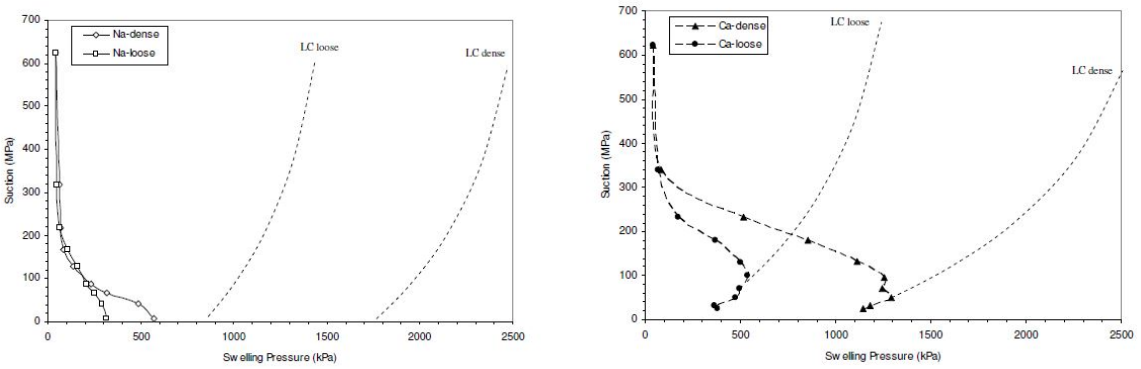

(a) *(b)*

Figure 2.20: Stress paths measured during constant volume wetting for loose and densely packed Na-smectite (a) and Ca-smectite (b) [36]. The LC curves are drawn qualitatively.

2.6.7 Initial Swell Allowance

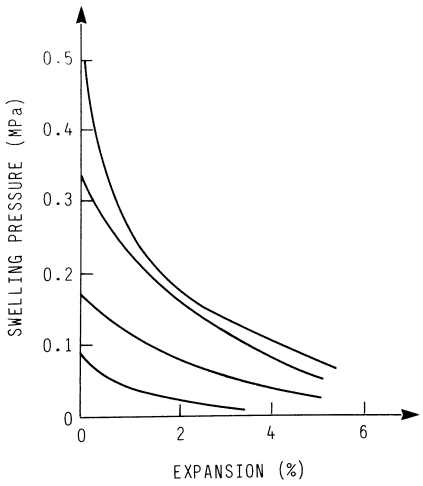

Figure 2.21: Permitting volume change prior to volumetric constraint may reduce the maximum swelling pressure obtained from oedometer testing [21]

The swelling pressure exerted by a material varies when the oedometer cell height changes. That is, when the material is allowed to swell prior to being volumetrically constrained, a significant reduction in swelling pressure is obtained. This behavior was illustrated experimentally by plot shown in Figure 2.21 [21].

Figure 2.21 indicates that permitting the material to swell just a few percent prior to constraining the cell by volume significantly reduces the measured swelling pressure. This scenario is representative of many in-situ conditions where the material has the capacity to swell before meeting a constraining subsurface structure.

2.7 Hypothesis

Based on the preliminary study and the literature review, the predicted outcome of the results will reveal that higher smectite content will produce a higher maximum swelling pressure, and a combination of swelling minerals and capillary action in the fine fraction will govern free swelling.

3 | Methodology

This study aims to tackle the ambiguities that arose in the preliminary study, by investigating two measures of swelling potential as a function of swelling mineral content and grain size distribution. 55 samples stored by SINTEF at NTNU were available for investigation. Swelling clay minerals are identified using X-ray diffraction analysis; the grain size distribution of is measured using laser diffraction; the swelling pressure exerted by the material is investigated over time using constant volume oedometer tests, and the volume change is measured using free swelling tests.

3.1 Material Preparation

The 55 samples available for investigation were samples from anonymous previous SINTEF projects with varying amounts of leftover material and preexisting data available. The gaps in the available data were then filled in with additional testing on the samples with sufficient material. All material preparation was previously performed by SINTEF.

Weakness zones are often highly consolidated with a high amount of coarse minerals. It is therefore difficult to obtain undisturbed samples, and examination of swelling potential is often performed on remolded samples with the coarse grains removed [28]. The material used in this study was carefully prepared prior to testing to ensure results are as reproducible and reliable as possible. The fine fraction of particles sized smaller than 20m was separated, as most active minerals are present in the fine fractions [3]. Separation was done by a combination of wet sieving and gravitational settlement (an application of Stoke's Law). Powder samples were prepared according to ISRM standard (1979). The sample is dried in a drying cabinet and the dried sample is crushed in a porcelain mill. The material which is larger than 20m was also dried and weighed to calculate the fraction of fine particles in the sample [10].

3.2 Mineral Identification Using X-Ray Diffraction

X-Ray Diffraction (XRD) is used for identification and quantification of mineral composition in this study, as it is a time-efficient and reliable method that is readily available at NTNU. An XRD pattern is a plot of the X-rays scattered at different angles by a sample [37]; each material has a unique diffraction pattern, which is directly related to the crystal structure and atomic spacing of the mineral composition under observation, given in Angstrom (Å) (Å $= 10^{-8}$cm) [37]. The XRD apparatus used at NTNU is shown in Figure 3.1. A fixed wavelength is used to scan through a range of angles to produce a diffraction peak at a specific angle θ which is determined by the unique spacing between diffracting planes of atoms. The basal reflections yield the spacing of the basal layer, indicating which atoms are present in the diffracting planes [26].

Figure 3.1: XRD apparatus used at NTNU labs [31]

Clay mineral separation
The fine-grained fraction is isolated to particle sizes less than 6m, allowing the pattern of swelling minerals to be identified without being overwhelmed by the diffraction peaks generated by quartz or feldspar. The <6µm fraction was separated using gravitational settling in a column of water. The preparation procedure is described below:

1. Rock fragments were placed in a beaker with 250ml of deionized water. The beaker was placed in an ultrasonic cell disruptor to separate the less than 2µm fraction using a centrifuge at 1000 rpm for 2 minutes.

2. The clays were distributed into individual beakers with 250ml of deionized water.

3. The particle-water solution was suspended in a 250ml graduated cylinder, thoroughly shaken to achieve a homogeneous mixture, and left to settle. The settling time required to achieve 6µm sized particles in the top 20cm of the graduated cylinder was 1 hour 45 minutes. The top 20cm of water-particle solution was pumped out.

4. The particles were transferred onto two glass slides using the filter-peel method through a 0.45µm filter; one was analyzed as-is and the other was solvated in an ethylene glycol atmosphere over night at 60 degrees C. The time elapsed between removal from the ethylene glycol chamber and scanning was minimized to reduce evaporation.

Bragg's Law
XRD utilizes constructive interference of monochromatic X-rays and a crystalline sample. The interaction of incident rays with the sample produces a diffracted ray when the conditions for Bragg's Law are satisfied. The reflection described by Bragg's Law is shown in Figure 3.2.

The equation describing Bragg's law is provided in Equation (3.1).

$$n\lambda = 2dsin\theta \tag{3.1}$$

Bragg's law relates beams of electromagnetic radiation of wavelength, λ, at certain angles of incidence, θ, to the diffraction angle and lattice spacing d in a crystalline sample. An integral multiple of the wavelength n, is equal to the extra distance AB+BC travelled by the

second beam as seen in Figure 3.2 [26].

Data Collection and Interpretation

A Bruker D8 Advance XRD Powder Diffractometer was used to scan the slides from 3 to 80 degrees (2θ) using the following parameters: wavelength λ = 1.54060nm or λ = 1.78886nm, step size = 0.0115 degrees/0.6 seconds, X-ray tube = cobalt. The intensities of diffracted X-rays were continuously recorded as the sample and detector rotated. Extreme angles of diffraction were adjusted by a predetermined weight factor.The results were plotted as peak positions at values of 2θ and X-ray counts, or intensities. The d-spacing of each peak was then obtained by solving Bragg's equation for the corresponding wavelength λ.

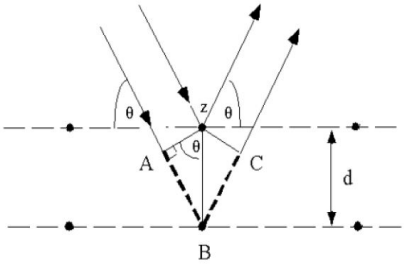

Figure 3.2: When Bragg's Law is satisfied, constructive interference between X-rays and a crystalline sample produces a diffracted ray at angle θ [4]

DIFFRAC.EVA XRD and Elemental Analysis software were used for identification. The software searches a standard reference file of inorganic compounds for a matching pattern of d-spacings exhibited by the specimen. Matching positions and intensities are required to identify a mineral.

Quantitative Analysis

The fine-grained XRD analysis does not provide quantitative information. However, since the fraction of fines within the bulk sample is known, a quantitative analysis can be made to understand swelling properties and stability implications of the material as a whole.

Because it is not possible to quantify smectite in the <6m fraction using the standard Rietveld method, the main minerals present in each material were quantified by hand using the ratio of peak intensities. 001 peaks identified using *webmineral.com* [2] were used for clay minerals [15]. The intensity of a mineral is equal to the area under the peak, found by multiplying the height by the width at half the height. The intensities were then multiplied by a scale factor (Table 3.1) to correct for the variation in intensities due to particle size, orientation, chemical composition, and crystal structure. The intensities were scaled against each other to calculate the relative amounts of each mineral constituent. As long as all samples were prepared in the same way, the minerals can be quantified as weighted fractions. The samples were prepared randomly and unoriented, making the diffraction patterns comparable for quantification.

Table 3.1: Correction Factors for XRD quantification [15]

Mineral	d-value (Å)	Correction Factor
Smectite	14-15	0.5
Mixed-layers	10-14	1.0
Mica/illite	10	1.4
Amphibole	8.40	0.5
Kaolinite	7.17	0.7
Chlorite	4.73	2.10
Quartz	4.26	1.0
K-feldspar	3.24	0.5
Plagioclase	3.19	0.5
Calcite	3.03	0.25
Epidote	2.89	1.0

Expansive soils are identified by solvating the fines in glycol or ethylene glycol, which enhances the distance between layers and may induce an additional peak in the XRD results [10]. For instance, the atomic distance for montmorillonite is around 14Å (1.4nm), but after addition of ethylene glycol it will be increased to 17.7Å.

Mixed-layer constituents can be especially difficult to identify. Regular mixed layers behave as pure minerals whose basal spacing is equal to the sum of the two interstratified layers. This means that a corrensite (14Å) - montmorillonite (14Å) mixed layer mineral shows a basal spacing equal to 28Å in dry conditions [17]. The highest visible spacings likely to be exhibited by various minerals and mixed-layer minerals after the addition of ethylene glycol are provided in Figure 3.3.

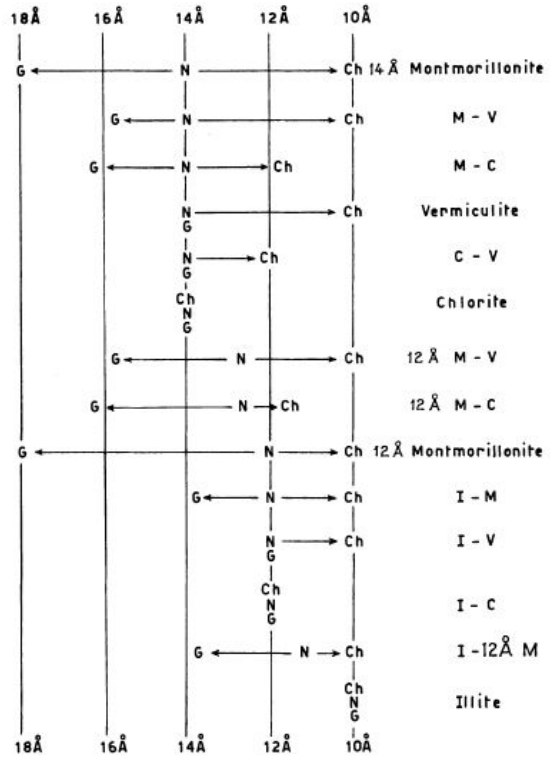

Figure 3.3: Basal spacings (Å) of various mixed-layer minerals treated with ethylene glycol, indicated by the "G" [3].

3.3 Swelling Pressure Measurements Using Constant Volume Oedometer Testing

Clay swelling is expressed by volume change and an induced pressure on its surroundings. The maximum magnitude of swelling pressure is therefore an essential measurement indicative of the worst case scenario of introducing additional stresses onto a subsurface structure

or hard rock tunnel that is incapable of accommodating volume change. Swelling potential of a material can be quantified by measuring swelling pressure. When volumetric expansion is prohibited by a subsurface structure, pressure increases. Swelling pressure is often measured using a one-dimensional consolidation apparatus such as an oedometer test on radially constrained samples. The apparatus used at NTNU is shown in Figure 3.4.

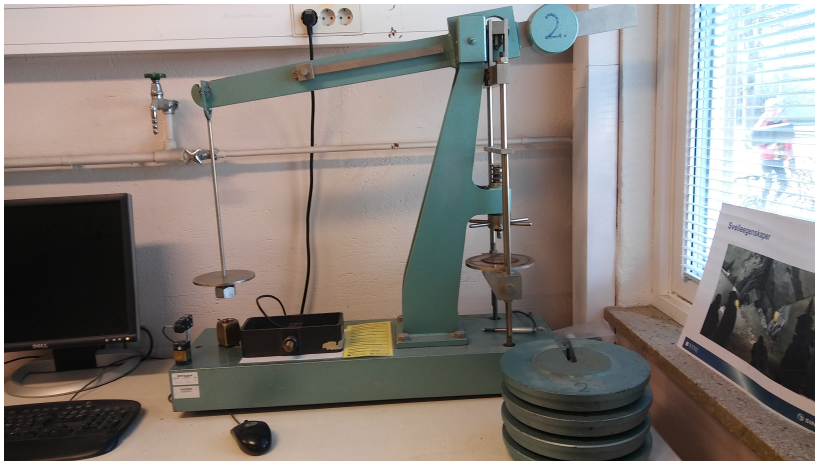

Figure 3.4: Oedometer apparatus used at NTNU labs

Hydrated material attempts to swell, but its volume is kept constant, resulting in a pressure exerted by the material. The axial pressure is measured over time and the maximum pressure obtained in 24 hours is recorded. The principal of the procedure used at NTNU is illustrated in Figures 3.5a and 3.5b.

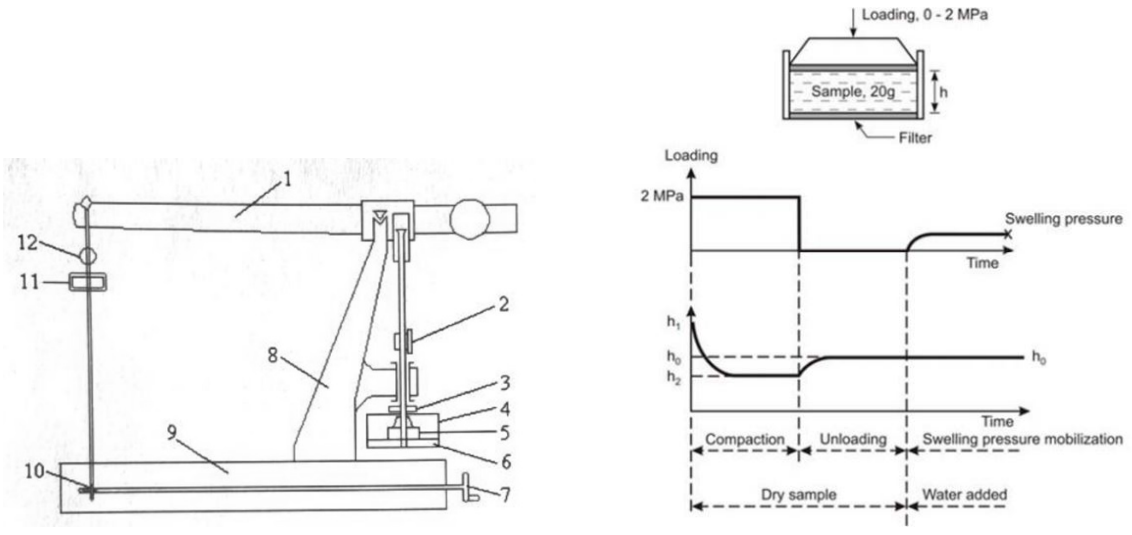

(a) *(b)*

Figure 3.5: (a) Schematic of oedometer test apparatus **1** Balance lever **2** Dial gauge for specimen height **3** Adjustment screw **4** Container **5** Cylinderical test cell **6** Steel base plate **7** Wheel **8** Frame **9** Base **10** Worm gear **11** Pressure ring **12** Dial gauge for pressure sensitivity [6]. (b) A basic schematic of the pressure cell (top) and the three stages of pressure measurements over time (bottom) [20]

A detailed description of the procedure is provided below. The samples are prepared and tested according to NTNU standard methods.

1. A rigid metal ring which provides radial restraint is lubricated to reduce side friction
2. 20 grams of pulverized material is distributed into a $20cm^2$ cylindrical pressure cell
3. Porous filters allowing water to infiltrate are inserted at the top and bottom of the specimen. Filter papers are inserted between the specimen and the plates
4. Distilled water is added to the cell to above the top porous plate
5. A micrometer dial gauge is mounted to measure the swelling displacement at the center of the cross section of the specimen
6. The pressure cell is placed in a loading device capable of measuring the force required to resist swelling
7. The screw is adjusted to balance the lever
8. Compression stage: and steel disc weights are applied to the balance lever to compress the dry specimen at 2MPa for 24 hours
9. Unloading stage: dry specimen is unloaded and allowed to increase in volume until the height stabilizes
10. Swelling stage: distilled water is added and sample is maintained at a constant volume with an automatic motor until the swelling has stabilized, usually about 24 hours

3.4 Volume Change Measurements Using Free Swelling Test

Swelling behavior can be described in the laboratory by their free swell index (FSI), the one-dimensional volume change of soil after hydration without any external constraints.

The FSI is determined at NTNU using the procedure listed below:

1. Sample particle size less than 20µm was separated, as nearly all the swelling minerals are contained in this grain fraction. After soaking overnight, the clay was fed through six sieves sized 4mm, 2mm, 0.5mm, 125µm, 63µm, and 20µm. >20µm and <20µm portions were placed in the oven separate glass bowls to dry. The dry weights of each portion were recorded. The dry weights were used to calculate the fine fraction of the material using equations (3.2) and (3.3).

$$m_{dry<20} = W_{dry<20+bowl} - W_{bowl} \tag{3.2}$$

$$fines = 100\% * \frac{m_{dry<20}}{m_{dry<20} + m_{dry>20}} \tag{3.3}$$

Where:
$m_{dry<20}$ is the dry mass of the <20µm fraction material
$m_{dry<20}$ is the dry mass of the <20µm fraction material
$W_{dry<20+bowl}$ is the measured mass of the dried sample in the bowl
W_{bowl} is the measured mass of the empty bowl

2. Deionized water was added up to the 45mL mark in a 50mL graduated cylinder. 10mL of the <20µm sample was suspended into the graduated cylinder. Entrapped air was removed by gently shaking. The suspension was left for more than 24 hours (Figure 3.6b).

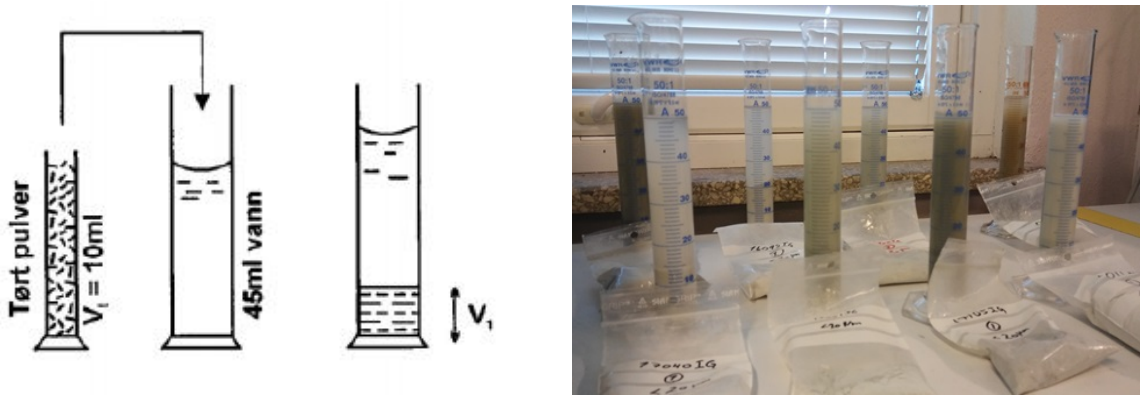

(a) *(b)*

Figure 3.6: (a) Free swell test schematic (left to right) 10mL dry powder mixed in 45mL water, and left to settle for 24 hours before observing the final volume of clay [29] (b) eight samples undergoing free swelling

3. The free swell was reported as the increase in clay volume after settling for 24 hours, according to Equation (3.4).

$$FS = 100\% * \frac{V_f}{V_i}[6] \tag{3.4}$$

Where:
FS = Free Swell
V_f is the final volume of material after 24 hours of swelling
V_i is the initial volume of material, 100mL

3.5 Grain Size Determination Using Laser Diffraction Spectroscopy

Particle size distribution can be determined using laser diffraction. Laser diffraction utilizes the theory of Fraunhofer diffraction, which relates particle size to the intensity of light it scatters [3]. It is suitable for determining a broad range of particle sizes, from 0.01 to 5000mm, at high precision. Laser diffraction at NTNU is performed with a Malvern Mastersizer 3000 (Figure 3.7). The procedure is as follows:

1. Launch Malvern Mastersizer 3000 and accessories used for measurements (Figure 3.7)
2. Clean the instrument by running the propeller in a beaker with tap water 4 times. Fill beaker with 450mL deionized water and place under propeller
3. Select desired settings. This study assumed a refractive index of 1.56, an adsorption density of 0.01 g/cm^3, and a density of 1 g/cm^3. Three measurements were taken in sequence for each sample for a data processing range of 0.005-100µm.
4. Initialize Instrument, turn on ultrasound to reduce air bubbles
5. Measure background
6. Add small amounts of sample until the Obscuration is above 50 %
7. Measure Sample; repeat measurements until reproducible results are obtained (until the D90 reading has a standard deviation of less than 1% for the same sample)
8. Repeat cleaning procedure before proceeding to next sample

Figure 3.7: Malvern Mastersizer 3000 and propellor used for laser diffraction at NTNU

Swelling pressure measurements are plotted with smectite content in the <6µm fraction obtained from XRD, in attempt to predict how much swelling resulted from the smectite alone, and eliminating the ambiguities resulting from other mechanisms of swelling, which cannot be distinguished during free swelling tests.

4 | Results

The data includes compiled results from previous laboratory tests performed by SINTEF at NTNU and additional tests aimed to fill in knowledge gaps on 55 clay samples which exhibited swelling potential of some kind. The results are presented as follows:

- Raw data, tabulated in *Appendix B*, including smectite content measured from XRD patterns on the <6µm fraction of the material (a full quantification and all XRD patterns are provided in *Appendix C*); fine (<20µm) fraction of the bulk sample; free swelling volume obtained from free swell tests; maximum swelling pressure obtained from constant volume oedometer tests
- Swelling pressure curves generated from oedometer tests illustrating pressure development as a function of time (*Appendix D*)
- Grain size distribution curves measured using laser diffraction (*Appendix E*)

4.1 Swelling Potential Parameters

Maximum swelling pressure was plotted against free swell volume in Figure 4.1. The data points called out in the Figure will be discussed in Section 5.

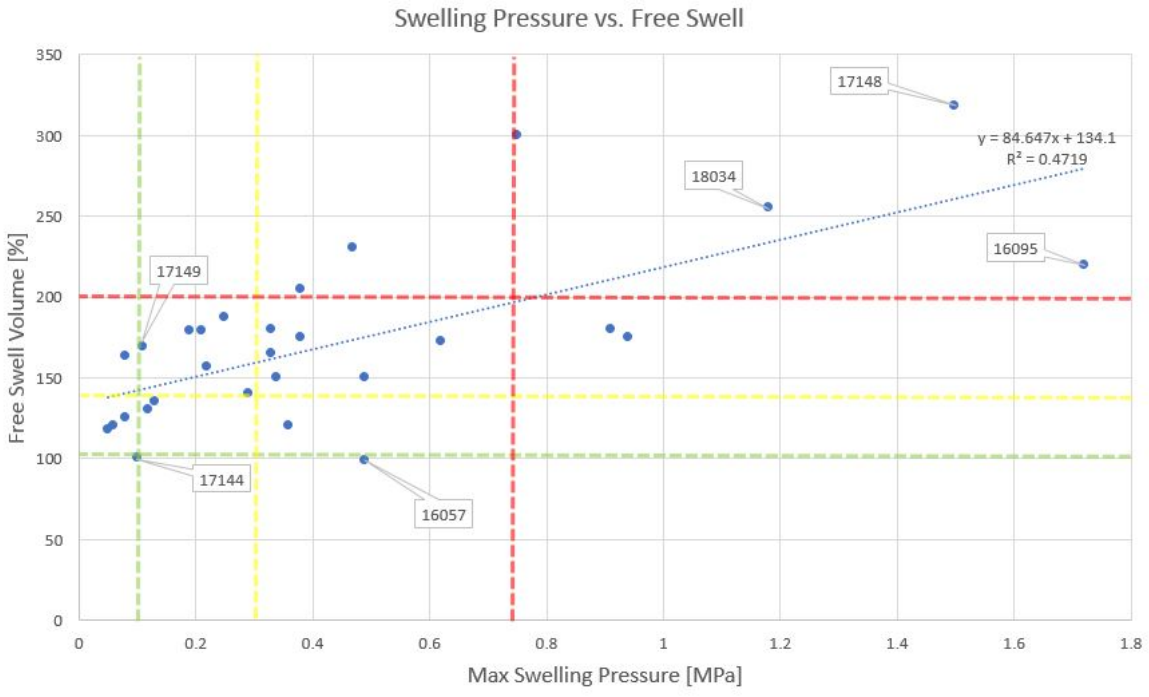

Figure 4.1: Maximum swelling pressure (MPa) vs. free swell volume (%). Dashed lines are the lower boundaries of slightly active (green), active (yellow), and very active (red) behavior

4.2 Smectite Content

The effect of the smectite content of the <6µm fraction was investigated for each swelling potential parameter separately. Figures 4.2 and 4.3 illustrate how the maximum swelling pressure varies with smectite content measured in the <6µm fraction for 28 samples.

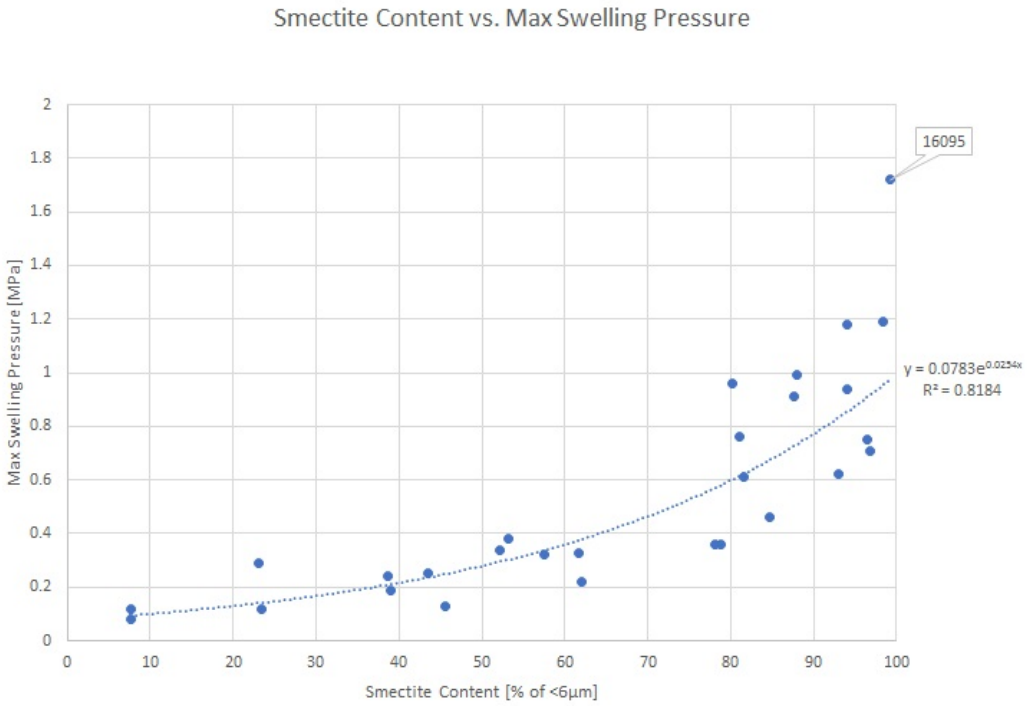

Figure 4.2: Maximum swelling pressure as a function of smectite content

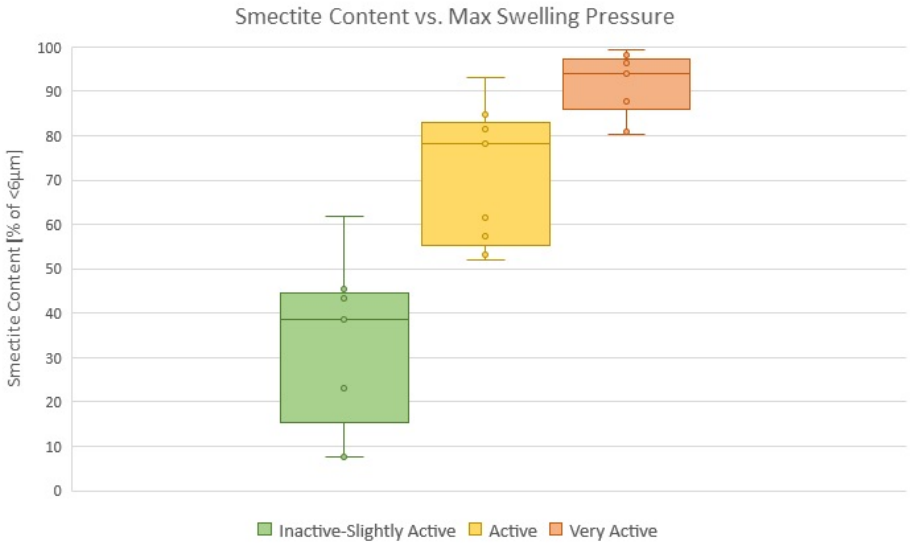

Figure 4.3: Smectite content in the <6µm fraction resulting in various levels of swelling pressure activity

Figure 4.4 was created to observe how the predominant cation present in the smectite affects the swelling behavior.

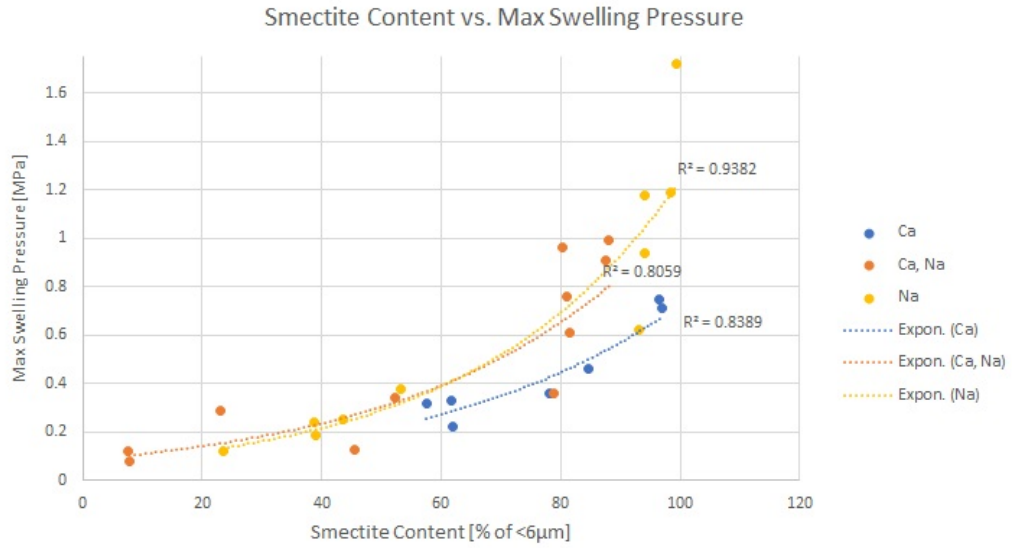

Figure 4.4: Dominant cation and swelling pressure

Figures 4.5 illustrates how the volume change varies with smectite content measured in the <6µm fraction for 17 samples. The figure also calls out samples with high mica content with an "x".

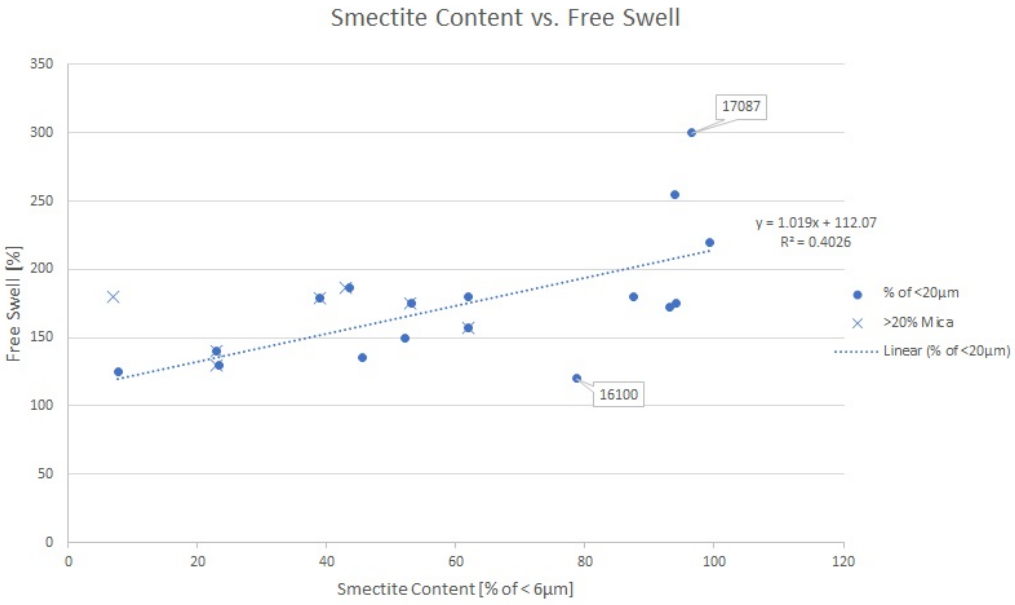

Figure 4.5: Free swelling volume change as a function of smectite content in the <6µm fraction. Samples with mica content greater than 20% are marked by "x"

A box-and-whisker plot was created to illustrate the range of smectite content for each level of free swell activity for 17 samples, as classified by Norsk Bergmekanikkgruppe.

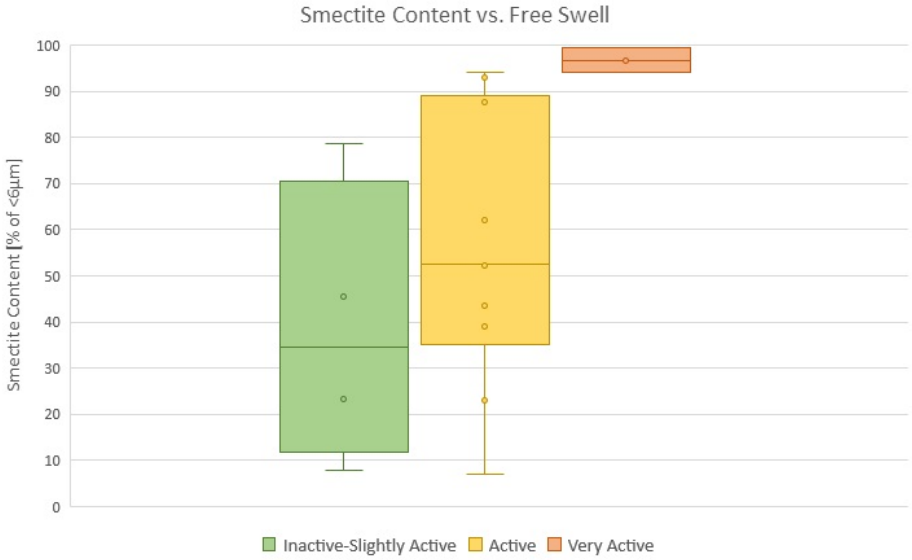

Figure 4.6: Smectite content in the <6µm fraction resulting in various levels of volume change

The swelling pressure development recorded during constant volume oedometer tests display swelling behavior as a function of time. The curves are compiled in Figure 4.8. The swelling classification according to Norsk Bergmekanikkgruppe are indicated by green, yellow, and red dashed lines. The average curve from each smectite group is plotted in Figure 4.7.

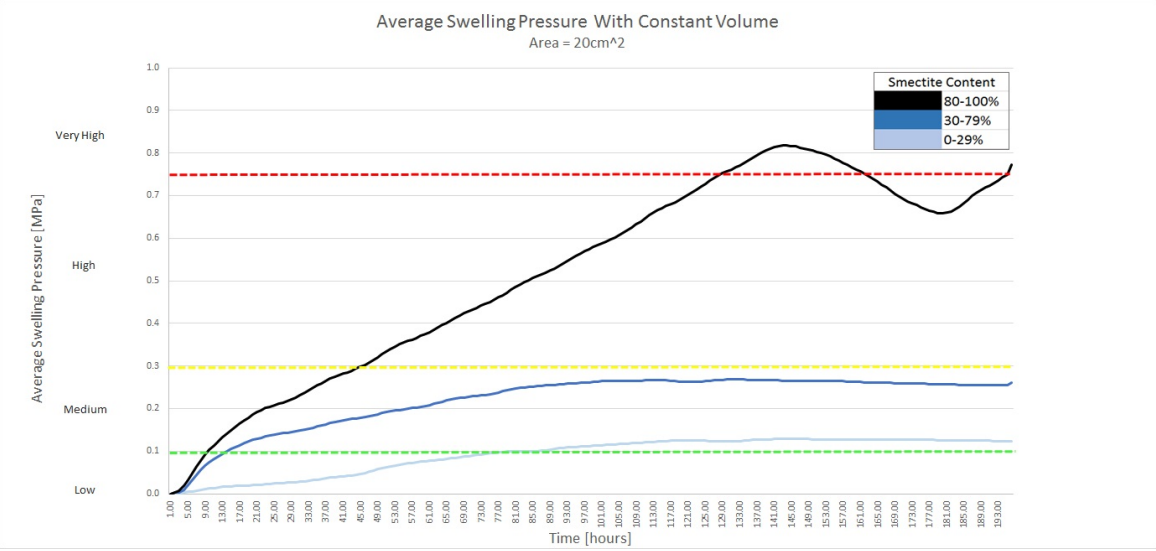

Figure 4.7: Average pressure curves over time plotted according to smectite content

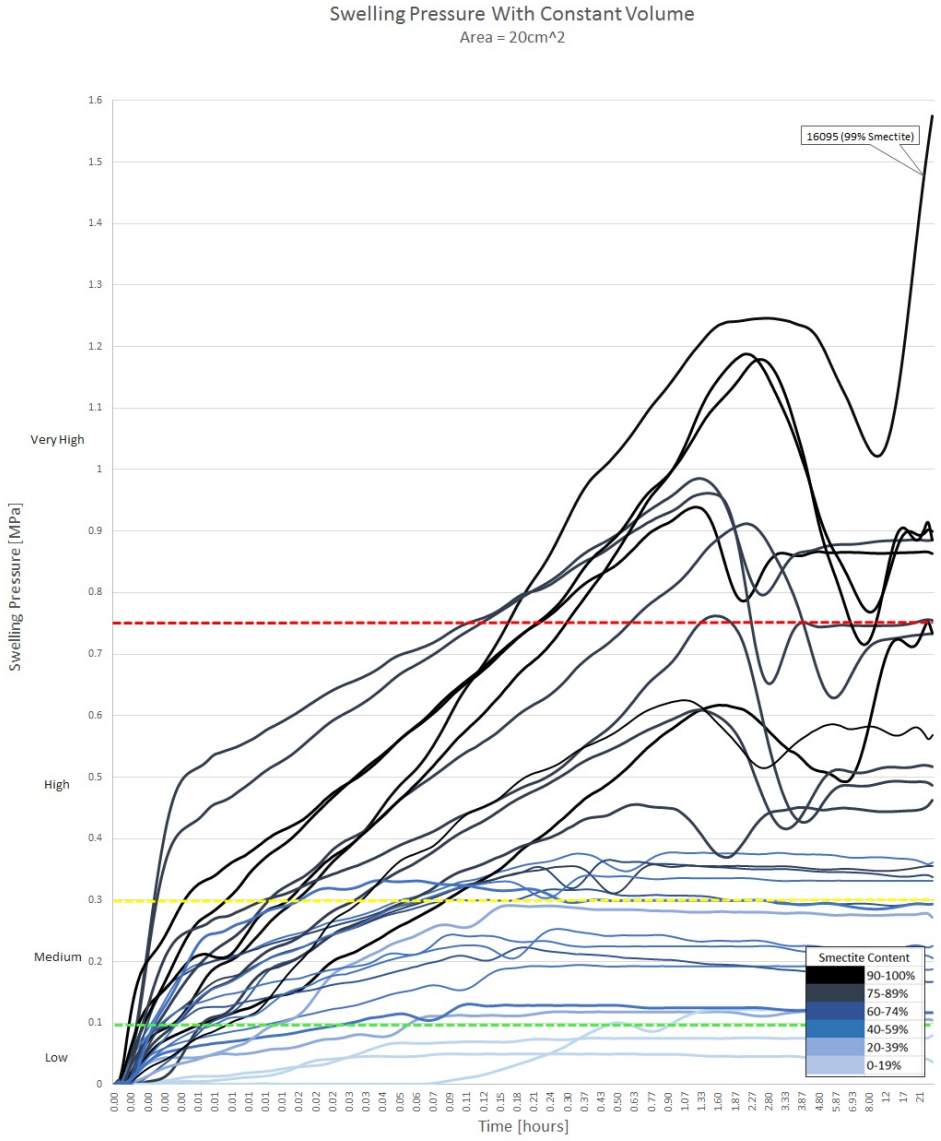

Figure 4.8: Swelling pressure over time generated from constant volume oedometer tests. The color scheme indicates the smectite content measured in the <6 micron fraction using XRD

4.3 Grain Size Distribution

Figures 4.9 and 4.10 illustrate the average grain size distribution curves from 35 individual samples, divided by the level of swelling pressure and free swell activity, respectively.

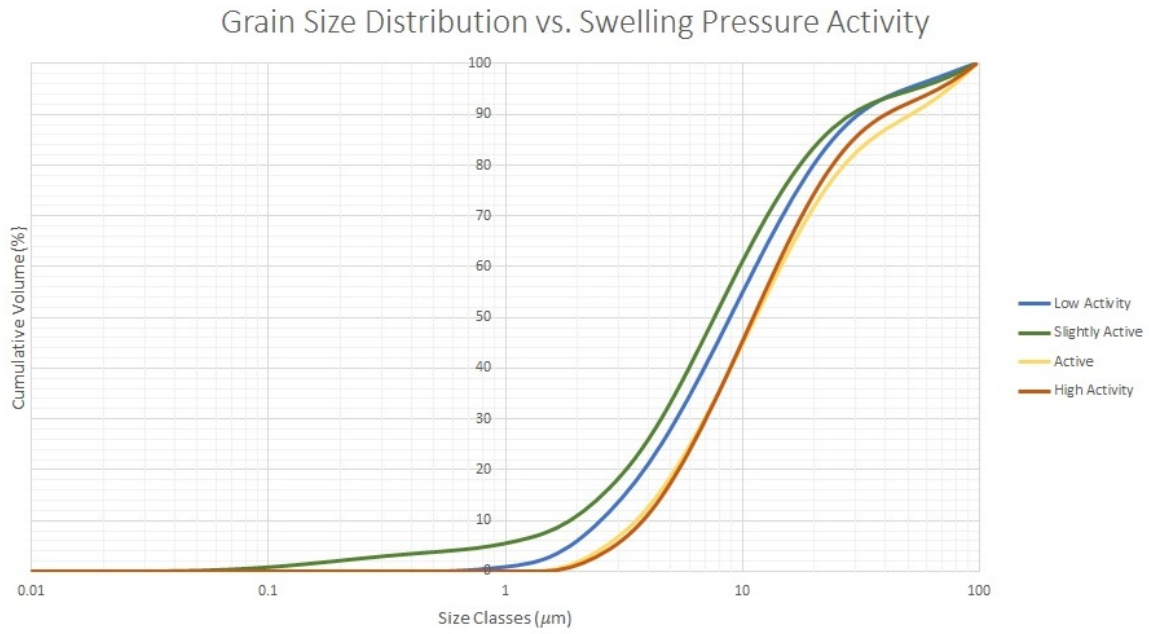

Figure 4.9: Average grain size distribution curves from 32 samples plotted according to maximum swelling pressure

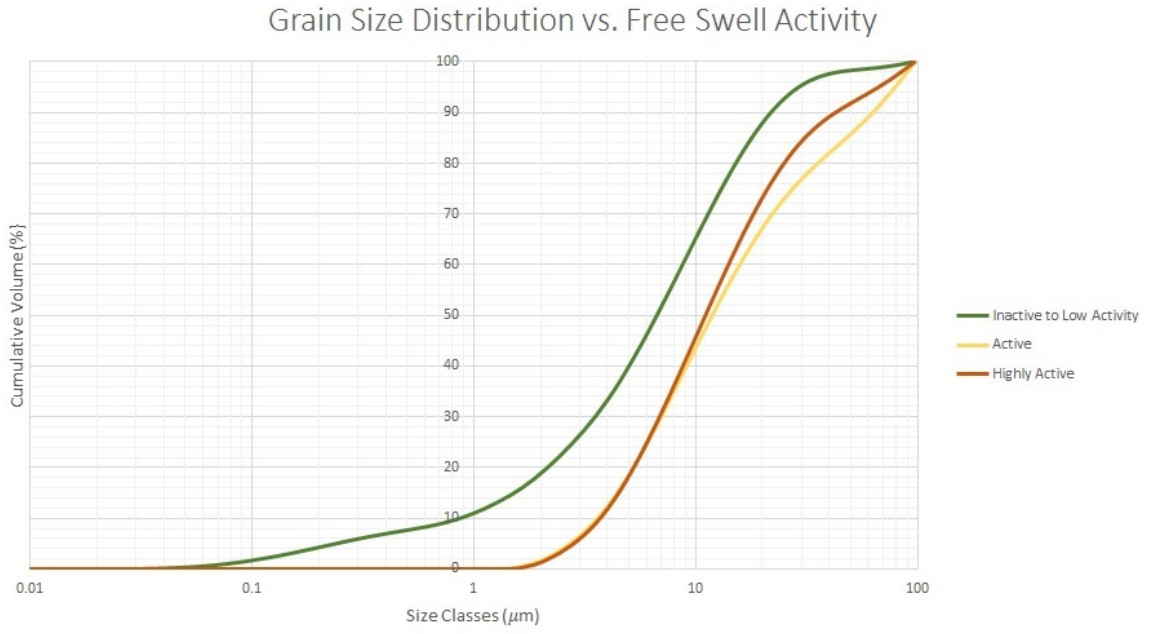

Figure 4.10: Average grain size distribution curves from 18 samples plotted according to free swell

The effect of multiple fine fraction values on free swell was investigated in Figure 4.11.

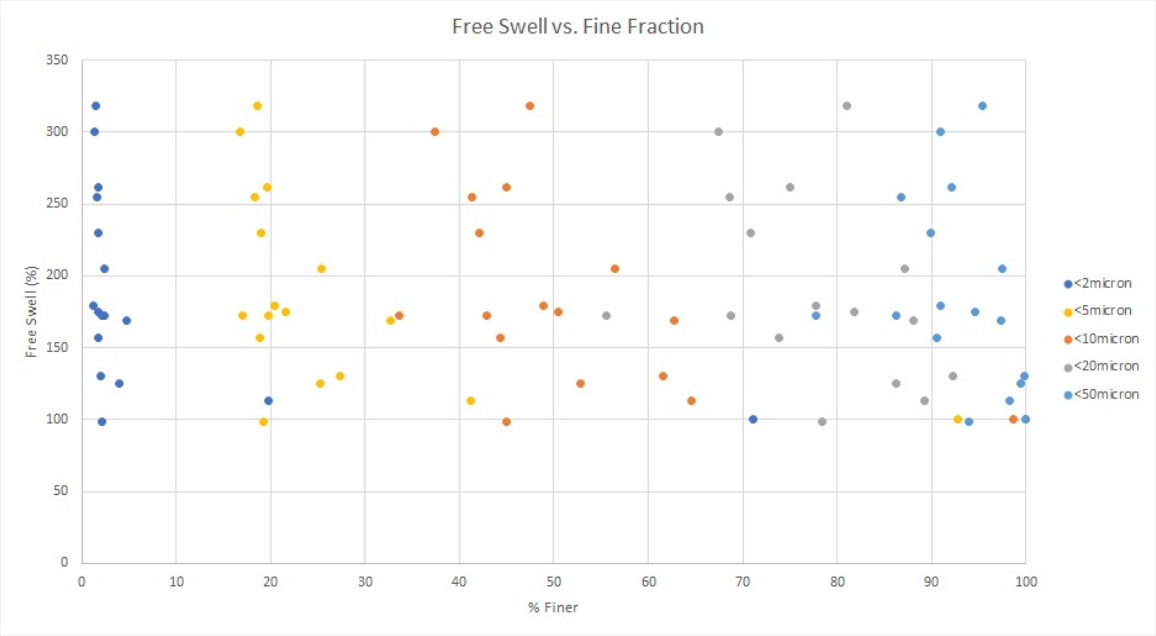

Figure 4.11: Free swelling vs. various fine fractions

Finally, the grain size distribution curves for samples which showed outstanding swelling behavior are provided in Figure 4.12.

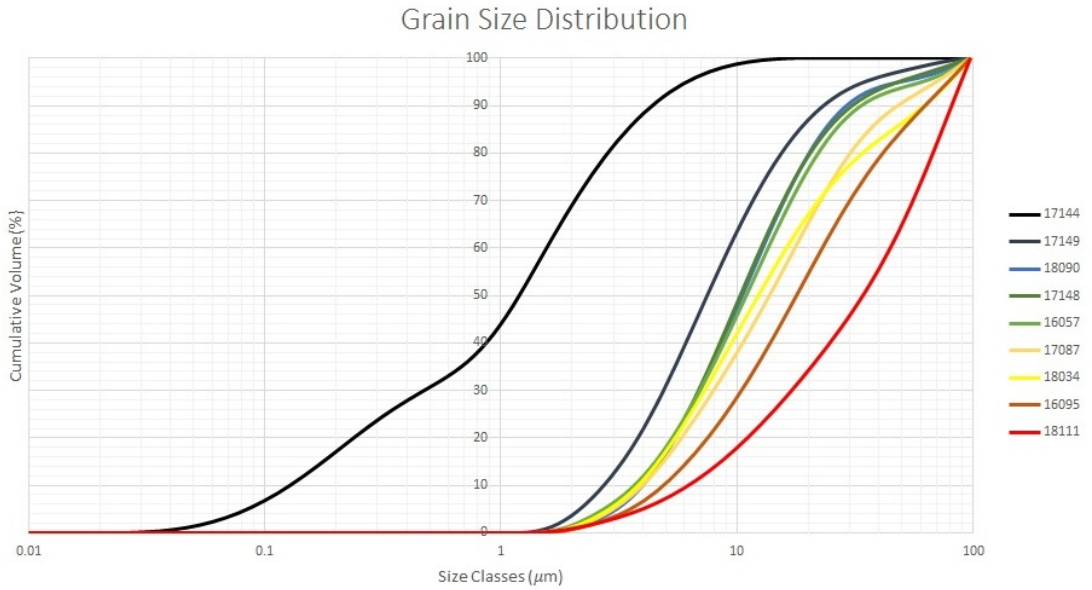

Figure 4.12: Grain size distribution curves from samples showing outstanding swelling potential

5 | Discussion

A discussion of the laboratory findings will be presented, followed by an assessment of the reliability of the procedures used.

5.1 Swelling Pressure and Volume Change

The two swelling potential parameters were plotted in Figure 4.1. The classification boundaries according to Norsk Bergmekanikkgruppen are indicated by the green, yellow, and red dashed lines. The relationship behaved as expected in general, creating a positive linear relationship between the maximum swelling pressure and free swell volume. The trendline fits the data with a potential of variance (r^2) of 0.5. While the correlation is not overwhelmingly strong, the trend between the two measures of swelling potential is clearly positive; there are a number of different physical properties governing the two swelling potential parameters, including mineralogy, particle size, particle arrangement, plasticity, consolidation, compaction and density, and initial swell, as introduced in 2.6. From Figure 4.1, 16057 and 17144 developed some swelling pressure but had totally inactive free swelling. The trendline, consequently, did not intersect the free swelling axis at 100%. 17149 experienced an active level of volume change but still exerted a small swelling pressure. 17148, 18034, and 16095 displayed very large swelling potential values in both tests. The samples called out in Figure 4.1 will be investigated further in attempt to explain divergences from the trend.

5.2 Smectite Content

Generally, swelling pressure was well correlated with smectite content, illustrated by Figures 4.2, 4.3, and 4.8. The exponential relationship found in Figure 4.2 between smectite content and maximum swelling pressure had a well-correlated r^2 value of 0.8. The spread of smectite percentages in each group in Figure 4.3 is quite compact. There is no overlap between first and third quartiles of the box plots, indicating that the level of swelling pressure produced is well defined by the amount of smectite present in the fine fraction of the sample. At least nine data points were present in each subgroup, making the conclusion reliable.

18034 and 16095 reached the most extreme pressures shown in Figure 4.1, and contained respectively 94% and 99% smectite in their fine fractions, which is a likely explanation to their very high swelling pressures. Unfortunately, 17148 did not undergo XRD, so its smectite content is unknown.

The swelling pressure curves divided by smectite content according to the dominant cation in Figure 4.4 showed a very good correlation in each curve. Ca^{2+} saturated smectite had the lowest curve, while Na^{+} saturated smectite had the highest curve, and samples identified with both Ca^{2+} and Na^{+} from XRD fell in between.

The swelling curves seen in Figure 4.8, color-coded by smectite content, revealed that the curves follow the trend very well. Black and dark blue lines are only in the high to very high

pressure areas, blue lines in the medium to high areas, and light blue lines are condensed in the low area. Sample 16095 developed a particularly high swelling pressure. Since it didn't stabilize within the typical 24 hour period and was allowed to develop for 45 hours until it reached a maximum of 1.72MPa. To reiterate, this sample contained 99% smectite in the fine fraction. According to Rokoengen [29], swelling pressure increases rapidly at first and collapses after some time due to unstable packing of the pulverized sample, detected by both a drop in sample height and pressure. Because the collapse of the curves occur at higher pressures with higher smectite content, the collapse of the swelling curve at high pressures is likely related to the elasticity of the material. Higher smectite contents must then provide higher elasticity in the clay volume. Most of the curves also show distinct stages of pressure development. The primary stage, which develops the most rapidly, is likely undergoing a combination of capillary suction and interlayer mineral hydration. The secondary stage is likely governed by interlayer hydration alone, explaining the variation in peaks governed by smectite content.

The average curves plotted in Figure 4.7 combine the averaged time-dependent pressure development for the 30 samples divided into 3 groups. The 80-100% group ultimately developed the greatest maximum pressure, stabilizing after a major collapse around 1.6 hours. The 0-29% and 30-79% groups stabilized just after reaching its maximum, also around 1.6 hours.

Free swell volume was correlated less well with smectite content. The linear relationship found in Figure 4.5 was relatively weak with an r^2 value of 0.4. 16100 contained 80% smectite and remained nearly inactive. 17087 contained 96% smectite and experienced a very large volume change of 300%. There were numerous instances of each case. The free swell volume clearly increases with smectite content on average, but the spread of smectite content for the slightly active and active groups shown in Figure 4.6 is quite large, making the correlation unconvincing. The large spread may be due to the mineral composition in the 6-20µm fraction and the grain size distribution, which is related to the elasticity of the samples. In addition, the very active group only had three data points, so reliable remarks about this group cannot be concluded. Mechanical deformation of elastic minerals, such as mica/illite, were also investigated in Figure 4.5 with the expectation that samples with high concentrations of elastic minerals would exhibit higher swelling [30]. The samples with high illite/mica content depicted in Figure 4.5 followed the trendline very well, and showed no exceptional behavior.

5.3 Grain Size Distribution

The grain size distribution curves, averaged over their maximum swelling pressure classification in Figure 4.9, showed no pattern. The slightly active samples (85% finer than 20µm) and low activity samples (78% finer than 20µm) had a finer fraction than the highly active samples (72% finer than 20µm) and active samples (68% finer than 20µm). The grain size distribution showed little relation to swelling pressure.

The grain size distribution curves when averaged over their free swell classification in Figure 4.10 showed a more organized, but counter intuitive pattern: the inactive and slightly active

samples had the finest grain sizes (87% finer than 20µm), and the active and highly active had very similar distributions with the active group slightly finer than the highly active group (both 70% finer than 20µm). Based on the literature review, finer particle size distributions were expected to show higher free swell values. Most active clay minerals are said to be found in the fine fractions [28], so samples with larger <20µm fractions were predicted to contain relatively more active clay minerals than samples with larger particle sizes. If capillary action does to some degree contribute to volume change, the samples in this study suggest that the effects of grain size distribution are negligible compared to the effects of smectite content present in the fines. However, the grain size alone does not reveal everything about the size distribution of the pores and pore throats, or the connectivity of the pore spaces. Additional information is needed clarifying the true nature of capillarity in the material.

This was investigated further by comparing multiple fine fractions measured by laser diffraction with free swell values in Figure 4.11. Figure 4.11 showed no strong trend between any fine fraction value and free swell value. All plots actually tend towards a negative relationship, but the correlation is very weak. Despite consistent claims from the literature review that smaller particles should yield higher free swell values, this was not supported by the results of this study.

5.4 Data Trends

5.4.1 Inactivity

16057 and 17144 showed both low swelling pressure and inactive free swelling. 16057 had a relatively fine particle size distribution with 50% of the material finer than 10µm, and 17144 had a very fine grain size with 99% of the material finer than 10µm. Despite having the largest fraction of fine grained particles, 17144 displayed no free swelling behavior. These samples indicate that while large fractions of fine grains can contribute to free swelling behavior, it is not an overwhelmingly dominant parameter. However, the smectite content was unknown for both samples, yielding inconclusive results.

5.4.2 Very Active Free Swell

17149 had an unknown smectite content and developed a low swelling pressure but a very high volume change. 17149 had a relatively fine particle size distribution, with 50% of the sample finer than 8µm and 90% finer than 20µm. The grain size distributions were not available for other samples that showed similar swelling behavior. As described in Section 2.3, it is possible that Na^{2+} dominating smectite is behind the high free swell values.

5.4.3 Very Active Pressure and Volume Change

Sample 18111 showed a very large deviation from the average grain size distribution curves, with only 35% of the sample finer than 20µm, and 50% of the material finer than 35µm. This sample was likely not prepared in the correct way. Despite the large particle size, both swelling potential parameters fell in the high classification range. 17148 showed grain size distribution very close to the average of the low series, with 50% of the material finer than 10µm and 85% finer than 20µm. The smectite content was unknown, but very high values were achieved for both swelling parameters.

17087, 18034, and 16095 had 96%, 94%, and 99% smectite respectively. All showed a grain size distribution coarser than the average of the active/very active series, and displayed exceptionally high swelling pressure and free swell values.

5.4.4 Incomplete Data

Because this study was dealing with old samples with varying available data and random amounts of leftover sample for further studies, it was not possible to perform all tests on the samples with data gaps. Knowledge of the smectite content from samples 16057, 17144, and 17149, which showed inactivity in one or both swelling parameters, is essential before drawing conclusions about the physical property dominating these mechanisms. In addition, since there is no mineral information about the 6-20µm fraction, it is difficult to fully interpret this behavior.

Elasticity is another factor thought to influence the swelling pressure, particularly affecting the magnitude of the collapse of the swelling curve. Obtaining elasticity information could provide more holistic conclusions to this data set. Porosity, consolidation, compression, and density information would have also have been useful in gaining a more holistic picture of the swelling behavior.

5.5 Uncertainties in Laboratory Testing

There are limitations associated with using laboratory test measurements. The uncertainties presented in the following sections are discussed to ensure test results are interpreted critically before being used as indicators for predicted in-situ behavior.

5.5.1 Material Preparation

Great uncertainties that arise from the fact that the samples were processed heavily, stored for up to 3 years, and that it is difficult to reproduce in-situ conditions in the laboratory. The grain size distributions obtained from laser diffraction revealed some critical flaws in the material preparation techniques used at NTNU. All samples were previously prepared and

stored by SINTEF, and labelled as <20µm. Around 90% of the finest grained samples were <20µm, but some of the samples contained up to just 35% <20µm. The separation method used clearly has poor reproducibility.

There were large differences in the fine fractions of the total material. Samples containing a large fine fraction, such as 698 and 699 in the preliminary study, are thought to draw in more water through capillary action, contributing to a certain degree of expansion even with zero smectite content. Sample 16107 contained 94% smectite in the <6µm fraction, and exhibited a very high swelling pressure of 0.95MPa, but the fine fraction only made up 1% of the total sample, making it difficult to say how indicative the results are of the material behavior as a whole.

5.5.2 Swelling Pressure

There are limitation associated with oedometer testing which will not necessarily result in a realistic representation of the in-situ swelling pressure behavior of the material. The results clearly display that smectite content is a governing factor in swelling pressure development, greater than inert fines undergoing capillary suction. However, the reproducability of the constant volume oedometer test is questionable, particularly from laboratory to laboratory. Various oedometer methods have been developed by different institutions to interpret swelling behavior of clay minerals, and there is no definite international standard detailing how swelling tests should be interpreted. The standard methods used at two universities, NTNU and the Karlsruhe Institute of Technology (KiT), were compared in a study performed by NTNU. The procedure followed at NTNU includes preloading the sample at 2 MPa for 24 hours, followed by an unloading of 2 hours, while KiT does not vertically load the specimens prior to testing. NTNU utilizes an automatic motor to ensure the volume remains constant during pressure development, and KiT utilizes manual adjustments in intervals from 1 minute to several hours. The same samples were tested at both universities, and KiT reached approximately two times higher swelling pressure than the same samples at NTNU. Preloading could be the cause of the discrepancy, as it might influence the mineral structure. As mentioned, compacted material creates a higher swelling pressure. However, due to the nature of the study, which was designed to find relationships among properties of clay samples, the results are still meaningful because all samples were prepared using the same procedure in the same lab.

The fit between the ring and specimen at NTNU was remarked to be poor, which could have allowed the specimen to swell in the ring to a certain degree undetected by the dial gauge [36]. According to Figure 2.21 this would have reduced the maximum recorded swelling pressure. Inaccuracies in swelling pressure measurements can also arise from incorrectly compensating for apparatus deformation, illustrated by the dotted line in Figure 2.16 in Section 2.6. A possible overestimated swelling pressure might also be recorded if the material does not swell enough after the collapse to compensate for the volume reduction. In this way, swelling pressure is also a function of the initial degree of packing of the sample, or the dry density, where swelling pressure will increase with dry density [19].

5.5.3 Free Swelling

The free swell behavior was affected by smectite content, and contrary to [15], was also effected at smectite contents less than 75%. Discrepancies in free swelling tests can arise from having a disproportionately small smectite content in the less than 20µm fraction. In this case, additional XRD analysis should be performed on the less than 20µm fraction samples to obtain the mineral breakdown of this fraction. That way, it would be possible to identify the contribution of swelling from smectite content. An additional swelling test can be used to differentiate volume change due to swelling clay minerals from that due to capillary action, by dispersing a second sample into kerosene instead of distilled water. The resultant difference in volume change between the water and kerosene samples describes the fraction attributed to capillary action [34].

The starting volume of the material is not consistently representative of the density of the material; unrepresentative free swell values can be obtained due to variation in the shape of the grain, grain size distribution, initial packing, and orientation. An unrepresentatively paralleled sample will result in a largely greater material weight, making "10mL of loosely packed material" a poorly defined amount. In addition, fine grained particles with high salt concentrations prepared in water are especially prone to flocculation, leading to an uneven sedimentation and in more extreme cases, large air pockets in the material separated by sedimentation [15]. Another source of uncertainty lies in the skill level of the person conducting the experiment. Sprinkling too much material at a time into the test cylinder can cause the particles to clump, air pockets to form, and material to adhere to the sides of the cylinder.

The material obtained and used for free swell tests would ideally come from undisturbed samples in their natural in-situ conditions. However, samples in this condition can rarely be obtained. The material is usually only obtained from a small part of the area of interest. Properties can vary within the same zone and with depth. Ideally, boreholes would be taken and studied so soil layer information with depth is known. A series of swell tests should be performed for each soil layer with different soil properties with a known orientation to a subsurface construction.

Finally, the water used for inundating the specimens should closely match the primary source of wetting that will take place in the field. The applications of this study involves tunnelling operations affected by groundwater percolation. Groundwater has an average total dissolved solids content (TDS) of 300-600 [8], a low organic content, and a chemical makeup reflective of the bedrock it permeates. Instead, deionized water was used during testing which undergoes ion exchange in which all charged ions are exchanged for Hydrogen and Hydroxyl ions, resulting in pure H_2O. The degree of swelling has the potential to increase under favorable ionic conditions present in the groundwater. Decreasing the salt concentration in a clay suspension when salt concentrations are relatively high causes the layer spacing (d) to increase as water enters the interlayer.

5.5.4 X-ray Diffraction

XRD Analysis is a powerful and relatively quick technique used to identify unknown mineral composition. In many cases, unambiguous results are obtained with straight-forward data interpretation. The use of ethylene glycol is essential in identifying the weathering products vermiculite, montmorillonite, and mixed layers as accurately as possible. However, a number of factors can alter XRD reflections and limit the accuracy of the quantitative analysis.

First, pure and homogeneous material in terms of grain size and composition is most ideal for identification using XRD. Clay minerals are almost always mixed with small amounts of non-clay material, including quartz, feldspars, and carbonates which might produce sharp intense peaks against the broader clay peaks [5]. Preparation techniques are often a huge source of error associated with XRD. Grinding of dried clay can affect the crystallinity of the material and reduce its diffraction intensity [15]. Intensities are also related to the proportion of minerals in the sample. A grain size of less than 1µm is recommended for a satisfactory number of grains to participate in diffraction. Grains sized greater than 10µm can result in standard deviations up to 18% [15].

Second, the quantification software used at NTNU is not capable of quantifying the <20µm fraction, and in most cases there was not enough material available to separate the <6µm fraction for additional XRD tests. Instead, quantification was done manually on the qualitative XRD patterns by scaling the intensity of peaks against each other under the supervision of an experienced geologist. Since the fraction of fines within the bulk sample is known, a quantitative analysis can be made to interpret the stability implications of the material as a whole. There is likely a large amount of human error associated with manual measurements. Also, the use of the weight factors are uncertain as they are intended for particular minerals with a certain chemical composition, crystallinity, grain size, and morphology which may be different than the ones in the sample. All in all, the quantification method was deemed appropriate for the self-comparative nature of this study. If a more refined relationship between smectite content and swelling pressure is to be established in the future, a quantification software should be used to accurately measure smectite content.

5.5.5 Laser Diffraction

The precision of the laser diffraction tests performed in this study is unknown due to the input parameters used in the Malvern Mastersizer 3000. However, as in the case of XRD, because all samples were prepared and analyzed in the same way, the results should be comparable for the intended purpose of this study. If absolute relationships are to be defined later, the input parameters should be refined for each sample (particularly the refractive index and adsorption densities) and multiple attempts should be made using a range of adsorption densities.

6 | Conclusion

Smectite is a type of saprolite found in the Trøndelag area that expands when hydrated. Its high cation exchange capacity allows it to heavily influence the physical properties of the soil it occupies, and high variability in its composition causes uncertainty in its behavior. This study attempted to link the microstructure of clay minerals to macroscopic swelling pressure and volume changes which can cause damage to subsurface structures. Fine grained XRD analysis was used to reveal the presence of smectite minerals, and its relative amount was determined using a manual quantification technique. Grain size distribution was measured using laser diffraction. Swelling pressure measurements obtained from constant volume oedometer tests were well correlated with swelling mineral content, but free swell was noticeably influenced by a combination of mineralogical content and other variables. Capillary suction showed a weak relationship to both swelling pressure and free swelling values. This study assumed capillarity is well described by grain size distribution, which is not necessarily the case. Because the correlation between free swell and swelling pressure was not exceptionally strong, free swell tests are not recommended to be used alone as an indicator of of the degree expansivity and pressure development. Mineralogy, specifically, smectite content in the fine grained fraction, proved to be a relatively accurate indicator of swelling pressure. However, a more accurate precise mineral quantification is needed to define a meaningful relationship between the smectite content of a material and its predicted in-situ swelling pressure.

The results of this study should be reinforced by comparing XRD analyses on the <20µm fraction with swelling pressure measurements to close the gap between the 6-20µm material fraction. This way, the contribution of swelling pressure from smectite content alone can be accurately identified. In addition, mineral quantification should be carried out using software to more accurately quantify the smectite fraction. Establishing a relationship between smectite content and swelling pressure would allow engineers to predict the pressure exerted by an expanding clay using relatively simple laboratory procedures, and design reinforcements in a cost effective way. Grain size distribution did not provide a complete understanding of capillary action acting in the material. A different approach should be used for interpreting pore sizes and connectivity in the material. Finally, several parameters that weren't included experimentally could have affected the results obtained. The plasticity of the material is expected to reveal larger volume change for more plastic materials. Both swelling potential parameters should increase with the degree of consolidation and compaction. Minerals orientated or paralleled during sedimentation, such as loosely packed mica, increase swelling potential for high swelling clays and decreases swelling potential for low to slightly active swelling clays. An initial swell allowance prior to volumetrically constraining can dramatically reduce the maximum swelling pressure obtained.

There were many parameters involved in this study that complicate the conclusions drawn from the two swelling potential measurements, and several additional parameters not included experimentally that are thought to influence swelling potential further.

References

[1] Lidmar-Bergström, K. Relief and saprolites through time on the Baltic Shield. *Geomorphology*, Vol. 12, 1995.

[2] Barthelmy, David. Mineralogy Database. `http://www.webmineral.com/`, 2014.

[3] Bergaya, F.; Lagaly, G. *Handbook of Clay Science*. Elsevier Ltd., 2006.

[4] Bleam, William. *Soil and Environmental Chemistry. Ch3: Mineralogy and Clay Chemistry*. Academic Press, 2012.

[5] Brindley, G.W; Brown, G. *Crystal Structures of Clay Minerals and their X-Ray Identification*. Mineralogical Society of Great Britain and Ireland, 1980. ISBN 9780903056373.

[6] Catrine Pettersen Skippervik. Study on the Swelling Potential of some Selected Rocks. 2014.

[7] Foster, Margaret. The Relation Between Composition and Swelling in Clays. *Clays and Clay Minerals*, DOI 3-1-205, 1954.

[8] Geological Survey of Norway. Grunnvann I Norge. `http://www.ngu.no/grunnvanninorge/`, 2018.

[9] Hofmann, Ulrich; Weiss, Armin; Koch, G.; Mehler, A.; Scholz, A. Intracrystalline Swelling, Cation Exchange, and Anion Exchange of Minerals of the Montmorillonite Group and of Kaolinite. *Clays and Clay Minerals*, Vol. 4(No. 1), 1955. doi: DOI:10.1346.

[10] A. H. Holter, Martin; Høien. Problems related to measuring of swelling pressure and determination of swelling pressure in weakness zone. journal =.

[11] Holtz, W. ; Gibbs, H. Engineering Properties of Expansive Soils. *Transactions of ASCE*, Vol. 121, 1956.

[12] ISRM Standards. Characterization of Swelling Rock. 1983.

[13] Jaakola, Leena. Deep Weathered Clay and its Stability Implications in Tunneling: TGB4500 Specialization Project. 2018.

[14] Kalantari, Behzad. Engineering Significance of Swelling Soils. *Research Journal of Applied Sciences, Engineering and Technology*, Vol. 4 no. 17, 2012. ISSN ISSN 2040-7467.

[15] Kocheise Rainer-Claus. *Svelleleire I Undersjøiske Tunneler*. Norges Tekniske Høgskole, 1994.

[16] McCave, N. ; Bryant, R. ; Cook, H. ; Coughanowr, C. Evaluation of a Laser-Diffraction-Size Analyzer for use with Natural Sediments. *Journal of Sedimentary Research*, Vol. 56 no. 4, 1986.

[17] Millot, Georges. *Geology of Clays*. Springer-Verlag Wien, 1970. ISBN 978-3-662-41611-2.

[18] Mitchell, J.K. *Fundamentals of Soil Behavior*. John Wiley, 1993.

[19] Nagaraj, Honne; Munnas, Mohammed; Sridharan, A. Swelling Behavior of Expansive Soils. *Journal of Geotechnical Engineering*, Vol. 4, 2010. doi: DOI:10.3328.

[20] Nilsen, Bjørn. Reliability of Swelling Pressure Testing for Tunnel Support Evaluation. 2007.

[21] Nilsen, Bjørn; Thidemann, Alf. *Rock Engineering Volume No 9*. Norwegian Institute of Technology, 1993. ISBN 82-7598-017-8.

[22] Norsk Bergmekanikkgruppe. *Ingeniørgeologi berg håndbok terminologi, symboler, tabeller, klassifikasjon, bergartsdannelse, berggrunnskart over Norge*. Trondheim, 1985.

[23] Olesen, Odleiv; Dehls, John; Ebbing, Jörg; Henriksen, Helge; Kihle, Ola; Lundin, Erik. Aeromagnetic mapping of deep-weathered fracture zones in the Oslo Region – a new tool for improved planning of tunnels. *Norwegian Journal of Geology*, Vol. 87, 2006. ISSN ISSN 029-196X.

[24] Olesen, Odleiv; Kierulf, Pascal; Brönne, Marco; Dalsegg, Einar; Fredin, Ola; Solbakk, Terje. Deep weathering, neotectonics and strandflat formation in Nordland, northern Norway. *Norwegian Journal of Geology*, Vol. 93, 2013. ISSN ISSN 029-196X.

[25] Patil, A. ; Parkhe, D. ; Shrigriwar, R. ; Panse, R. Establishing Relationship Between Swelling Pressure and Free Swell Index of Soils - A Case Study. *International Journal of Advances in Science Engineering and Technology*, 3, 2016. ISSN ISSN 2321-9009.

[26] Paul Shields. Bragg's Law and Diffraction: How waves reveal the atomic structure of crystals. `http://skuld.bmsc.washington.edu/~merritt/bc530/bragg/`, 2004.

[27] Pusch, R. *Environmental Soil Properties and Behaviour, Swelling Clays*. CRC Press, Taylor Francis Group, 2012.

[28] Rokoengen, Kåre. Kompendium Utarbeidet av Sivilingeniör Kåre Rokoengen. *Geologisk Institutt, NTH*, 1973.

[29] Rokoengen, Kåre. Måling Av Svelletrykk og Fri Svelling Hos Jordarter. *Geologisk Institutt, NTH*, Rapport nr. 10, 1973.

[30] Rokoengen, Kåre. Klassifisering av Leirsoner I Fjell. *Geologisk Institutt, NTH*, Rapport nr. 11, 1973.

[31] Selen, Lena; Panthi, Krishna Kanta; Vergara, Maximiliano. Swelling Pressures of Some Rocks Using Different Test Procedures. *2018 EUROPEAN ROCK MECHANICS SYMPOSIUM*, vol. 1, 2018.

[32] Selmer-Olsen, R. ; Rokoengen, K. . About Swelling Tests and Stability of Clay Zones in Hard Rock. *Third International Congress of Rock Mechanics, Denver*, 1974.

[33] Slagstad, Trond; Dahl, Rolv. *Geology for Society for 150 Years - The Legacy after Kjerulf*. Geological Survey of Norway, 2008. ISBN 978-82-7385-121-5.

[34] Y. R. H. Tahasildara, Janardhan; Erzin. Development of relationships between swelling and suction properties of expansive soils. journal =.

[35] Warkentin, B. Water Retention and Swelling Pressure of Clay Soils. *Canadian Journal of Science*, Vol. 42, 1962.

[36] Wayllace, Alexandra. Ph.D. Civil and Environmental Engineering Volume Change and Swelling Pressure of Expansive Clay in the Crystalline Swelling Regime. 2008.

[37] Xiang, Zhou; Dong, Liu; Hongling, Bu; Liangliang, Deng; Hongmei, Liu; Peng, Yuan; Peixin, Du; Hongzhe, Song. XRD-based quantitative analysis of clay minerals using reference intensity ratios, mineral intensity factors, Rietveld, and full pattern summation methods: A critical review. *Science Direct*, Vol. 3, 2018. doi: DOI10.1016.

A | HSE Certificate and Risk Assessment

The mentionable safety precautions taken during practical work are described below:

- Tour of all lab facilities and an introduction to the eyewash stations, first aid kits, fire blankets and fire extinguishers, and fire exits.
- All tools, devices, vessels, and utensils in contact with samples were washed with water, dried, disinfected with ethanol, and dried again between every step to avoid contamination
- Ear and eye protection, safety shoes, and ventilation were used during crushing
- All work was performed under the supervision of the lab manager

db68aa3ea

Certificate

of core competence awarded September 11th 2018 to

Leena Jaakola

for having successfully completed the e-learning course

NTNU - HSE in the laboratories

The training was performed in accordance to ISO 9001 with relevant procedures, regulations and standards from IEC/CENELEC/NEK/DSB/NEMKO /NBF ***The course is valid until September 11th 2021***

Further details of the course may be found in a separate attachment (Ref. No. db68aa3ea). Please note that the course certificate can be verified at trainor.no.

Steinar Nilsen
Course manager

Terje Gravdal
CEO

B | Raw Data

Table B.1: Compiled laboratory results including smectite content measured from the <6µm fraction in XRD, <20µm fraction measured from the bulk sample, free swell percentage measured from free swell tests, and maximum swelling pressure obtained in the constant volume oedometer test

Sample Name	**Smectite Content % in <6µm**	**Fines <20µm**	**Free Swell [%]**	**Max Swelling Pressure [MPa]**
16002_1	23	3	130	0.12
16002_2	53	16	175	0.38
16002_3	39	3	179	0.19
16028	x	7	163	0.08
16057	unknown	22	99	0.03
16083_3	x	5		0.84
16083	8	5		0.12
16093	46	8	135	0.13
16095	99	11	220	1.72
16100	79	18	120	0.36
16101	8	12	125	0.08
16104	x	8		1.03
16107	94	1	175	0.94
16111	88	1		0.99
16114	80	2		0.96
17035	x	26	118	0.05
17035	x	13	120	0.06
17040	unknown	3	150	0.49
17051	88	3	180	0.91
17070	x	11		0.19
17074	x	3		0.28
17075	unknown	20	205	0.38
17087	96	6	300	0.75
17088	98	3		1.19
17103	x	2		0.51
17105	52	3	150	0.34
17115	x	3		0.71
17116	57	4		0.32
17117	x	2		0.83
17125	85	3		0.46
17138	x	6		0.23
17139	x	7		0.14
17142	unknown	9	179	0.21
17144	unknown	60	100	0.1
17148	unknown	5	318	1.5
17149	unknown	7	169	0.11
17155	x	11		0.33
17157	78	3		0.36
18009	81	5		0.61
18011	23	20	140	0.29
18012	x	17		0.3
18018	39	3		0.24
18022	43	9	187	0.25

Sample Name	**Smectite Content % in <6µm**	**Fines <20µm**	**Free Swell [%]**	**Max Swelling Pressure [MPa]**
18034	94	6	255	1.18
18037	0	1	167	
18055	0	22		0.05
18066	x	10		0.9
18068	x	10	230	0.47
18085	0	6	165	0.33
18090	12	11		0.76
18100	97	2		0.71
18103	62	14	157	0.22
18108	unknown	2		0.59
18111	7	0.4	180	0.33
18128	93	9	172	0.62

C | X-Ray Diffraction Patterns

Table C.1: Mineral quantification of XRD patterns

Mineral	Smectite	Quartz	K-Feldspar	Plagioclase	Illite	Calcite	Chlorite	Amphibole	Pyrophyllite	Talc	Chlorite-Smectite	Pyrite
16002_1	23.4	1.1	3.0	1.5	68.2	0.0	0.6	2.1	0.0	0.0	0.0	0.0
16002_2	53.1	20.7	0.0	0.0	15.1	0.0	11.0	0.0	0.0	0.0	0.0	0.0
16002_3	39.0	0.3	0.0	0.0	51.9	0.0	8.8	0.0	0.0	0.0	0.0	0.0
16093	45.6	0.9	2.8	0.0	0.0	0.0	44.1	6.7	0.0	0.0	0.0	0.0
16095	99.3	0.0	0.0	0.0	0.0	0.0	0.7	0.0	0.0	0.0	0.0	0.0
16100	78.8	0.5	0.0	1.5	9.3	0.0	0.0	0.0	2.3	0.0	0.0	7.6
16101	7.7	0.0	3.4	15.9	0.0	0.0	65.1	5.7	0.0	2.2	0.0	0.0
16107	94.0	0.4	0.0	0.0	0.0	0.5	2.9	0.0	0.0	0.0	2.2	0.0
17051	87.6	1.1	0.0	1.4	0.4	0.0	9.5	0.0	0.0	0.0	0.0	0.0
17087	96.5	2.6	0.0	0.0	0.9	0.0	0.0	0.0	0.0	0.0	0.0	0.0
17088	98.3	0.2	0.0	0.0	0.6	0.0	1.0	0.0	0.0	0.0	0.0	0.0
17105	52.1	1.8	17.8	13.8	6.4	2.8	5.2	0.0	0.0	0.0	0.0	0.0
18009	81.5	0.1	0.0	9.7	8.2	0.0	0.6	0.0	0.0	0.0	0.0	0.0
18022	43.5	10.1	0.0	11.1	24.6	1.7	1.4	2.8	0.0	0.0	0.0	4.9
18034	94.0	0.0	0.0	0.0	0.0	0.0	6.0	0.0	0.0	0.0	0.0	0.0
18103	61.9	2.6	8.4	2.4	17.9	0.0	6.7	0.0	0.0	0.0	0.0	0.0
18128	93.1	1.2	0.0	0.0	3.7	0.0	2.0	0.0	0.0	0.0	0.0	0.0
16083	7.7	4.0	34.5	16.3	7.6	11.6	18.4	0.0	0.0	0.0	0.0	0.0
16111	88.0	0.9	0.0	0.0	0.0	0.9	10.2	0.0	0.0	0.0	0.0	0.0
16114	80.2	0.4	0.0	0.0	0.0	0.7	18.7	0.0	0.0	0.0	0.0	0.0
17116	57.5	2.8	14.3	5.0	5.1	2.1	13.2	0.0	0.0	0.0	0.0	0.0
17125	84.7	0.0	1.1	2.2	7.2	1.1	3.8	0.0	0.0	0.0	0.0	0.0
17157	78.2	0.1	0.0	7.7	6.1	0.0	7.9	0.0	0.0	0.0	0.0	0.0
18011	23.0	0.8	11.4	15.7	20.6	0.0	28.5	0.0	0.0	0.0	0.0	0.0
18018	38.6	1.2	0.0	0.0	21.2	2.6	36.4	0.0	0.0	0.0	0.0	0.0
18090	81.0	0.0	5.0	0.0	3.0	0.0	11.0	0.0	0.0	0.0	0.0	0.0
18100	96.9	0.0	0.0	0.0	1.4	0.0	1.7	0.0	0.0	0.0	0.0	0.0
18111	61.7	0.7	12.9	0.0	44.4	0.0	35.6	7.1	0.0	0.0	0.0	0.0

16002_1 < 6 µm

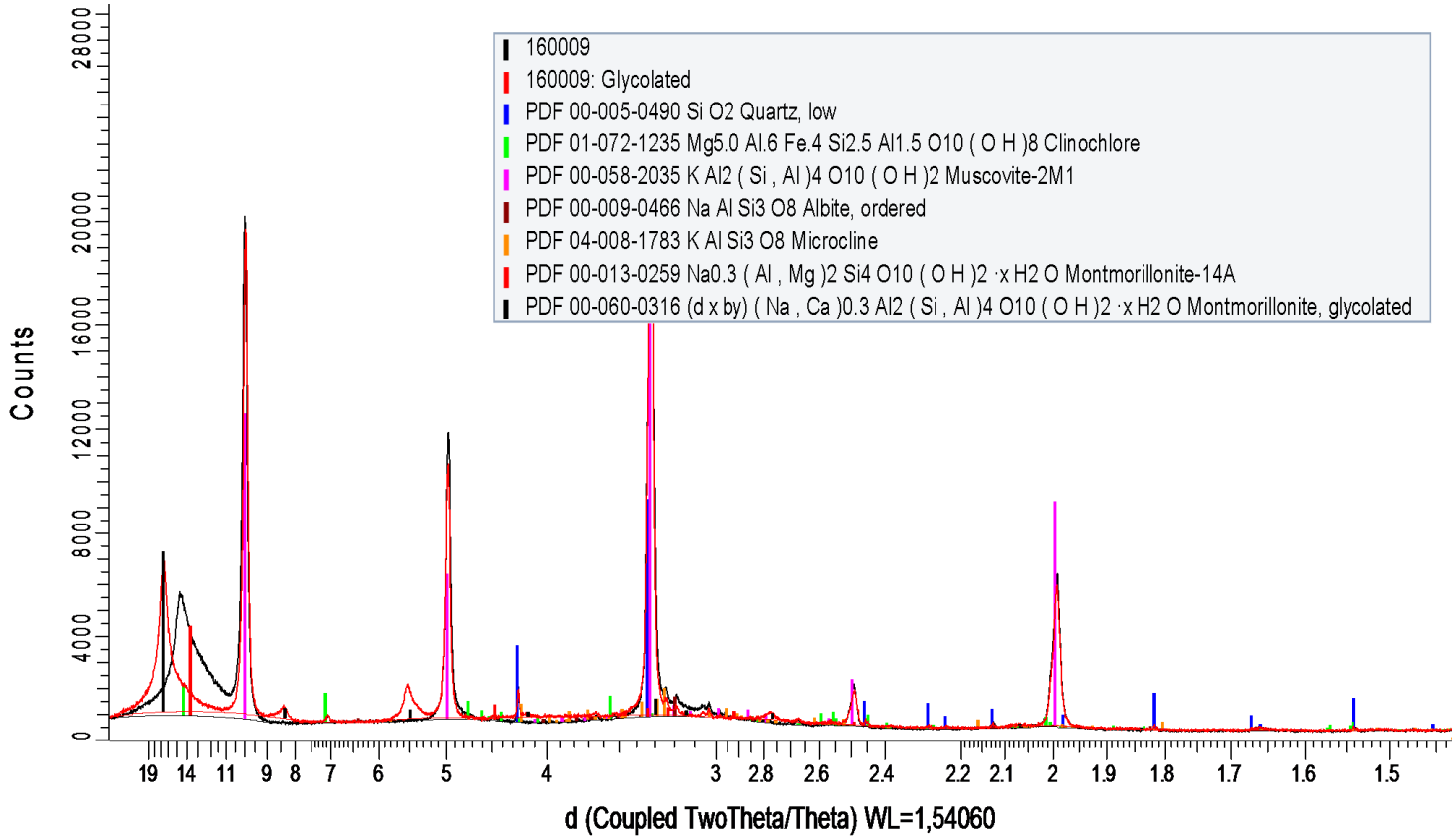
160009
160009: Glycolated
PDF 00-005-0490 Si O2 Quartz, low
PDF 01-072-1235 Mg5.0 Al.6 Fe.4 Si2.5 Al1.5 O10 (O H)8 Clinochlore
PDF 00-058-2035 K Al2 (Si , Al)4 O10 (O H)2 Muscovite-2M1
PDF 00-009-0466 Na Al Si3 O8 Albite, ordered
PDF 04-008-1783 K Al Si3 O8 Microcline
PDF 00-013-0259 Na0.3 (Al , Mg)2 Si4 O10 (O H)2 ·x H2 O Montmorillonite-14A
PDF 00-060-0316 (d x by) (Na , Ca)0.3 Al2 (Si , Al)4 O10 (O H)2 ·x H2 O Montmorillonite, glycolated
Counts
0
4000
8000
12000
16000
20000
28000
19
14
11
9
8
7
6
5
4
3
2.8
2.6
2.4
2.2
2.1
2
1.9
1.8
1.7
1.6
1.5
d (Coupled TwoTheta/Theta) WL=1,54060

Norges teknisk-naturvitenskapelige universitet

16002_2 < 6 µm

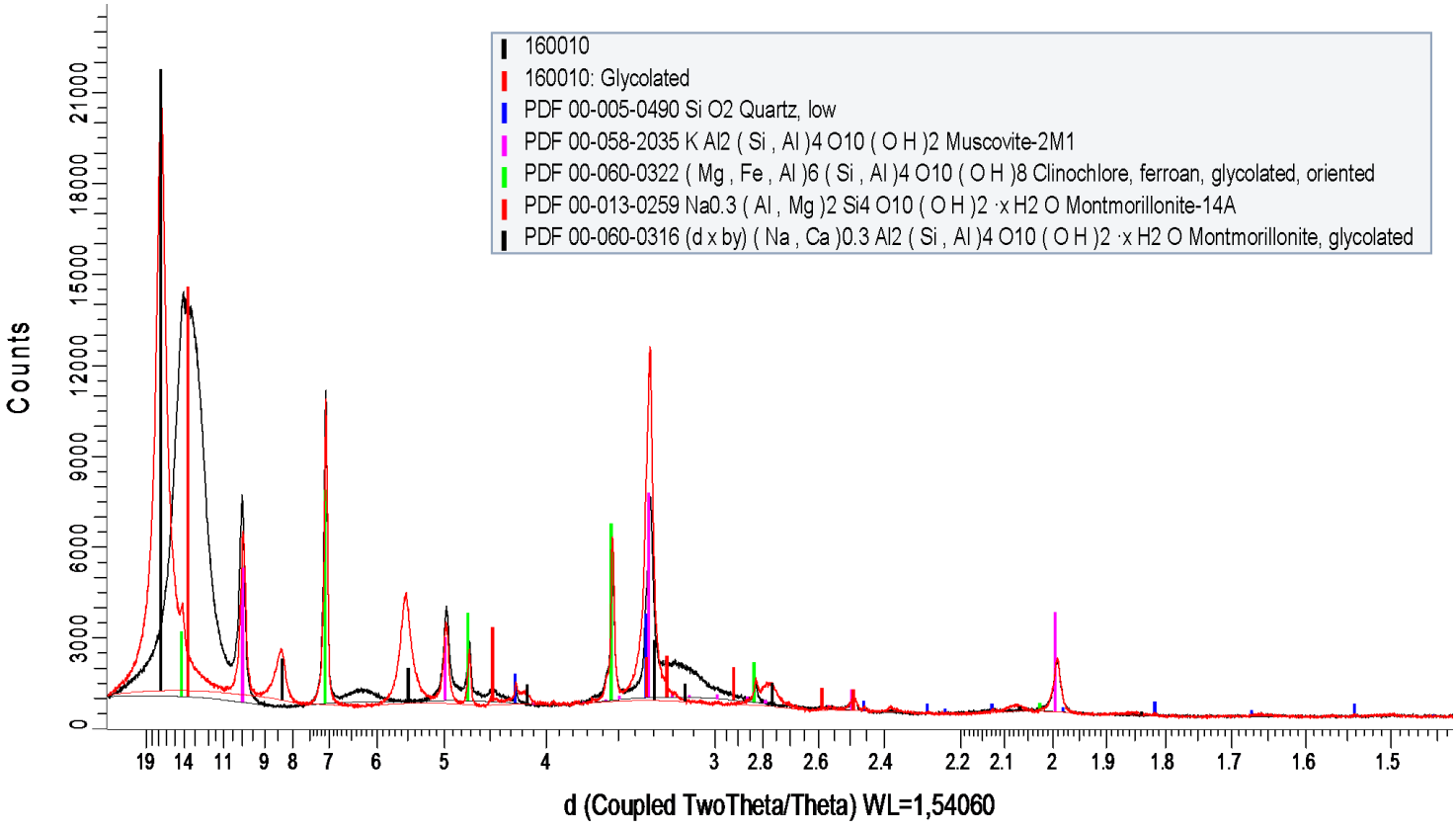

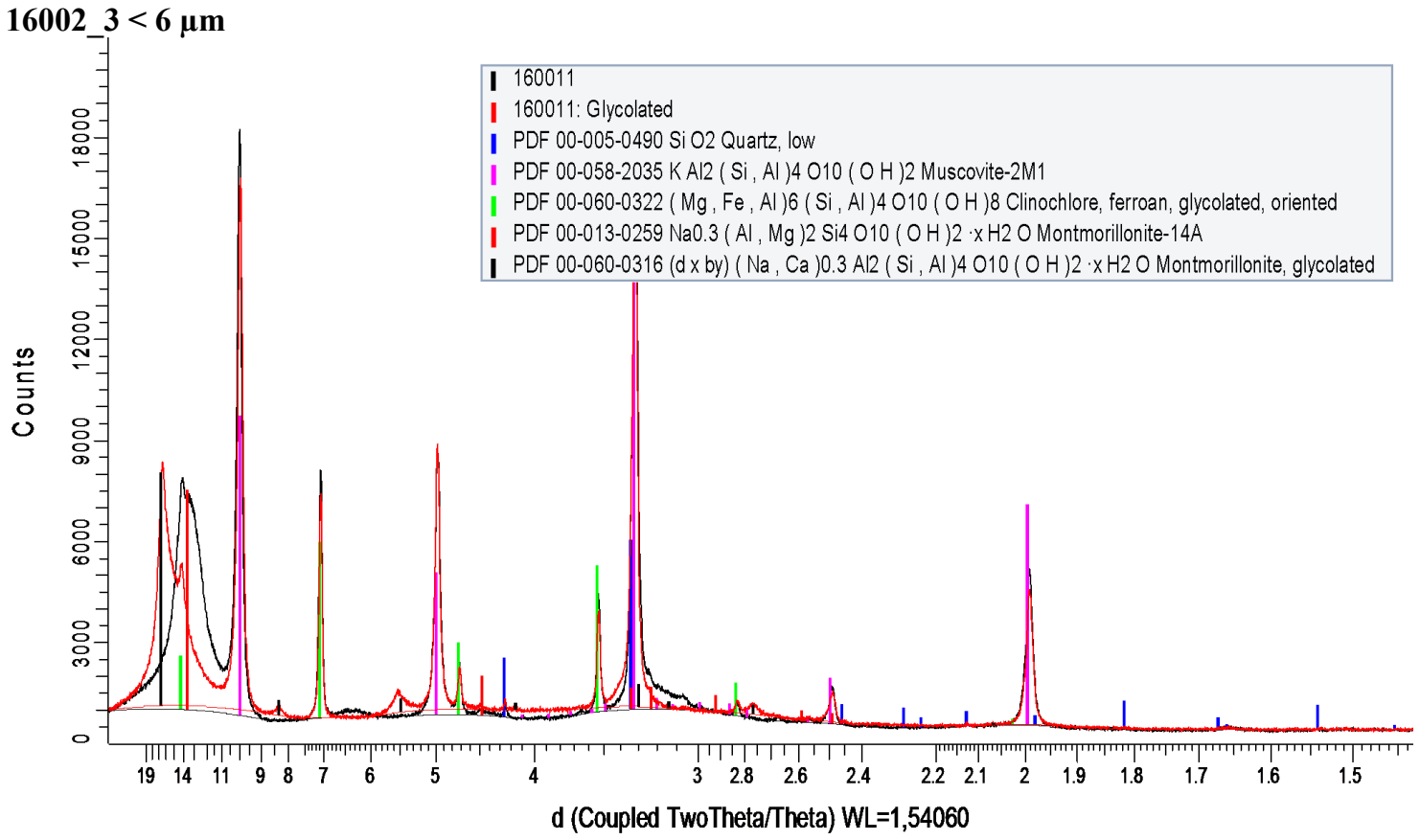
16002_3 < 6 µm
160011
160011: Glycolated
PDF 00-005-0490 Si O2 Quartz, low
PDF 00-058-2035 K Al2 (Si , Al)4 O10 (O H)2 Muscovite-2M1
PDF 00-060-0322 (Mg , Fe , Al)6 (Si , Al)4 O10 (O H)8 Clinochlore, ferroan, glycolated, oriented
PDF 00-013-0259 Na0.3 (Al , Mg)2 Si4 O10 (O H)2 ·x H2 O Montmorillonite-14A
PDF 00-060-0316 (d x by) (Na , Ca)0.3 Al2 (Si , Al)4 O10 (O H)2 ·x H2 O Montmorillonite, glycolated
Counts
0
3000
6000
9000
12000
15000
18000
19 14 11 9 8 7 6 5 4 3 2.8 2.6 2.4 2.2 2.1 2 1.9 1.8 1.7 1.6 1.5
d (Coupled TwoTheta/Theta) WL=1,54060

16083 < 6 µm

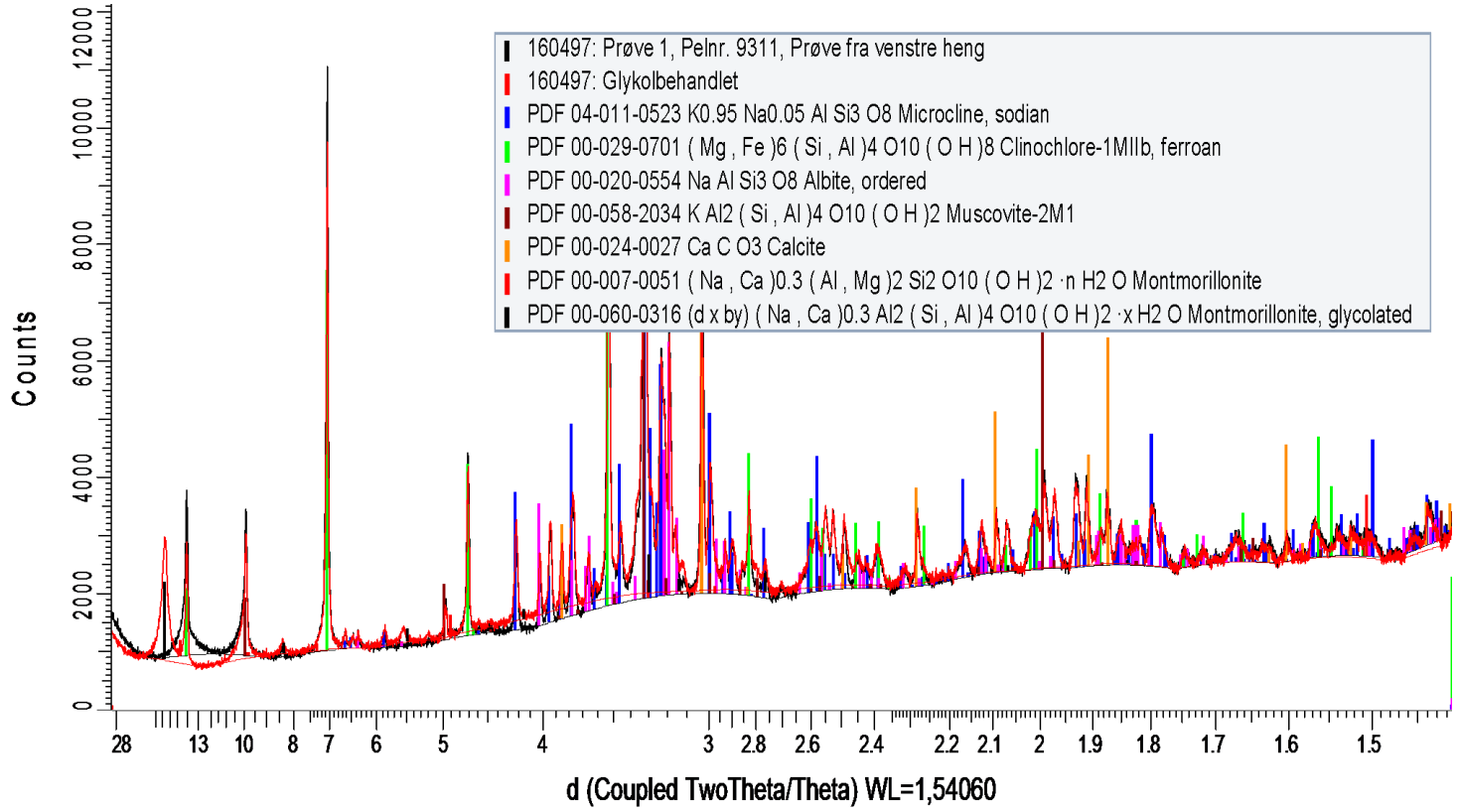
160497: Prøve 1, Pelnr. 9311, Prøve fra venstre heng
160497: Glykolbehandlet
PDF 04-011-0523 K0.95 Na0.05 Al Si3 O8 Microcline, sodian
PDF 00-029-0701 (Mg , Fe)6 (Si , Al)4 O10 (O H)8 Clinochlore-1MIIb, ferroan
PDF 00-020-0554 Na Al Si3 O8 Albite, ordered
PDF 00-058-2034 K Al2 (Si , Al)4 O10 (O H)2 Muscovite-2M1
PDF 00-024-0027 Ca C O3 Calcite
PDF 00-007-0051 (Na , Ca)0.3 (Al , Mg)2 Si2 O10 (O H)2 ·n H2 O Montmorillonite
PDF 00-060-0316 (d x by) (Na , Ca)0.3 Al2 (Si , Al)4 O10 (O H)2 ·x H2 O Montmorillonite, glycolated
Counts
0
2000
4000
6000
8000
10000
12000
28
13
10
8
7
6
5
4
3
2.8
2.6
2.4
2.2
2.1
2
1.9
1.8
1.7
1.6
1.5
d (Coupled TwoTheta/Theta) WL=1,54060

16093 < 6 µm

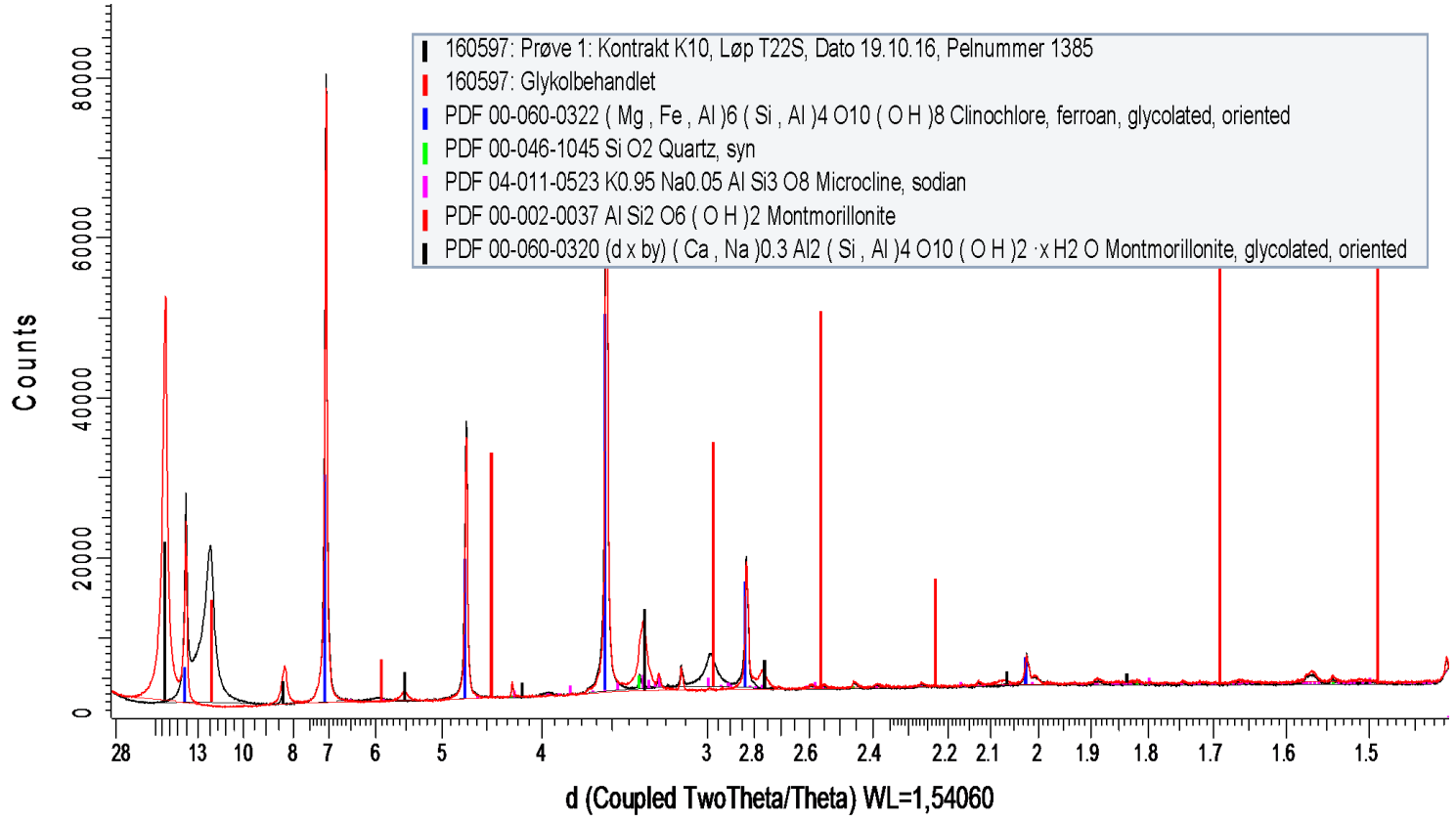
160597: Prøve 1: Kontrakt K10, Løp T22S, Dato 19.10.16, Pelnummer 1385
160597: Glykolbehandlet
PDF 00-060-0322 (Mg , Fe , Al)6 (Si , Al)4 O10 (O H)8 Clinochlore, ferroan, glycolated, oriented
PDF 00-046-1045 Si O2 Quartz, syn
PDF 04-011-0523 K0.95 Na0.05 Al Si3 O8 Microcline, sodian
PDF 00-002-0037 Al Si2 O6 (O H)2 Montmorillonite
PDF 00-060-0320 (d x by) (Ca , Na)0.3 Al2 (Si , Al)4 O10 (O H)2 ·x H2 O Montmorillonite, glycolated, oriented
Counts
0
20000
40000
60000
80000
28
13
10
8
7
6
5
4
3
2.8
2.6
2.4
2.2
2.1
2
1.9
1.8
1.7
1.6
1.5
d (Coupled TwoTheta/Theta) WL=1,54060

16095 < 6 µm

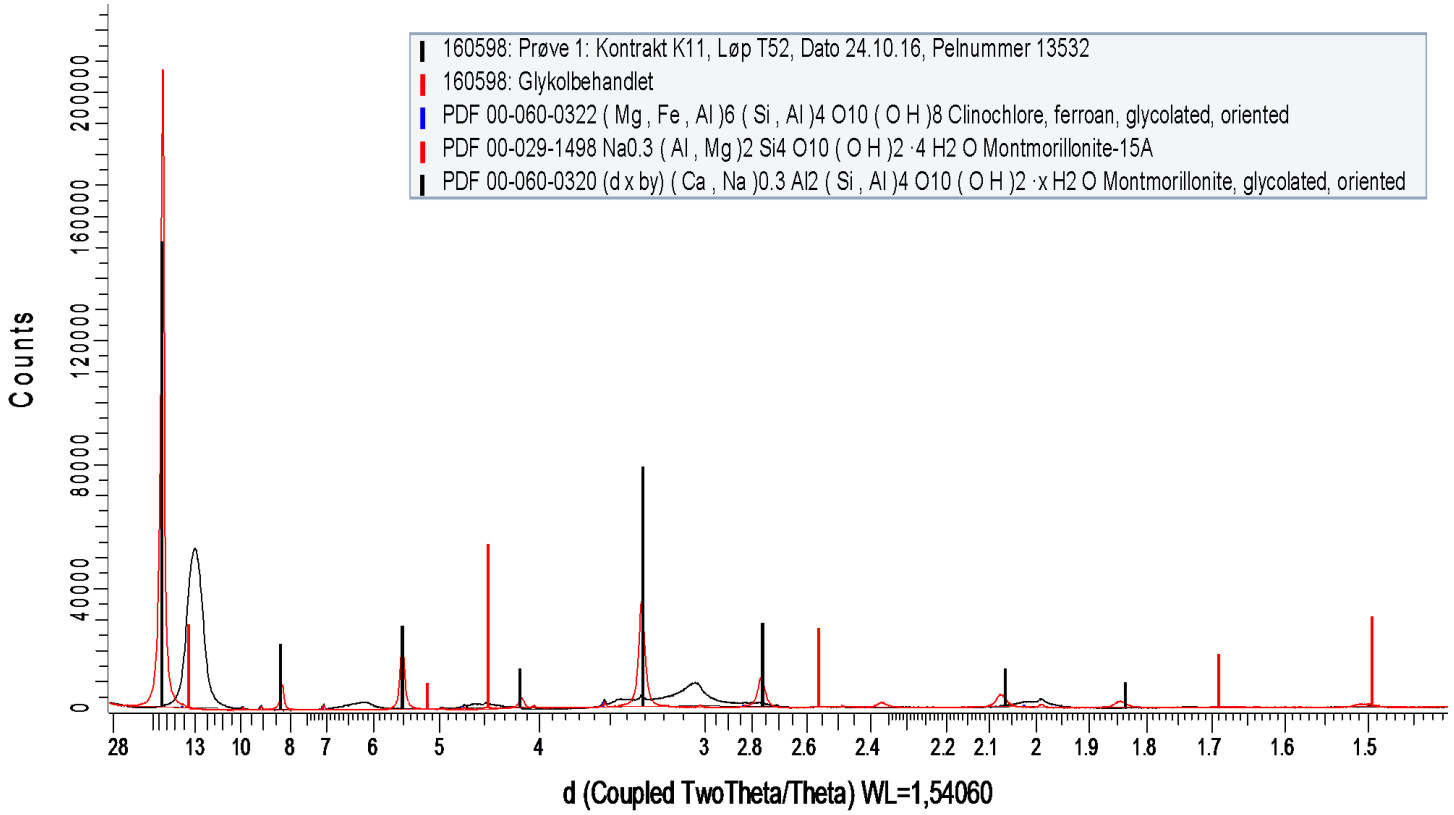
160598: Prøve 1: Kontrakt K11, Løp T52, Dato 24.10.16, Pelnummer 13532
160598: Glykolbehandlet
PDF 00-060-0322 (Mg , Fe , Al)6 (Si , Al)4 O10 (O H)8 Clinochlore, ferroan, glycolated, oriented
PDF 00-029-1498 Na0.3 (Al , Mg)2 Si4 O10 (O H)2 ·4 H2 O Montmorillonite-15A
PDF 00-060-0320 (d x by) (Ca , Na)0.3 Al2 (Si , Al)4 O10 (O H)2 ·x H2 O Montmorillonite, glycolated, oriented
Counts
0
40000
80000
120000
160000
200000
28
13
10
8
7
6
5
4
3
2.8
2.6
2.4
2.2
2.1
2
1.9
1.8
1.7
1.6
1.5
d (Coupled TwoTheta/Theta) WL=1,54060

16100 < 6 µm

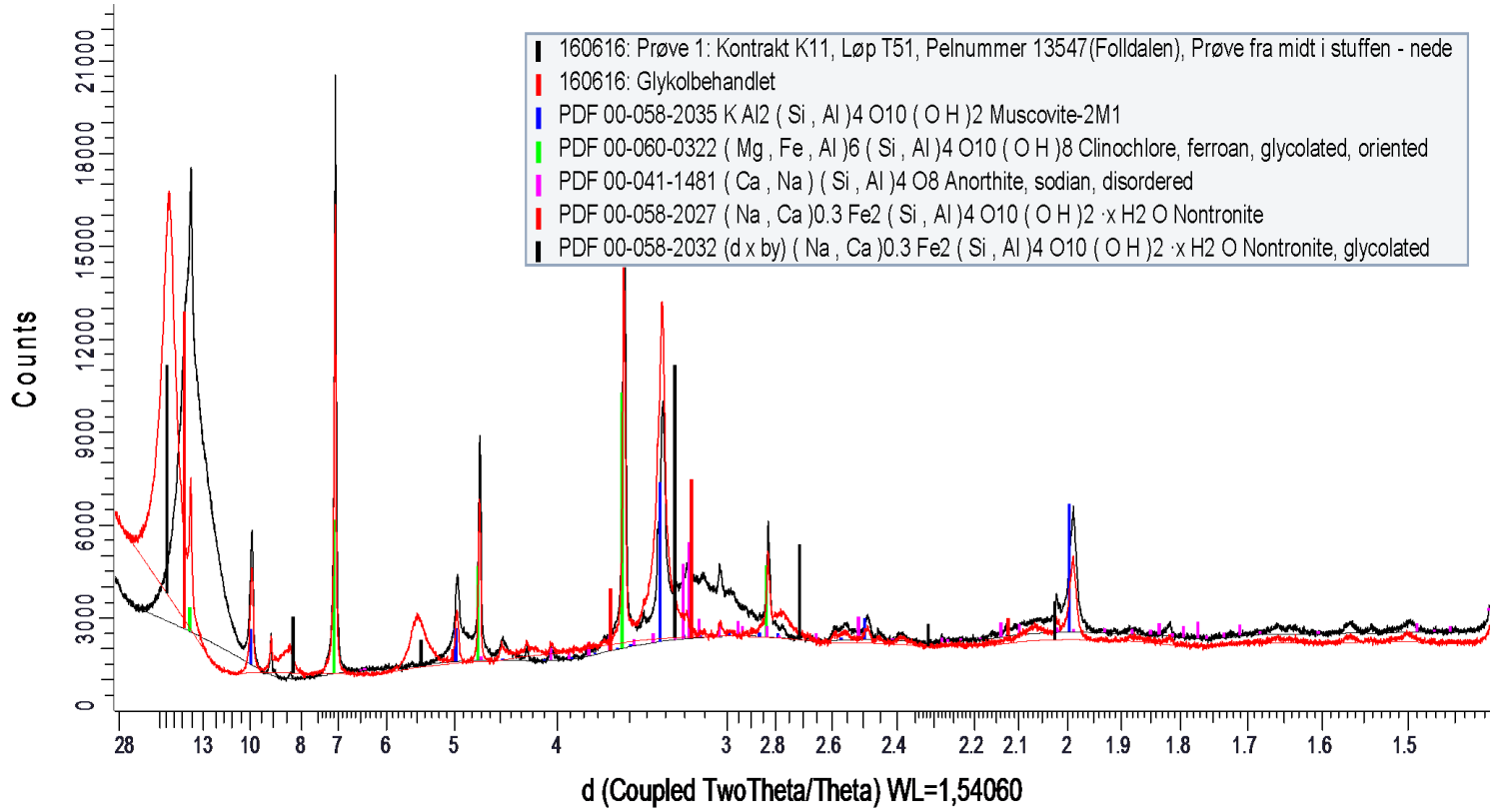
160616: Prøve 1: Kontrakt K11, Løp T51, Pelnummer 13547(Folldalen), Prøve fra midt i stuffen - nede
160616: Glykolbehandlet
PDF 00-058-2035 K Al2 (Si , Al)4 O10 (O H)2 Muscovite-2M1
PDF 00-060-0322 (Mg , Fe , Al)6 (Si , Al)4 O10 (O H)8 Clinochlore, ferroan, glycolated, oriented
PDF 00-041-1481 (Ca , Na) (Si , Al)4 O8 Anorthite, sodian, disordered
PDF 00-058-2027 (Na , Ca)0.3 Fe2 (Si , Al)4 O10 (O H)2 ·x H2 O Nontronite
PDF 00-058-2032 (d x by) (Na , Ca)0.3 Fe2 (Si , Al)4 O10 (O H)2 ·x H2 O Nontronite, glycolated
Counts
0
3000
6000
9000
12000
15000
18000
21000
28
13
10
8
7
6
5
4
3
2.8
2.6
2.4
2.2
2.1
2
1.9
1.8
1.7
1.6
1.5
d (Coupled TwoTheta/Theta) WL=1,54060

16101 < 6 µm

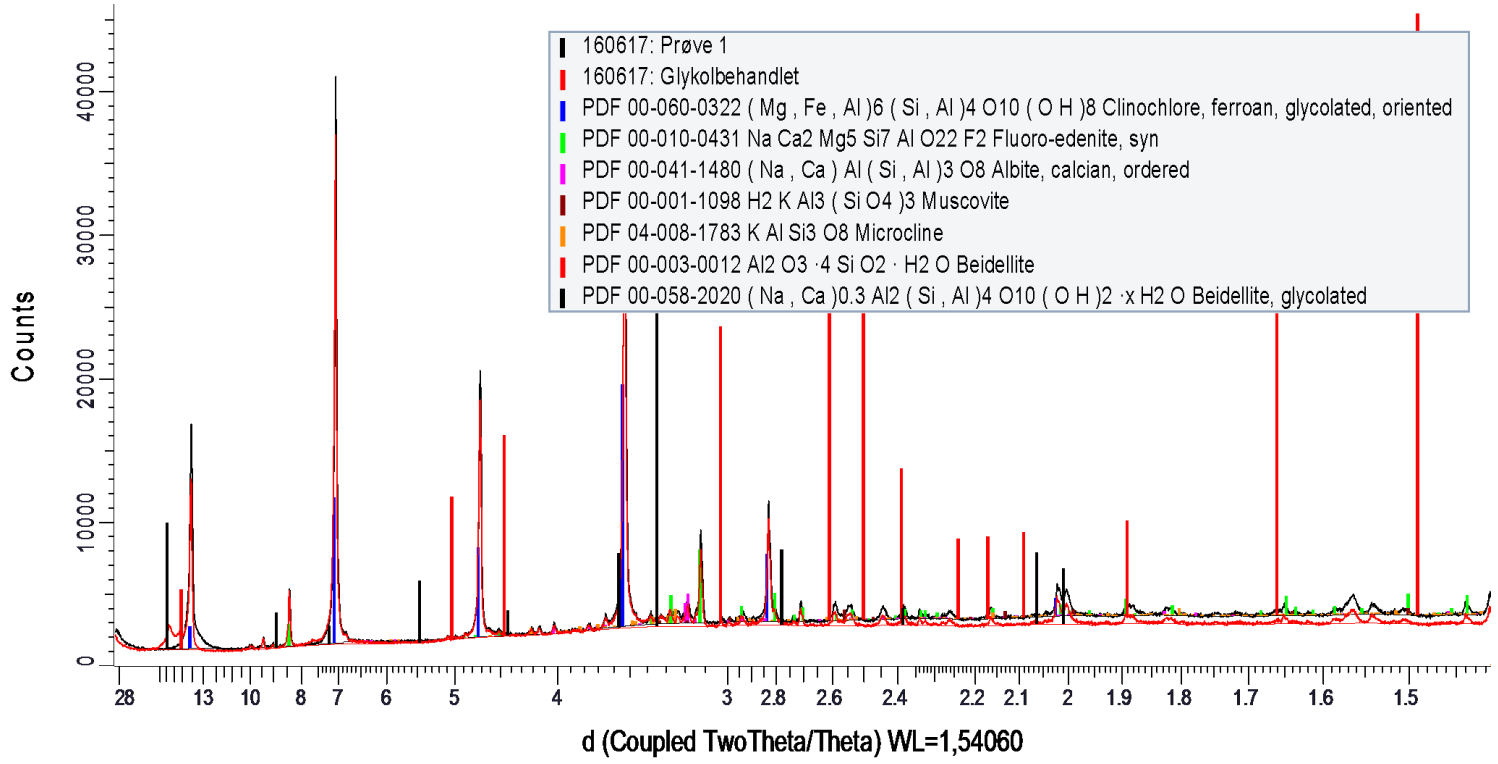
160617: Prøve 1
160617: Glykolbehandlet
PDF 00-060-0322 (Mg , Fe , Al)6 (Si , Al)4 O10 (O H)8 Clinochlore, ferroan, glycolated, oriented
PDF 00-010-0431 Na Ca2 Mg5 Si7 Al O22 F2 Fluoro-edenite, syn
PDF 00-041-1480 (Na , Ca) Al (Si , Al)3 O8 Albite, calcian, ordered
PDF 00-001-1098 H2 K Al3 (Si O4)3 Muscovite
PDF 04-008-1783 K Al Si3 O8 Microcline
PDF 00-003-0012 Al2 O3 ·4 Si O2 · H2 O Beidellite
PDF 00-058-2020 (Na , Ca)0.3 Al2 (Si , Al)4 O10 (O H)2 ·x H2 O Beidellite, glycolated
Counts
0
10000
20000
30000
40000
28
13
10
8
7
6
5
4
3
2.8
2.6
2.4
2.2
2.1
2
1.9
1.8
1.7
1.6
1.5
d (Coupled TwoTheta/Theta) WL=1,54060

16107 < 6 µm

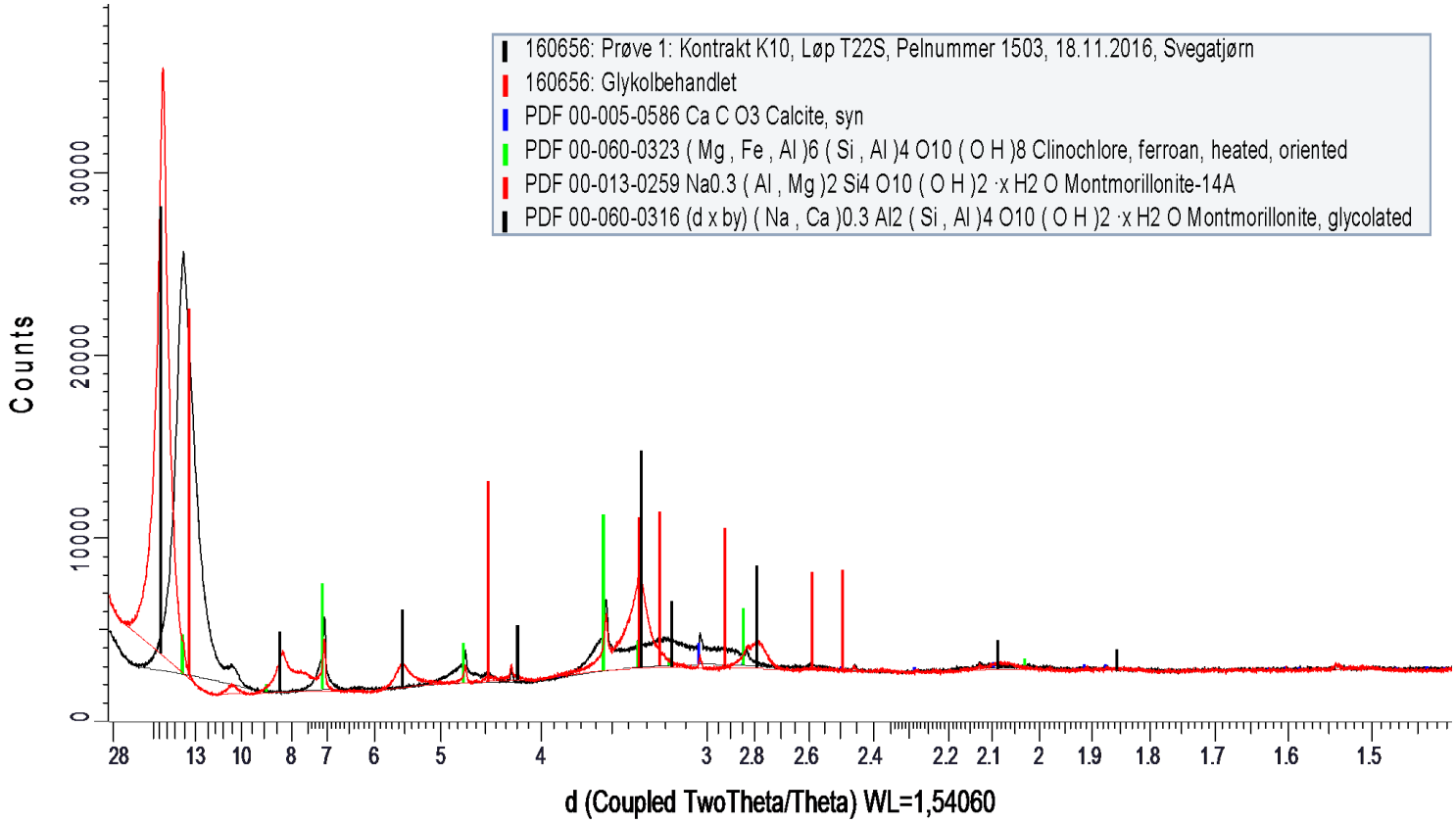
160656: Prøve 1: Kontrakt K10, Løp T22S, Pelnummer 1503, 18.11.2016, Svegatjørn
160656: Glykolbehandlet
PDF 00-005-0586 Ca C O3 Calcite, syn
PDF 00-060-0323 (Mg , Fe , Al)6 (Si , Al)4 O10 (O H)8 Clinochlore, ferroan, heated, oriented
PDF 00-013-0259 Na0.3 (Al , Mg)2 Si4 O10 (O H)2 ·x H2 O Montmorillonite-14A
PDF 00-060-0316 (d x by) (Na , Ca)0.3 Al2 (Si , Al)4 O10 (O H)2 ·x H2 O Montmorillonite, glycolated
Counts
0
10000
20000
30000
28
13
10
8
7
6
5
4
3
2.8
2.6
2.4
2.2
2.1
2
1.9
1.8
1.7
1.6
1.5
d (Coupled TwoTheta/Theta) WL=1,54060

16111 < 6 µm

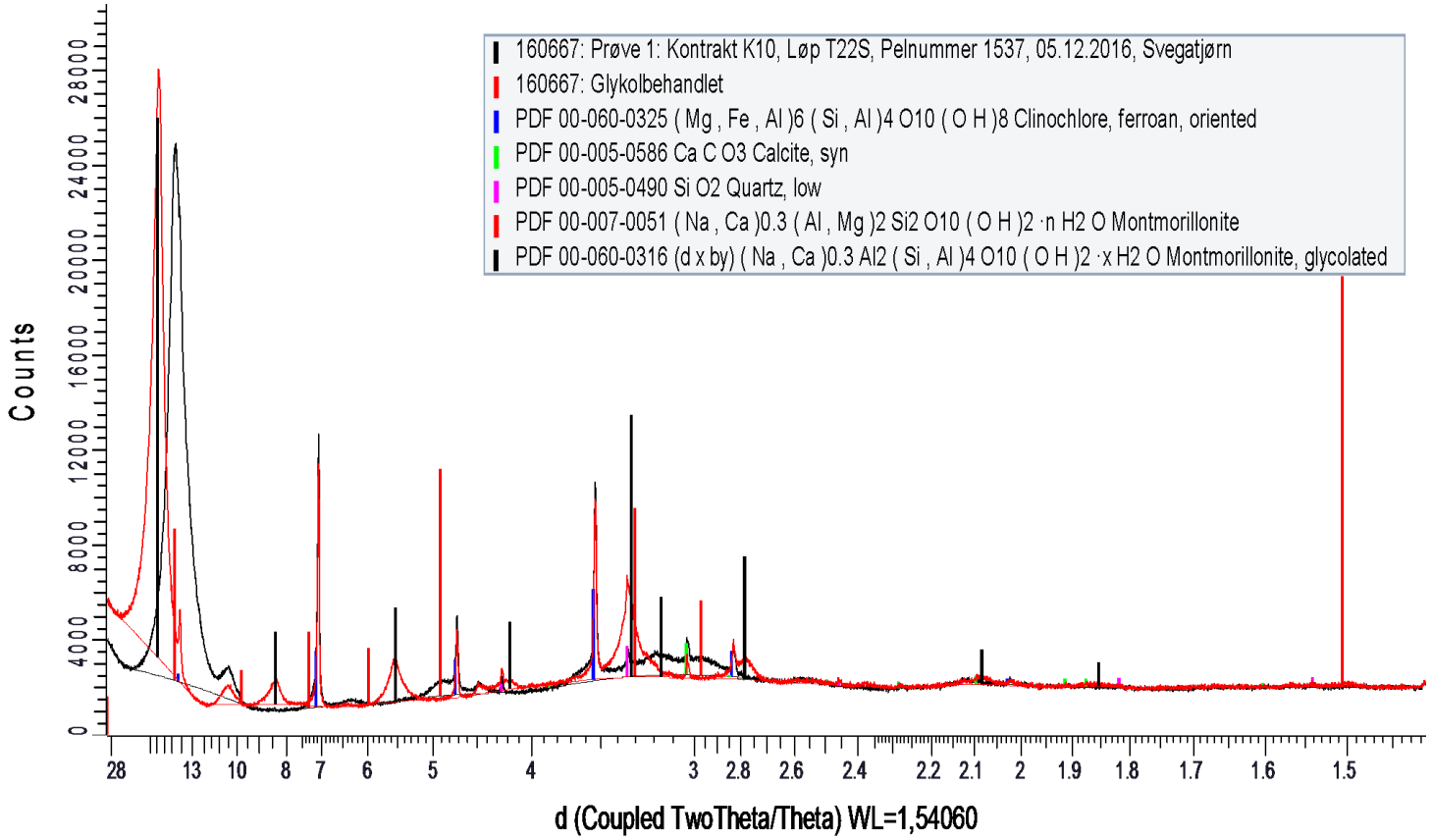
160667: Prøve 1: Kontrakt K10, Løp T22S, Pelnummer 1537, 05.12.2016, Svegatjørn
160667: Glykolbehandlet
PDF 00-060-0325 (Mg , Fe , Al)6 (Si , Al)4 O10 (O H)8 Clinochlore, ferroan, oriented
PDF 00-005-0586 Ca C O3 Calcite, syn
PDF 00-005-0490 Si O2 Quartz, low
PDF 00-007-0051 (Na , Ca)0.3 (Al , Mg)2 Si2 O10 (O H)2 ·n H2 O Montmorillonite
PDF 00-060-0316 (d x by) (Na , Ca)0.3 Al2 (Si , Al)4 O10 (O H)2 ·x H2 O Montmorillonite, glycolated
Counts
0
4000
8000
12000
16000
20000
24000
28000
28
13
10
8
7
6
5
4
3
2.8
2.6
2.4
2.2
2.1
2
1.9
1.8
1.7
1.6
1.5
d (Coupled TwoTheta/Theta) WL=1,54060

16114 < 6 µm

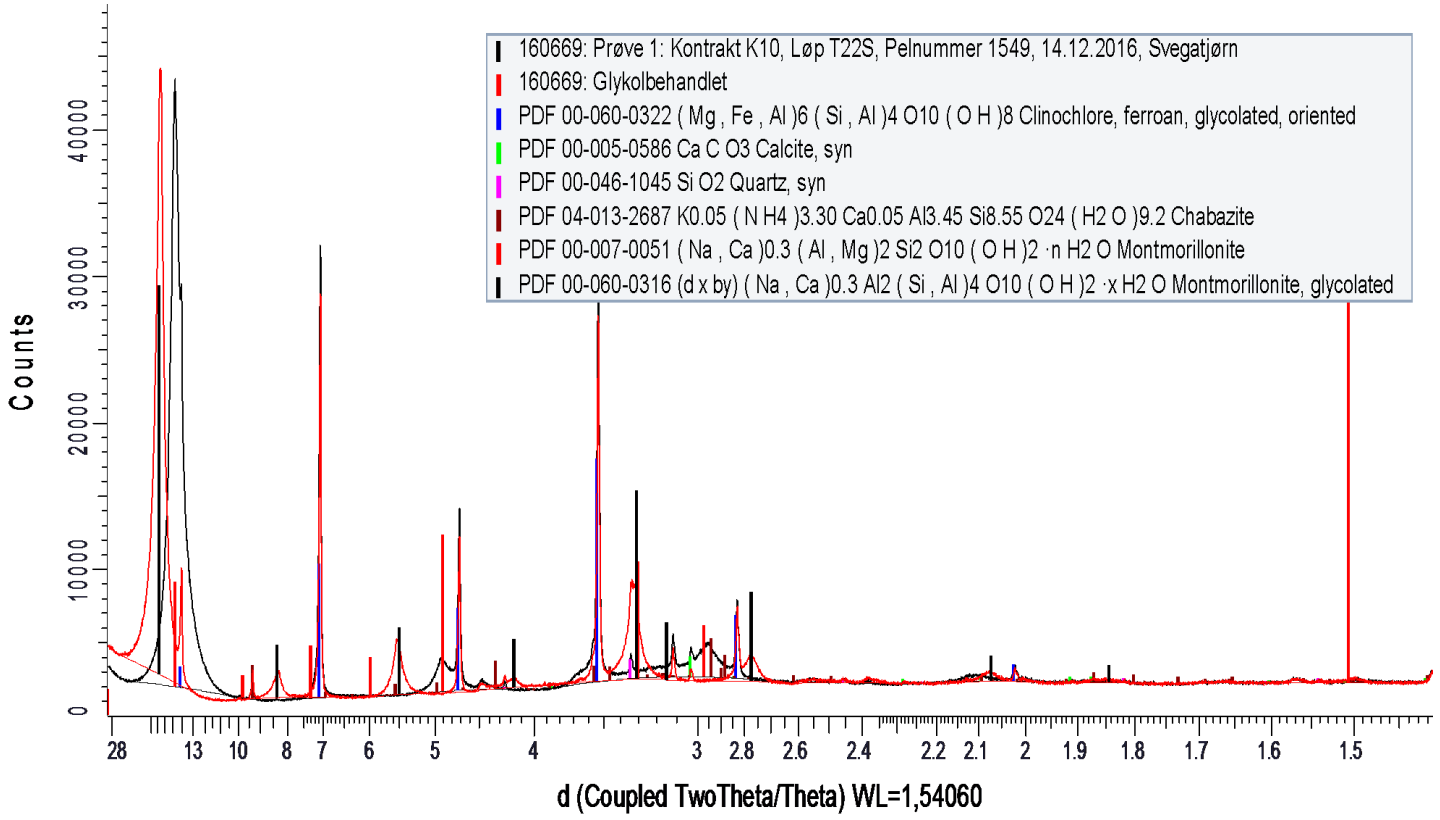
160669: Prøve 1: Kontrakt K10, Løp T22S, Pelnummer 1549, 14.12.2016, Svegatjørn
160669: Glykolbehandlet
PDF 00-060-0322 (Mg , Fe , Al)6 (Si , Al)4 O10 (O H)8 Clinochlore, ferroan, glycolated, oriented
PDF 00-005-0586 Ca C O3 Calcite, syn
PDF 00-046-1045 Si O2 Quartz, syn
PDF 04-013-2687 K0.05 (N H4)3.30 Ca0.05 Al3.45 Si8.55 O24 (H2 O)9.2 Chabazite
PDF 00-007-0051 (Na , Ca)0.3 (Al , Mg)2 Si2 O10 (O H)2 ·n H2 O Montmorillonite
PDF 00-060-0316 (d x by) (Na , Ca)0.3 Al2 (Si , Al)4 O10 (O H)2 ·x H2 O Montmorillonite, glycolated
Counts
0
10000
20000
30000
40000
28
13
10
8
7
6
5
4
3
2.8
2.6
2.4
2.2
2.1
2
1.9
1.8
1.7
1.6
1.5
d (Coupled TwoTheta/Theta) WL=1,54060

17051 < 6 µm

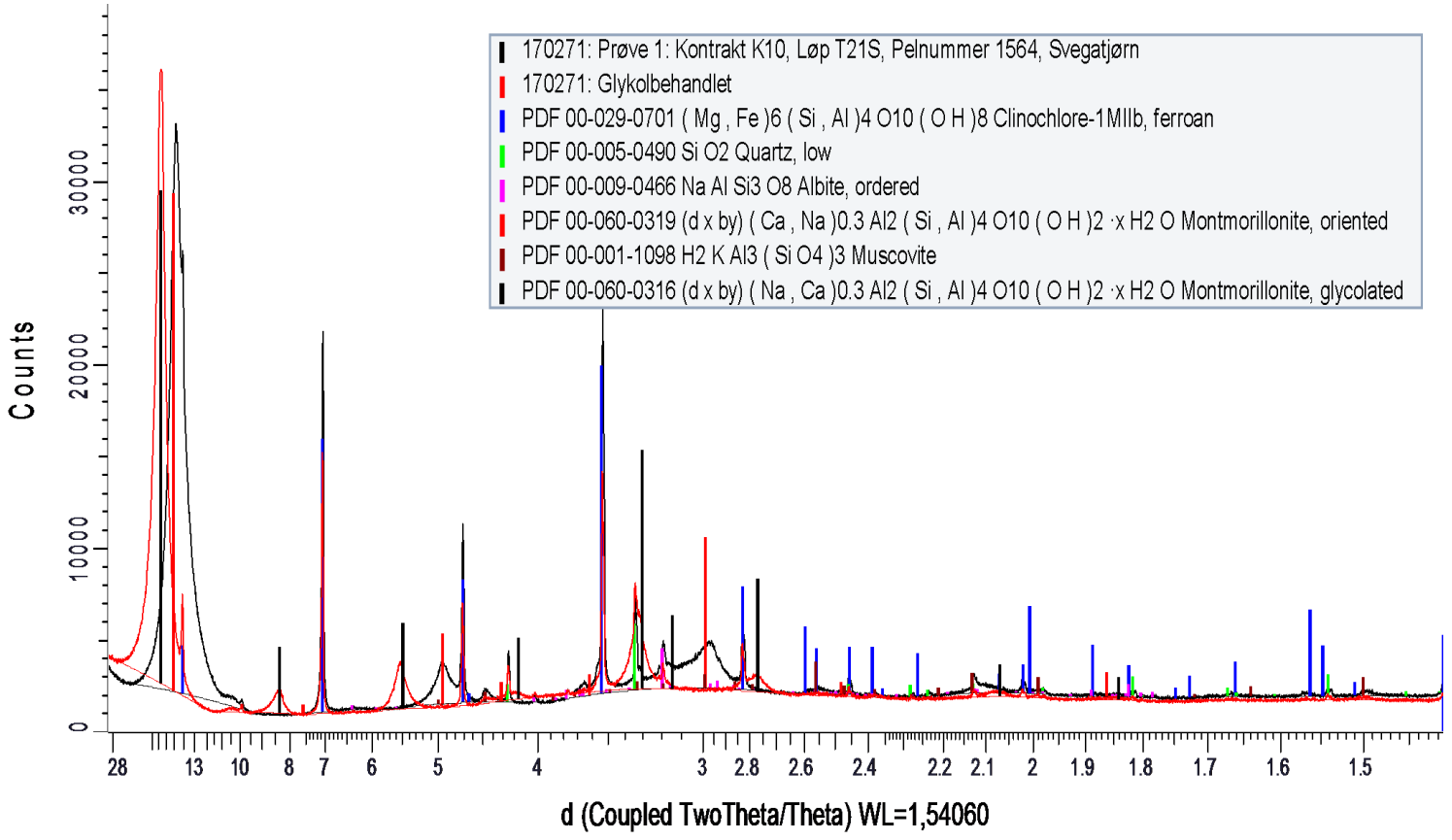
170271: Prøve 1: Kontrakt K10, Løp T21S, Pelnummer 1564, Svegatjørn
170271: Glykolbehandlet
PDF 00-029-0701 (Mg , Fe)6 (Si , Al)4 O10 (O H)8 Clinochlore-1MIIb, ferroan
PDF 00-005-0490 Si O2 Quartz, low
PDF 00-009-0466 Na Al Si3 O8 Albite, ordered
PDF 00-060-0319 (d x by) (Ca , Na)0.3 Al2 (Si , Al)4 O10 (O H)2 ·x H2 O Montmorillonite, oriented
PDF 00-001-1098 H2 K Al3 (Si O4)3 Muscovite
PDF 00-060-0316 (d x by) (Na , Ca)0.3 Al2 (Si , Al)4 O10 (O H)2 ·x H2 O Montmorillonite, glycolated
Counts
0
10000
20000
30000
28
13
10
8
7
6
5
4
3
2.8
2.6
2.4
2.2
2.1
2
1.9
1.8
1.7
1.6
1.5
d (Coupled TwoTheta/Theta) WL=1,54060

17087< 6 µm

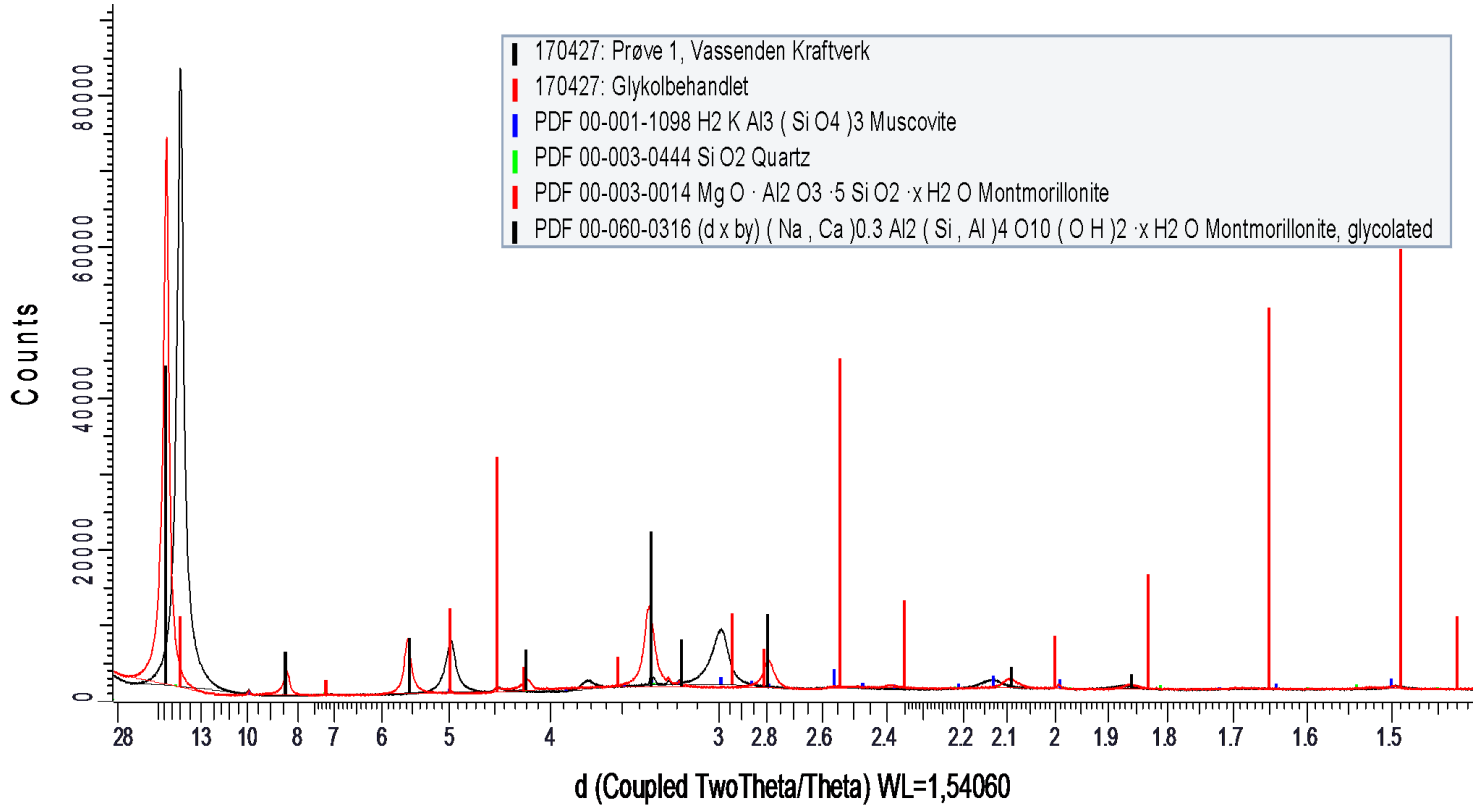
170427: Prøve 1, Vassenden Kraftverk
170427: Glykolbehandlet
PDF 00-001-1098 H2 K Al3 (Si O4)3 Muscovite
PDF 00-003-0444 Si O2 Quartz
PDF 00-003-0014 Mg O · Al2 O3 ·5 Si O2 ·x H2 O Montmorillonite
PDF 00-060-0316 (d x by) (Na , Ca)0.3 Al2 (Si , Al)4 O10 (O H)2 ·x H2 O Montmorillonite, glycolated
Counts
0
20000
40000
60000
80000
28
13
10
8
7
6
5
4
3
2.8
2.6
2.4
2.2
2.1
2
1.9
1.8
1.7
1.6
1.5
d (Coupled TwoTheta/Theta) WL=1,54060

17088< 6 µm

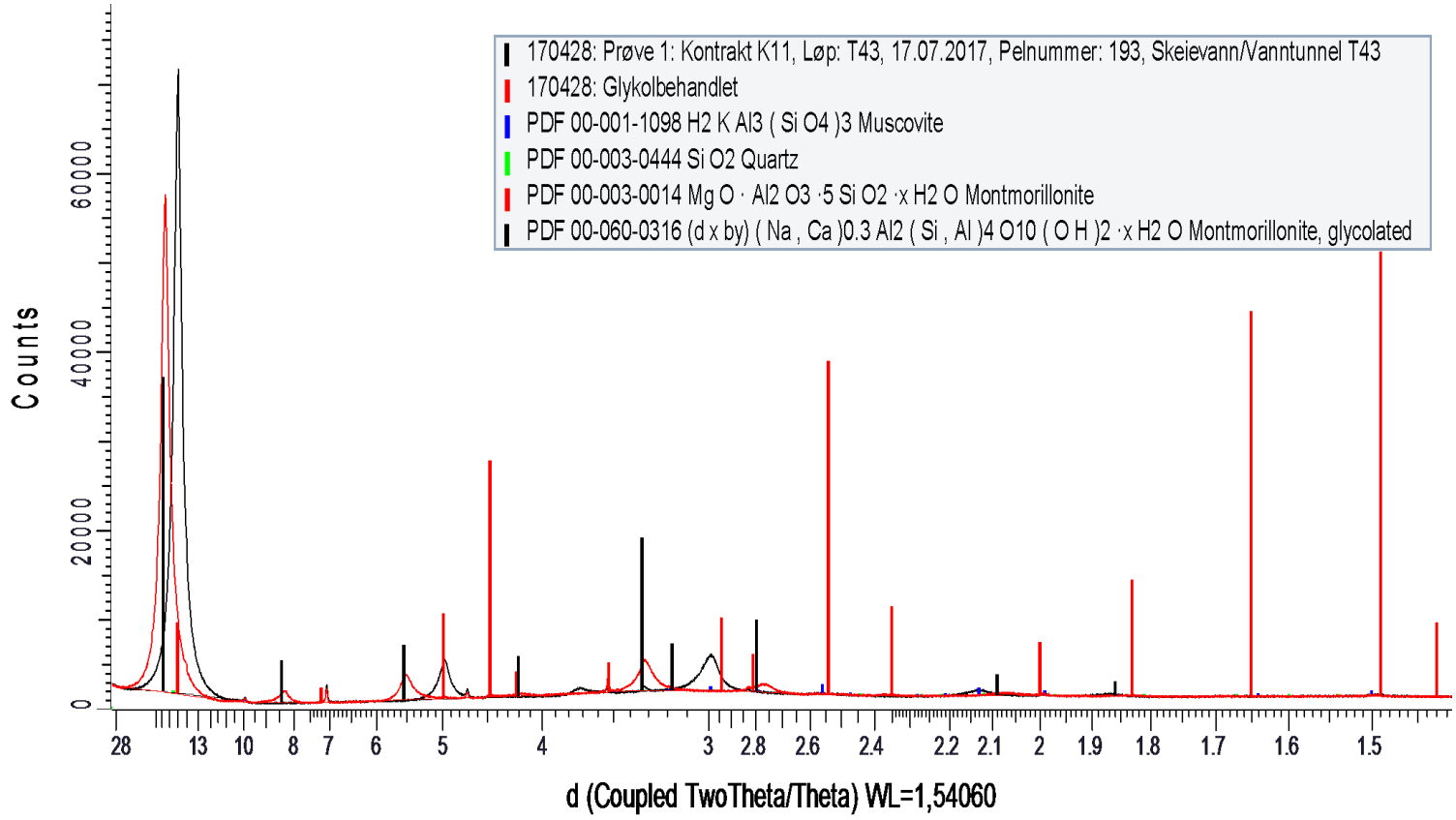
170428: Prøve 1: Kontrakt K11, Løp: T43, 17.07.2017, Pelnummer: 193, Skeievann/Vanntunnel T43
170428: Glykolbehandlet
PDF 00-001-1098 H2 K Al3 (Si O4)3 Muscovite
PDF 00-003-0444 Si O2 Quartz
PDF 00-003-0014 Mg O · Al2 O3 ·5 Si O2 ·x H2 O Montmorillonite
PDF 00-060-0316 (d x by) (Na , Ca)0.3 Al2 (Si , Al)4 O10 (O H)2 ·x H2 O Montmorillonite, glycolated
Counts
0
20000
40000
60000
28
13
10
8
7
6
5
4
3
2.8
2.6
2.4
2.2
2.1
2
1.9
1.8
1.7
1.6
1.5
d (Coupled TwoTheta/Theta) WL=1,54060

17105 < 6 µm

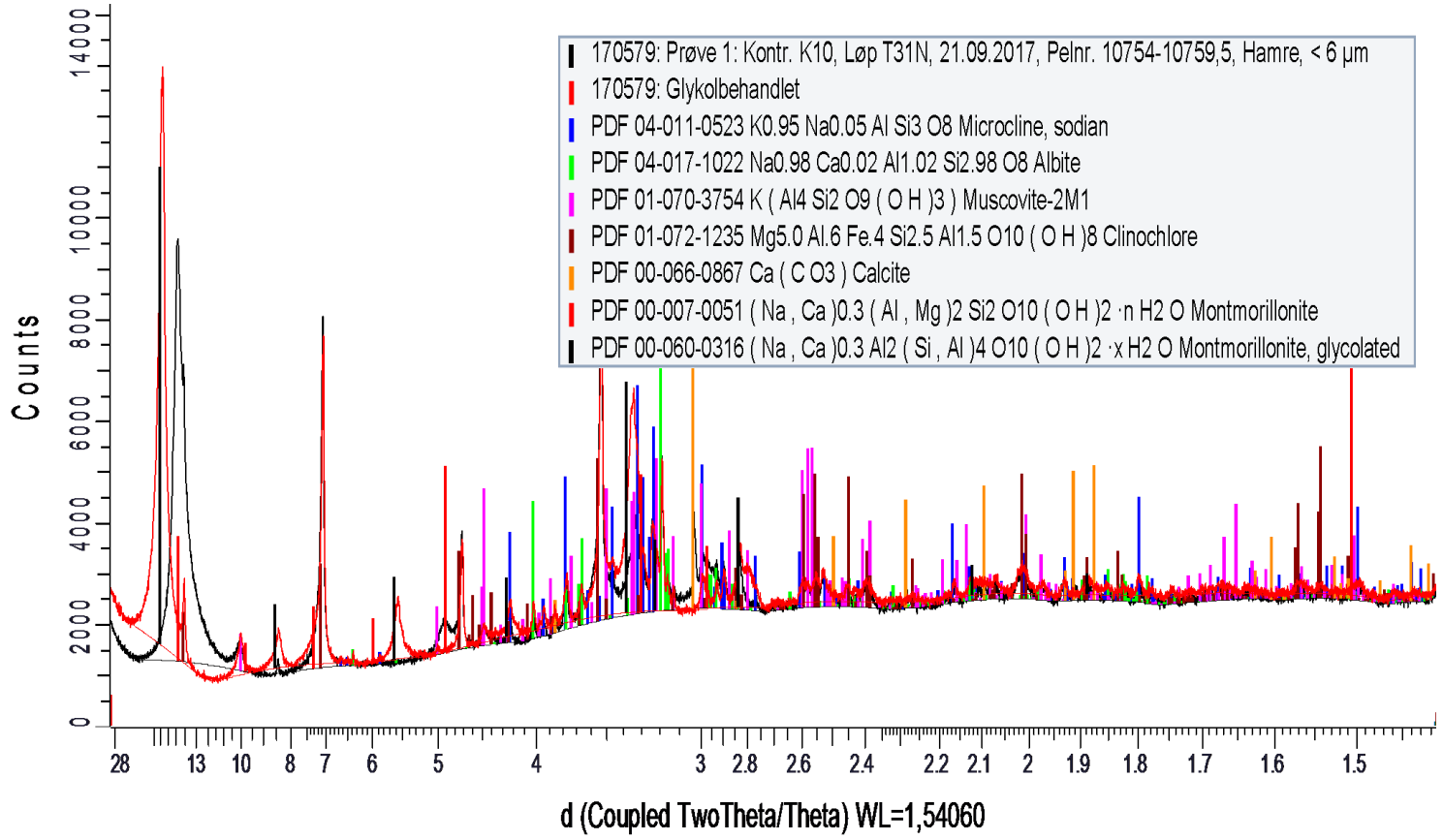
170579: Prøve 1: Kontr. K10, Løp T31N, 21.09.2017, Pelnr. 10754-10759,5, Hamre, < 6 µm
170579: Glykolbehandlet
PDF 04-011-0523 K0.95 Na0.05 Al Si3 O8 Microcline, sodian
PDF 04-017-1022 Na0.98 Ca0.02 Al1.02 Si2.98 O8 Albite
PDF 01-070-3754 K (Al4 Si2 O9 (O H)3) Muscovite-2M1
PDF 01-072-1235 Mg5.0 Al.6 Fe.4 Si2.5 Al1.5 O10 (O H)8 Clinochlore
PDF 00-066-0867 Ca (C O3) Calcite
PDF 00-007-0051 (Na , Ca)0.3 (Al , Mg)2 Si2 O10 (O H)2 ·n H2 O Montmorillonite
PDF 00-060-0316 (Na , Ca)0.3 Al2 (Si , Al)4 O10 (O H)2 ·x H2 O Montmorillonite, glycolated
Counts
0
2000
4000
6000
8000
10000
14000
28
13
10
8
7
6
5
4
3
2.8
2.6
2.4
2.2
2.1
2
1.9
1.8
1.7
1.6
1.5
d (Coupled TwoTheta/Theta) WL=1,54060

17116 < 6 µm

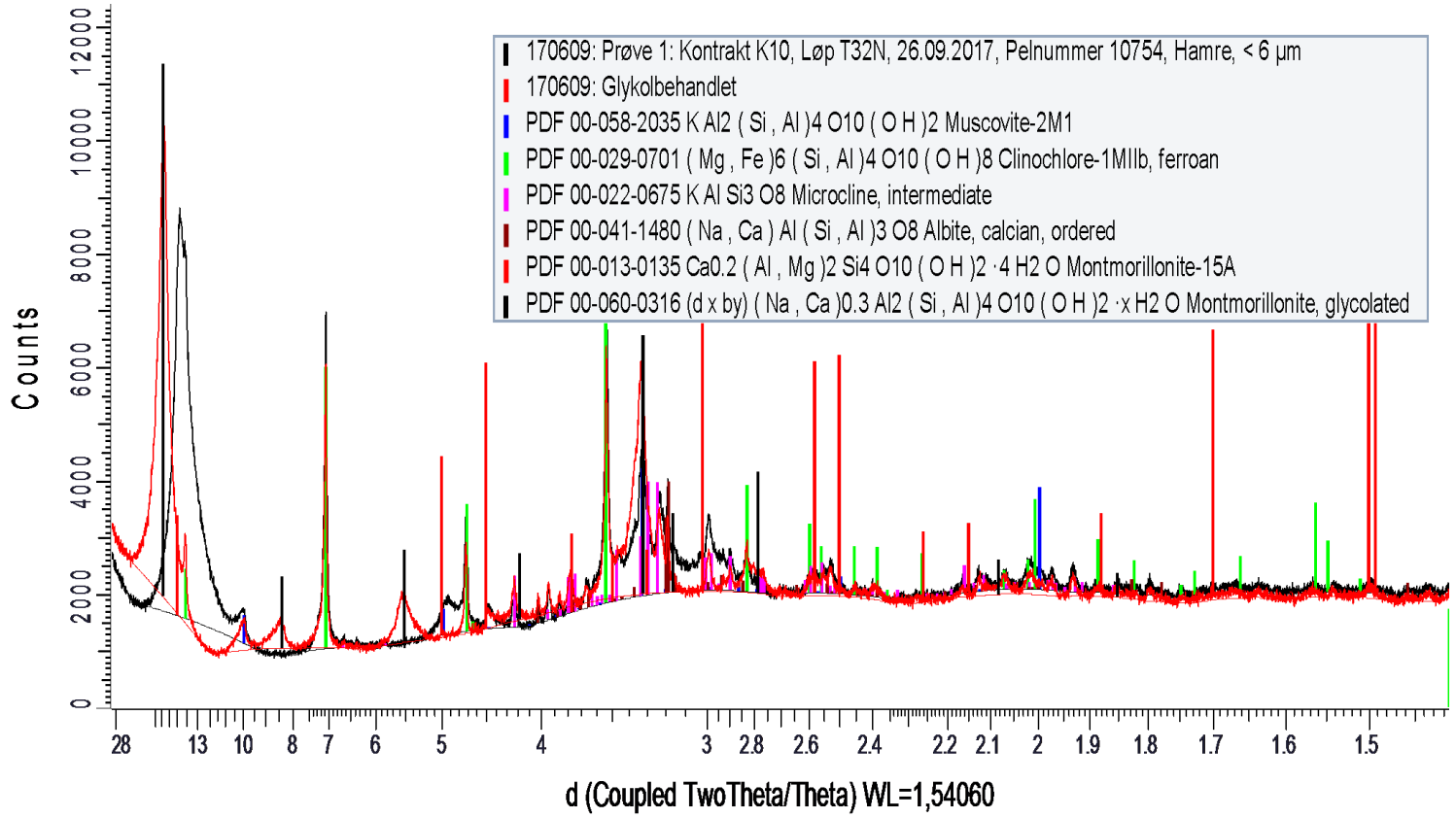
170609: Prøve 1: Kontrakt K10, Løp T32N, 26.09.2017, Pelnummer 10754, Hamre, < 6 µm
170609: Glykolbehandlet
PDF 00-058-2035 K Al2 (Si , Al)4 O10 (O H)2 Muscovite-2M1
PDF 00-029-0701 (Mg , Fe)6 (Si , Al)4 O10 (O H)8 Clinochlore-1MIIb, ferroan
PDF 00-022-0675 K Al Si3 O8 Microcline, intermediate
PDF 00-041-1480 (Na , Ca) Al (Si , Al)3 O8 Albite, calcian, ordered
PDF 00-013-0135 Ca0.2 (Al , Mg)2 Si4 O10 (O H)2 ·4 H2 O Montmorillonite-15A
PDF 00-060-0316 (d x by) (Na , Ca)0.3 Al2 (Si , Al)4 O10 (O H)2 ·x H2 O Montmorillonite, glycolated
Counts
0
2000
4000
6000
8000
10000
12000
28
13
10
8
7
6
5
4
3
2.8
2.6
2.4
2.2
2.1
2
1.9
1.8
1.7
1.6
1.5
d (Coupled TwoTheta/Theta) WL=1,54060

17125 < 6 µm

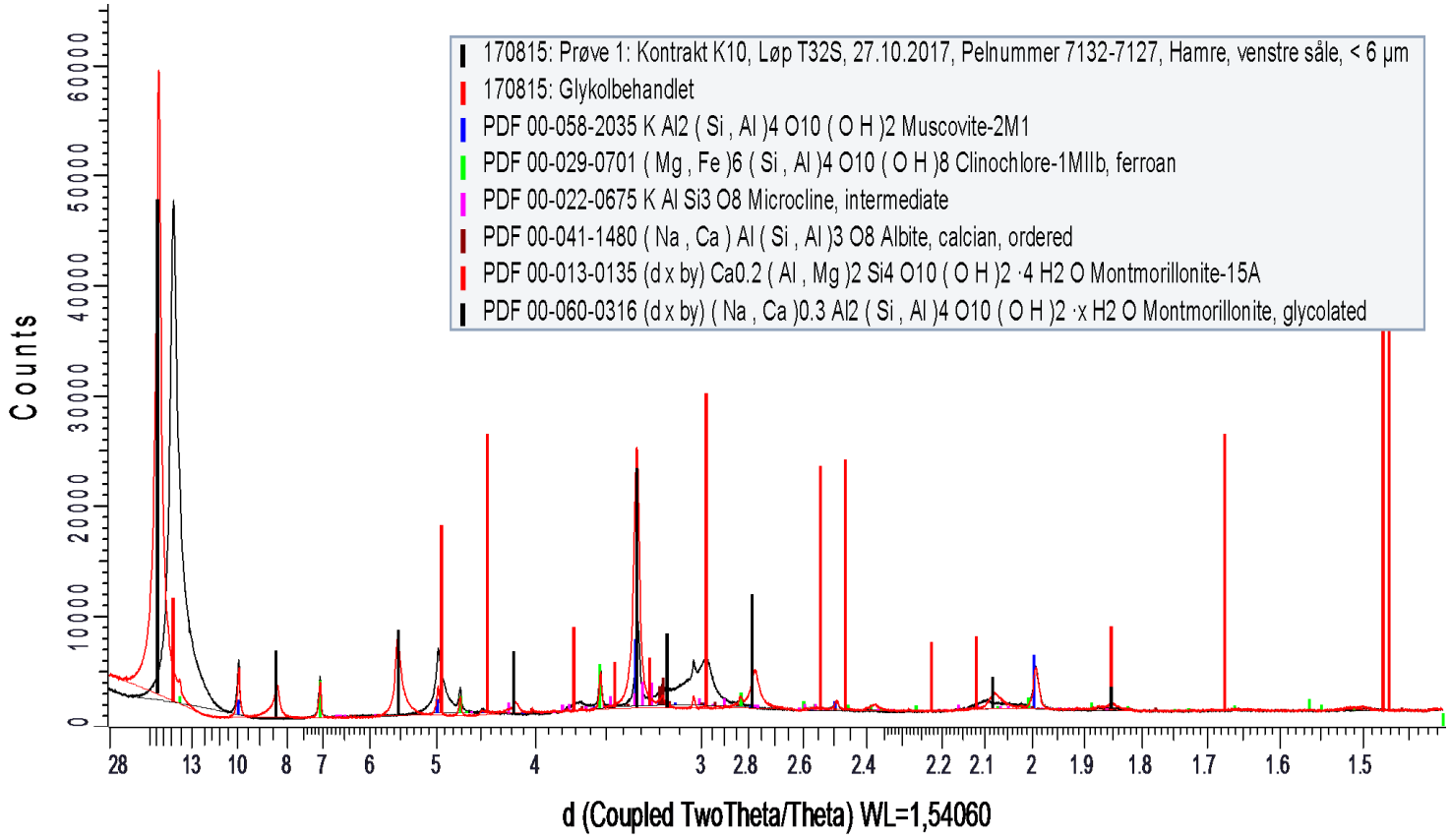
170815: Prøve 1: Kontrakt K10, Løp T32S, 27.10.2017, Pelnummer 7132-7127, Hamre, venstre såle, < 6 µm
170815: Glykolbehandlet
PDF 00-058-2035 K Al2 (Si , Al)4 O10 (O H)2 Muscovite-2M1
PDF 00-029-0701 (Mg , Fe)6 (Si , Al)4 O10 (O H)8 Clinochlore-1MIIb, ferroan
PDF 00-022-0675 K Al Si3 O8 Microcline, intermediate
PDF 00-041-1480 (Na , Ca) Al (Si , Al)3 O8 Albite, calcian, ordered
PDF 00-013-0135 (d x by) Ca0.2 (Al , Mg)2 Si4 O10 (O H)2 ·4 H2 O Montmorillonite-15A
PDF 00-060-0316 (d x by) (Na , Ca)0.3 Al2 (Si , Al)4 O10 (O H)2 ·x H2 O Montmorillonite, glycolated
Counts
0
10000
20000
30000
40000
50000
60000
28
13
10
8
7
6
5
4
3
2.8
2.6
2.4
2.2
2.1
2
1.9
1.8
1.7
1.6
1.5
d (Coupled TwoTheta/Theta) WL=1,54060

17157 < 6 µm

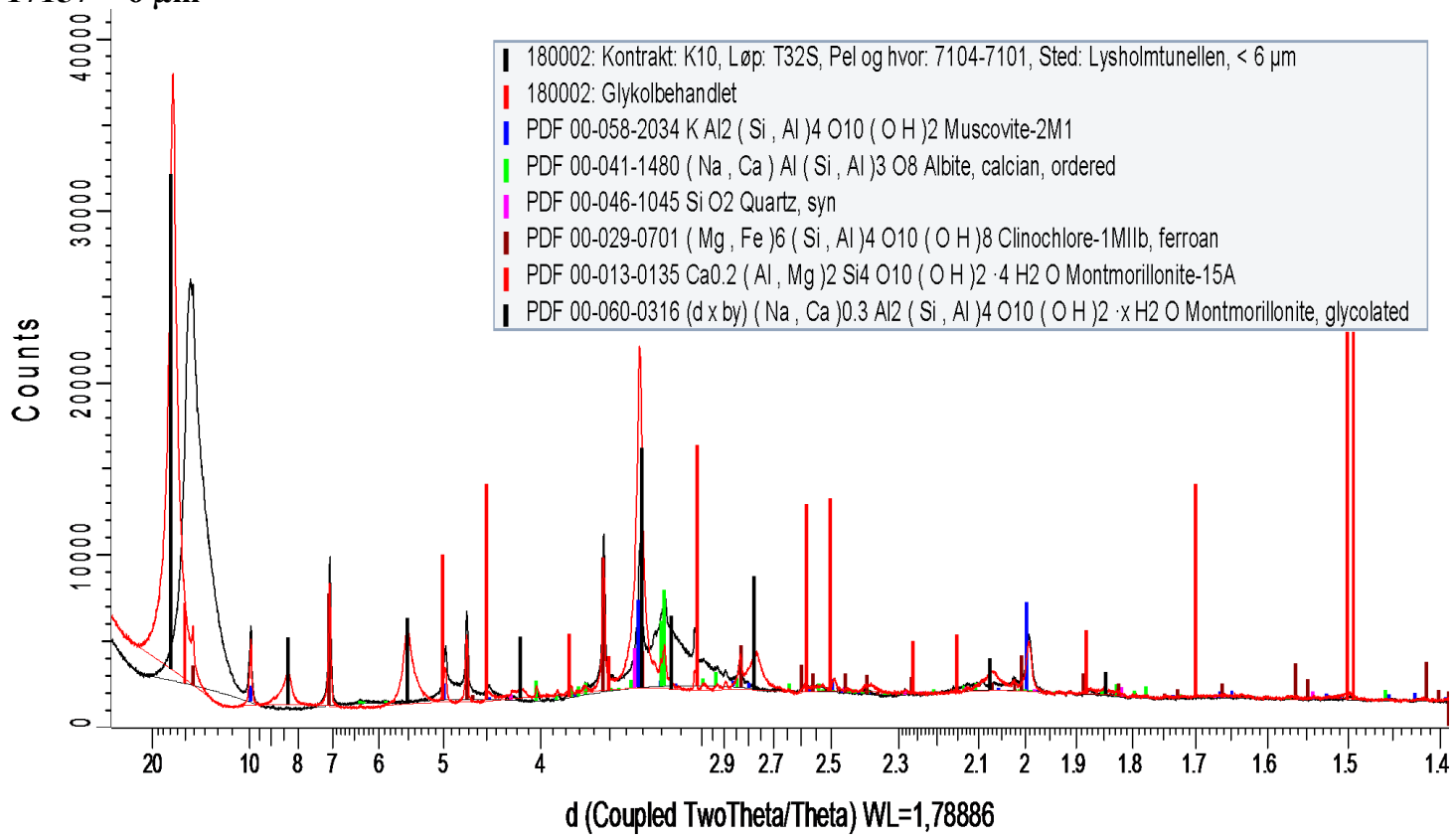
180002: Kontrakt: K10, Løp: T32S, Pel og hvor: 7104-7101, Sted: Lysholmtunellen, < 6 µm
180002: Glykolbehandlet
PDF 00-058-2034 K Al2 (Si , Al)4 O10 (O H)2 Muscovite-2M1
PDF 00-041-1480 (Na , Ca) Al (Si , Al)3 O8 Albite, calcian, ordered
PDF 00-046-1045 Si O2 Quartz, syn
PDF 00-029-0701 (Mg , Fe)6 (Si , Al)4 O10 (O H)8 Clinochlore-1MIIb, ferroan
PDF 00-013-0135 Ca0.2 (Al , Mg)2 Si4 O10 (O H)2 ·4 H2 O Montmorillonite-15A
PDF 00-060-0316 (d x by) (Na , Ca)0.3 Al2 (Si , Al)4 O10 (O H)2 ·x H2 O Montmorillonite, glycolated
Counts
0
10000
20000
30000
40000
20
10
8
7
6
5
4
2.9
2.7
2.5
2.3
2.1
2
1.9
1.8
1.7
1.6
1.5
1.4
d (Coupled TwoTheta/Theta) WL=1,78886

18009 < 6 µm

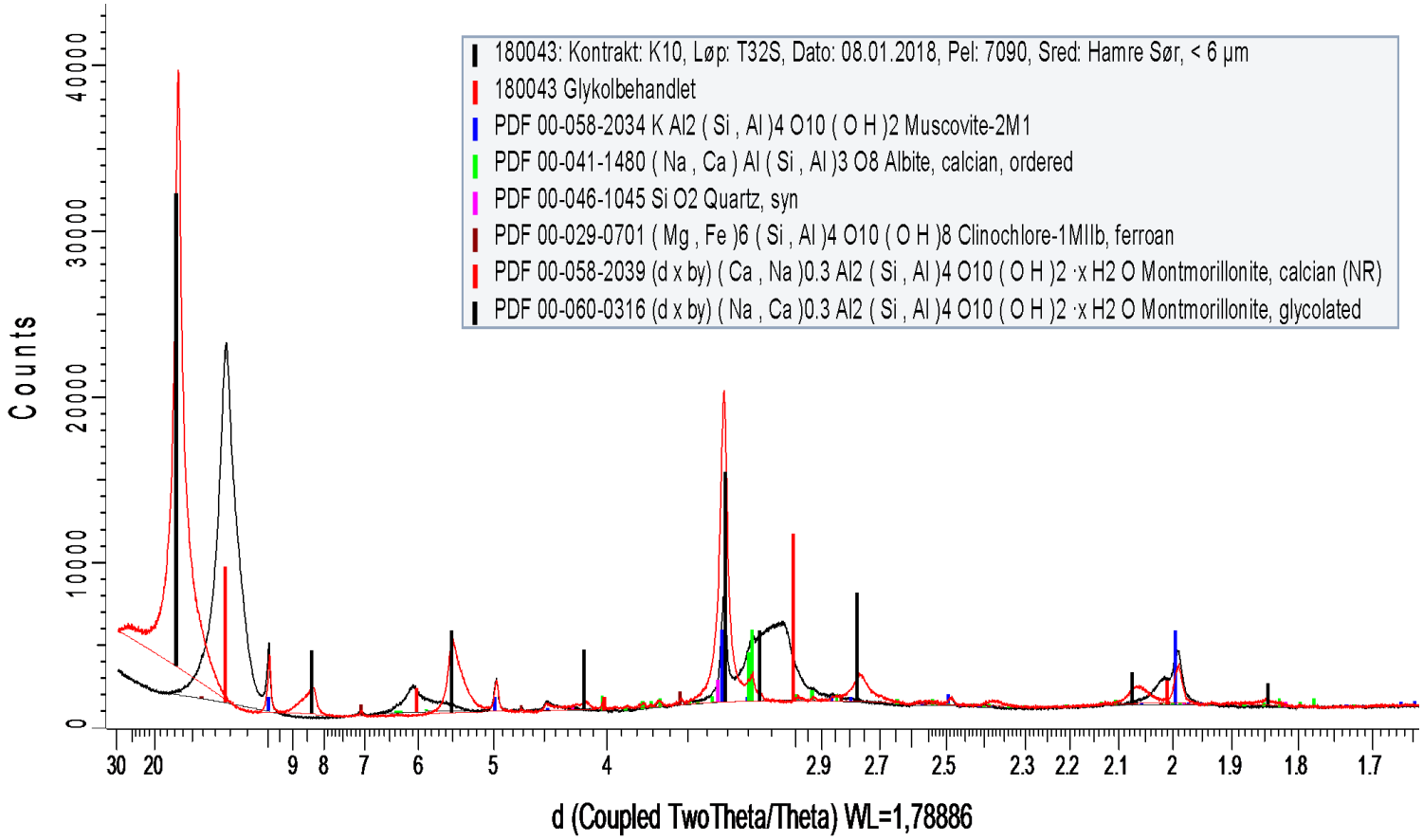
180043: Kontrakt: K10, Løp: T32S, Dato: 08.01.2018, Pel: 7090, Sred: Hamre Sør, < 6 µm
180043 Glykolbehandlet
PDF 00-058-2034 K Al2 (Si , Al)4 O10 (O H)2 Muscovite-2M1
PDF 00-041-1480 (Na , Ca) Al (Si , Al)3 O8 Albite, calcian, ordered
PDF 00-046-1045 Si O2 Quartz, syn
PDF 00-029-0701 (Mg , Fe)6 (Si , Al)4 O10 (O H)8 Clinochlore-1MIIb, ferroan
PDF 00-058-2039 (d x by) (Ca , Na)0.3 Al2 (Si , Al)4 O10 (O H)2 ·x H2 O Montmorillonite, calcian (NR)
PDF 00-060-0316 (d x by) (Na , Ca)0.3 Al2 (Si , Al)4 O10 (O H)2 ·x H2 O Montmorillonite, glycolated
Counts
0
10000
20000
30000
40000
30 20 9 8 7 6 5 4 2.9 2.7 2.5 2.3 2.2 2.1 2 1.9 1.8 1.7
d (Coupled TwoTheta/Theta) WL=1,78886

18011 < 6 µm

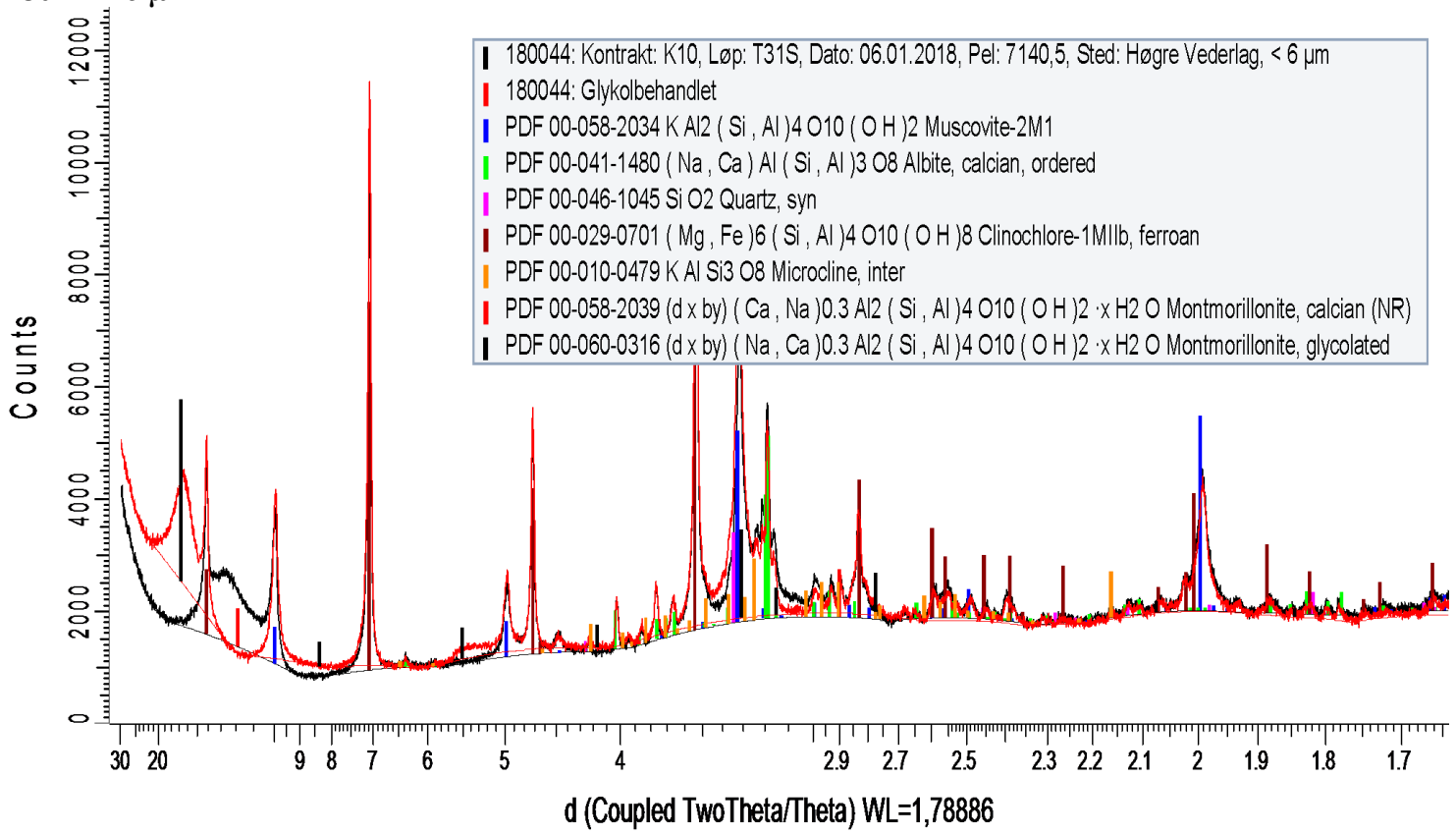
180044: Kontrakt: K10, Løp: T31S, Dato: 06.01.2018, Pel: 7140,5, Sted: Høgre Vederlag, < 6 µm
180044: Glykolbehandlet
PDF 00-058-2034 K Al2 (Si , Al)4 O10 (O H)2 Muscovite-2M1
PDF 00-041-1480 (Na , Ca) Al (Si , Al)3 O8 Albite, calcian, ordered
PDF 00-046-1045 Si O2 Quartz, syn
PDF 00-029-0701 (Mg , Fe)6 (Si , Al)4 O10 (O H)8 Clinochlore-1MIIb, ferroan
PDF 00-010-0479 K Al Si3 O8 Microcline, inter
PDF 00-058-2039 (d x by) (Ca , Na)0.3 Al2 (Si , Al)4 O10 (O H)2 ·x H2 O Montmorillonite, calcian (NR)
PDF 00-060-0316 (d x by) (Na , Ca)0.3 Al2 (Si , Al)4 O10 (O H)2 ·x H2 O Montmorillonite, glycolated
Counts
0
2000
4000
6000
8000
10000
12000
30
20
9
8
7
6
5
4
2.9
2.7
2.5
2.3
2.2
2.1
2
1.9
1.8
1.7
d (Coupled TwoTheta/Theta) WL=1,78886

18018 < 6 µm

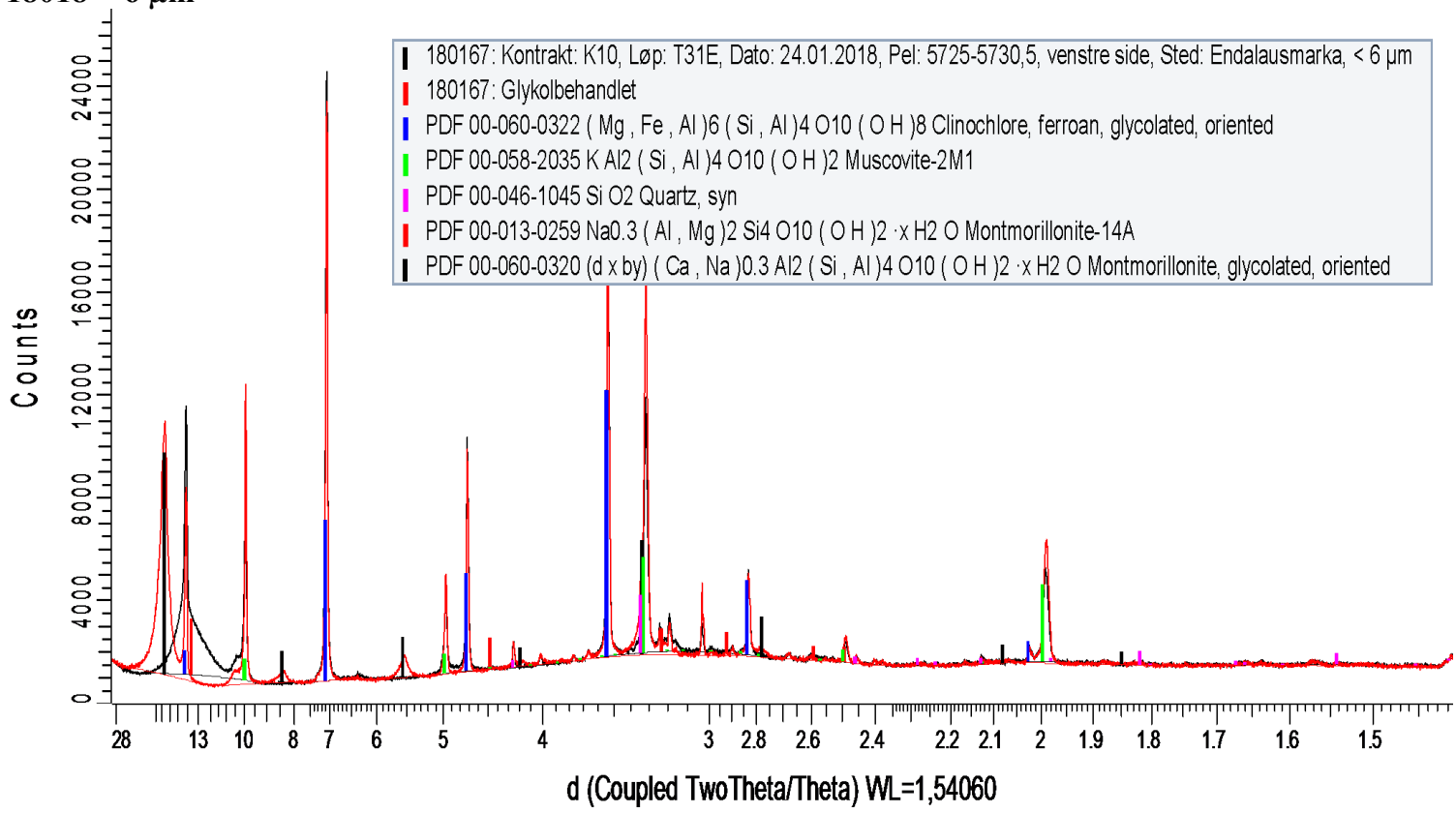
180167: Kontrakt: K10, Løp: T31E, Dato: 24.01.2018, Pel: 5725-5730,5, venstre side, Sted: Endalausmarka, < 6 µm
180167: Glykolbehandlet
PDF 00-060-0322 (Mg , Fe , Al)6 (Si , Al)4 O10 (O H)8 Clinochlore, ferroan, glycolated, oriented
PDF 00-058-2035 K Al2 (Si , Al)4 O10 (O H)2 Muscovite-2M1
PDF 00-046-1045 Si O2 Quartz, syn
PDF 00-013-0259 Na0.3 (Al , Mg)2 Si4 O10 (O H)2 ·x H2 O Montmorillonite-14A
PDF 00-060-0320 (d x by) (Ca , Na)0.3 Al2 (Si , Al)4 O10 (O H)2 ·x H2 O Montmorillonite, glycolated, oriented
Counts
0
4000
8000
12000
16000
20000
24000
28
13
10
8
7
6
5
4
3
2.8
2.6
2.4
2.2
2.1
2
1.9
1.8
1.7
1.6
1.5
d (Coupled TwoTheta/Theta) WL=1,54060

18022 < 6 µm

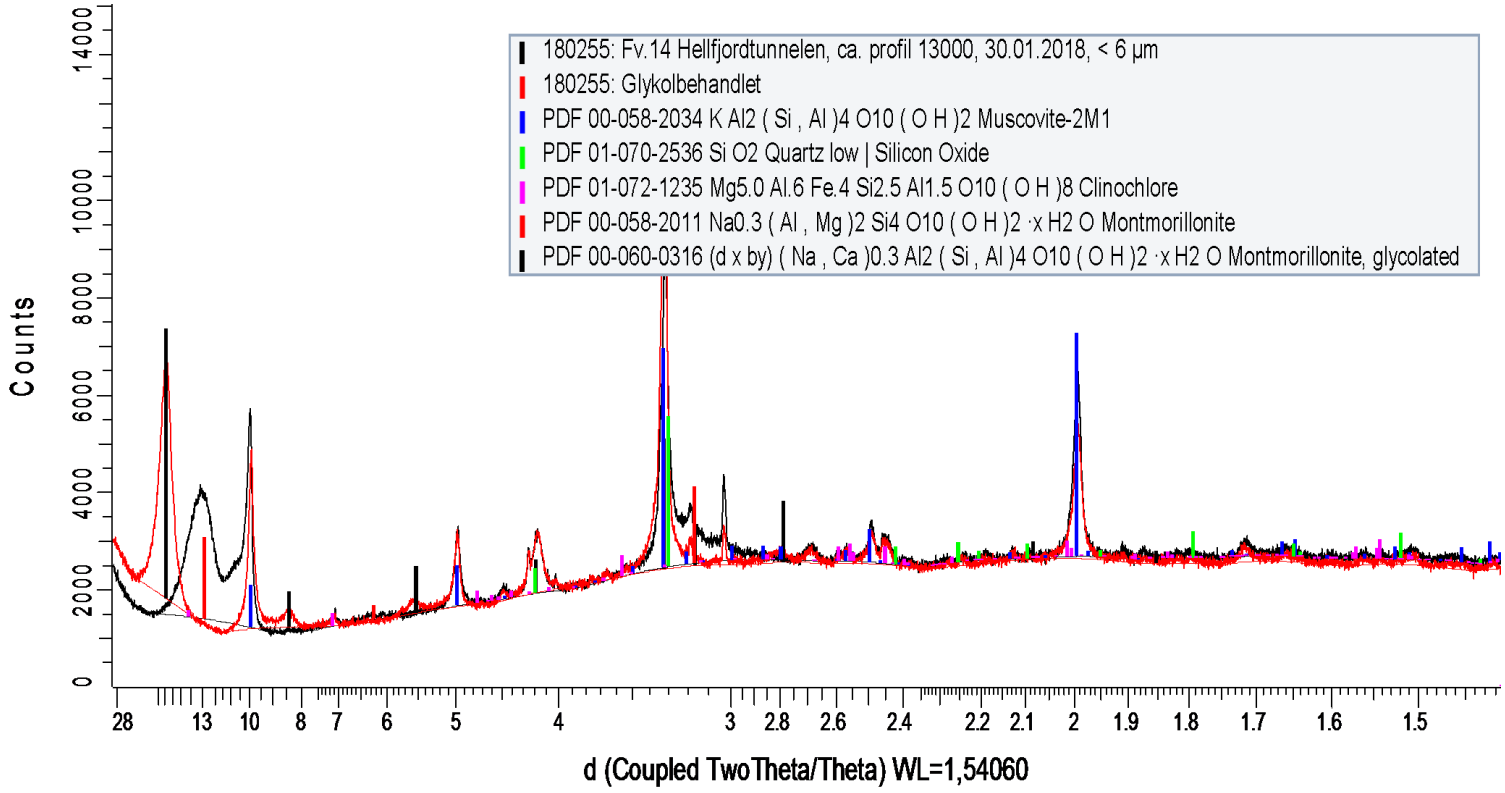
180255: Fv.14 Hellfjordtunnelen, ca. profil 13000, 30.01.2018, < 6 µm
180255: Glykolbehandlet
PDF 00-058-2034 K Al2 (Si , Al)4 O10 (O H)2 Muscovite-2M1
PDF 01-070-2536 Si O2 Quartz low | Silicon Oxide
PDF 01-072-1235 Mg5.0 Al.6 Fe.4 Si2.5 Al1.5 O10 (O H)8 Clinochlore
PDF 00-058-2011 Na0.3 (Al , Mg)2 Si4 O10 (O H)2 ·x H2 O Montmorillonite
PDF 00-060-0316 (d x by) (Na , Ca)0.3 Al2 (Si , Al)4 O10 (O H)2 ·x H2 O Montmorillonite, glycolated
Counts
0
2000
4000
6000
8000
10000
14000
28
13
10
8
7
6
5
4
3
2.8
2.6
2.4
2.2
2.1
2
1.9
1.8
1.7
1.6
1.5
d (Coupled TwoTheta/Theta) WL=1,54060

18034 < 6 µm

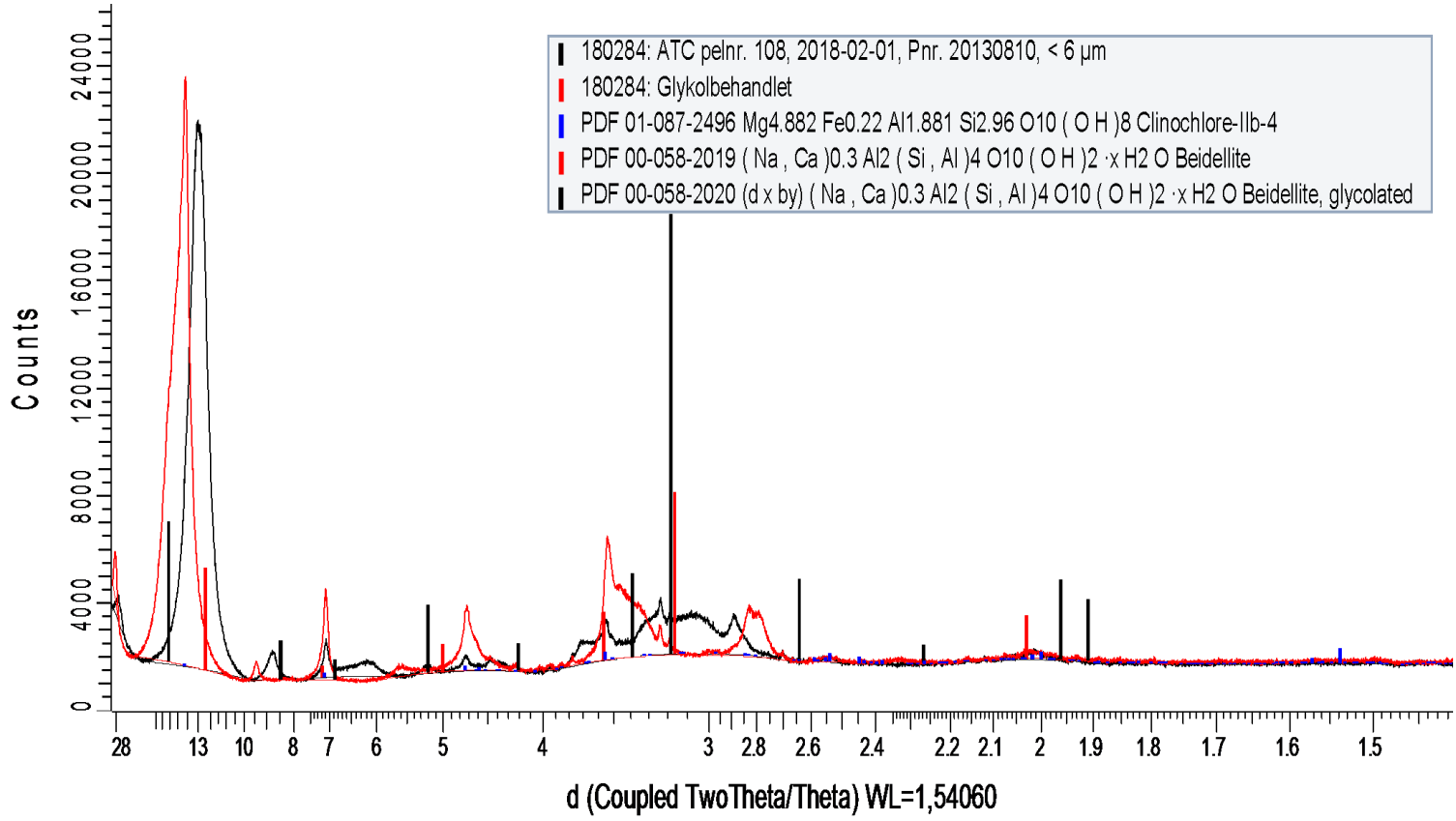
180284: ATC pelnr. 108, 2018-02-01, Pnr. 20130810, < 6 µm
180284: Glykolbehandlet
PDF 01-087-2496 Mg4.882 Fe0.22 Al1.881 Si2.96 O10 (O H)8 Clinochlore-IIb-4
PDF 00-058-2019 (Na , Ca)0.3 Al2 (Si , Al)4 O10 (O H)2 ·x H2 O Beidellite
PDF 00-058-2020 (d x by) (Na , Ca)0.3 Al2 (Si , Al)4 O10 (O H)2 ·x H2 O Beidellite, glycolated
Counts
0
4000
8000
12000
16000
20000
24000
28
13
10
8
7
6
5
4
3
2.8
2.6
2.4
2.2
2.1
2
1.9
1.8
1.7
1.6
1.5
d (Coupled TwoTheta/Theta) WL=1,54060

18090 < 6 µm

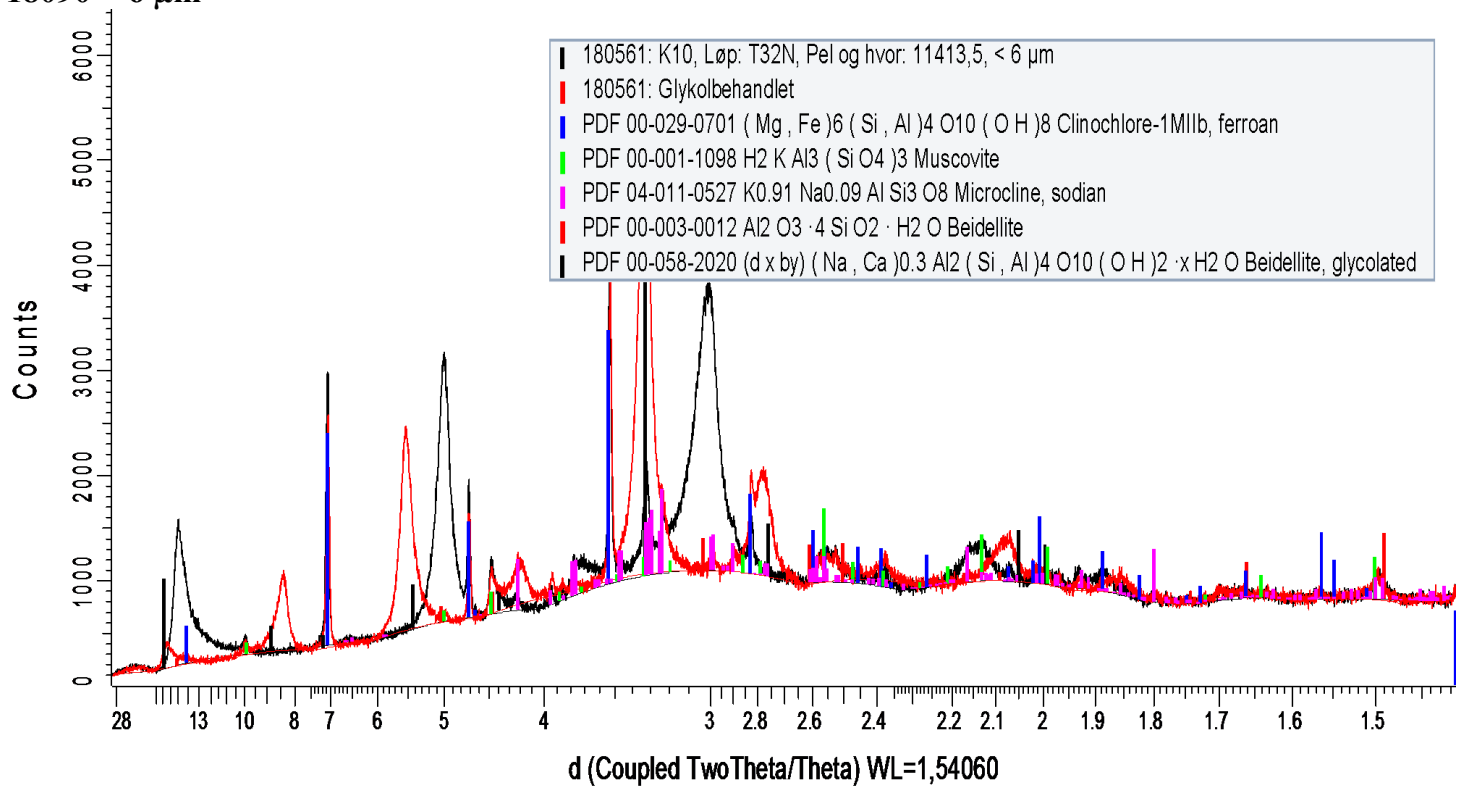
180561: K10, Løp: T32N, Pel og hvor: 11413,5, < 6 µm
180561: Glykolbehandlet
PDF 00-029-0701 (Mg , Fe)6 (Si , Al)4 O10 (O H)8 Clinochlore-1MIIb, ferroan
PDF 00-001-1098 H2 K Al3 (Si O4)3 Muscovite
PDF 04-011-0527 K0.91 Na0.09 Al Si3 O8 Microcline, sodian
PDF 00-003-0012 Al2 O3 · 4 Si O2 · H2 O Beidellite
PDF 00-058-2020 (d x by) (Na , Ca)0.3 Al2 (Si , Al)4 O10 (O H)2 · x H2 O Beidellite, glycolated
Counts
0
1000
2000
3000
4000
5000
6000
28
13
10
8
7
6
5
4
3
2.8
2.6
2.4
2.2
2.1
2
1.9
1.8
1.7
1.6
1.5
d (Coupled TwoTheta/Theta) WL=1,54060

18100 < 6 µm

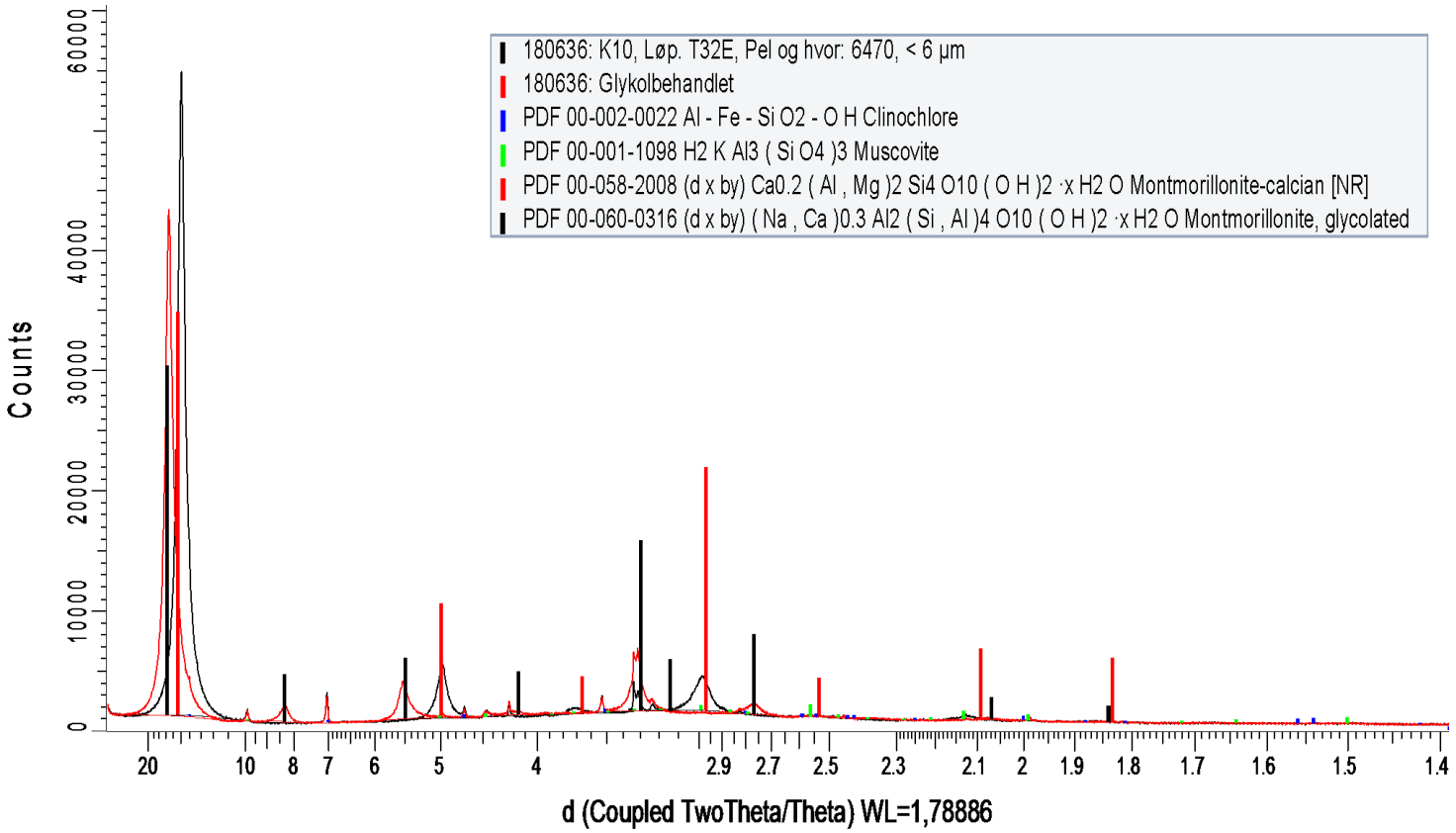
180636: K10, Løp. T32E, Pel og hvor: 6470, < 6 µm
180636: Glykolbehandlet
PDF 00-002-0022 Al - Fe - Si O2 - O H Clinochlore
PDF 00-001-1098 H2 K Al3 (Si O4)3 Muscovite
PDF 00-058-2008 (d x by) Ca0.2 (Al , Mg)2 Si4 O10 (O H)2 ·x H2 O Montmorillonite-calcian [NR]
PDF 00-060-0316 (d x by) (Na , Ca)0.3 Al2 (Si , Al)4 O10 (O H)2 ·x H2 O Montmorillonite, glycolated
Counts
0
10000
20000
30000
40000
60000
20
10
8
7
6
5
4
2.9
2.7
2.5
2.3
2.1
2
1.9
1.8
1.7
1.6
1.5
1.4
d (Coupled TwoTheta/Theta) WL=1,78886

18103 < 6 µm

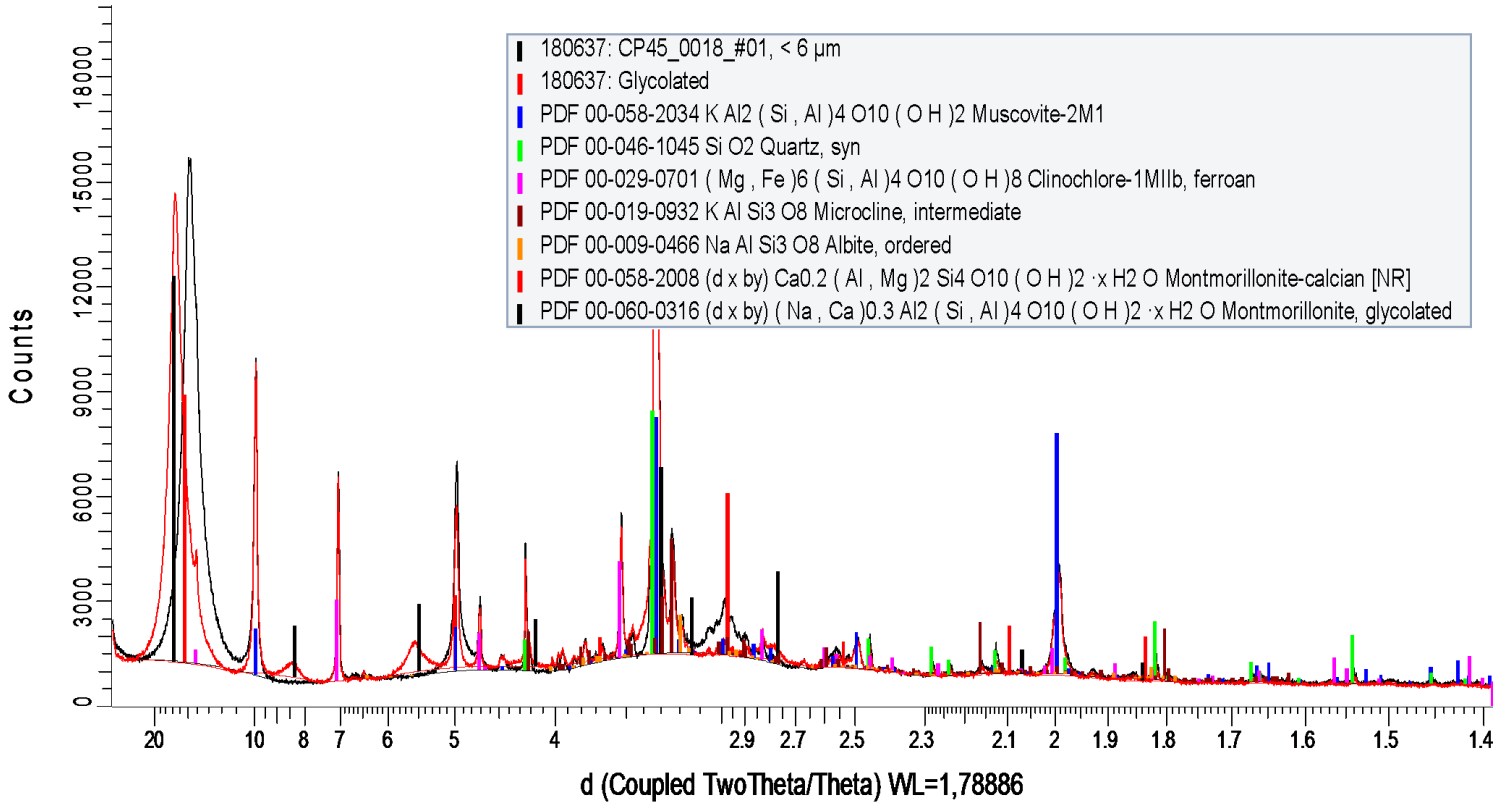
180637: CP45_0018_#01, < 6 µm
180637: Glycolated
PDF 00-058-2034 K Al2 (Si , Al)4 O10 (O H)2 Muscovite-2M1
PDF 00-046-1045 Si O2 Quartz, syn
PDF 00-029-0701 (Mg , Fe)6 (Si , Al)4 O10 (O H)8 Clinochlore-1MIIb, ferroan
PDF 00-019-0932 K Al Si3 O8 Microcline, intermediate
PDF 00-009-0466 Na Al Si3 O8 Albite, ordered
PDF 00-058-2008 (d x by) Ca0.2 (Al , Mg)2 Si4 O10 (O H)2 ·x H2 O Montmorillonite-calcian [NR]
PDF 00-060-0316 (d x by) (Na , Ca)0.3 Al2 (Si , Al)4 O10 (O H)2 ·x H2 O Montmorillonite, glycolated
Counts
0
3000
6000
9000
12000
15000
18000
20
10
8
7
6
5
4
2.9
2.7
2.5
2.3
2.1
2
1.9
1.8
1.7
1.6
1.5
1.4
d (Coupled TwoTheta/Theta) WL=1,78886

18111 < 6 µm

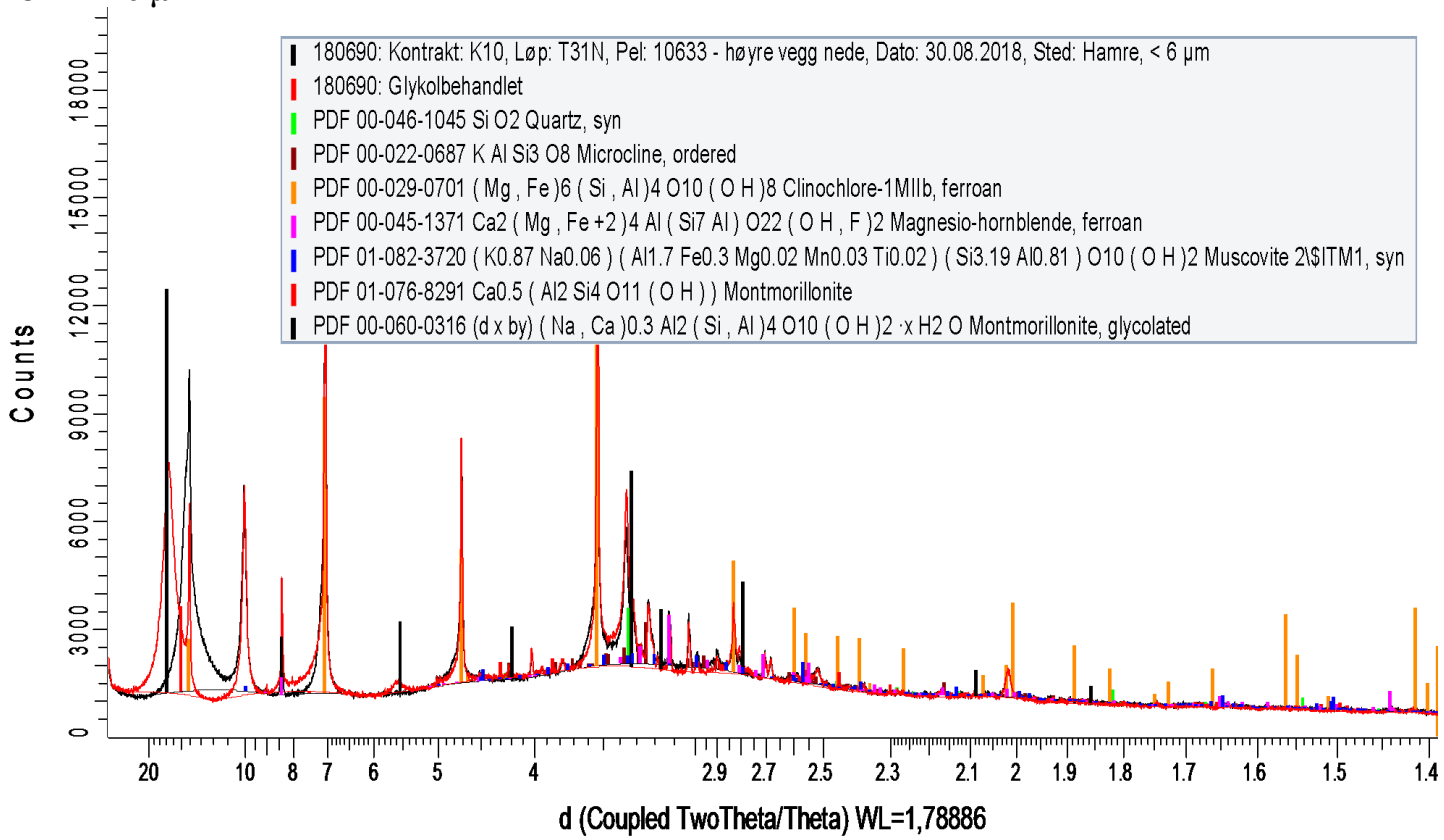
180690: Kontrakt: K10, Løp: T31N, Pel: 10633 - høyre vegg nede, Dato: 30.08.2018, Sted: Hamre, < 6 µm
180690: Glykolbehandlet
PDF 00-046-1045 Si O2 Quartz, syn
PDF 00-022-0687 K Al Si3 O8 Microcline, ordered
PDF 00-029-0701 (Mg , Fe)6 (Si , Al)4 O10 (O H)8 Clinochlore-1MIIb, ferroan
PDF 00-045-1371 Ca2 (Mg , Fe +2)4 Al (Si7 Al) O22 (O H , F)2 Magnesio-hornblende, ferroan
PDF 01-082-3720 (K0.87 Na0.06) (Al1.7 Fe0.3 Mg0.02 Mn0.03 Ti0.02) (Si3.19 Al0.81) O10 (O H)2 Muscovite 2\$ITM1, syn
PDF 01-076-8291 Ca0.5 (Al2 Si4 O11 (O H)) Montmorillonite
PDF 00-060-0316 (d x by) (Na , Ca)0.3 Al2 (Si , Al)4 O10 (O H)2 ·x H2 O Montmorillonite, glycolated
Counts
0
3000
6000
9000
12000
15000
18000
20
10
8
7
6
5
4
2.9
2.7
2.5
2.3
2.1
2
1.9
1.8
1.7
1.6
1.5
1.4
d (Coupled TwoTheta/Theta) WL=1,78886

18128 < 6 µm

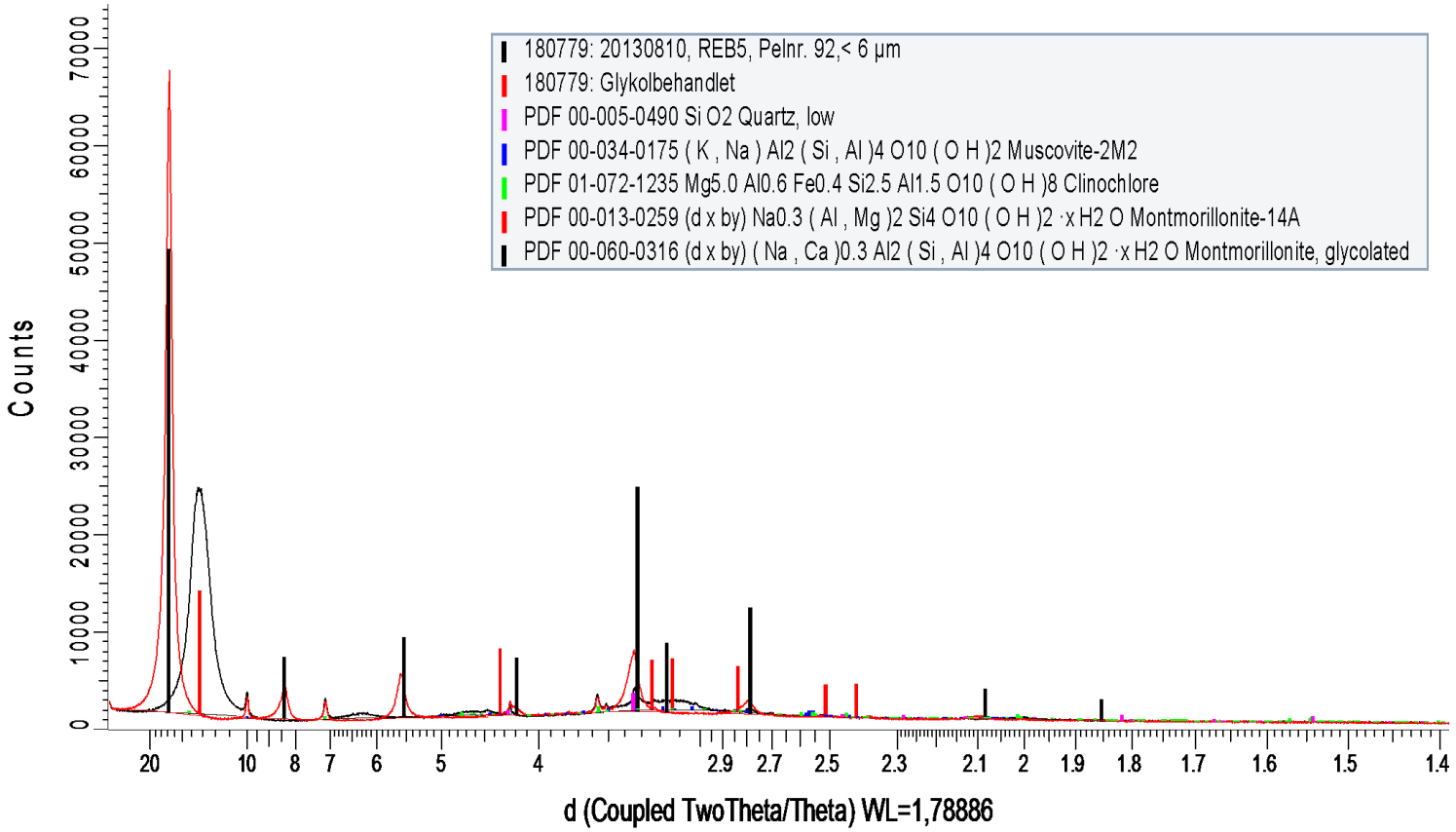
180779: 20130810, REB5, Pelnr. 92,< 6 µm
180779: Glykolbehandlet
PDF 00-005-0490 Si O2 Quartz, low
PDF 00-034-0175 (K , Na) Al2 (Si , Al)4 O10 (O H)2 Muscovite-2M2
PDF 01-072-1235 Mg5.0 Al0.6 Fe0.4 Si2.5 Al1.5 O10 (O H)8 Clinochlore
PDF 00-013-0259 (d x by) Na0.3 (Al , Mg)2 Si4 O10 (O H)2 ·x H2 O Montmorillonite-14A
PDF 00-060-0316 (d x by) (Na , Ca)0.3 Al2 (Si , Al)4 O10 (O H)2 ·x H2 O Montmorillonite, glycolated
Counts
0
10000
20000
30000
40000
50000
60000
70000
20
10
8
7
6
5
4
2.9
2.7
2.5
2.3
2.1
2
1.9
1.8
1.7
1.6
1.5
1.4
d (Coupled TwoTheta/Theta) WL=1,78886

D | Swelling Pressure Curves

16002_1 Swelling pressure at constant volume

Oedometer cell area: 20cm^2

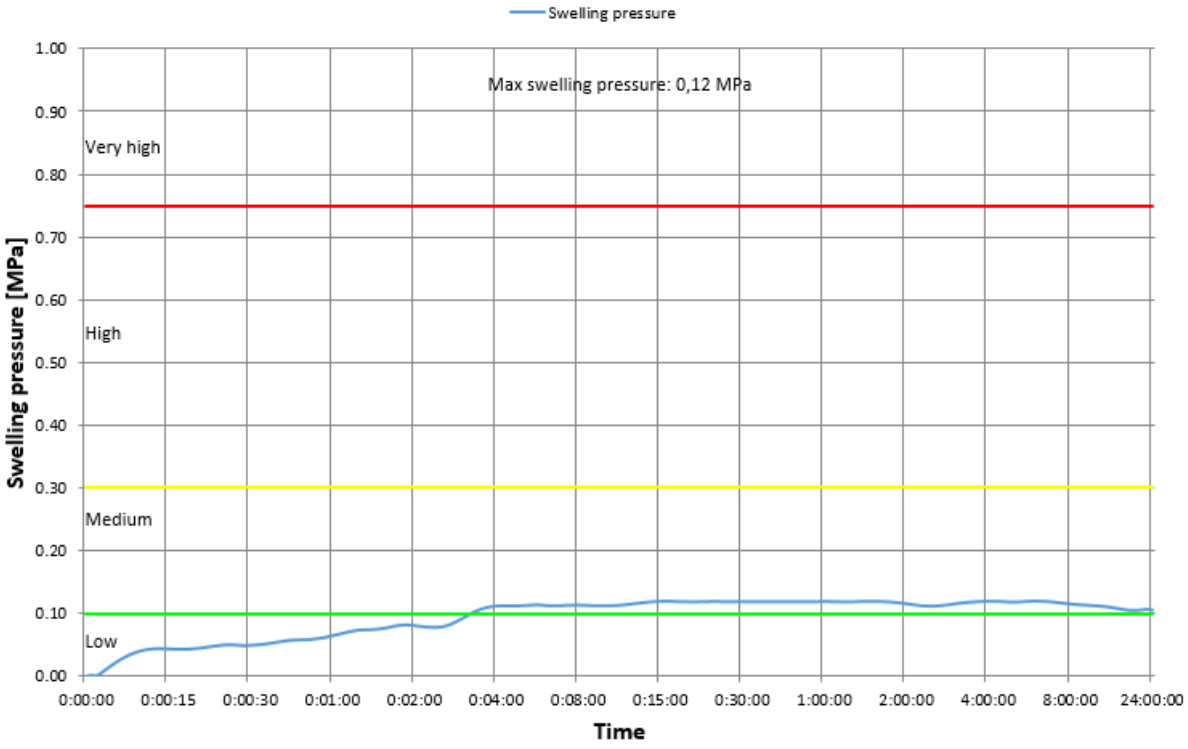

16002_2 Swelling pressure at constant volume

Oedometer cell area: 20cm^2

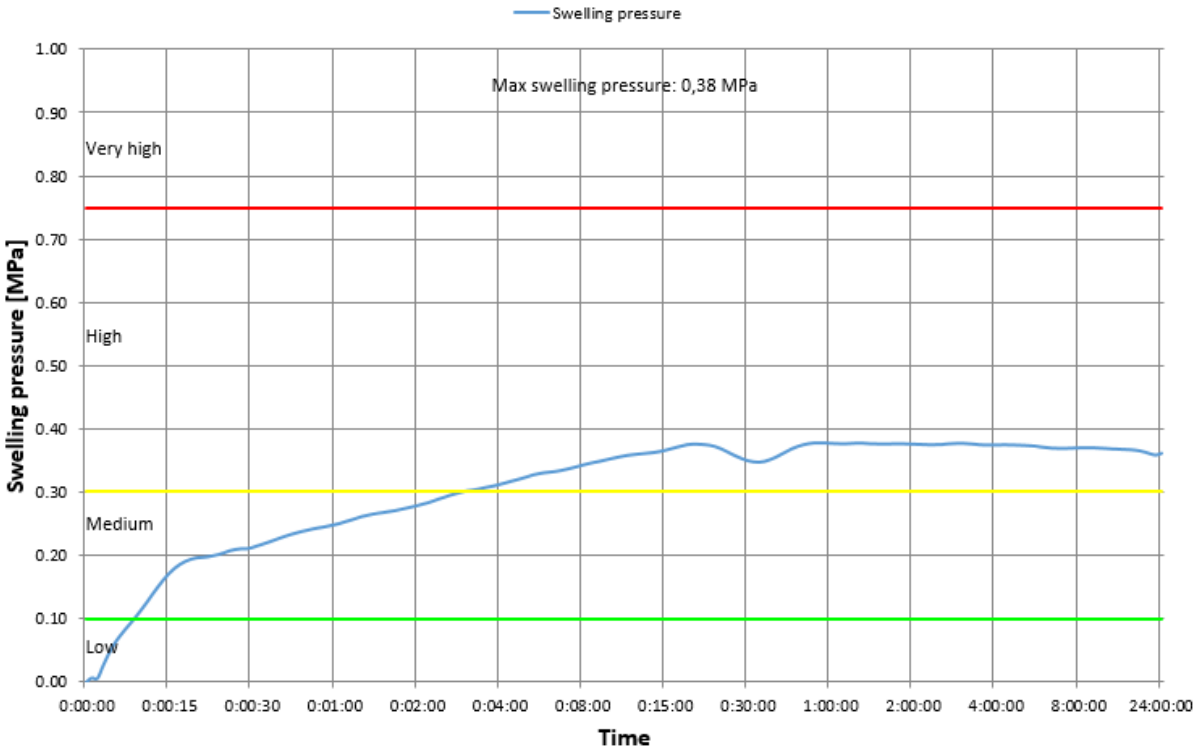

16003_3 Swelling pressure at constant volume

Oedometer cell area: 20cm^2

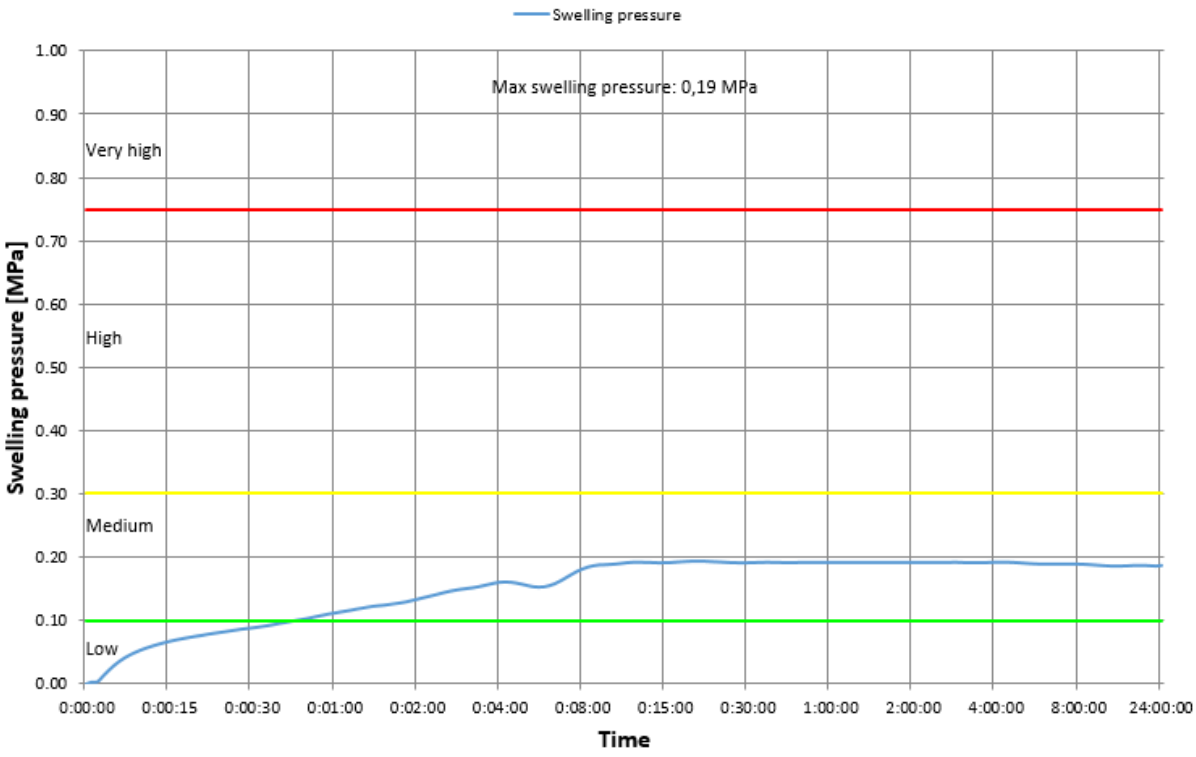

16028 Svelletrykksmåling ved konstant volum

Areal: 20 cm^2

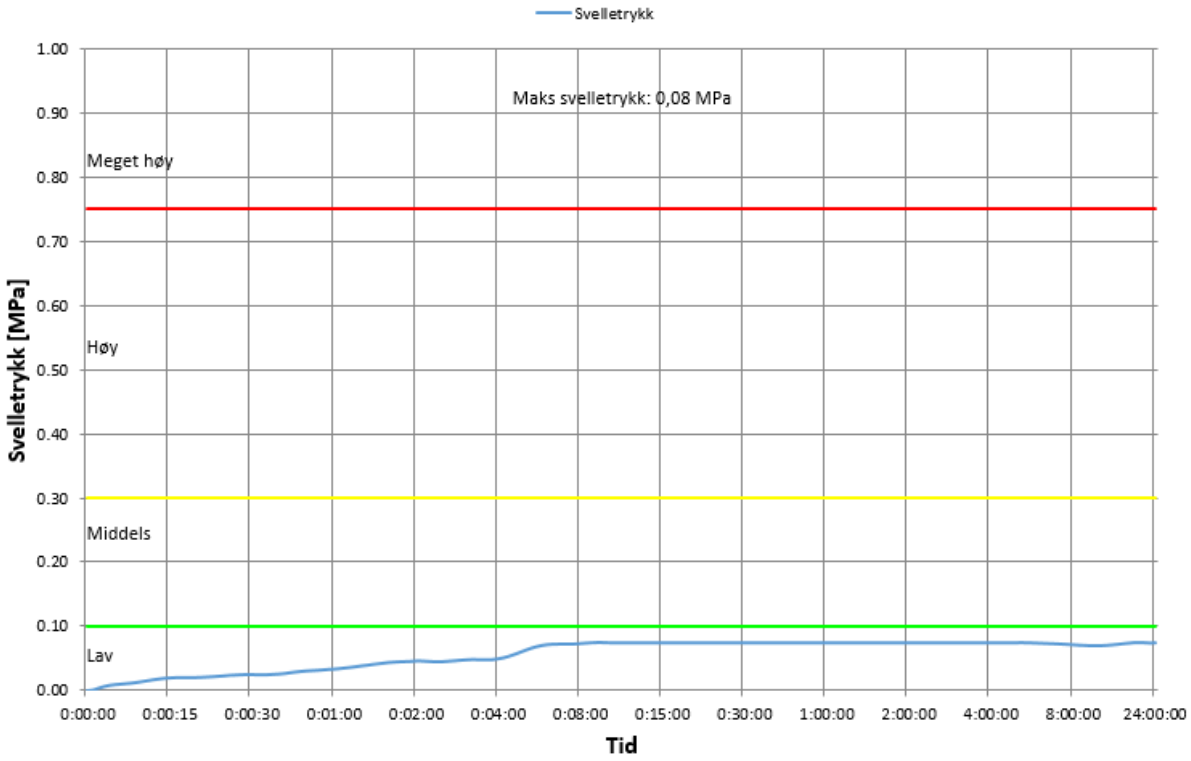

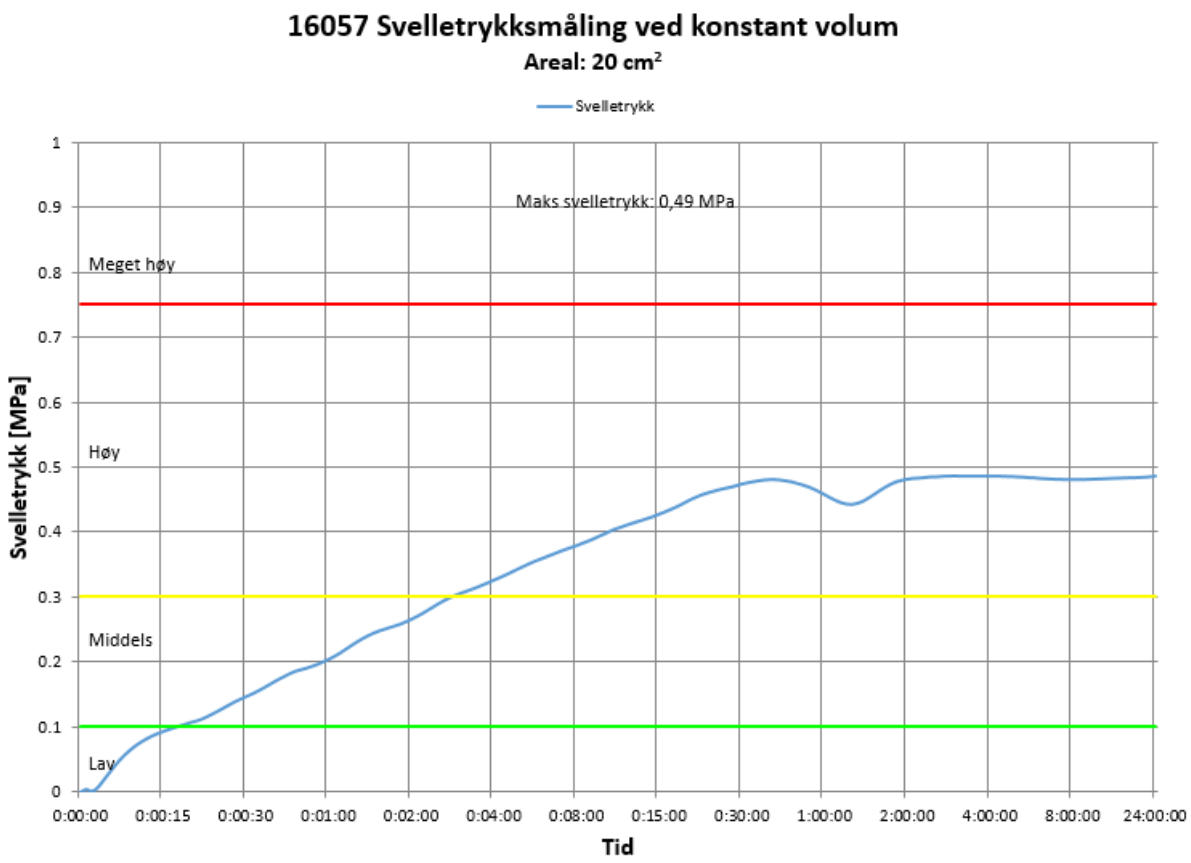
16057 Svelletrykksmåling ved konstant volum
Areal: 20 cm²
Svelletrykk
Maks svelletrykk: 0,49 MPa
Meget høy
Høy
Middels
Lav
Svelletrykk [MPa]
Tid
0
0.1
0.2
0.3
0.4
0.5
0.6
0.7
0.8
0.9
1
0:00:00
0:00:15
0:00:30
0:01:00
0:02:00
0:04:00
0:08:00
0:15:00
0:30:00
1:00:00
2:00:00
4:00:00
8:00:00
24:00:00

16083 Svelletrykksmåling ved konstant volum

Areal: 20 cm^2

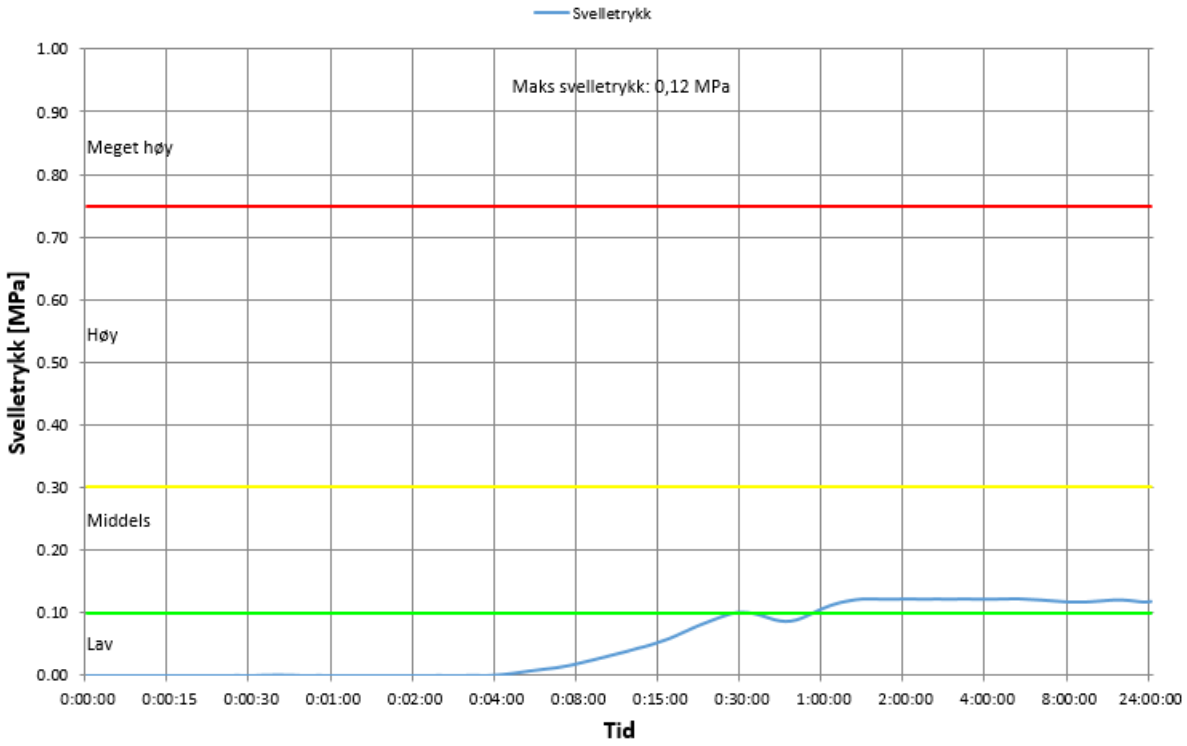

16093 Svelletrykksmåling ved konstant volum

Areal: 20 cm^2

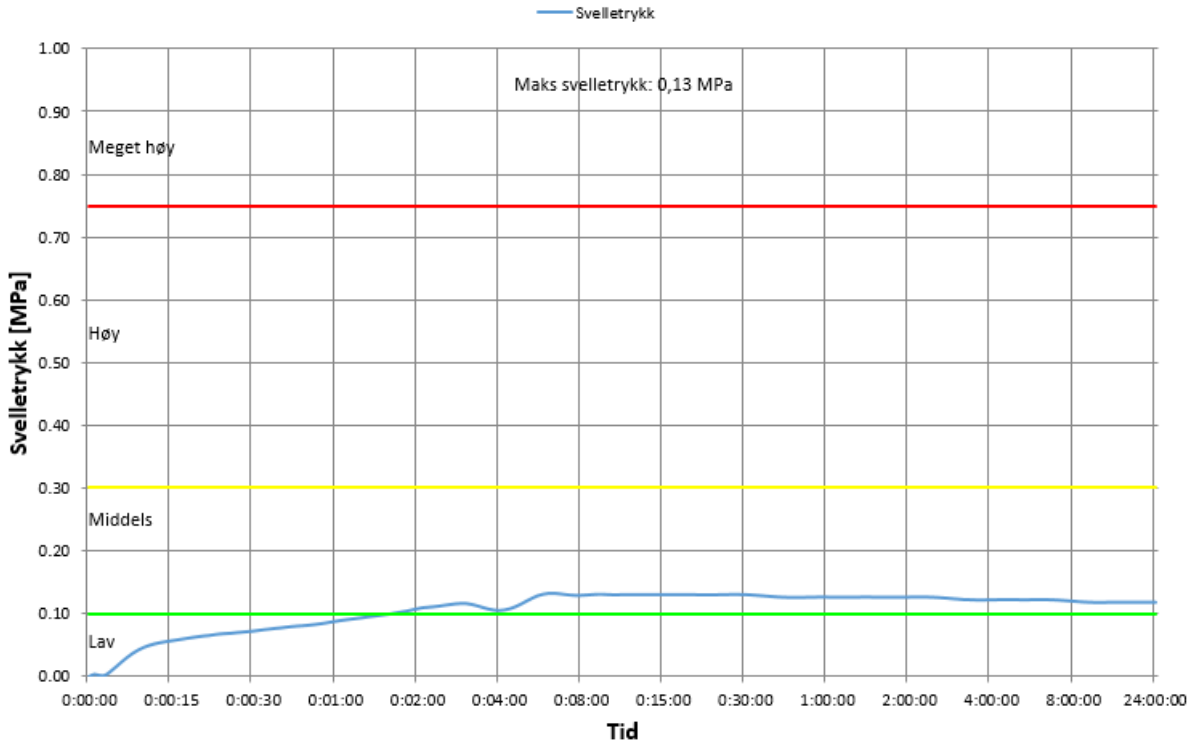

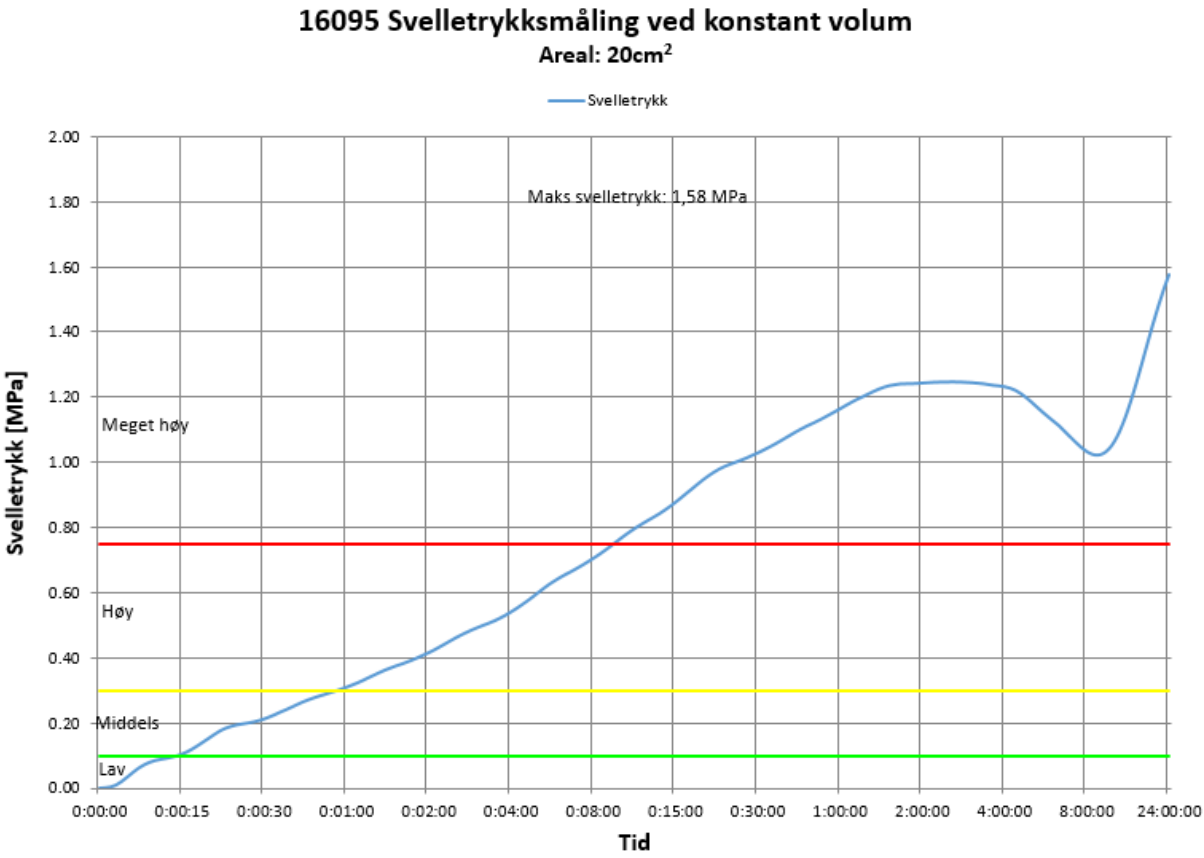
16095 Svelletrykksmåling ved konstant volum
Areal: 20cm2
Svelletrykk
Maks svelletrykk: 1,58 MPa
Meget høy
Høy
Middels
Lav
Svelletrykk [MPa]
Tid
2.00
1.80
1.60
1.40
1.20
1.00
0.80
0.60
0.40
0.20
0.00
0:00:00
0:00:15
0:00:30
0:01:00
0:02:00
0:04:00
0:08:00
0:15:00
0:30:00
1:00:00
2:00:00
4:00:00
8:00:00
24:00:00

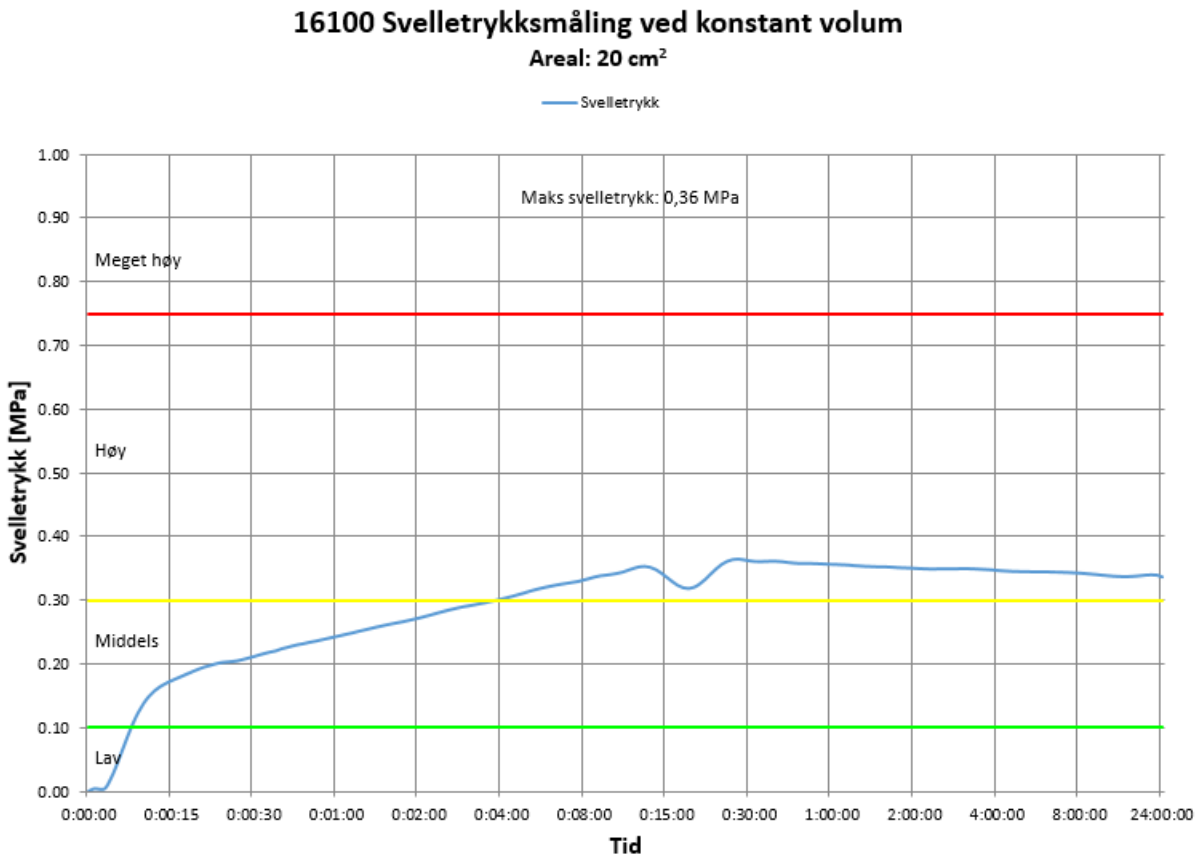
16100 Svelletrykksmåling ved konstant volum
Areal: 20 cm²
Svelletrykk
Maks svelletrykk: 0,36 MPa
Meget høy
Høy
Middels
Lav
Svelletrykk [MPa]
1.00
0.90
0.80
0.70
0.60
0.50
0.40
0.30
0.20
0.10
0.00
0:00:00
0:00:15
0:00:30
0:01:00
0:02:00
0:04:00
0:08:00
0:15:00
0:30:00
1:00:00
2:00:00
4:00:00
8:00:00
24:00:00
Tid

16101 Svelletrykksmåling ved konstant volum

Areal: 20 cm^2

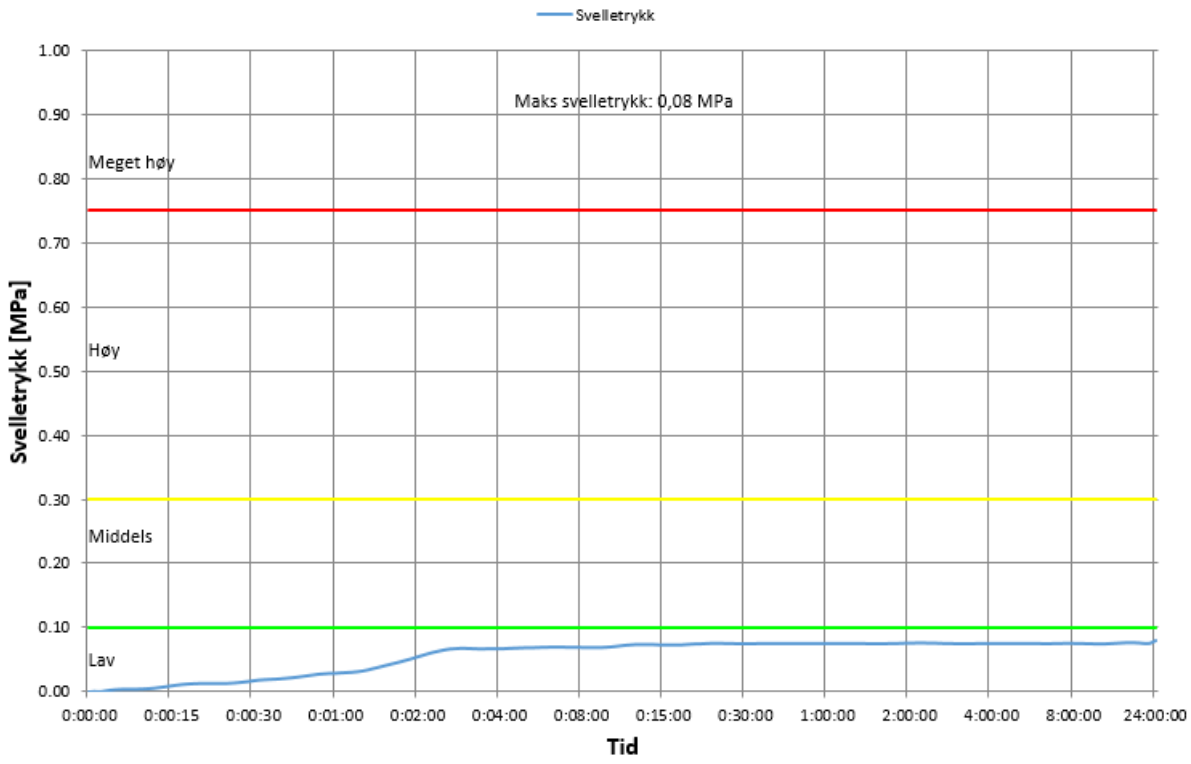

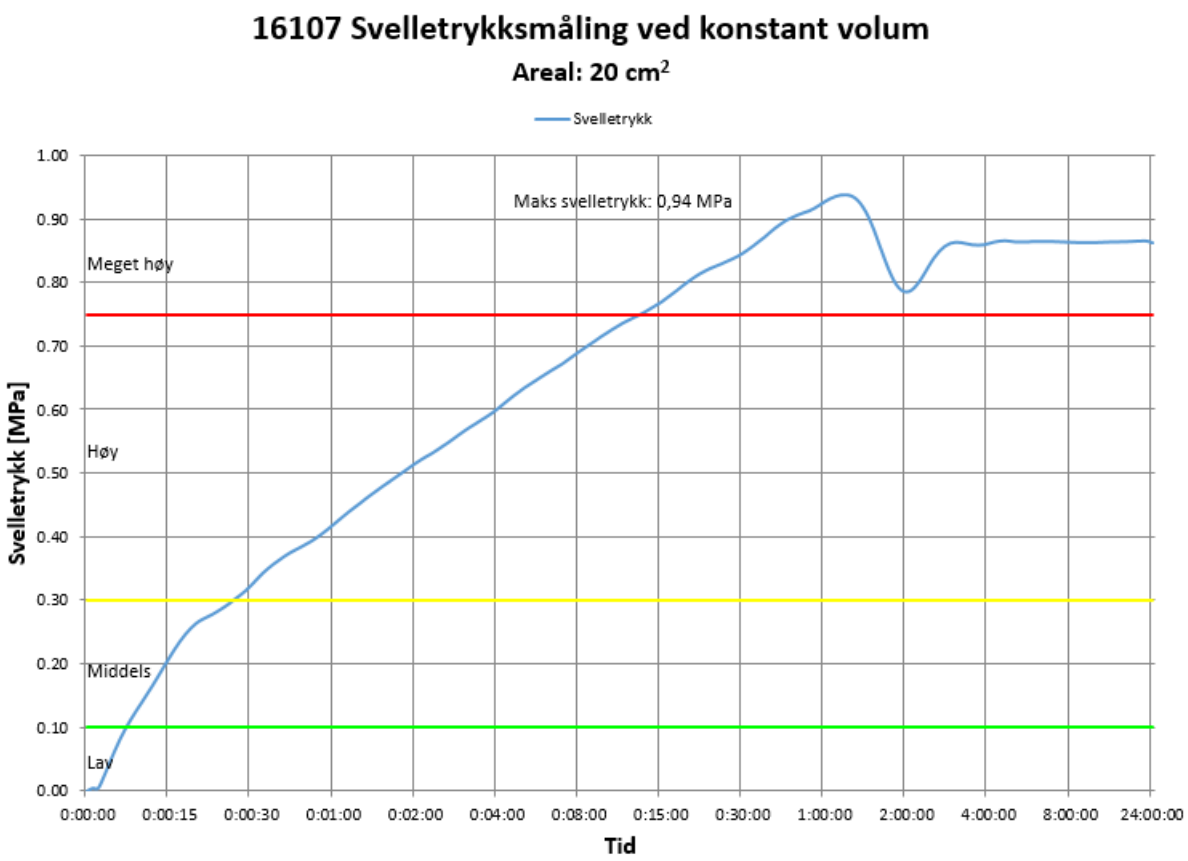
16107 Svelletrykksmåling ved konstant volum
Areal: 20 cm2
Svelletrykk
Maks svelletrykk: 0,94 MPa
Meget høy
Høy
Middels
Lav
Svelletrykk [MPa]
1.00
0.90
0.80
0.70
0.60
0.50
0.40
0.30
0.20
0.10
0.00
0:00:00
0:00:15
0:00:30
0:01:00
0:02:00
0:04:00
0:08:00
0:15:00
0:30:00
1:00:00
2:00:00
4:00:00
8:00:00
24:00:00
Tid

16111 Svelletrykksmåling ved konstant volum

Areal: 20 cm^2

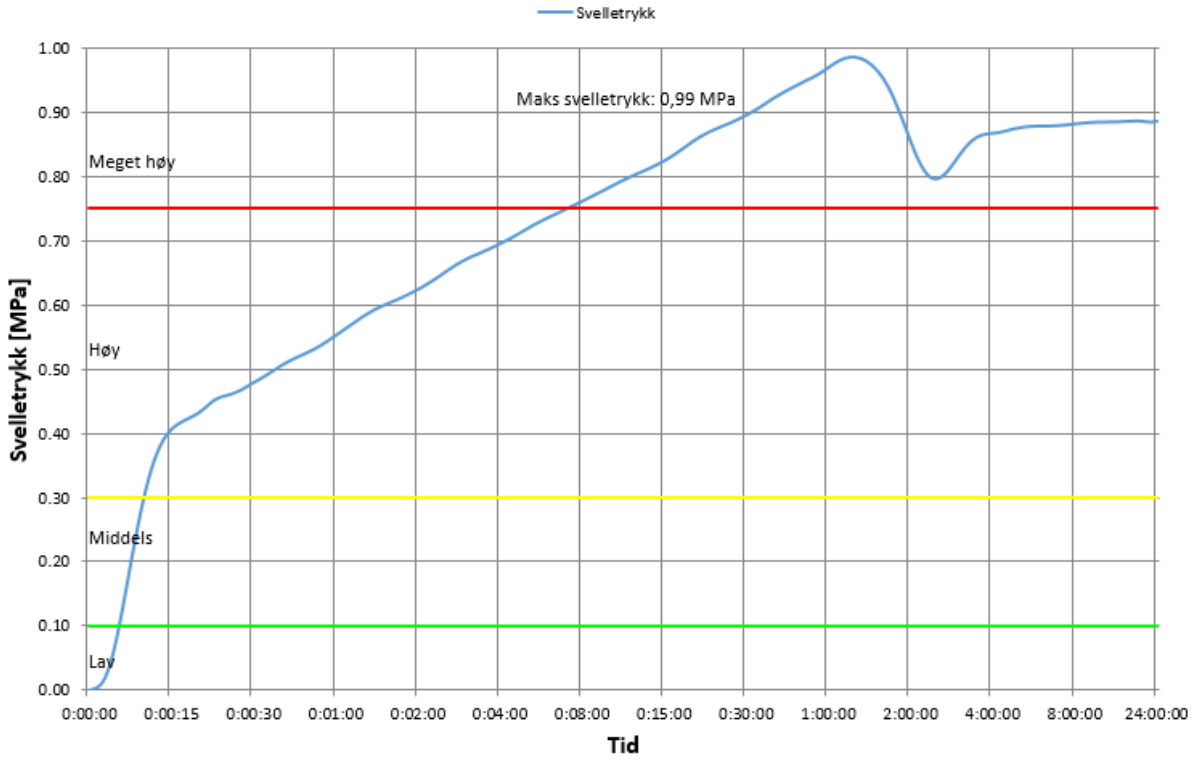

16114 Svelletrykksmåling ved konstant volum

Areal: 20 cm²

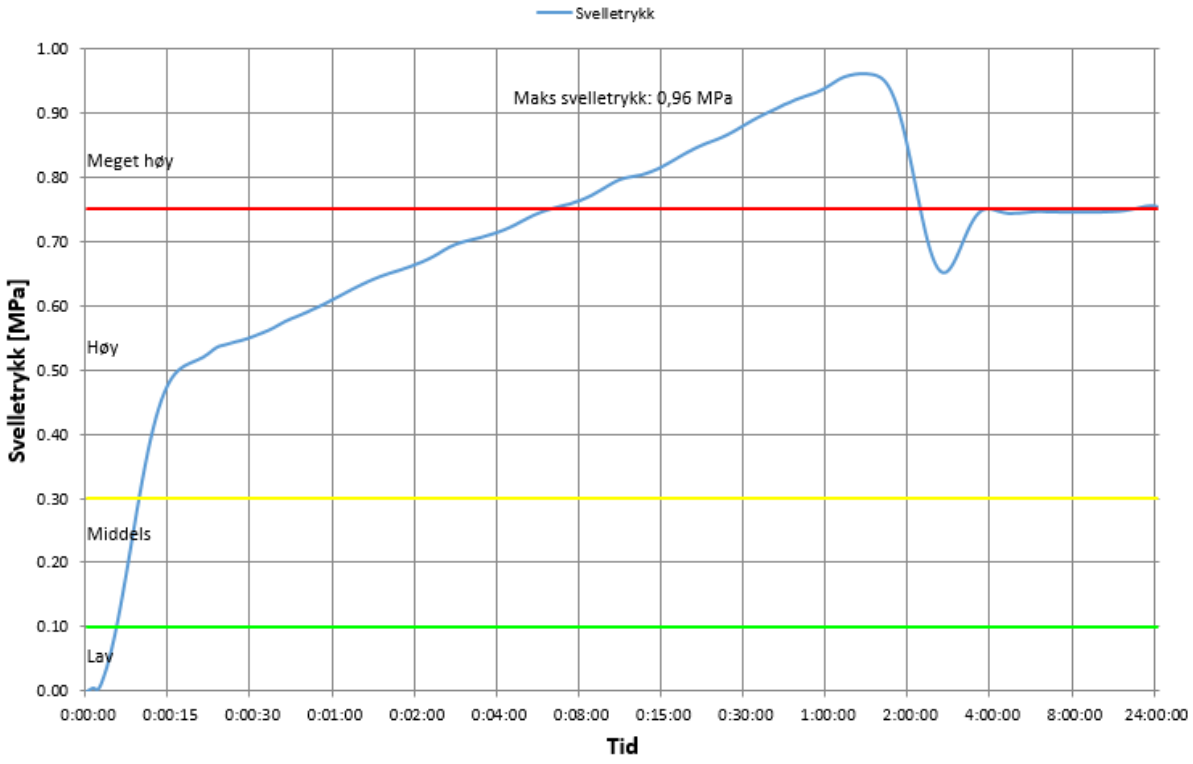

17035_2 Swelling pressure at constant volume

Oedometer cell area: 20cm^2

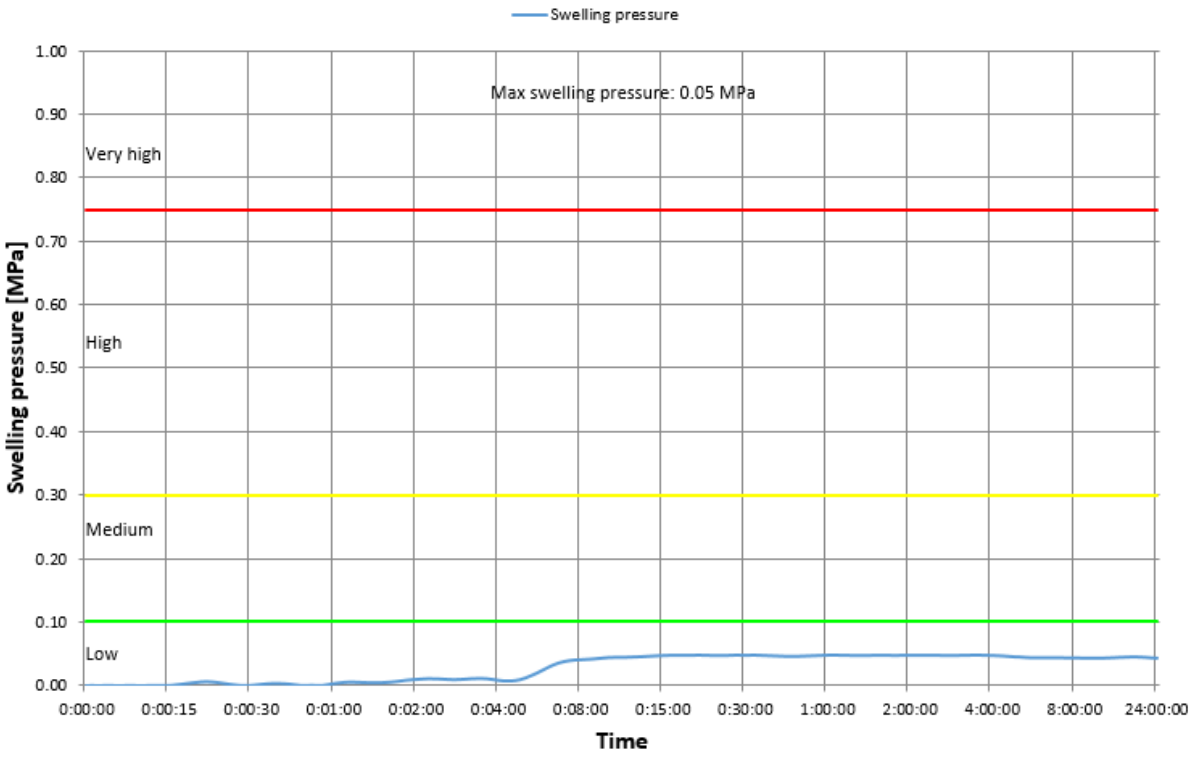

17035_3 Swelling pressure at constant volume

Oedometer cell area: 20cm^2

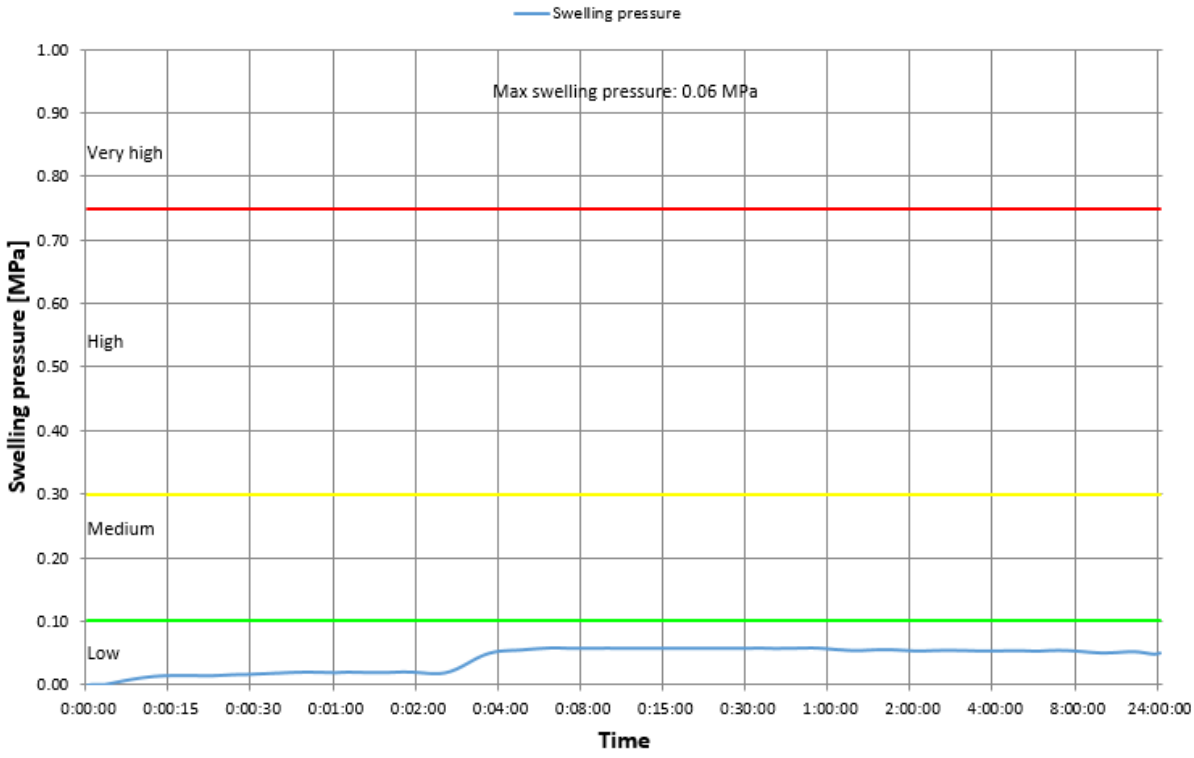

17051 Svelletrykksmåling ved konstant volum

Areal: 20 cm^2

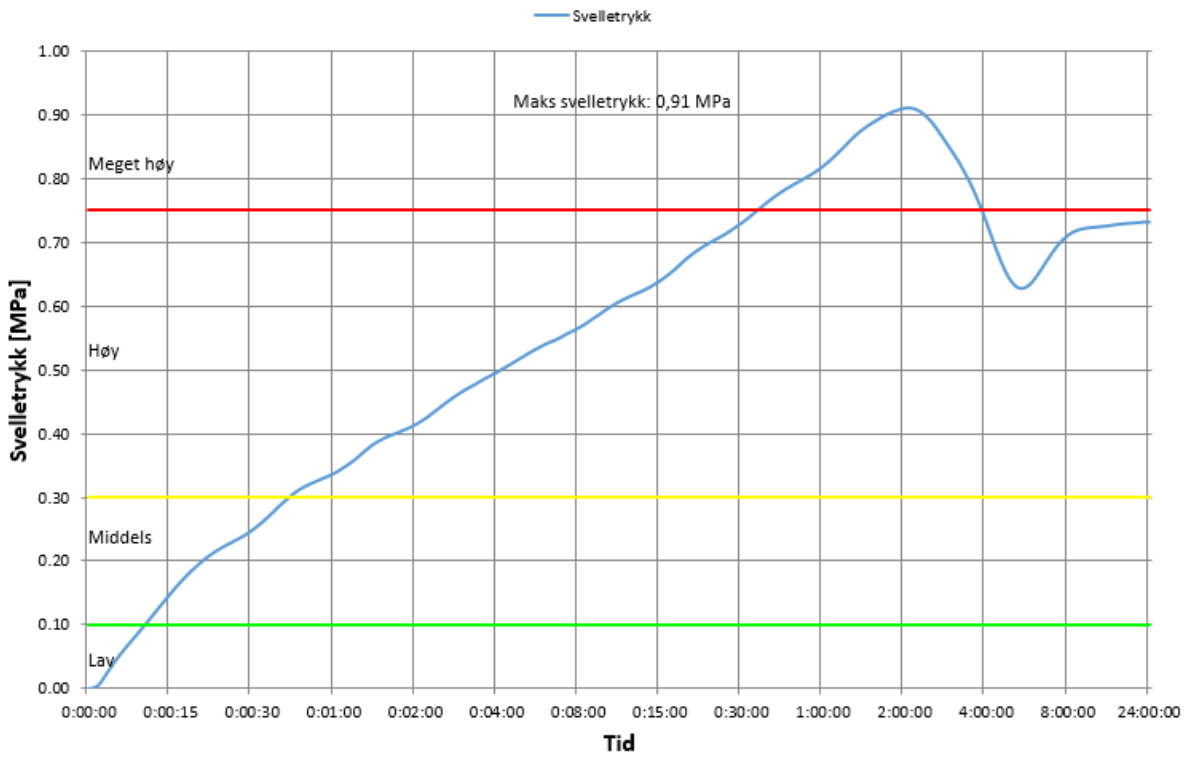

17087 Svelletrykksmåling ved konstant volum

Areal: 20 cm^2

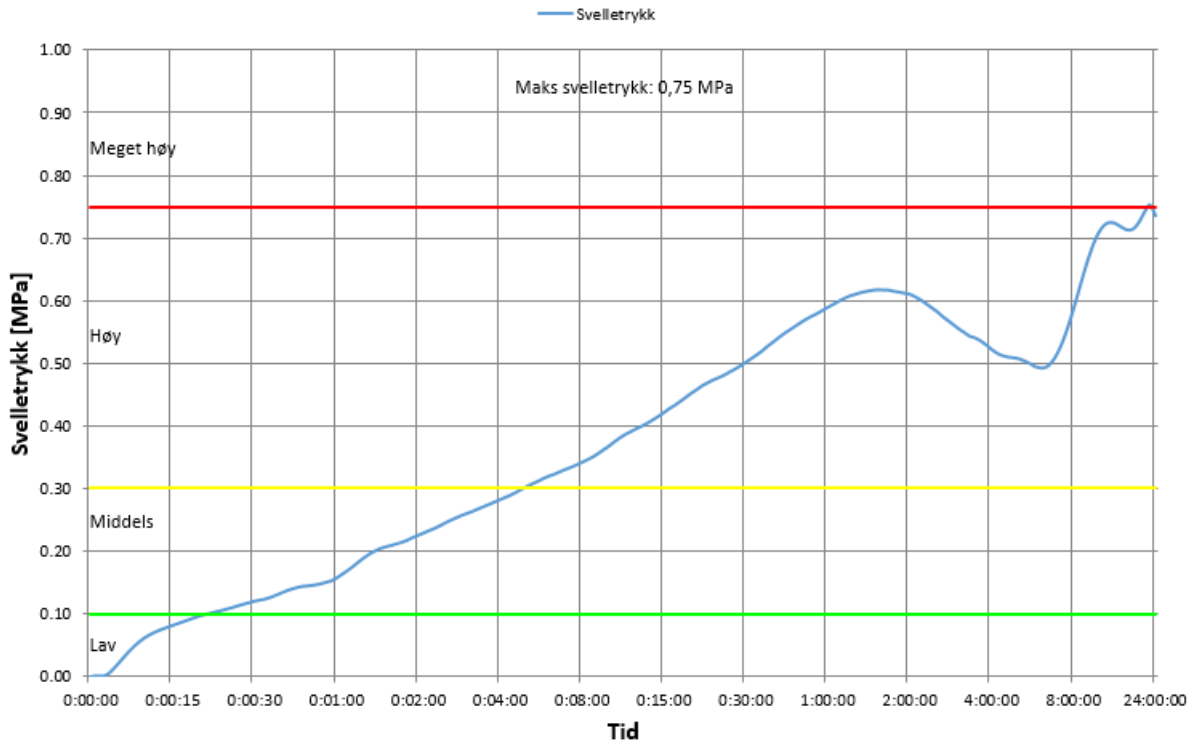

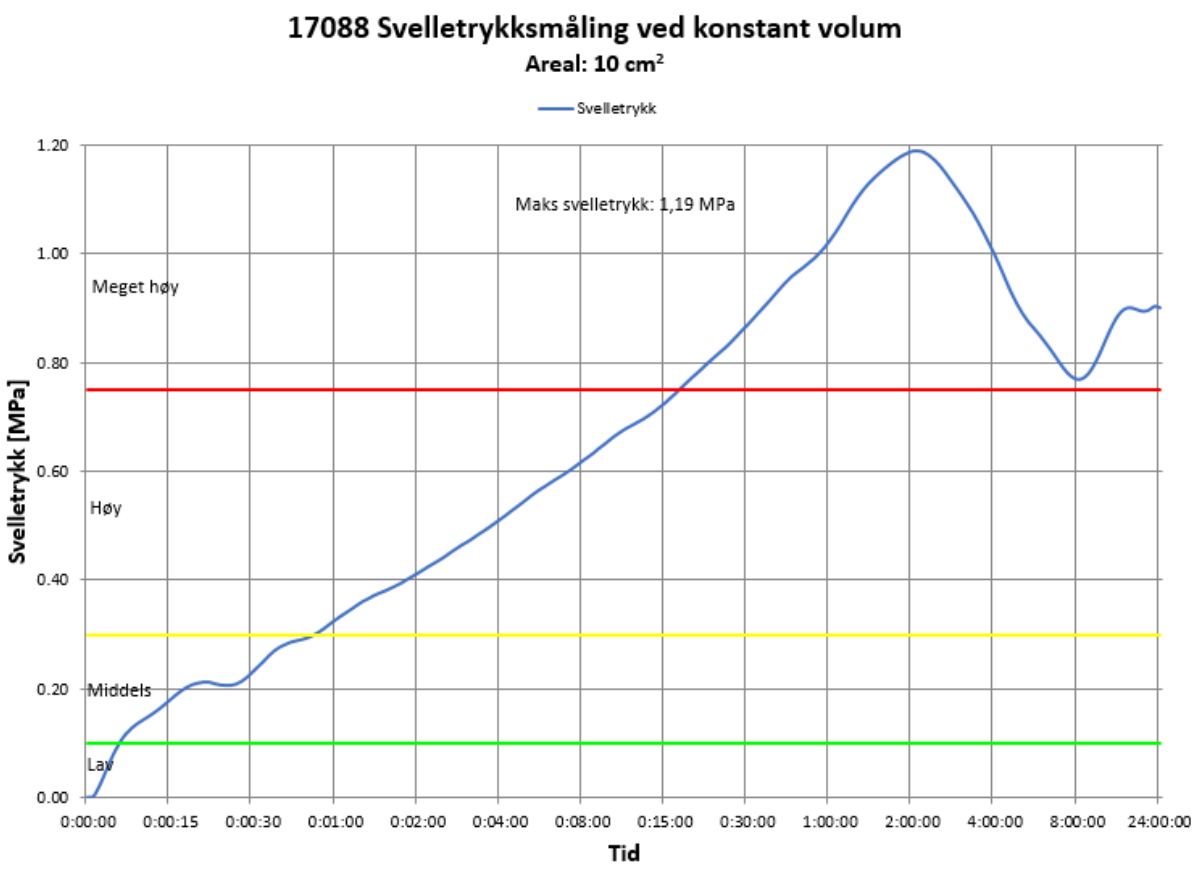
17088 Svelletrykksmåling ved konstant volum
Areal: 10 cm²
Svelletrykk
Maks svelletrykk: 1,19 MPa
Meget høy
Høy
Middels
Lav
Svelletrykk [MPa]
1.20
1.00
0.80
0.60
0.40
0.20
0.00
0:00:00
0:00:15
0:00:30
0:01:00
0:02:00
0:04:00
0:08:00
0:15:00
0:30:00
1:00:00
2:00:00
4:00:00
8:00:00
24:00:00
Tid

17105 Svelletrykksmåling ved konstant volum

Areal: 20 cm²

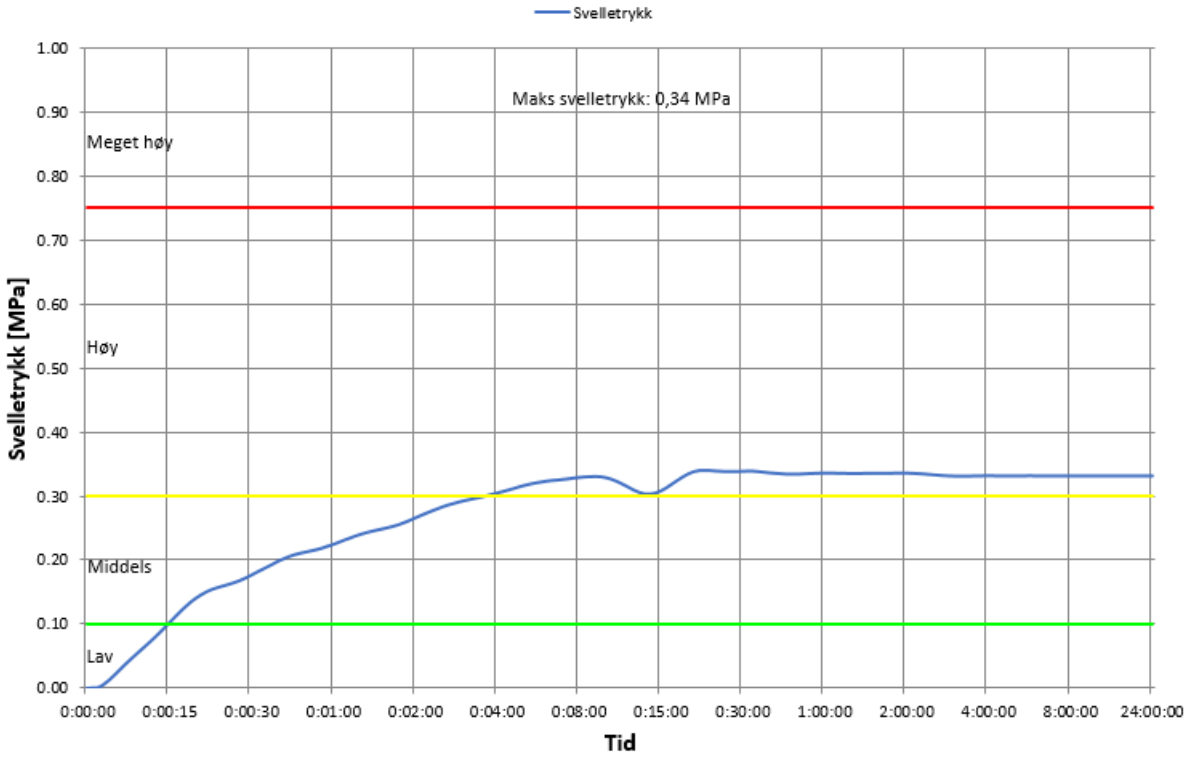

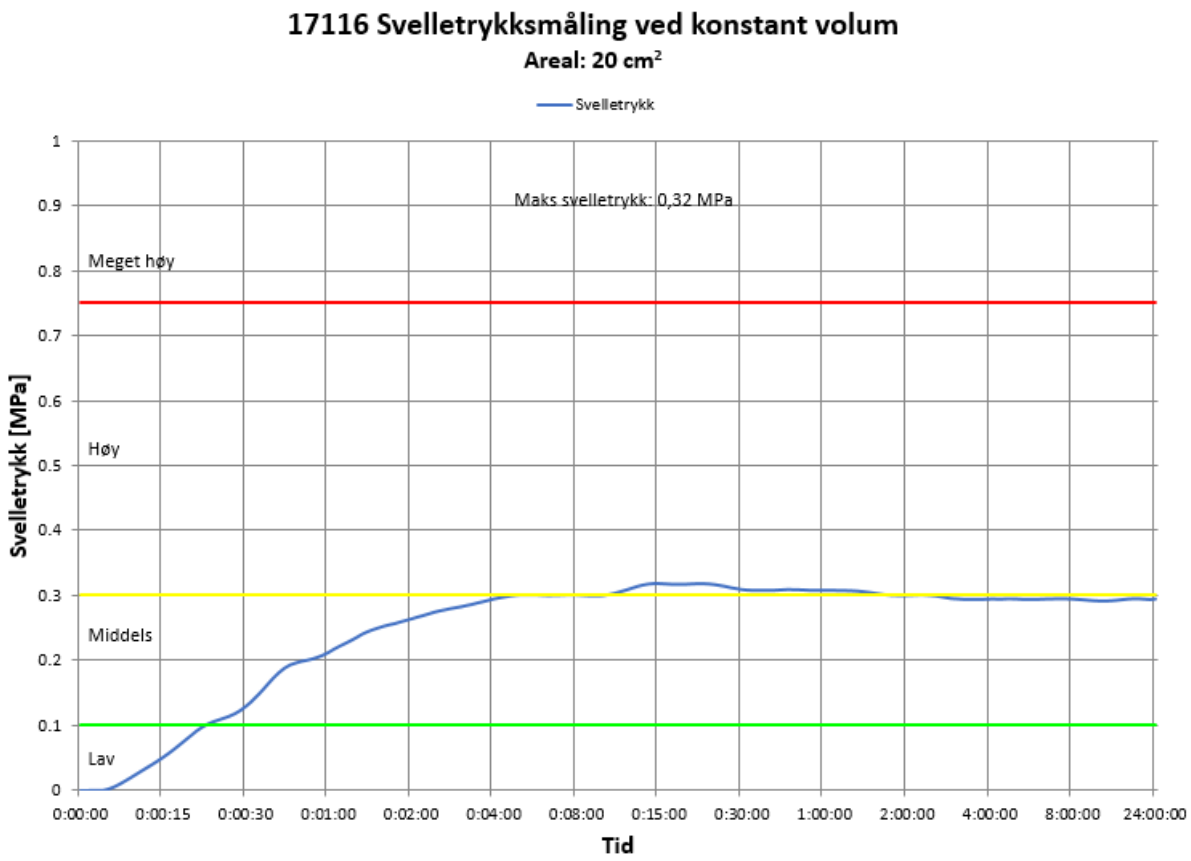
17116 Svelletrykksmåling ved konstant volum
Areal: 20 cm²
Svelletrykk
Maks svelletrykk: 0,32 MPa
Meget høy
Høy
Middels
Lav
Svelletrykk [MPa]
Tid
1
0.9
0.8
0.7
0.6
0.5
0.4
0.3
0.2
0.1
0
0:00:00
0:00:15
0:00:30
0:01:00
0:02:00
0:04:00
0:08:00
0:15:00
0:30:00
1:00:00
2:00:00
4:00:00
8:00:00
24:00:00

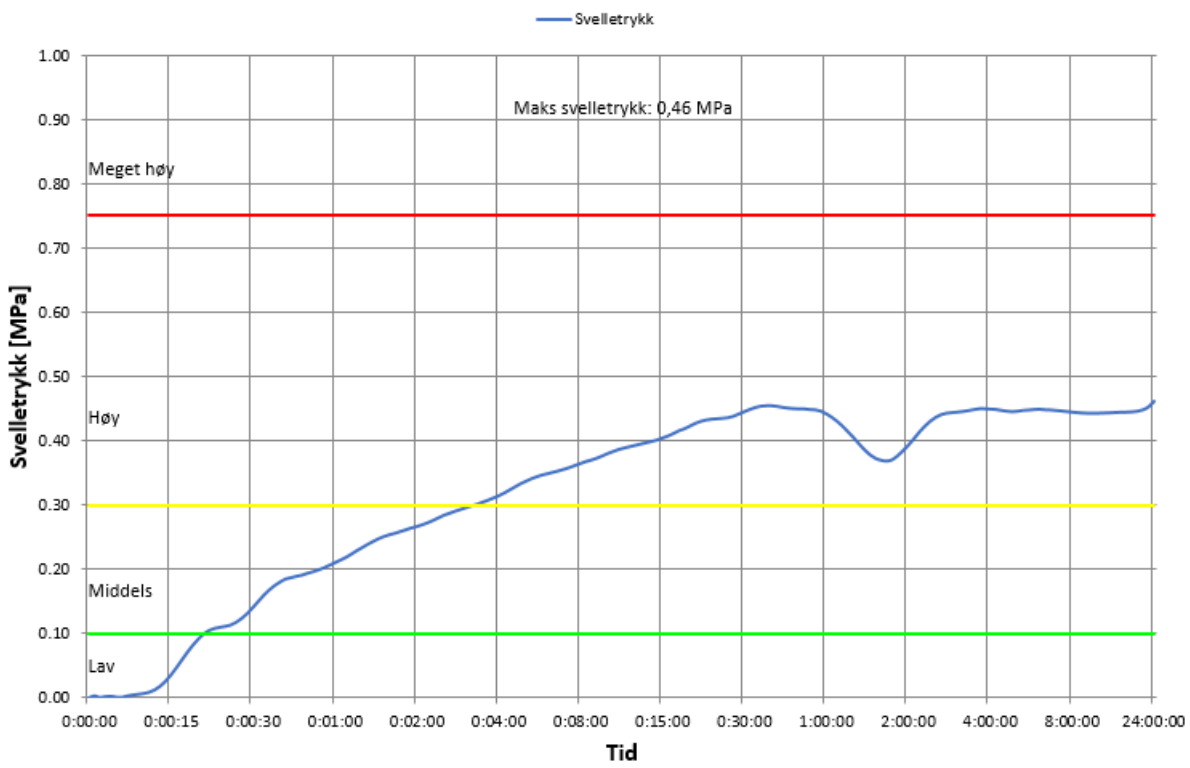
17125 Svelletrykksmåling ved konstant volum
Areal: 20 cm²
Svelletrykk
Maks svelletrykk: 0,46 MPa
Meget høy
Høy
Middels
Lav
Svelletrykk [MPa]
1.00
0.90
0.80
0.70
0.60
0.50
0.40
0.30
0.20
0.10
0.00
0:00:00
0:00:15
0:00:30
0:01:00
0:02:00
0:04:00
0:08:00
0:15:00
0:30:00
1:00:00
2:00:00
4:00:00
8:00:00
24:00:00
Tid

17144 Svelletrykksmåling ved konstant volum

Areal: 20 cm^2

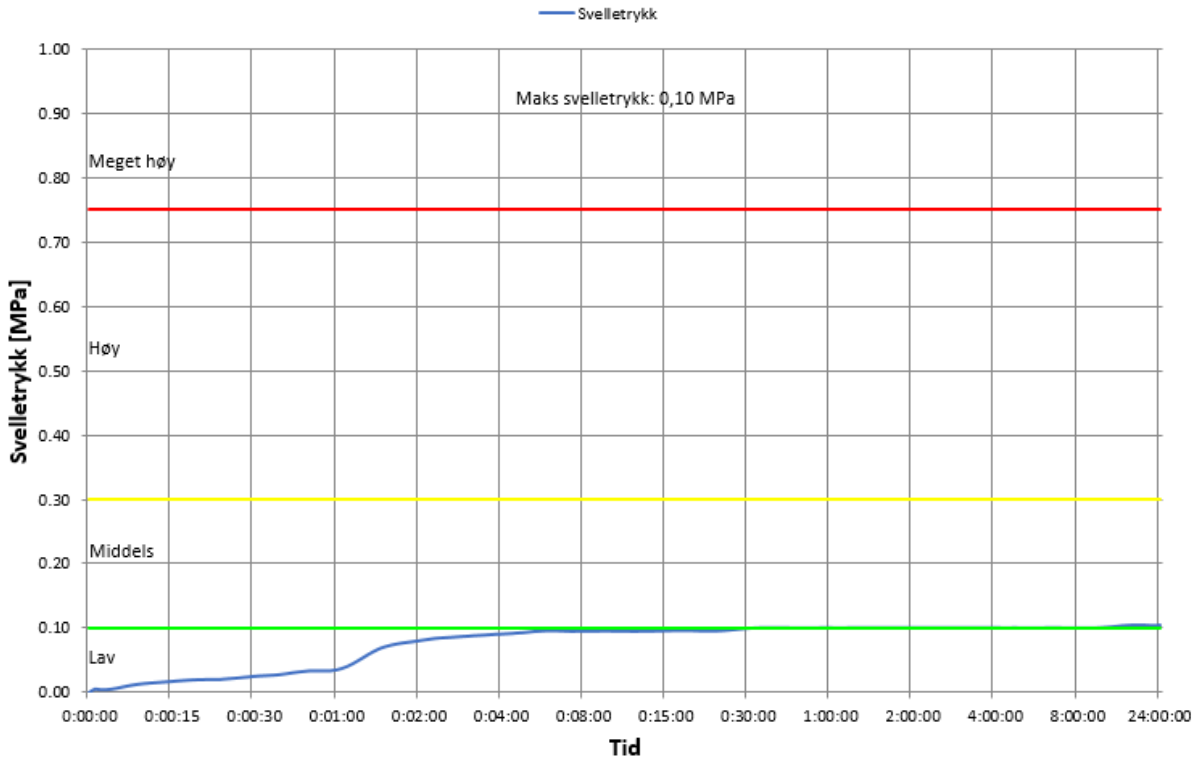

17157 Svelletrykksmåling ved konstant volum

2 Areal: 20 cm^2

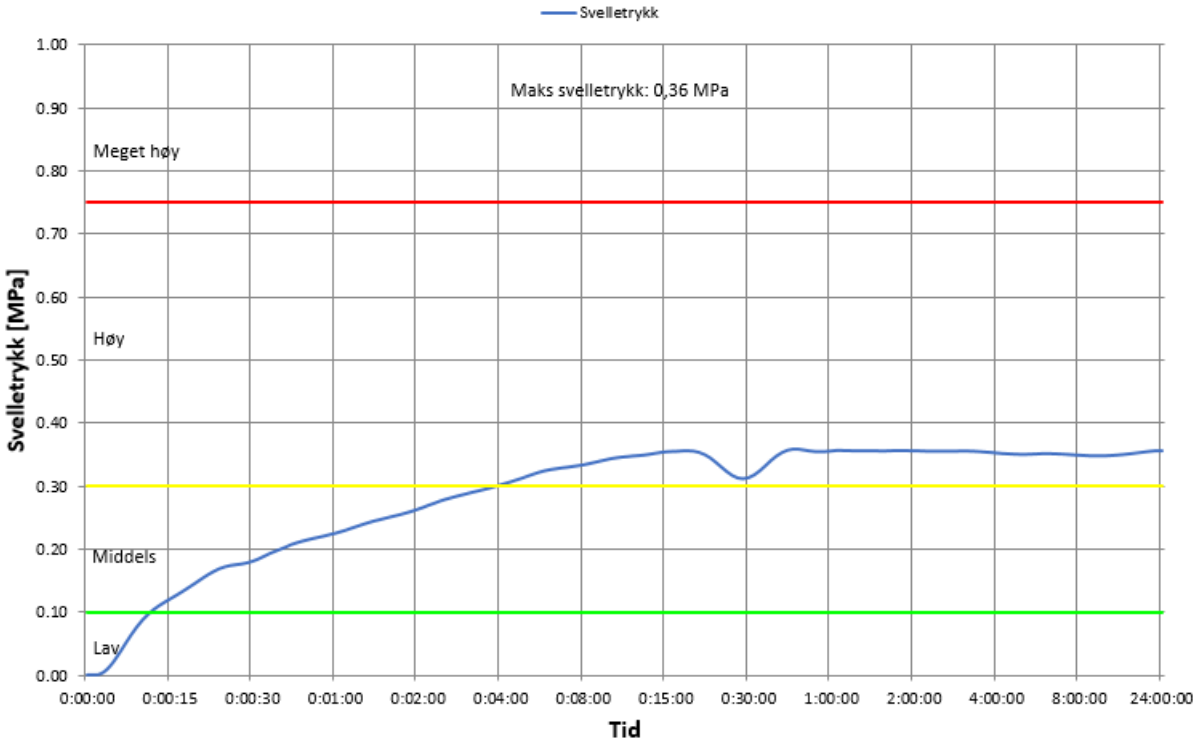

18009 Svelletrykksmåling ved konstant volum

Areal: 20 cm²

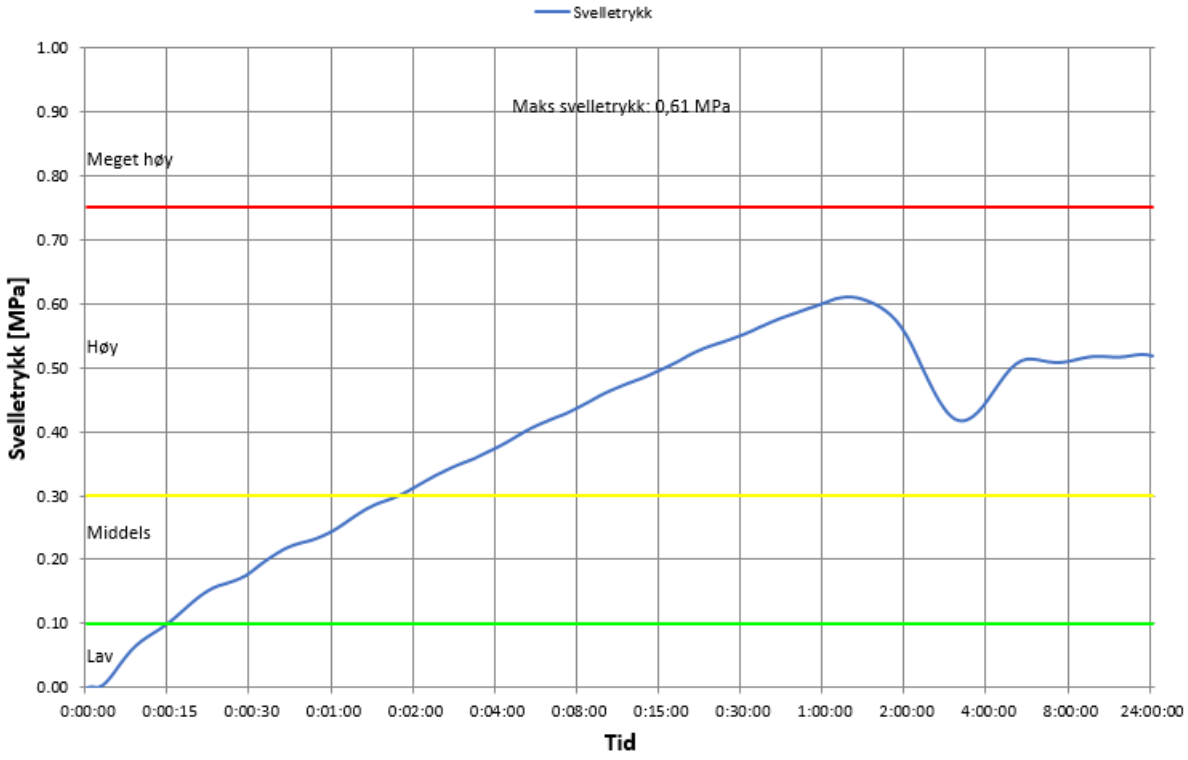

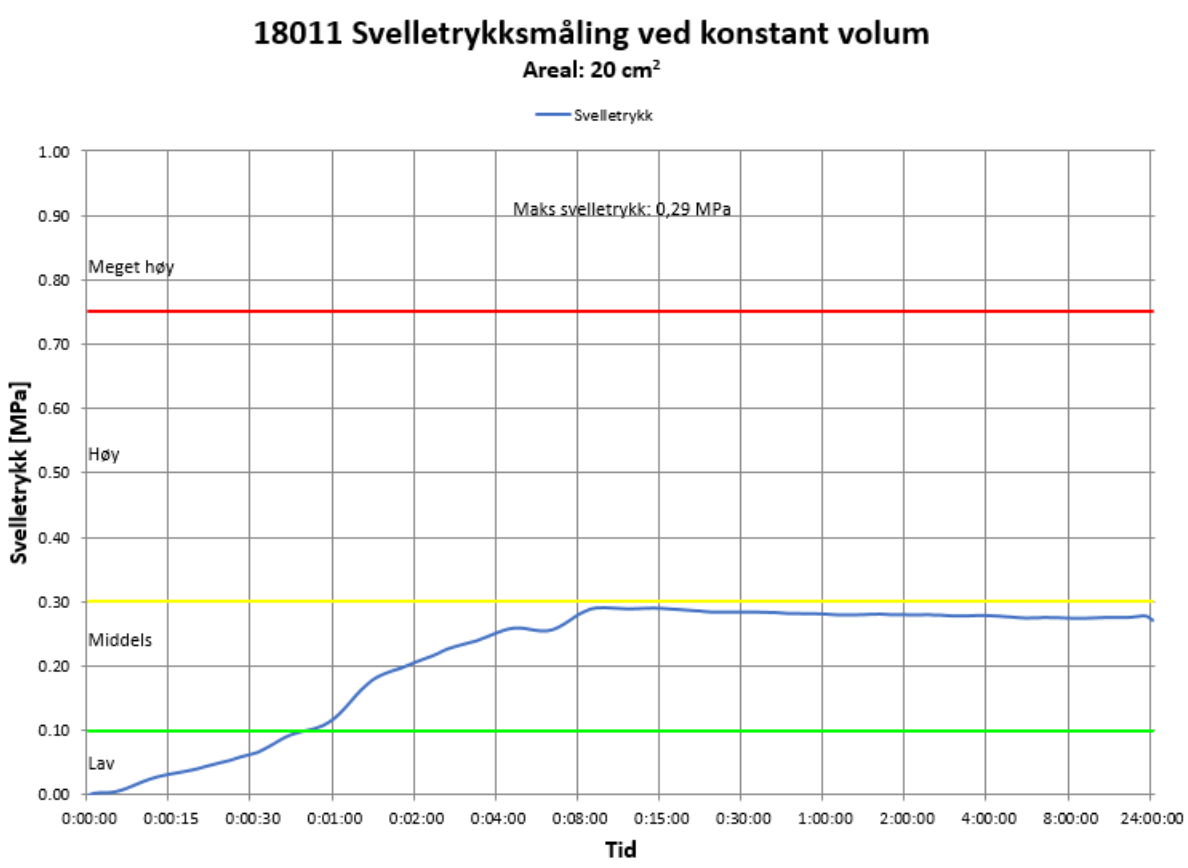
18011 Svelletrykksmåling ved konstant volum
Areal: 20 cm²
Svelletrykk
Maks svelletrykk: 0,29 MPa
Meget høy
Høy
Middels
Lav
Svelletrykk [MPa]
1.00
0.90
0.80
0.70
0.60
0.50
0.40
0.30
0.20
0.10
0.00
0:00:00
0:00:15
0:00:30
0:01:00
0:02:00
0:04:00
0:08:00
0:15:00
0:30:00
1:00:00
2:00:00
4:00:00
8:00:00
24:00:00
Tid

18018 Svelletrykksmåling ved konstant volum

Areal: 20 cm^2

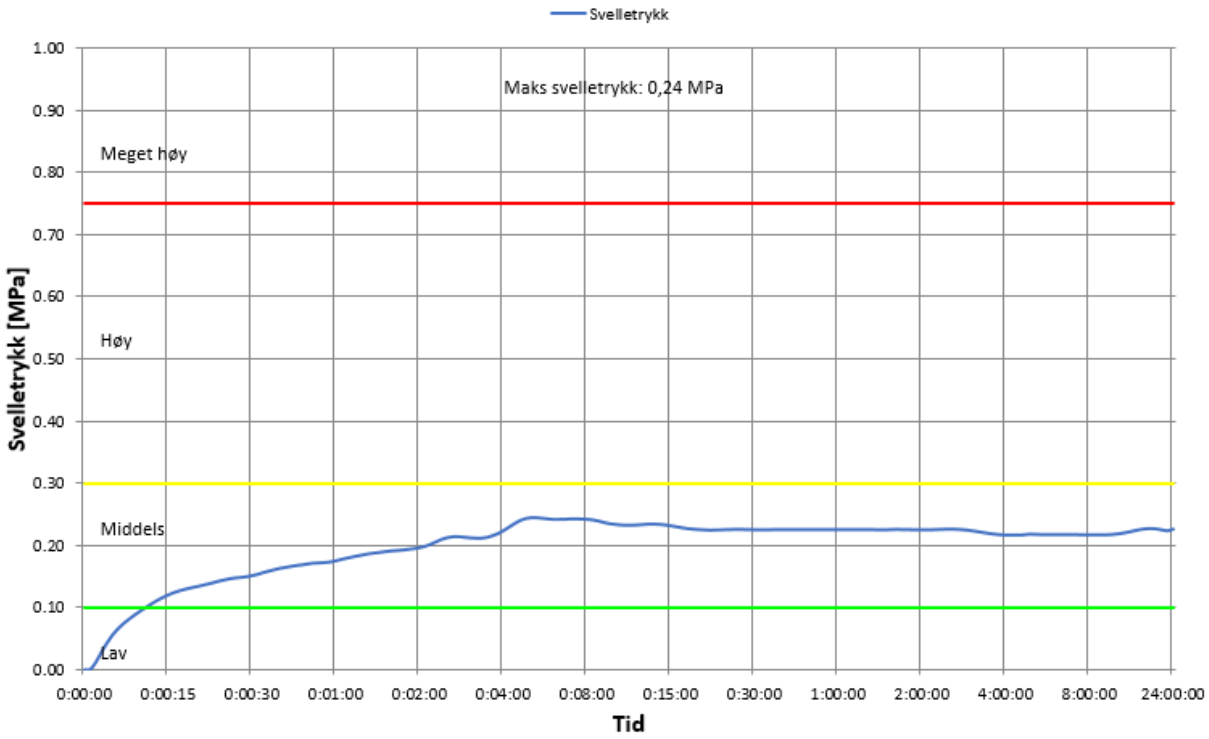

18022 Svelletrykksmåling ved konstant volum

Areal: 20 cm²

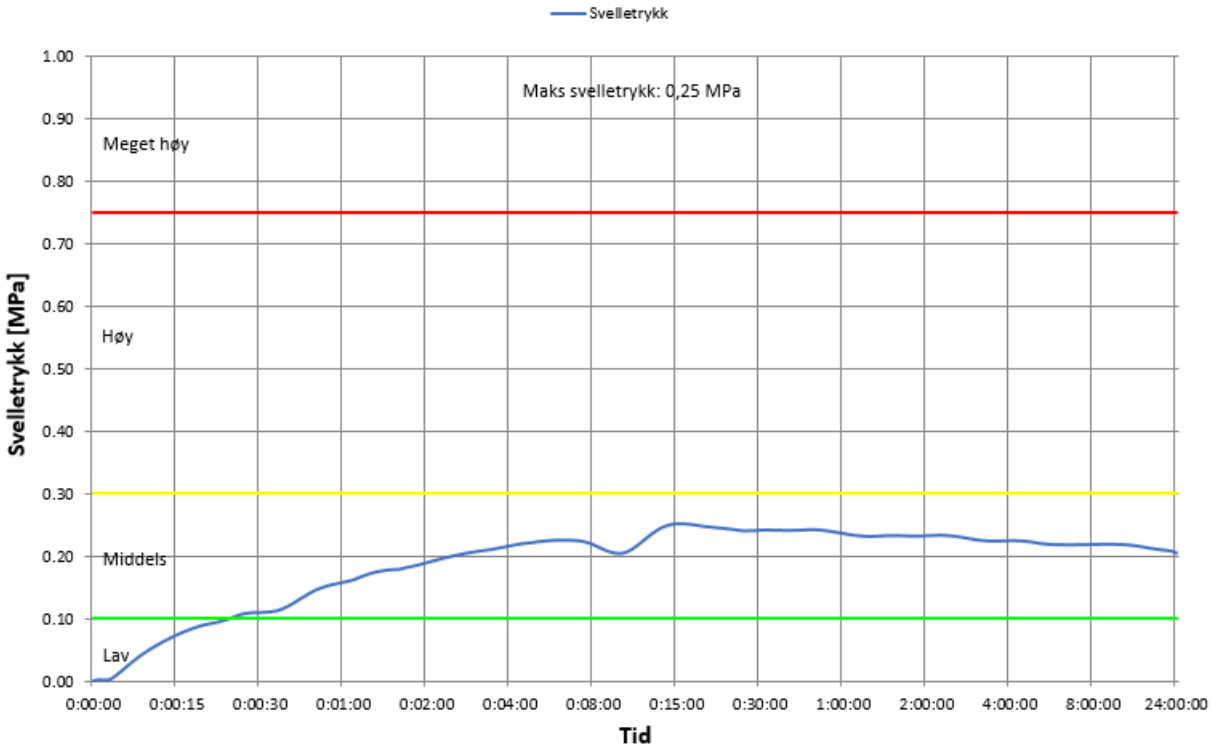

18034 Svelletrykksmåling ved konstant volum

Areal: 20 cm²

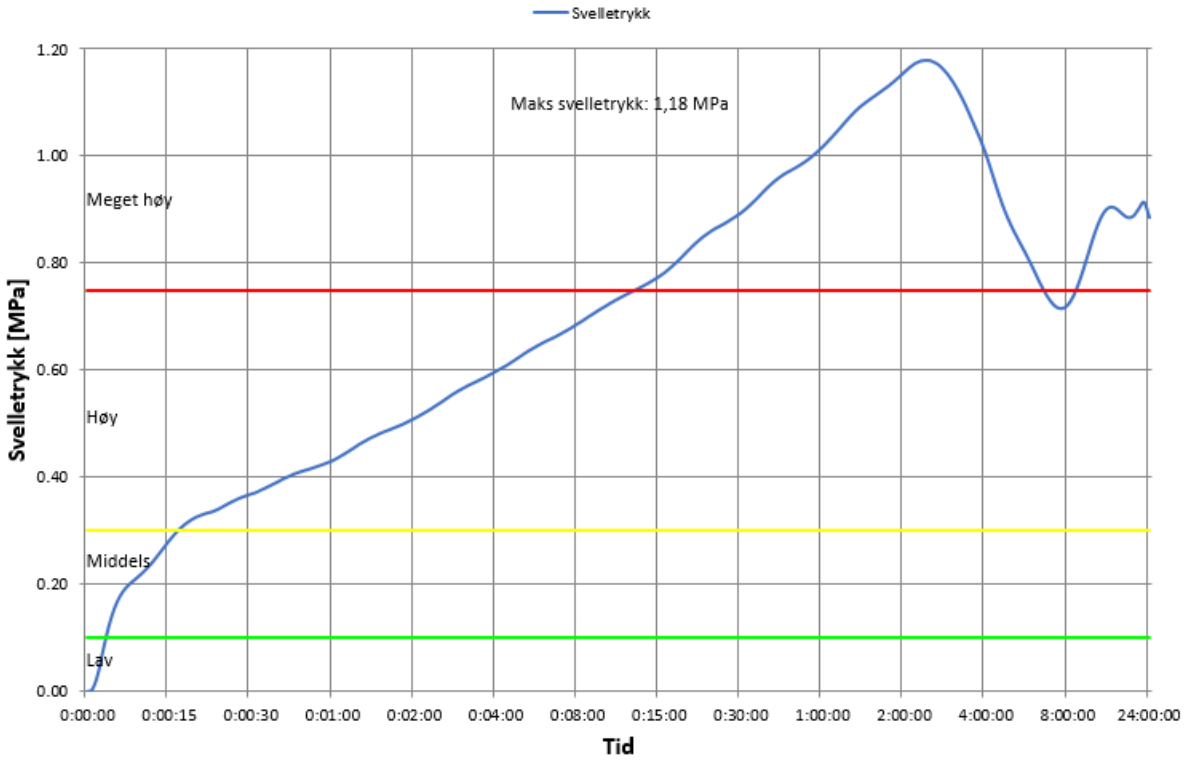

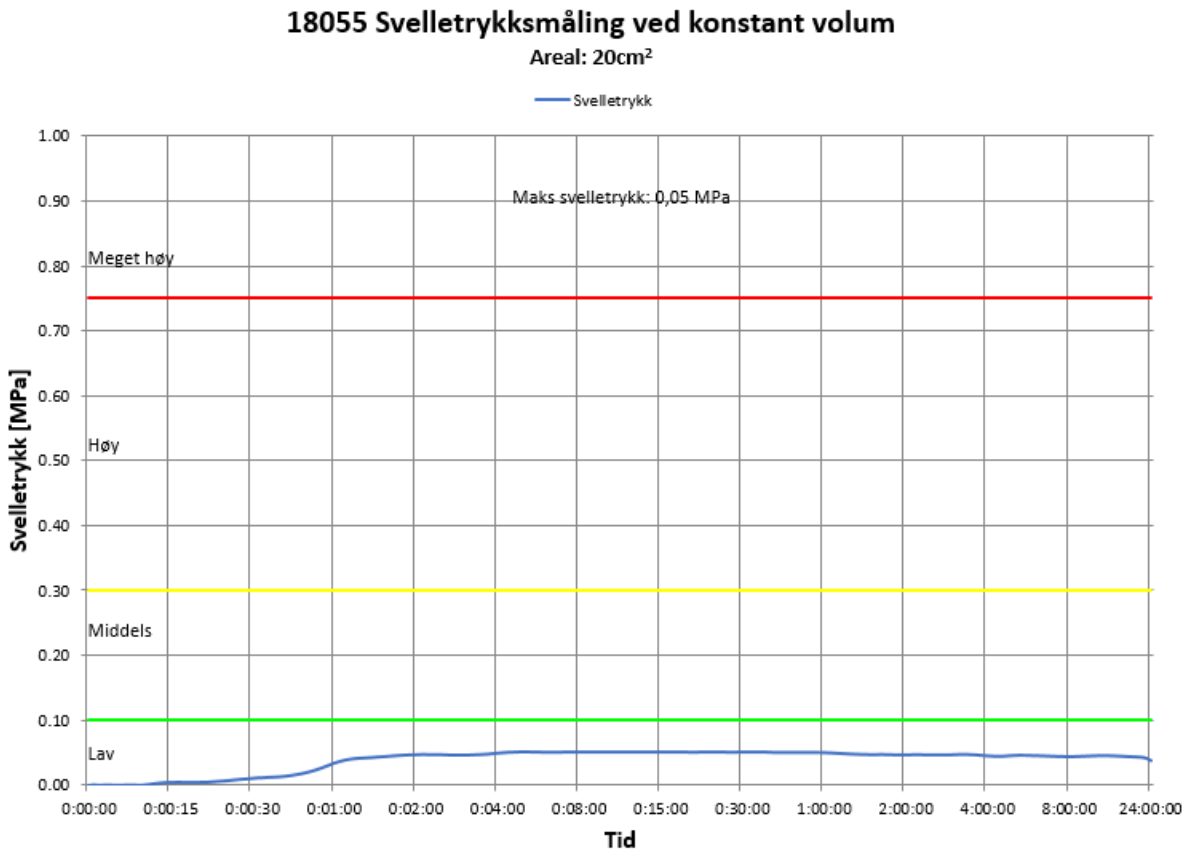
18055 Svelletrykksmåling ved konstant volum
Areal: 20cm²
Svelletrykk
Maks svelletrykk: 0,05 MPa
Meget høy
Høy
Middels
Lav
Svelletrykk [MPa]
1.00
0.90
0.80
0.70
0.60
0.50
0.40
0.30
0.20
0.10
0.00
0:00:00
0:00:15
0:00:30
0:01:00
0:02:00
0:04:00
0:08:00
0:15:00
0:30:00
1:00:00
2:00:00
4:00:00
8:00:00
24:00:00
Tid

18085 Svelletrykksmåling ved konstant volum

Areal: 20 cm²

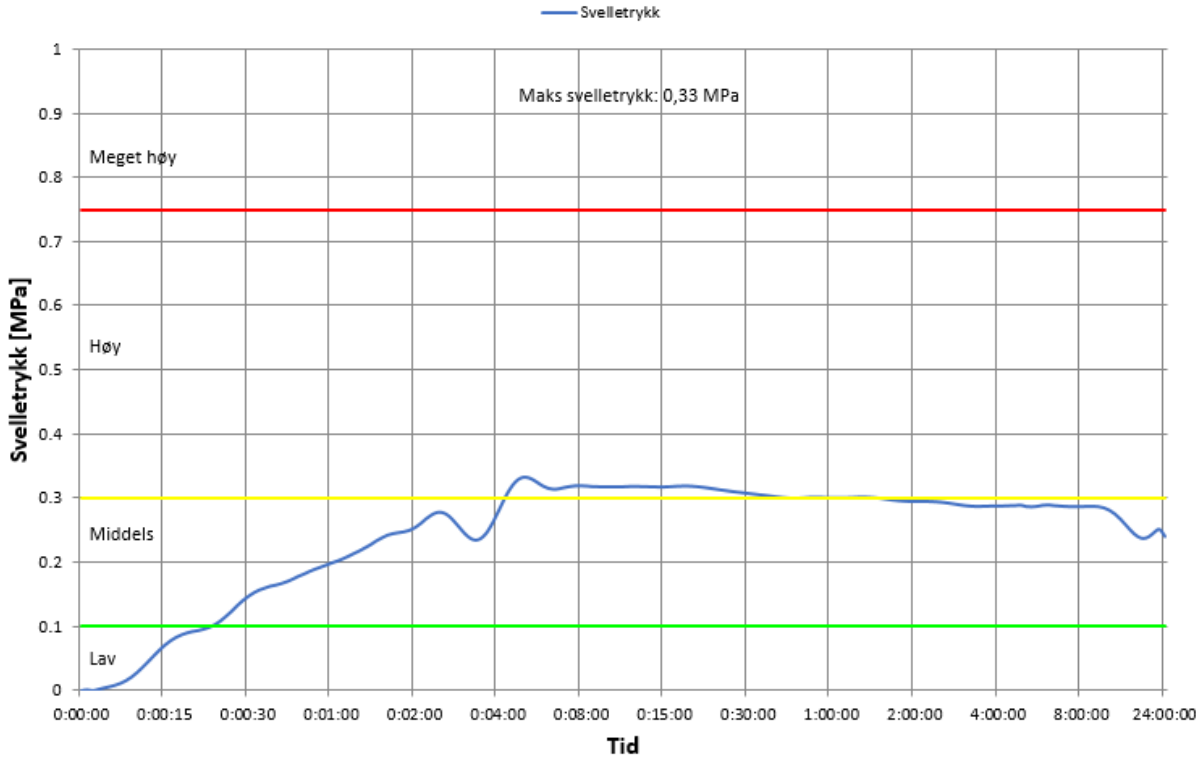

18090 Svelletrykksmåling ved konstant volum

Areal: 20 cm²

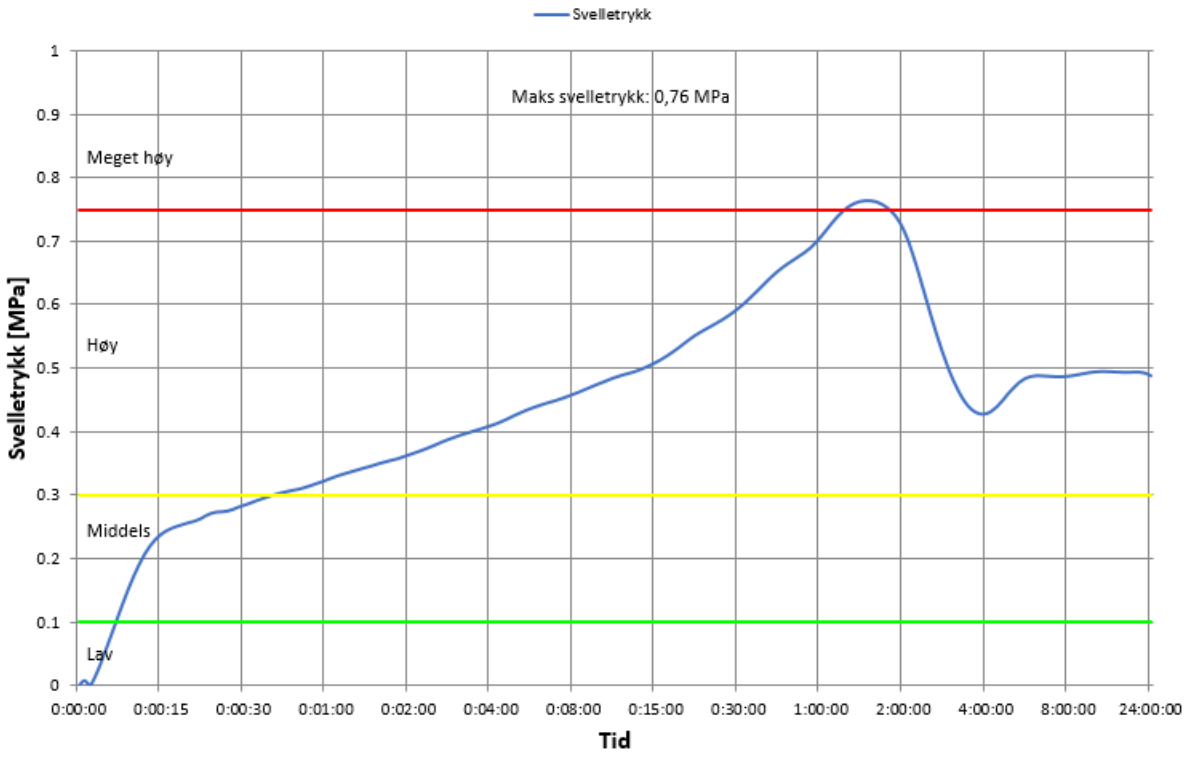

18100 Svelletrykksmåling ved konstant volum

Areal: 20 cm²

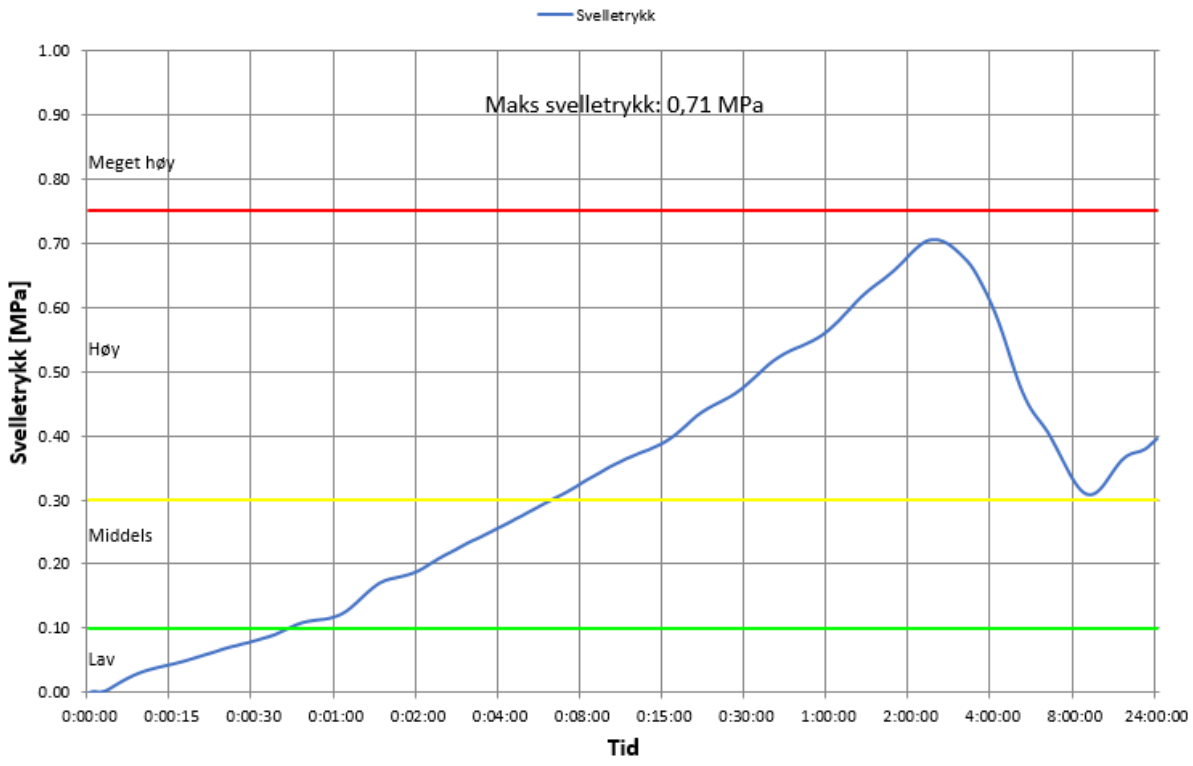

18103 Swelling pressure at constant volume

Oedometer cell area: 20cm^2

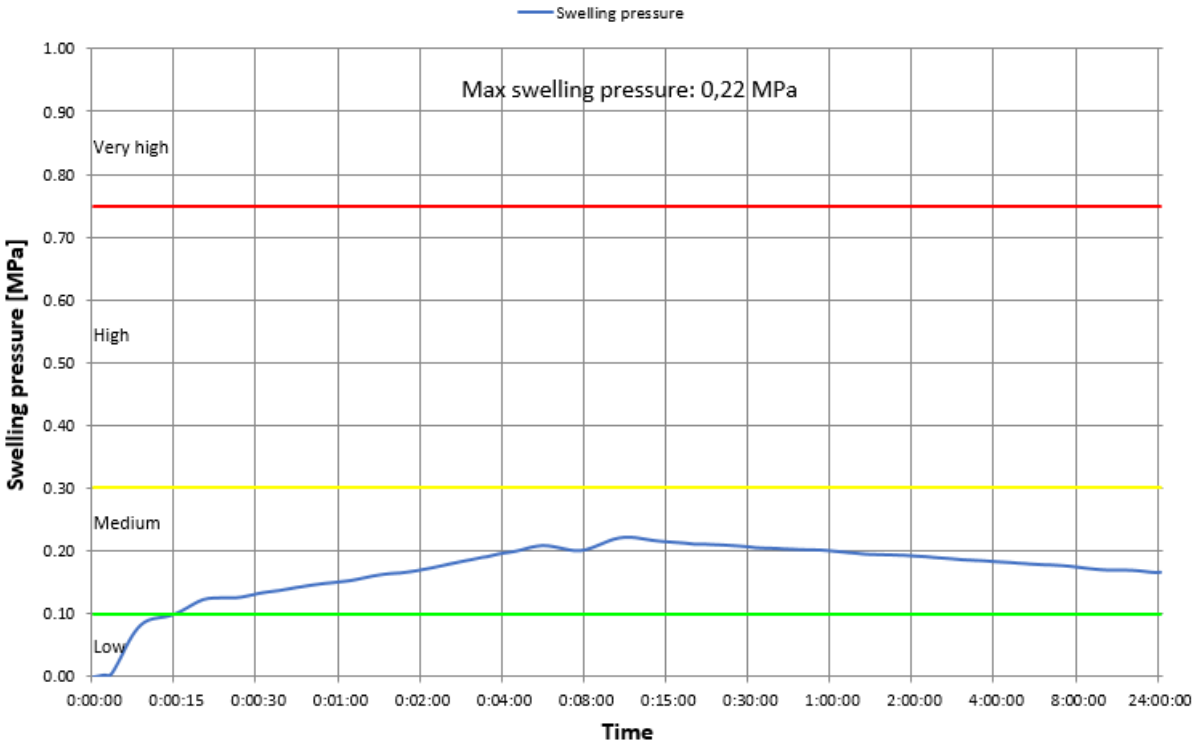

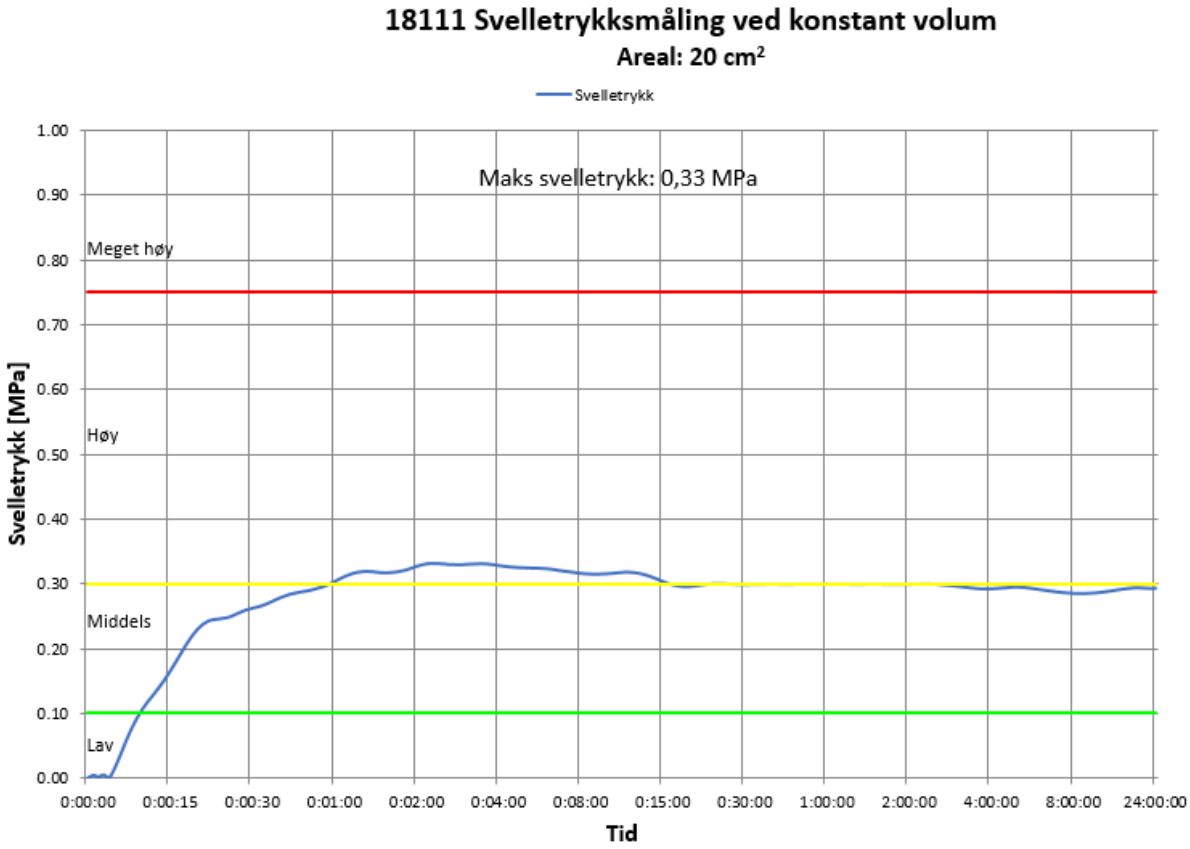
18111 Svelletrykksmåling ved konstant volum
Areal: 20 cm²
Svelletrykk
Maks svelletrykk: 0,33 MPa
Meget høy
Høy
Middels
Lav
Svelletrykk [MPa]
1.00
0.90
0.80
0.70
0.60
0.50
0.40
0.30
0.20
0.10
0.00
0:00:00
0:00:15
0:00:30
0:01:00
0:02:00
0:04:00
0:08:00
0:15:00
0:30:00
1:00:00
2:00:00
4:00:00
8:00:00
24:00:00
Tid

18128 Svelletrykksmåling ved konstant volum

18128 Areal: 20 cm^2

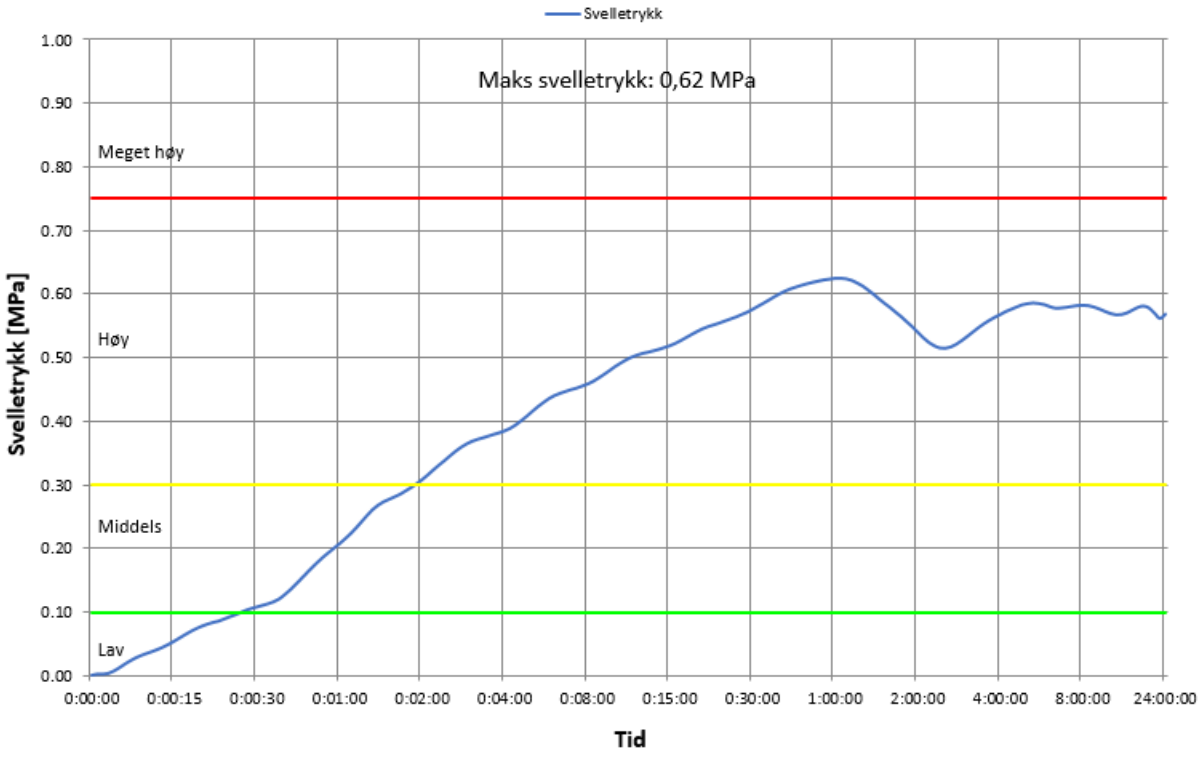

E | Laser Diffraction Curves

Table E.1: Grain size distribution measured using laser diffraction. D-values indicate the percentage of mass finer than or equal to a particular diameter (e.g. d10 gives the diameter at which 10% of the cumulative mass is equal to or finer than).

Sample	d5	d10	d25	d50	d75	d80	d84	d90	d95	d100
16002.1	2.62	3.3	4.95	7.96	12.9	14.5	16.1	19.5	24.3	84.6
16002.2	2.79	3.61	5.66	9.76	17.3	20	23	31	55.3	98.1
16002.3	2.96	3.78	5.83	10.1	19.2	23.3	28.5	47.1	73.2	98.1
16057	2.73	3.67	6.13	11	19.3	22.2	25.4	34	61.4	98.1
16083	3.15	4.15	6.69	11.6	19.9	22.7	25.8	33.5	54.2	98.1
16093	2.37	3.04	4.88	8.68	16.6	19.9	23.9	40.2	72.8	98.1
16095	3.53	4.89	8.95	17.9	35.2	41.8	48.8	63	78.9	98.1
16100	2.28	2.89	4.59	8.09	14.9	17.3	19.8	25.5	35.9	98
16101	2.28	3.02	5.17	9.29	15.9	17.9	19.9	23.9	29.8	97.9
16107	2.49	3.29	5.53	10.1	19.5	23.6	29	50.1	75.8	98.1
16111	2.51	3.23	5.08	8.74	15.8	18.5	21.6	30.8	68.9	98.1
16114	2.6	3.34	5.22	8.89	15.7	18.1	20.7	27.3	51.5	98.1
17040	2.84	3.93	6.93	13.2	24.8	29.6	35.5	53.2	74.7	98.1
17051	2.98	3.84	5.98	10.3	18.8	22.2	26.2	39.1	68.3	98.1
17075	2.55	3.29	5.15	8.67	14.8	16.8	19	23.9	33.2	98
17087	2.98	3.98	6.85	13.8	26.1	30.4	35.2	48.5	70.3	98.1
17088	3.19	4.31	7.1	12.1	19.2	21.4	23.6	28.4	37.2	98.1
17105	2.37	3.18	5.53	10.4	20.1	24.1	29.6	53.7	78.4	98.1
17116	2.31	3	5.02	9.36	18.5	22.4	27.6	51.5	76.7	98.1
17125	2.82	3.8	6.34	11.4	20.1	23.2	26.8	37.3	67.3	98.1
17144	0.084	0.128	0.326	1.2	2.4	2.85	3.32	4.4	6.18	18.6
17148	2.97	3.9	6.14	10.4	17.9	20.6	23.5	31	48.9	98
17149	2.16	2.73	4.34	7.5	13.4	15.5	17.9	23.5	35.1	97.9
17157	2.47	3.24	5.36	9.58	17.2	20	22.9	30.8	60.1	98.1
18009	3.03	4.09	6.8	12.1	21.7	25.3	29.6	42.7	69.7	98.1
18011	1.97	2.64	4.83	10.3	24.8	32.2	41.5	61.5	79.7	98.1
18018	2.23	2.81	4.47	7.68	13	14.7	16.3	19.6	23.9	40.1
18034	2.88	3.81	6.36	12.4	27	34.3	43.5	62.5	79.8	98.1
18055	1.55	2.15	3.96	8.37	19.4	24.5	30.8	47.3	67.5	98.1
18068	2.81	3.72	6.24	12.1	24.3	29.4	35.4	52.3	73.1	98.1
18090	3.09	3.99	6.21	10.6	17.9	20.3	23	29.4	49.9	98.1
18100	3.08	4.16	7.03	12.6	21.5	24.6	28	37.2	60.6	98.1
18103	2.86	3.78	6.17	11.3	22.1	26.8	32.6	49.7	72.9	98.1
18111	3.97	6.24	13.9	34.3	61.8	68	73.2	81.6	89.5	98.1
18128	2.68	3.7	7.16	17.5	46.5	56.3	64.4	76.7	87.2	98.1

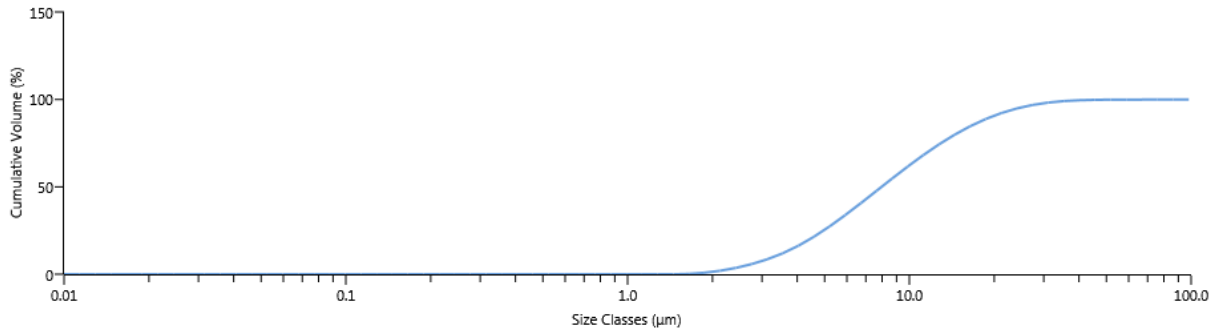

[132] 16002_1-10.04.2019 12:58:45

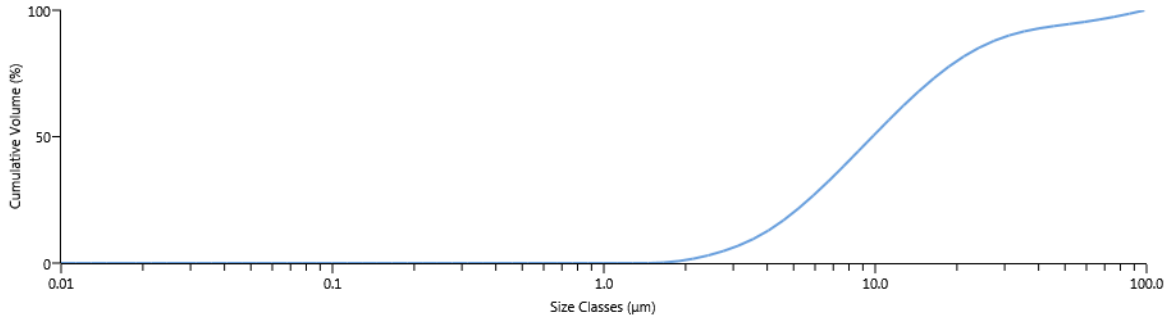

[38] 16002-10.04.2019 09:43:34

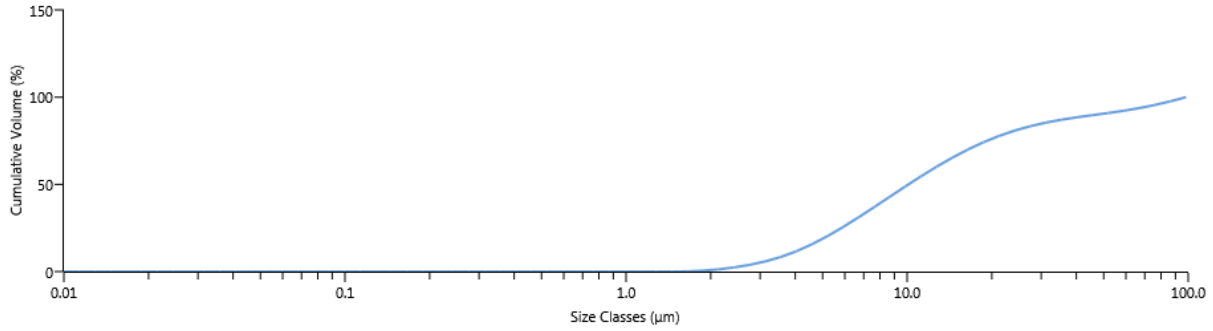

[143] 16002_3-10.04.2019 12:00:20

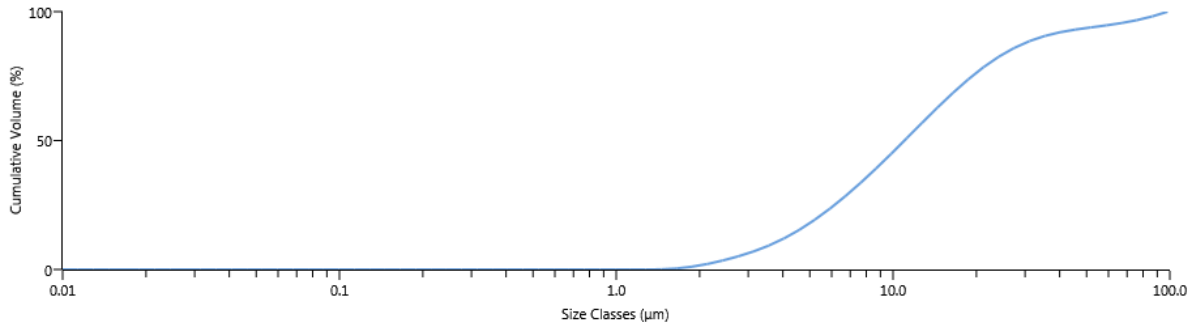

[148] 16057-10.04.2019 12:51:57

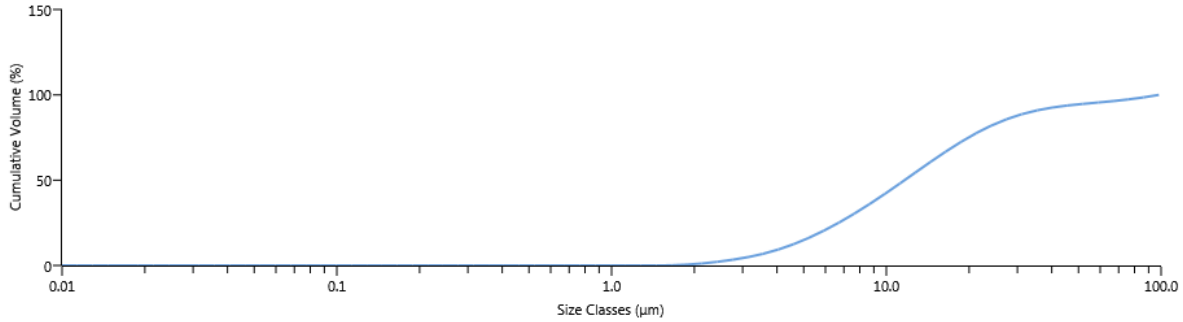

[146] 16083-10.04.2019 12:14:00

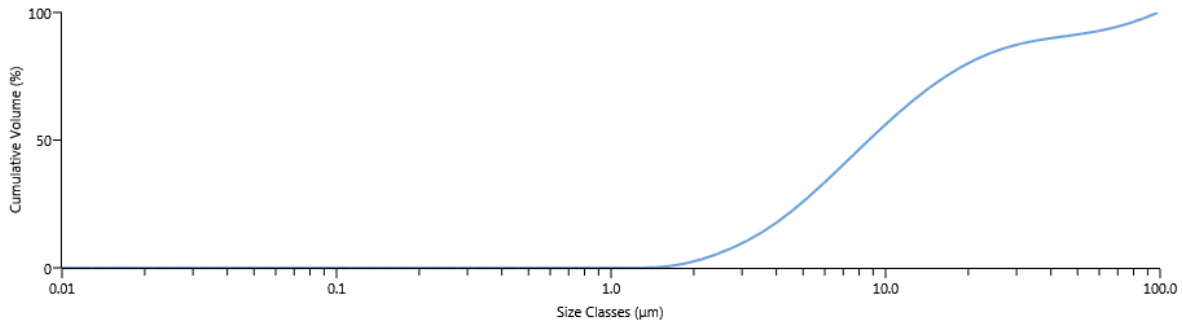

[56] 16093-10.04.2019 09:50:10

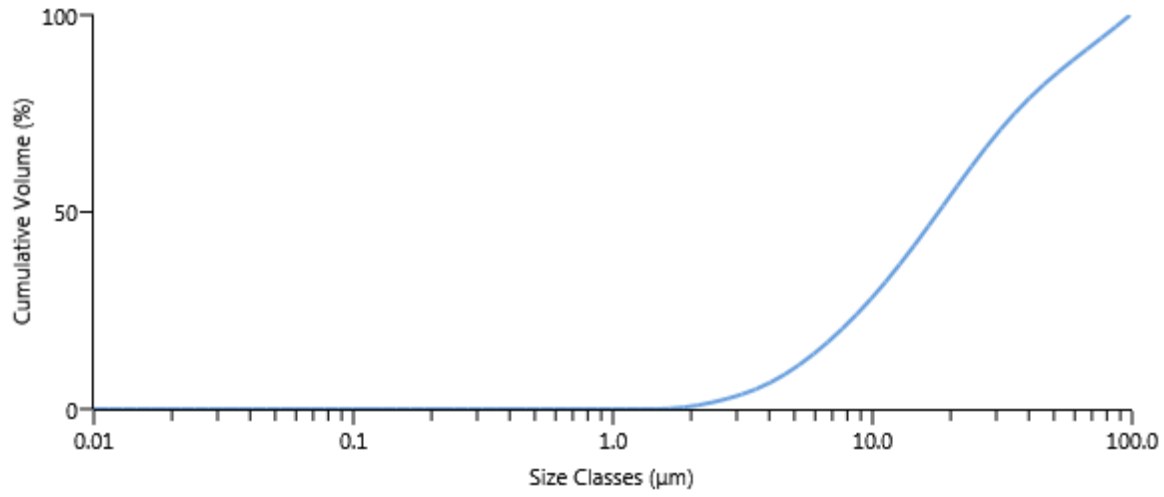

[18] 16095-10.04.2019 09:22:26

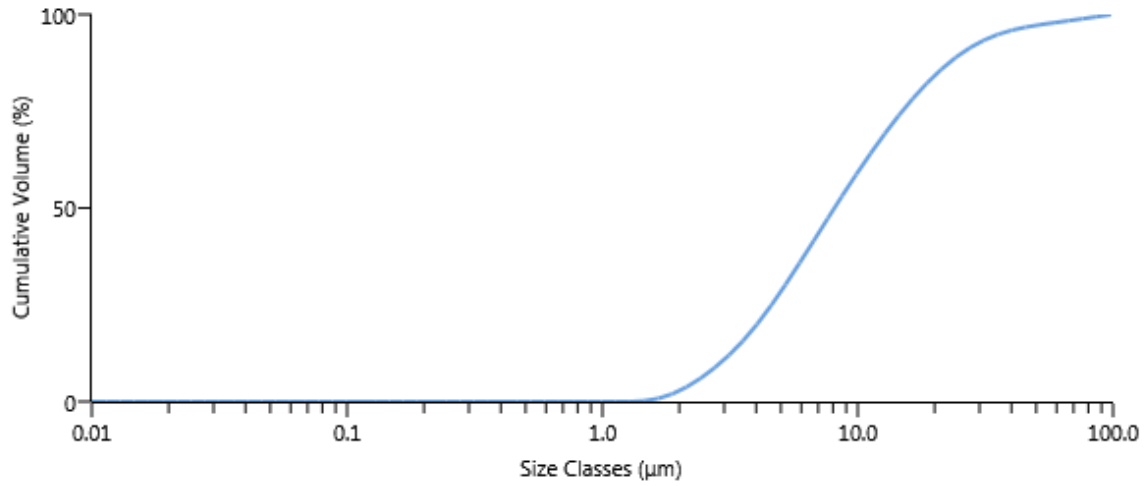

[13] 16100-27.03.2019 12:58:11

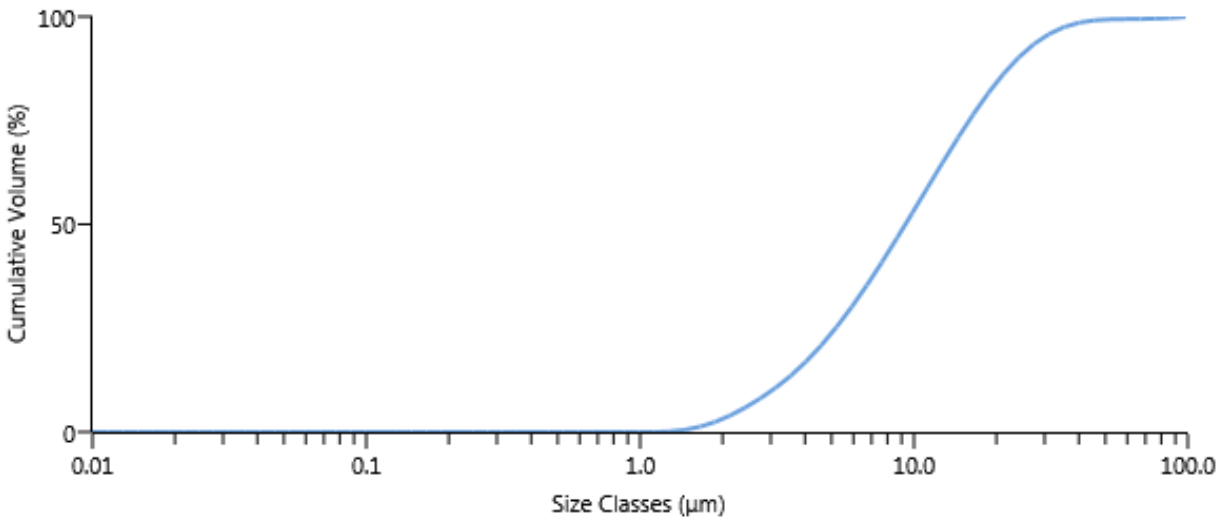

[14] 16101-27.03.2019 13:24:18

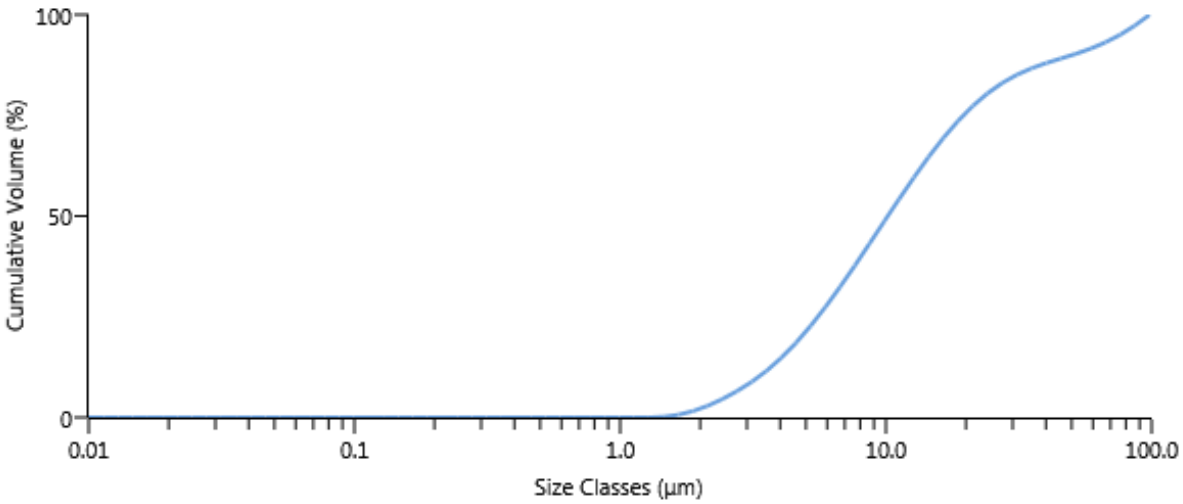

[37] 16107-10.04.2019 09:31:03

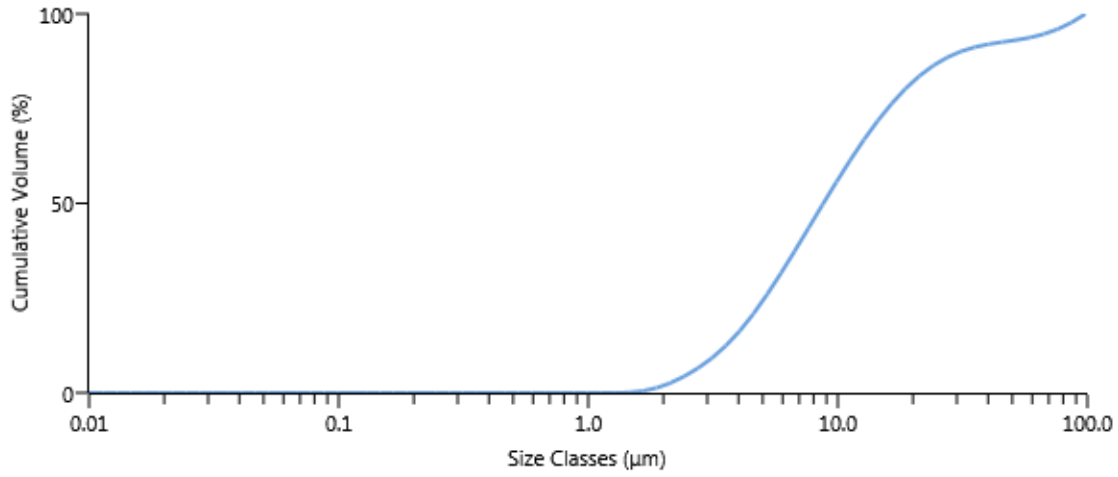

[145] 16111-10.04.2019 12:09:32

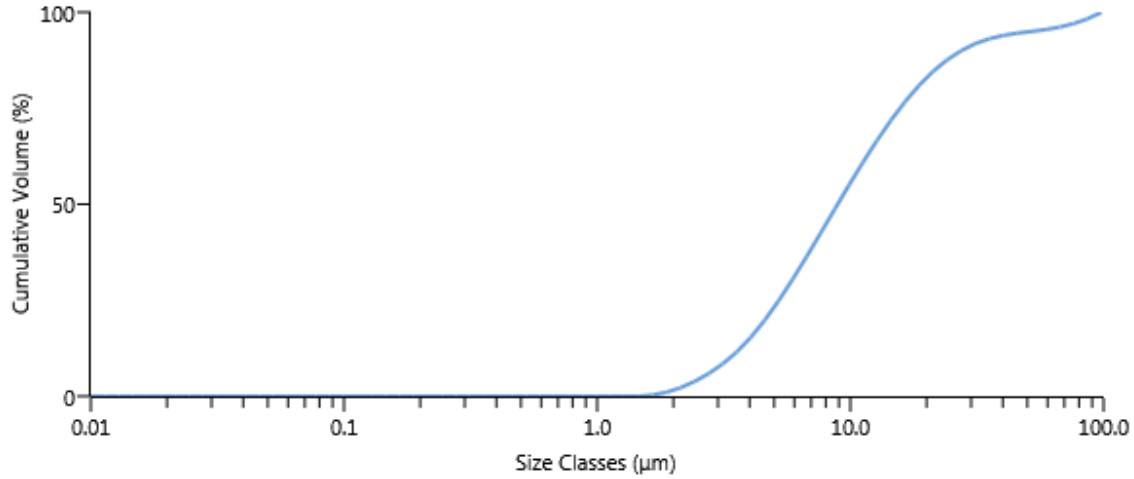

[147] 16114-10.04.2019 12:55:30

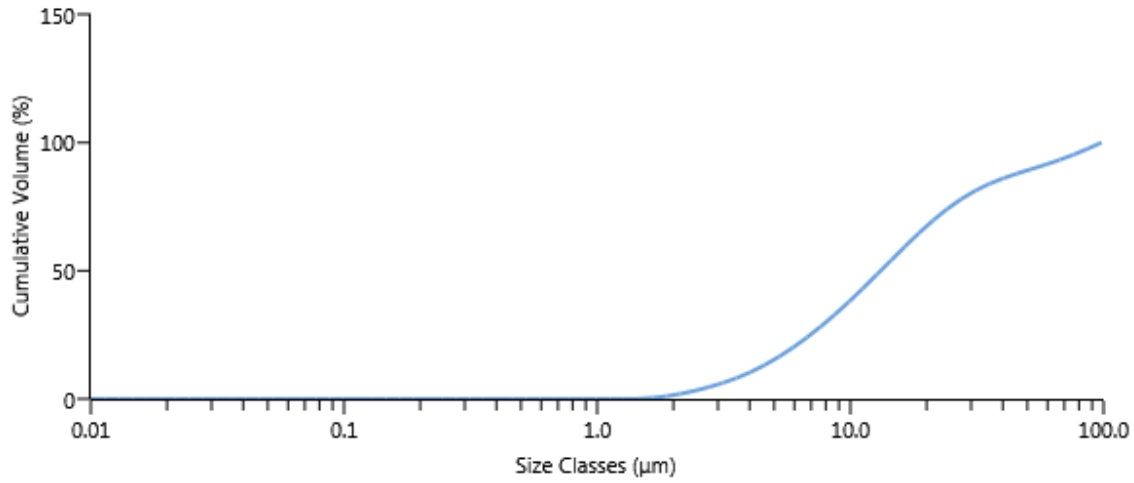

[133] 17040-10.04.2019 10:53:17

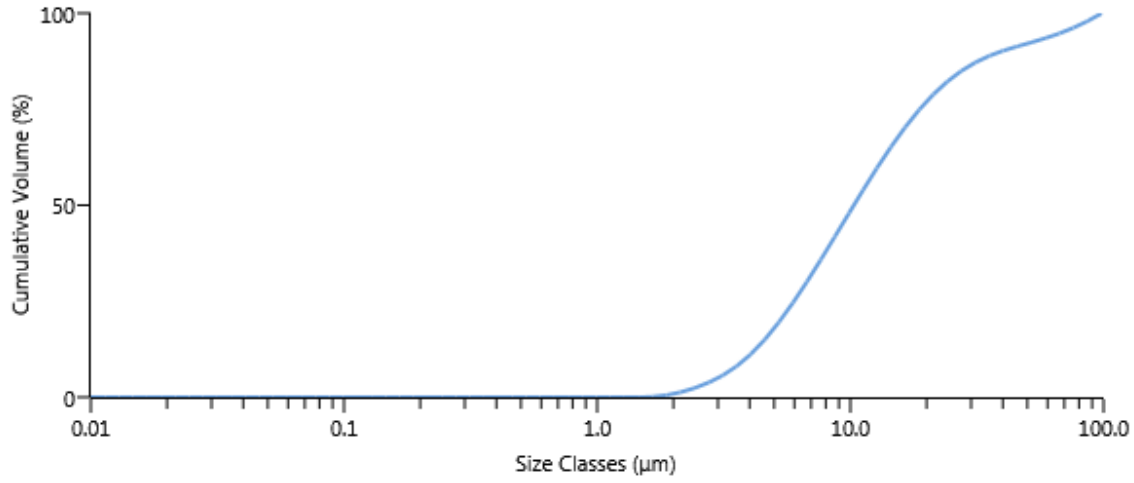

[134] 17051-10.04.2019 10:58:09

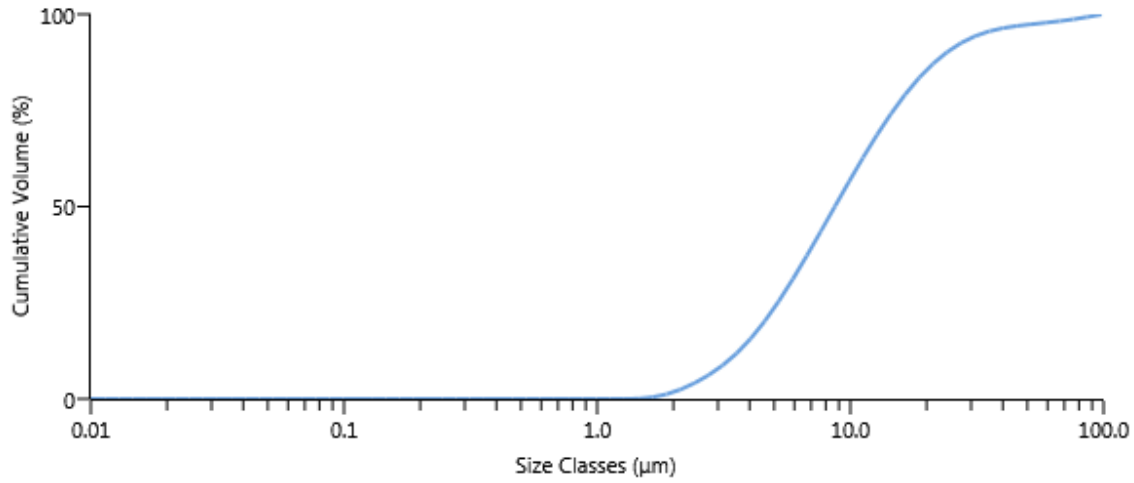

[54] 17075-10.04.2019 10:45:07

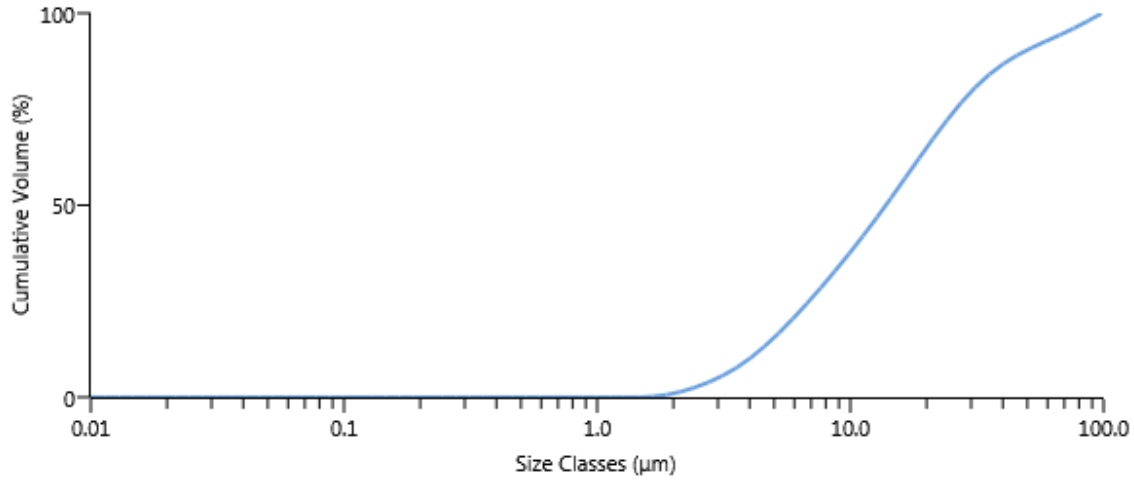

[136] 17087-10.04.2019 11:10:28

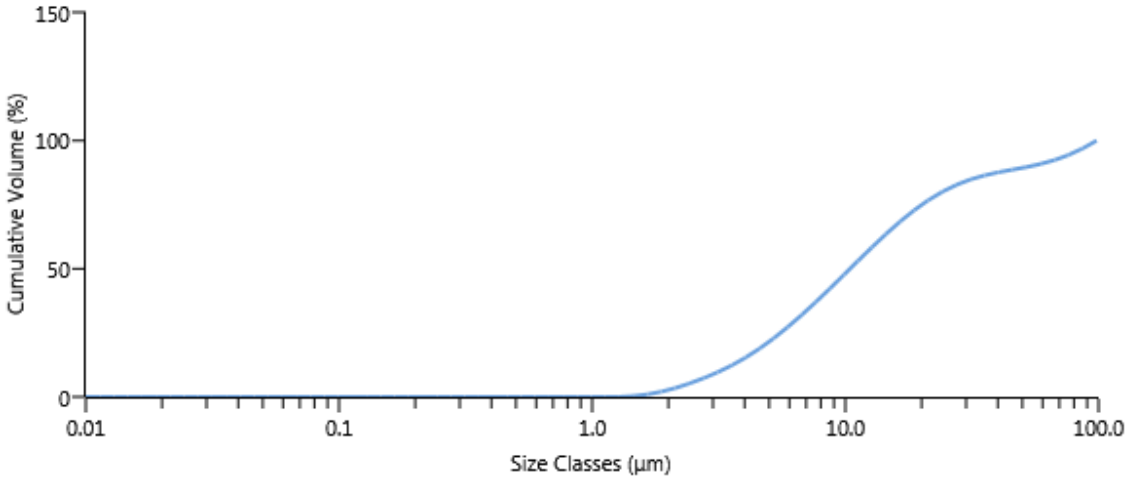

[52] 17105-10.04.2019 10:24:22

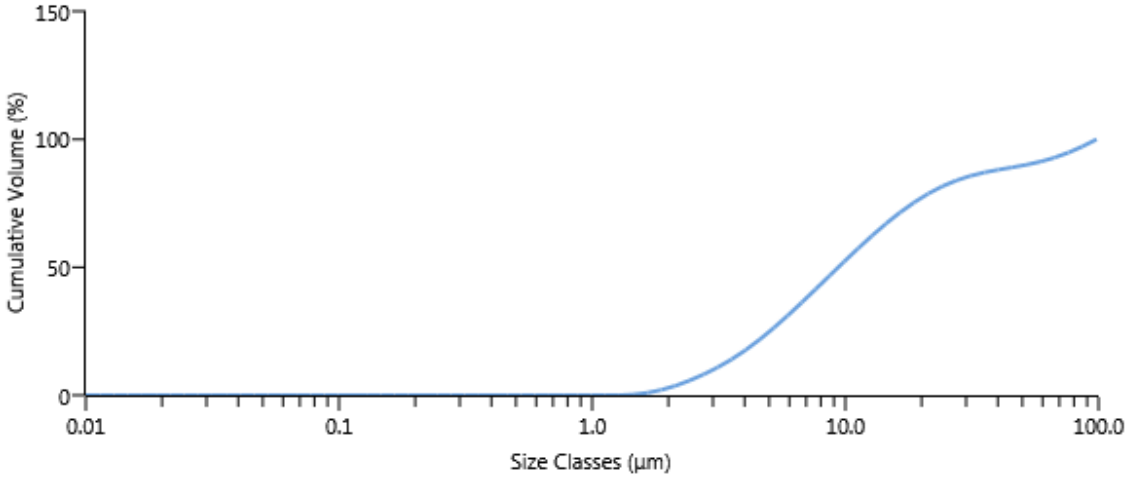

[153] 17116-10.04.2019 12:30:14

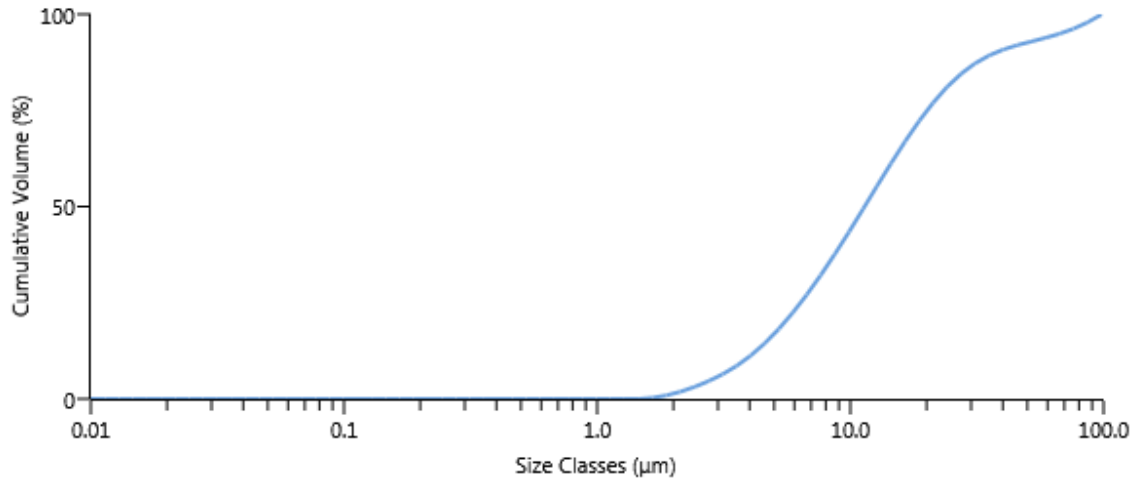

[152] 17125-10.04.2019 12:34:57

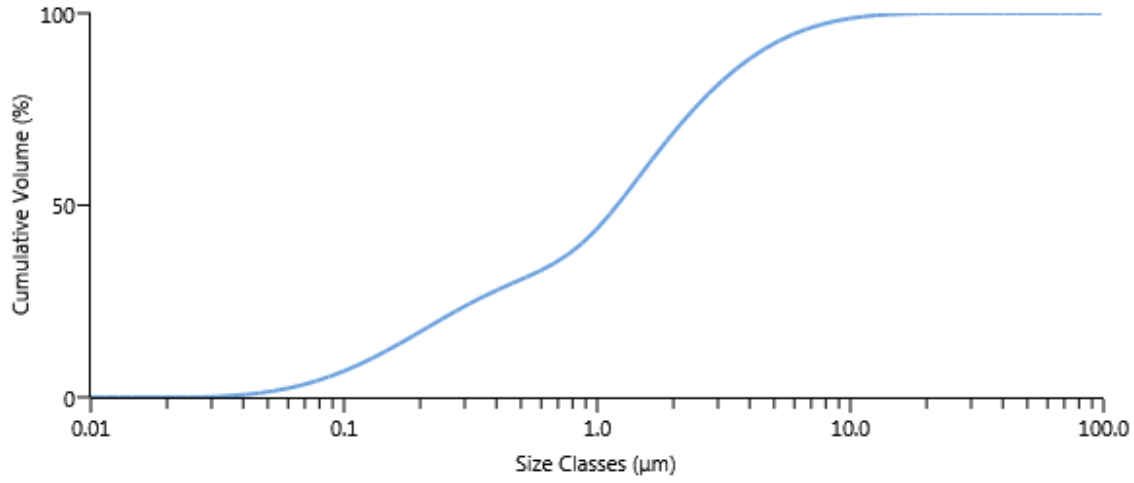

[53] 17144-10.04.2019 10:32:40

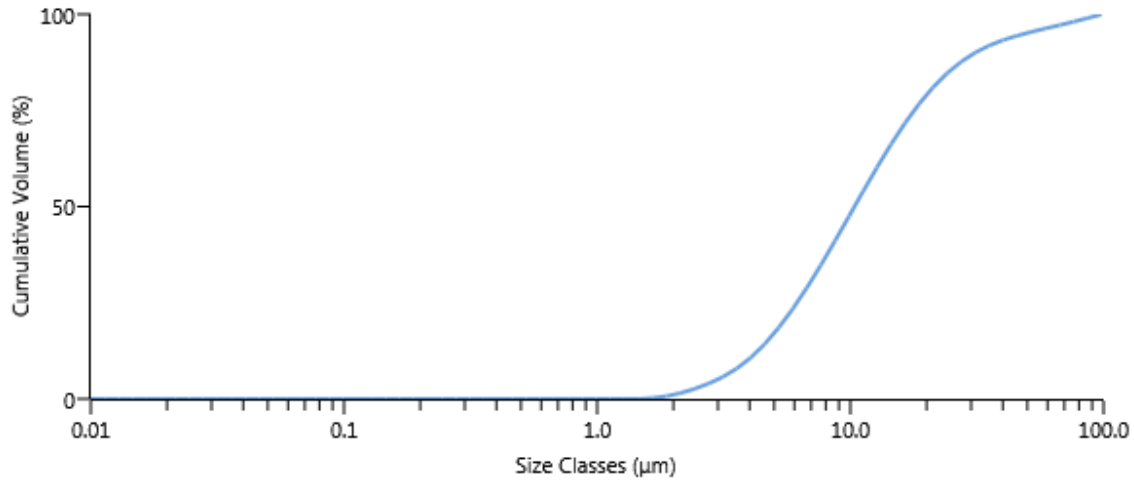

[51] 17148-10.04.2019 10:18:18

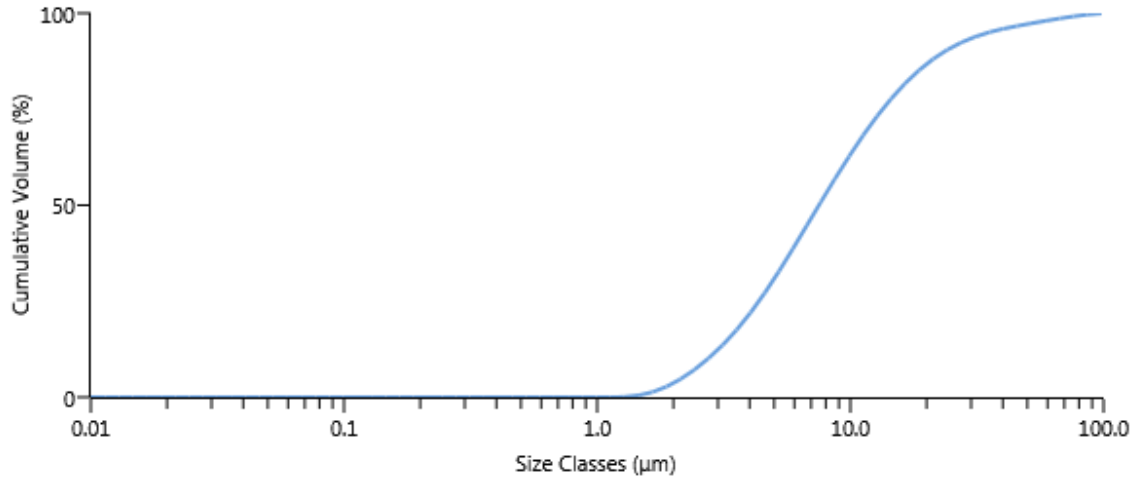

[55] 17149-10.04.2019 10:11:04

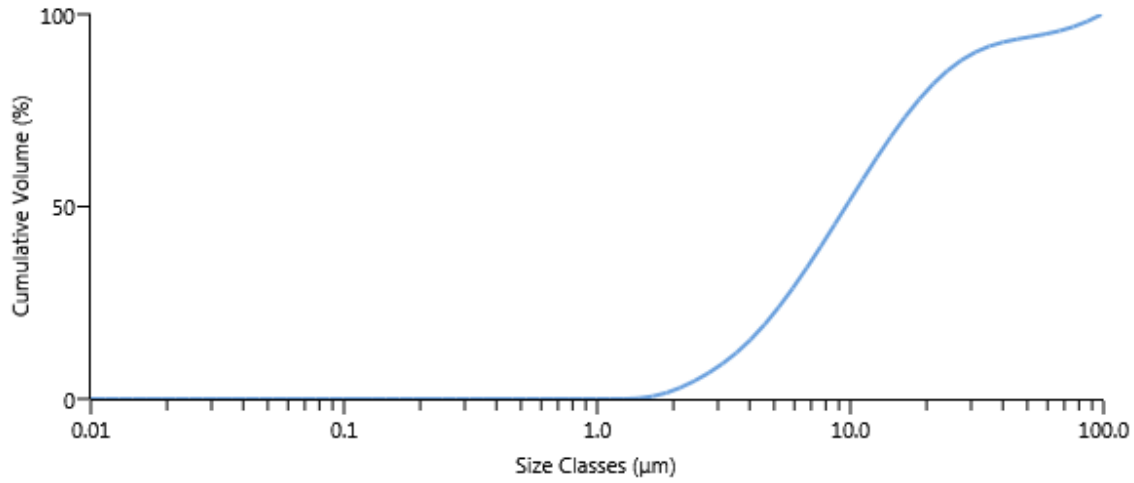

[151] 17157-10.04.2019 12:41:33

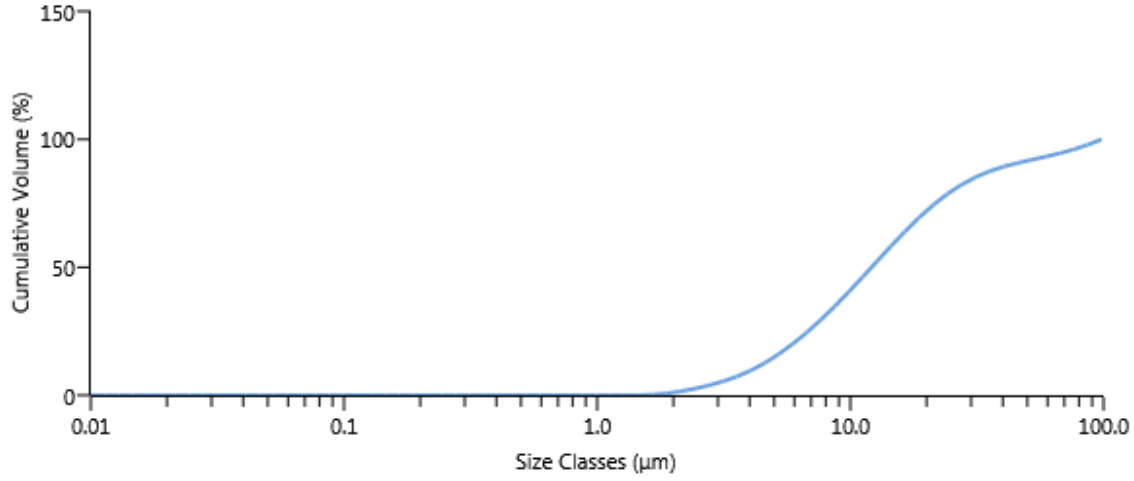

[137] 18009-10.04.2019 11:15:17

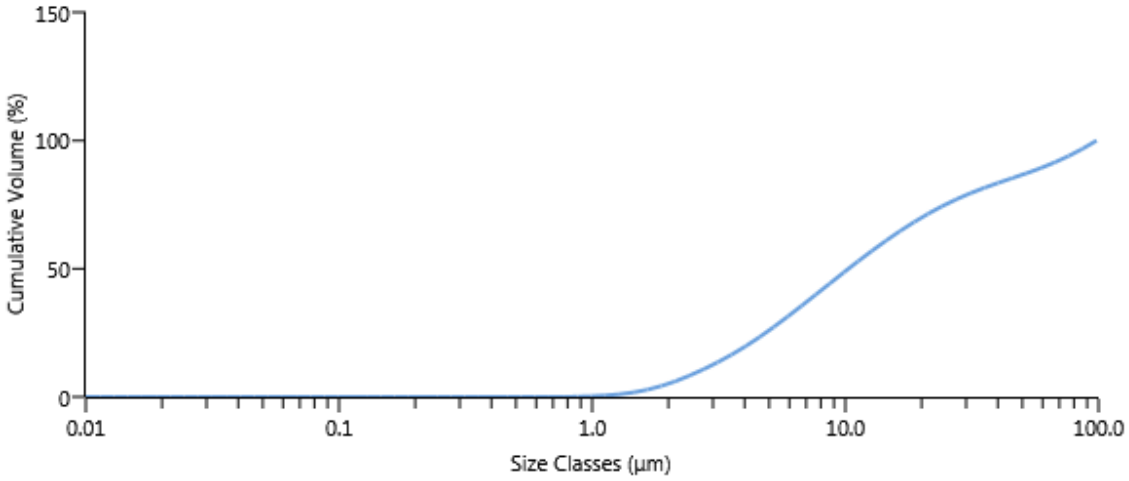

[139] 18011-10.04.2019 11:27:04

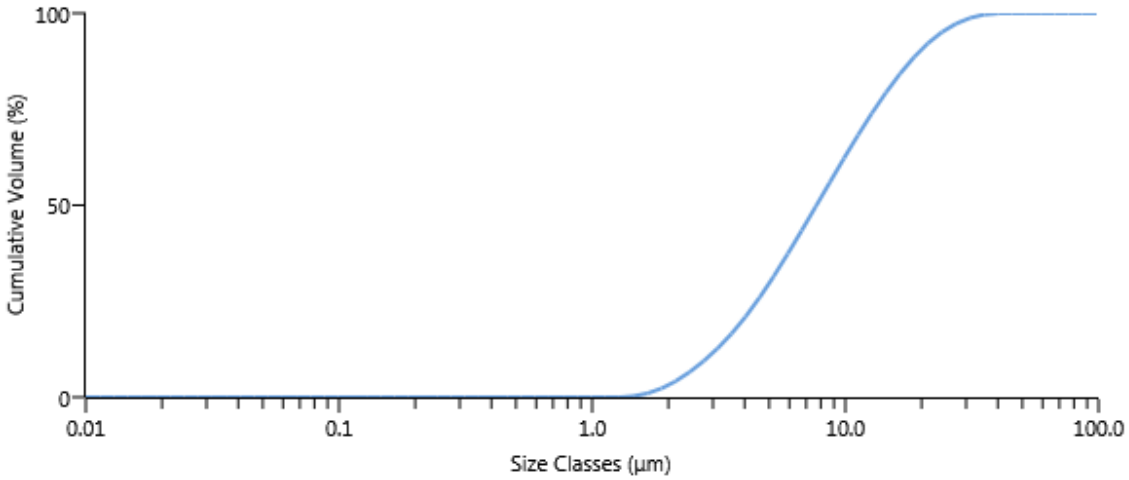

[144] 18018-10.04.2019 12:05:07

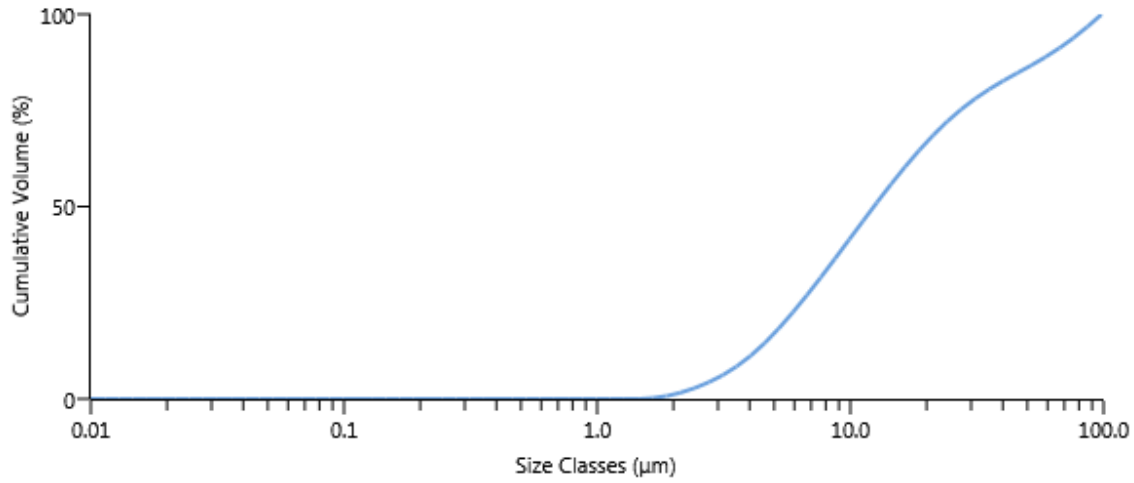

[155] 18034-10.04.2019 12:23:57

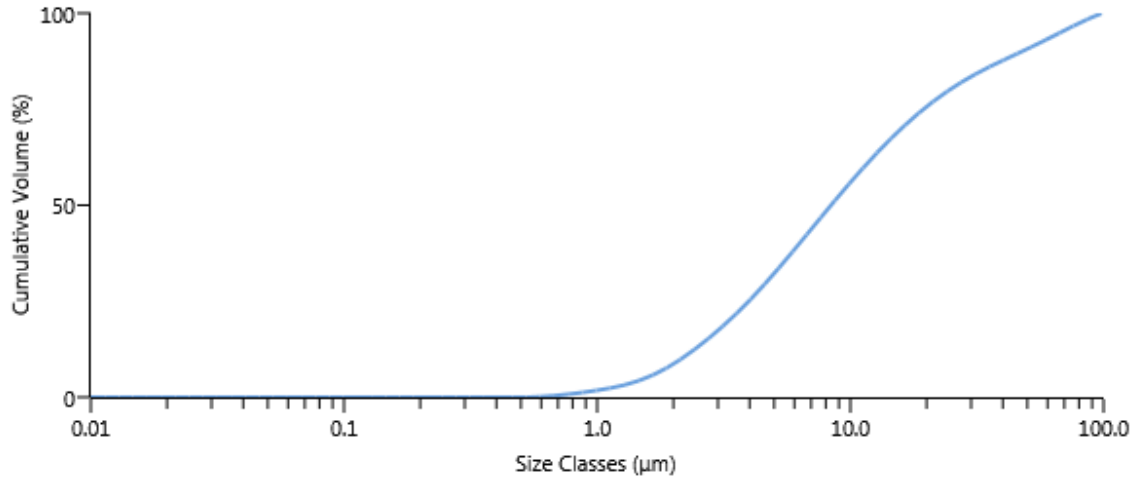

[154] 18055-10.04.2019 12:27:15

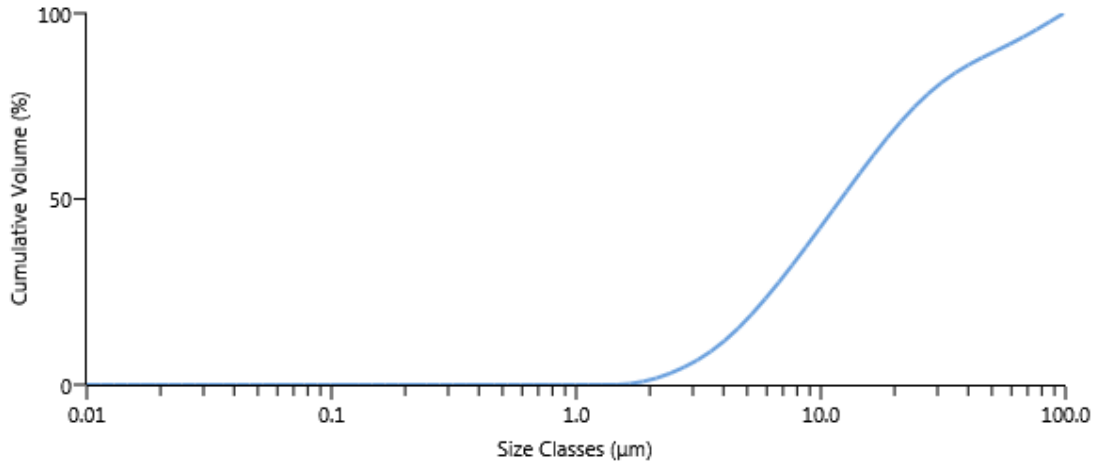

[150] 18068-10.04.2019 12:45:16

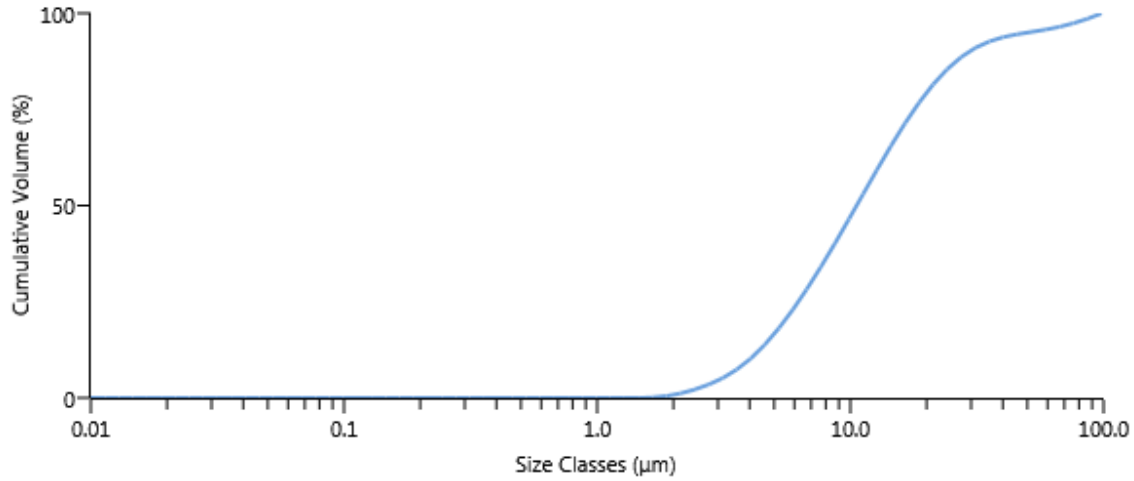

[142] 18090-10.04.2019 11:51:27

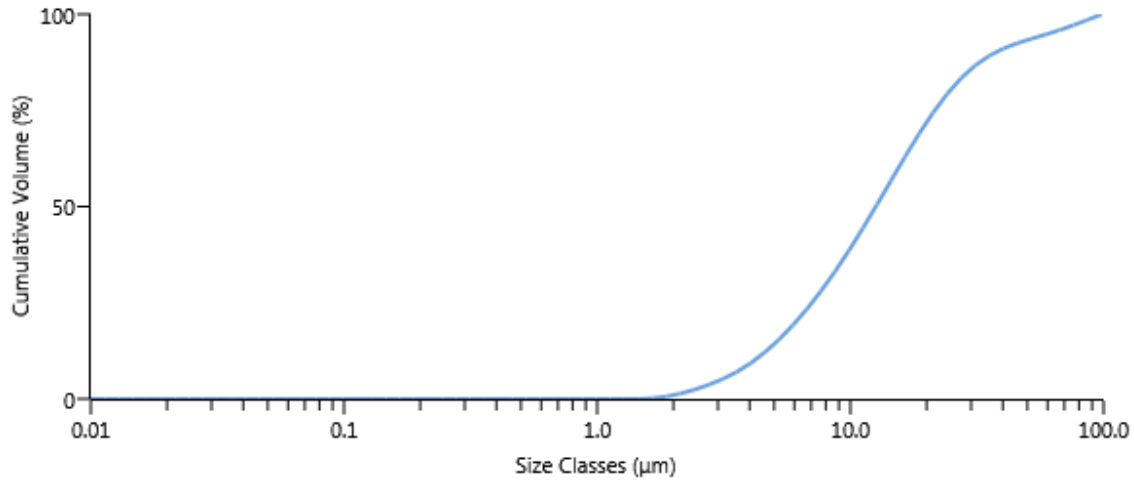

[149] 18100-10.04.2019 12:48:44

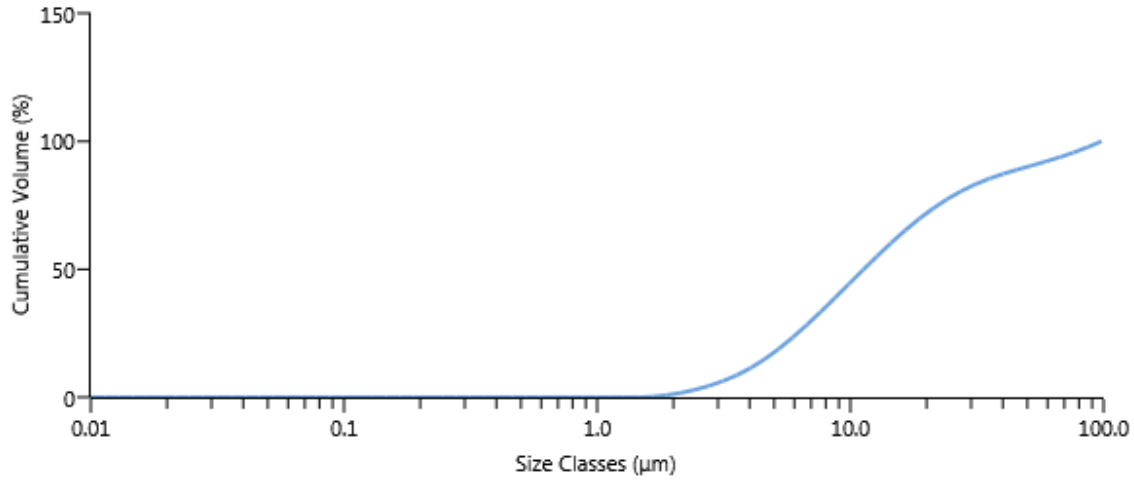

[141] 18103-10.04.2019 11:40:13

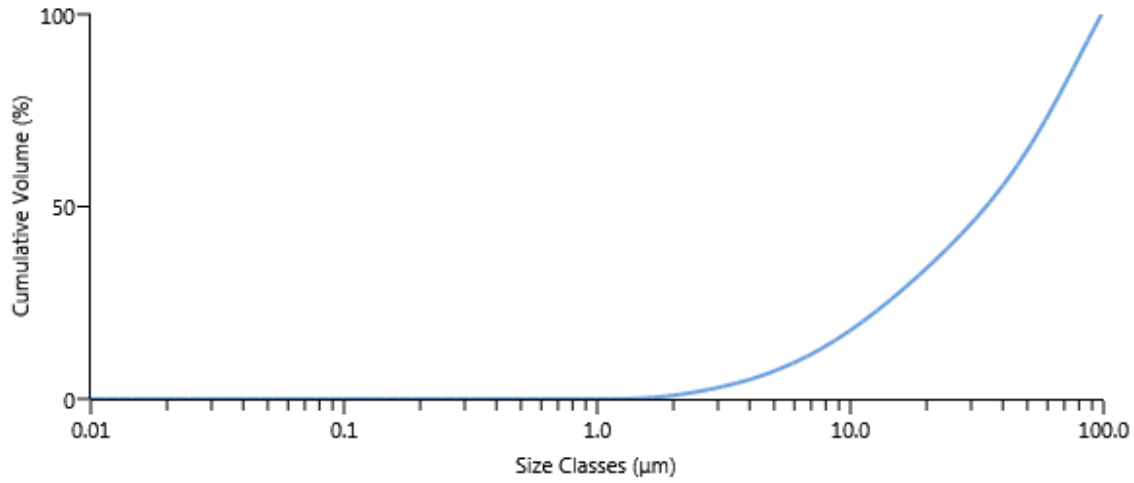

[156] 18111-10.04.2019 12:19:21

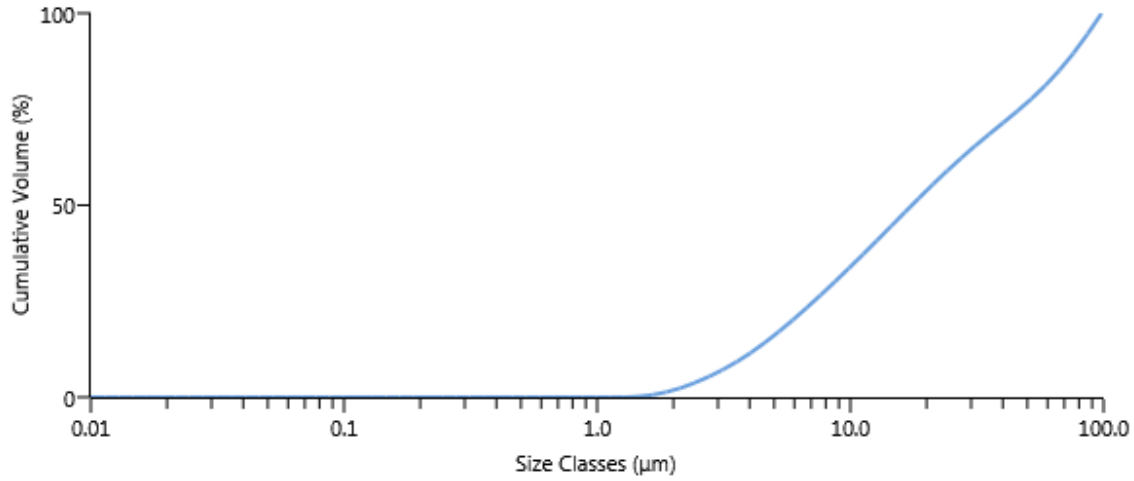

[140] 18128-10.04.2019 11:31:59

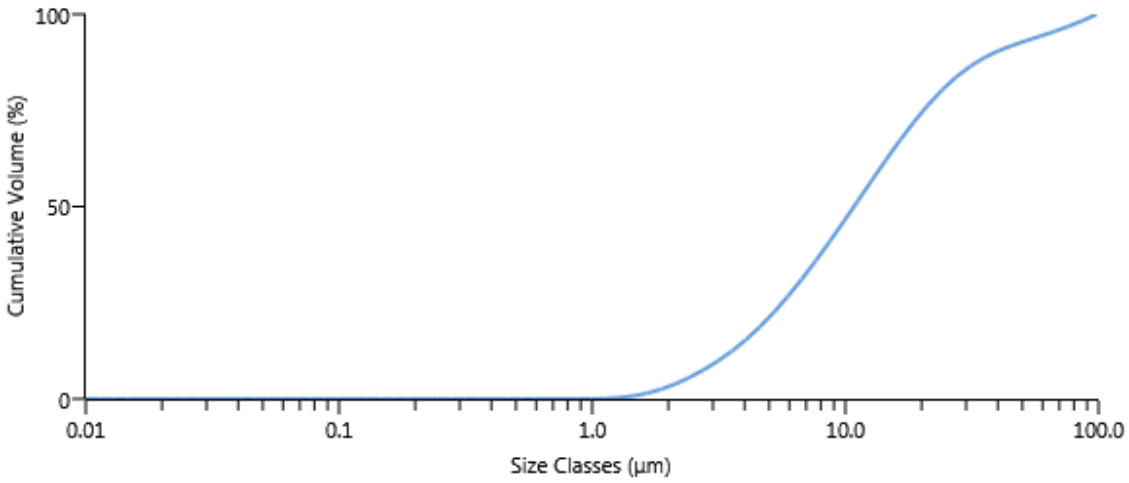

[138] 18134-10.04.2019 11:21:59